BUBBLE CHAMBER STUDIES OF NUCLEAR STRUCTURE

A dissertation submitted for the degree of Doctor of Philosophy

in the University of Oxford

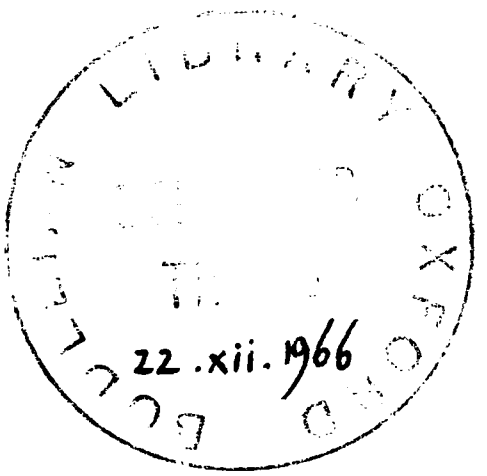

A. R. BOWDEN

The Queen's College

Oxford

'This is not the end. It is not even the beginning of the end. But it is, perhaps, the end of the beginning.

Winston Churchill, 1942.

CONTENTS

PART 3 THE ANALYSIS OF THE RESULTS

Chapter 6 Introduction to the experimental results

Chapter 7 - The cross-sections

Chapter 8 - The $C^{12}(p,2p)B^{11}$ reaction for zero and low excitation energies of B^{11}

APPENDICES

Preface

The research work reported in this thesis is the result of an experiment performed at AERE, Harwell and at the Nuclear Physics Laboratory, Oxford in collaboration with Dr. M.R. Bowman and under the supervision of Professor D.H. Wilkinson FRS. Dr. J. McKenzie and Dr. D.W. Anderson were responsible for the construction of the bubble chamber that has been used, and in many ways the experiment is a continuation of the work started by them with an experiment using a smaller bubble chamber.

The main aim of the present work has been an attempt to improve our understanding of the reaction mechanisms that determine the interaction of protons with C^{12} in the energy interval of 50 MeV to 130 MeV.

It has been a very great pleasure to work in collaboration with Martin Bowman from whom I have learned a great deal and with whom I have had many helpful discussions. Much of the work discussed in section two of this thesis is the result of our joint efforts, but the remainder of the work was performed solely by me.

I should like to thank Professor Wilkinson for the opportunity to work at the Nuclear Physics Laboratory and for his support and encouragement on the many occasions when it has been needed. It has been particularly interesting to watch the development of the laboratory from its inception with a small nucleus of people to the very large and active organization that it is now.

A bubble chamber experiment cannot be conducted without a great deal of support from many sources. I am greatly indebted to very many people for their generous help, and I should particularly like to thank:

Mr. S.A. Tolan and other members of the workshop staff for their very substantial work on the apparatus;

Mr. B. Rose for the facilities made available to us by the Cyclotron Division at AERE, Harwell, and the crew of the cyclotron whose efforts were responsible for the smooth running of our proton source;

Mr. Cyril Band for his continued willingness to produce photographs and reproductions at short notice;

the large number of physicists and assistants who made possible the use of the semi-automatic measuring and scanning machines, and in particular Mrs. Janet Warne for her very conscientious and hard work at all states of the data reduction process;

Professor L. Fox, for the use of the Mercury computer and later the KDF9 computer, and Dr. C. Phelps for advice and assistance concerning these machines.

I am very grateful to Professor A.B. Clegg and to Mlle. T. Yuasa of Orsay for the many helpful discussions that I had with them concerning the analysis and interpretation of the experimental results.

I shall always be grateful to my future wife, Jill, for her immense patience, her very hard work in the data reduction stages of the analysis, and her assistance in the compilation of the thesis.

I should like to thank Miss Gill Wymer, my typist, for her patience with me and for her careful presentation of the thesis in its present form.

My thanks are also due to the Department of Scientific and Industrial Research, the University of Oxford, and the English Electric Company, for financial support during the period of research.

July 1966

A. R. Bowden.

Abstract

The proton-C^{12} interaction has been investigated using a twelve-inch propane bubble chamber and the full energy proton beam from the Harwell synchrocyclotron.

A series of experiments on the external proton beam led to the establishment of a beam with an energy spread of less than 0.5 MeV; this enabled the bubble chamber to be used at the limit of its resolving power which was then determined by straggling.

2-prong, 3-prong and 4-prong events have been analysed. The quasi-elastic nature of the reaction $C^{12}(p, 2p)B^{11}$ g.s. has been confirmed and its cross-section has been seen to be independent of the proton energy from 50 MeV to 130 MeV and equal to 16 ± 1.5 mb. The energy independence of the cross-section is shown to be explained by the operation of the Pauli principle within the nucleus.

The (p, 2p) reaction leading to the low excited states of B^{11}, the 2-prong events with high energy-losses (when reconstructed on the assumption that they are (p, 2p) reactions), the 3-prong events, and the 4-prong events have been analysed with a view to establishing the reactions and the reaction mechanisms giving rise to them. The analysis was facilitated by setting up a reaction model, of the Monte Carlo type, to calculate the energies of final reaction products from various hypothesized reactions. The conclusion reached is that multiple scattering of nucleons

within the nucleus is the key to the production of the above-cited events; intranuclear nucleon cascades are set up which lead to reactions of the type $C^{12}(p, 2pxn)B^{11-x}$, $C^{12}(p, 3pxn)Be^{11-x}$ and $C^{12}(p, 4pxn)Li^{9-x}$, where $x = 1, 2, \ldots$ With the exception of the quasi-elastic (p, 2p) reaction the reactions with $x=0$ contribute only a small part of the total cross-sections.

There is evidence that the production of Be^{8}, or two α-particles, as the final products of cascade and evaporation mechanisms is highly favoured and as an interpretation of this it is suggested that α-particle substructures in C^{12} are important in influencing the course of the proton-C^{12} reaction. There is no evidence for a significant proportion of α-particles amongst the reaction products but this could well be due to the fact that the probability of observing an α-particle is zero for α-particles below 16 MeV and only reaches unity at an energy of 40 MeV.

Part 1 Introductory Remarks

CHAPTER 1

INTRODUCTION TO THE PHYSICS AND METHODS

1.1 The experiment

In the experiment, C^{12} nuclei are bombarded with protons of energy between 50 MeV and 130 MeV, with a view to obtaining a better understanding of the reaction mechanisms that are important in this energy region for the light nuclei.

Because the internucleon law of force is still not completely understood there is no fundamental theory of nuclear matter as there is a theory to account for atomic electron structure, and the advancement of our understanding of the nucleus is based upon the models put forward to interpret experimental results. These models can be divided into two classes: those concerned with the structure and stationary states of nuclei, and those concerned with reaction mechanisms and so with the behaviour of nuclear matter under perturbation. To study the structure of the nucleus it is necessary to perturb the stable configuration of its nucleons, so the two types of models are interrelated and tend to develop together. It has been found to date that different models are needed to describe different aspects of nuclear behaviour and no single model has been found that can encompass all the experimental results. Thus, for example, the Independent Particle Models, which can account for a wide range of experimental information such as pick-up reactions, knock-out reactions,

the giant resonance, etc., fail by up to two orders of magnitude to predict the quadrupole moments of nuclei with $90 < N < 114$ or $Z \geqslant 88$ (the maximum quadrupole moment calculated on the basis of the deformation of one nucleon orbitals is $\sim 3 \times 10^{-25} cm^2$, whereas typical measured values in the above ranges are $\sim 10^{-23} cm^2$). However, the Collective Model, which can account for these quadrupole moments, fails to yield any detailed information about the single particle aspects of nuclear behaviour.

A summary of the interpretive framework relevant to the experiment is given in the next section.

A propane bubble chamber has been used for the study and this provides both the target nuclei and the means of detecting the charged particles resulting from the proton-carbon reactions. The limitations of the apparatus are discussed in section 1.3.

The reactions that have been studied are those in which one or more charged particles are knocked out of the nucleus. Details have been accumulated by careful measurement for all the reactions leading to two or more observable bubble chamber tracks. The 2-prong events have been unambiguously divided into those originating from interactions between incident protons and target hydrogen nuclei (henceforth referred to as hydrogen events), and those originating from interactions of the incident protons and target C^{12} nuclei (carbon events). The events representing the reaction $C^{12}(p, 2p)B^{11}_{g.s.}$, in which one proton from a p-state in the nucleus is cleanly knocked out (p-shell event), have been well separated from the other carbon events.

Of the events with more than 2 prongs, 89% are 3-prong events and 11% are 4-prong events (one 5-prong event was seen). Because of the small number of 4-prong events (55 of the 84 detected were measurable) and the poor accuracy of the information obtained from them due to measurement uncertainties on very short tracks, these events are dealt with only briefly. The 3-prong events have been the subject of a more detailed analysis and it is seen that most of them cannot be attributed to the $C^{12}(p,3p)Be^{10}$ reaction. The complex nature of these events explains the difficulty experienced by ANDERSON (1969) in drawing any conclusions from the analysis of the twenty-seven 3-prong events observed in the four inch propane bubble chamber.

1.2 Interpretation of high energy nucleon-nucleus reactions

The present theoretical framework for the interpretation of the nucleon-nucleus reaction mechanism in the energy range relevant to the current experiment is based upon the 'direct interaction' concept established by SERBER (1947). It was at this time that the first high energy nucleon beams became available and it was the experimental work of COOK et al. (1948), on the reactions of 90 MeV neutrons with a wide range of target nuclei, that provided the first experimental evidence for the validity of the model.

Until this time the predominant theory for the interpretation of low energy experimental information had been based upon the "compound nucleus" theory of BOHR (1937). At energies of a few MeV and below, the nucleon de Broglie wavelength ($\gtrsim 10^{-12}$cm) is much larger than the typical light nucleus radius

($\sim 4 \times 10^{-13}$ cms), and its mean free path in nuclear matter ($\lesssim 10^{-14}$ cms) is much less than the nuclear radius. The incident nucleon, on entering the nucleus, is caught up in the gas-like motions of the nucleons, and the energy it carries in with it is rapidly shared amongst all the nucleons. Once this has happened a relatively long time will elapse before sufficient energy is concentrated in any one nucleon to enable it to escape from the system; the narrow resonance widths measured in slow neutron (< 100 eV) absorption experiments indicate a lifetime of the order of 10^{-15} secs and even at several MeV excitation the lifetime is still very long ($\sim 10^{-18}$ secs) compared with the time it would take the incident nucleon to cross the nucleus ($\sim 10^{-21}$ secs).

At energies above 100 MeV the de Broglie wavelength of the incident nucleon ($\lesssim 5 \times 10^{-14}$ cms) is much smaller than the nuclear radius and, also, the reduction in the nucleon-nucleon cross-section with increased energy increases the mean free path of the incident nucleon ($\gtrsim 5 \times 10^{-13}$ cms) to a size comparable with the nuclear size. The relatively small size of the incident nucleon and the nuclear transparency thus make it possible to visualize the nucleus as a collection of individual nucleons, and the incident nucleon-target nucleon collisions within it as classical billiard-ball type collisions or 'direct interactions'. The incident nucleon, which crosses the nucleus in a much shorter time than the time between collisions of the nuclear nucleons, no longer becomes trapped in the nucleus, and the characteristic reaction time is of the order of 10^{-22} secs. Although the relevant conditions are not fully met at energies much below 100 MeV, considerable success has been achieved

by applying the direct interaction concept down to energies as low as 5 MeV (LANE & WANDEL 1955).

The description of the complete reaction induced by a high energy nucleon is usually separated into two parts.

In the first, an intranuclear nucleon cascade, characterized by a series of two-body direct interactions is assumed to develop within the nucleus; the latter manifests itself through:

(a) the Pauli principle (forbidding low energy transfer scatters),

(b) the momentum distribution of the struck nucleons, and

(c) the change in the kinetic energy of nucleons as they cross the nuclear boundary.

Bearing in mind these nucleus effects, the two-body collisions are assumed to be characterized by the free nucleon-nucleon interaction. This premiss, known as the Impulse Approximation, has been formalised by CHEW & WICK (1952) under the following assumptions:

(a) the incident particle interacts with only one nucleon at a time,

(b) the binding forces between the constituents of the system are negligible during the decisive phase of the collision, when the incident particle interacts strongly, and

(c) the amplitude of the incident nucleon wave is not appreciably diminished in crossing the nucleus, i.e. the nucleus is virtually transparent to the incident nucleon.

The cascade is visualized as continuing until each nucleon involved either has

escaped from the nucleus or has had its energy reduced below the minimum required for it to escape direct from the nucleus (in this case the remaining energy is assumed to be shared amongst the remaining nucleons). The whole cascade develops very rapidly and is over in a time less than 10^{-22} secs. Generally speaking, the residual nucleus is left in an excited state and can be compared with the excited compound nucleus of the Bohr low energy model, although the excitation energies are normally much larger.

In the second part of the reaction, we are concerned with the de-excitation, by particle emission, of the nucleus resulting from the cascade stage. This particle evaporation is usually treated by the statistical model of the nucleus and the WEISSKOPF (1937) evaporation theory and the decay modes are sensitive to parameters such as binding energy and the Coulomb barrier.

For a nucleus with excitation U, the probability per unit time that a particle of type i with binding energy B_i and spin S_i is emitted in the energy interval de_i at e_i is:

$$W(e_i)de_i = \frac{2S_i + 1}{\pi^2\hbar^3} \mu_i \sigma_i(e_i) e_i \frac{\rho'(U-B_i-e_i)}{\rho(U)} de_i$$

where $\rho(U)$ = density of energy levels in the original nucleus at its excitation energy U - usually obtained from the statistical model

$\rho'(U-B_i-e_i)$ = density of energy levels in the residual nucleus

μ_i = reduced mass of the system after emission

$\sigma_i(e_i)$ = cross-section for the exact inverse of the emission process - this term contains the Coulomb effect explicitly.

The usual method of reconstructing the evaporation part of the reaction is to follow an evaporation cascade stochastically, applying the above equation

successively until the nucleus has been reduced to some nucleus of lower mass with an excitation energy less than the threshold for particle emission.

Characteristic times for this part of the reaction are less well defined than for the direct interaction cascade due to the large variety of ways in which de-excitation may occur, but the lower limit is 10^{-21} sec.

MILLER & HUDIS (1959) write the cross-section for the complete reaction in terms of the two separate phases as shown:

$$\sigma(A, Z|A^o, Z^o, q, E) = \sum_{A'Z'} \int_o^\infty \sigma(A', Z', U', I|A^o, Z^o, q, E) \times \eta(A, Z|A', Z', U', I)dU$$

where (A^o, Z^o) characterize the target nucleus,
(A', Z'), the intermediate nucleus,
(A, Z), the final nucleus, and
q, the incident particle.
$\sigma(A', Z', U', I|A^o, Z^o, q, E)$ is the differential cross-section for the formation, in the first stage, of the nucleus A'Z' with spin I and excitation energy in the interval dU at U, and
$\eta(A, Z|A', Z', U', I)$ is the probability that the product nucleus A, Z remains after the de-excitation of A'Z'.

Both stages of the reaction lend themselves to analysis by the Monte Carlo method of calculation. For the light nuclei, several calculations have been reported for the cascade stage of the reaction and one particularly successful calculation has been reported for the complete reaction for protons with C^{12}. Some of these results are summarized below.

1.3 Monte Carlo calculations

GOLDBERGER (1948) was the first to use the Monte Carlo method to simulate an intranuclear nucleon cascade. His calculation was for neutrons

of 87 MeV incident upon a heavy nucleus of radius [illegible] $\times 10^{-13}$ cms; he used a zero temperature Fermi momentum distribution for the nuclear nucleons (E_F = 18 MeV), and assumed that they were contained in a uniform density spherical nucleus represented by a square well potential 26 MeV deep. The calculations were performed graphically in two dimensions and only 100 incident neutrons were followed. Some of the results obtained are tabulated below:

No. of particles emerging from the nucleus	No. of cases	Average excitation energy of the residual nucleus
	[illegible]	94.5 MeV
1	[illegible]	41.[illegible] "
2	21	35.2 "
[illegible]	2	40 "

15 neutrons passed through the nucleus without collision; this number corresponds closely to that expected from the total measured cross-section for neutrons on Pb.

Of the particles emerging with an energy greater than 15 MeV, 36 suffered 1 collision, 2[illegible]: 2 collisions, 3: 3 collisions, 4: 4 collisions and 1: 5 collisions.

It is immediately evident that an abundance of data directly comparable with experimental results is produced by the method, but it was not until high speed computers became available that the method could be developed into a powerful tool. With computers, calculations could be made in three dimensions

for a wide range of nuclear parameters, and enough cases could be followed to make statistical variations in the results insignificant.

Essentially, the Monte Carlo method for simulating nucleon cascade reaction results consists of following, for a large number of cases, the progress of a nucleon, and the products of any of its collisions, through a target nucleus until all the particles of the cascade either have escaped from the nucleus or have been absorbed by it. The complete reaction is split up into a series of basic parts, and for each part a random selection is made from a choice of equally probable occurrences; the following steps are usually taken in reconstructing each cascade:

1. the point of entry into the nucleus is chosen;
2. the distance of travel to a collision position is chosen;
3. the position of the collision is examined to see whether or not it lies within the nucleus; if it does not, the complete history of the particle has been followed and its angle and energy are stored. If it does lie within the nucleus, then;
4. the nature of the struck particle is chosen (i.e. n or p, or in more sophisticated calculations d, t, α etc) together with its vector momentum;
5. the dynamics of the collision are calculated in the centre of mass frame of reference and transformed to the laboratory frame;
6. the Pauli principle is applied to see whether or not the collision constructed in step 5 is "allowed"; both particles must have energies

above the Fermi energy for the collision to be allowed. If the collision is forbidden, the calculation is recommenced at step 2 and a new distance (from the collision point) is chosen, etc;

7. for an allowed collision the histories of the two product particles are followed;
8. the cascade is followed until all the particles either have escaped from the nucleus or have been absorbed by it;
9. the residual nucleus excitation energy and the case history of the cascade are stored and the next incident nucleon is followed from step 1.

METROPOLIS et al. (1958), using the Los Alamos "Maniac" computer made extensive calculations for cascade reactions for nucleons in the energy range 100–400 MeV on nuclei ranging between Al^{27} and U^{238}. The results presented were in good agreement with experimental results from photographic plate experiments by BERNARDINI et al. (1952) and FRIEDMAN (1956) for the distribution of the number of knocked-out protons and for their angular distributions. The excitation energy of the residual nucleus was found to be not very sensitive to the bombarding energy; for example, for Cu^{64} the average excitation energy of the residual nucleus changes by only 18 MeV for an incident energy change from 80 MeV to 360 MeV, and the dependence of the excitation energy on the incident energy also decreases as the mass number of the target nucleus decreases. Extrapolating the results to a mass number of 12 gives an excitation energy change of approximately 4 MeV over the same

energy range as quoted for Cu^{64}. Total inelastic cross-sections were also found to be independent of the incident energy for all the nuclei studied; this independence was attributed to the compensating effects, as the incident energy increases, of (a) the decreasing importance of the Pauli principle and hence the reduction of the mean free path of the nucleons in the nucleus, and of (b) the decreasing nucleon-nucleon cross-section. Another interesting result, presented for Cu^{64}, was the difference between the excitation energy distributions for the residual nuclei left after the knock-out of 0, 1, 2 and 3 nucleons respectively. All the distributions were found to be Maxwellian in shape except for the case of the single nucleon knock-out reactions for which the distribution was peaked at zero excitation energy. The calculated excitation energy spectra for the reactions (p, p'), (p, 2p), (p, 3p) and (p, 4p), initiated by 286 MeV protons on Cu^{64}, are reproduced in figure 1.1.

ABATE et al. (1961), following the initial suggestion of COMBE et al. (1958, 1955) found that for calculations for 300 MeV protons incident on [illegible], the agreement between calculated results and published results for cascade reactions could be markedly improved if each cascade nucleon was given a 30–40% probability of colliding with an α-cluster instantaneously formed inside the nucleus. The relative strengths of cascades producing different numbers of charged particles were found to be sensitive to the presence of substructures.

BERTINI (1963) made several refinements to the model used by Metropolis and in particular investigated the effect of non-uniform nucleon density; he used the nucleon density distribution obtained by HOFSTADTER (1956) from electron

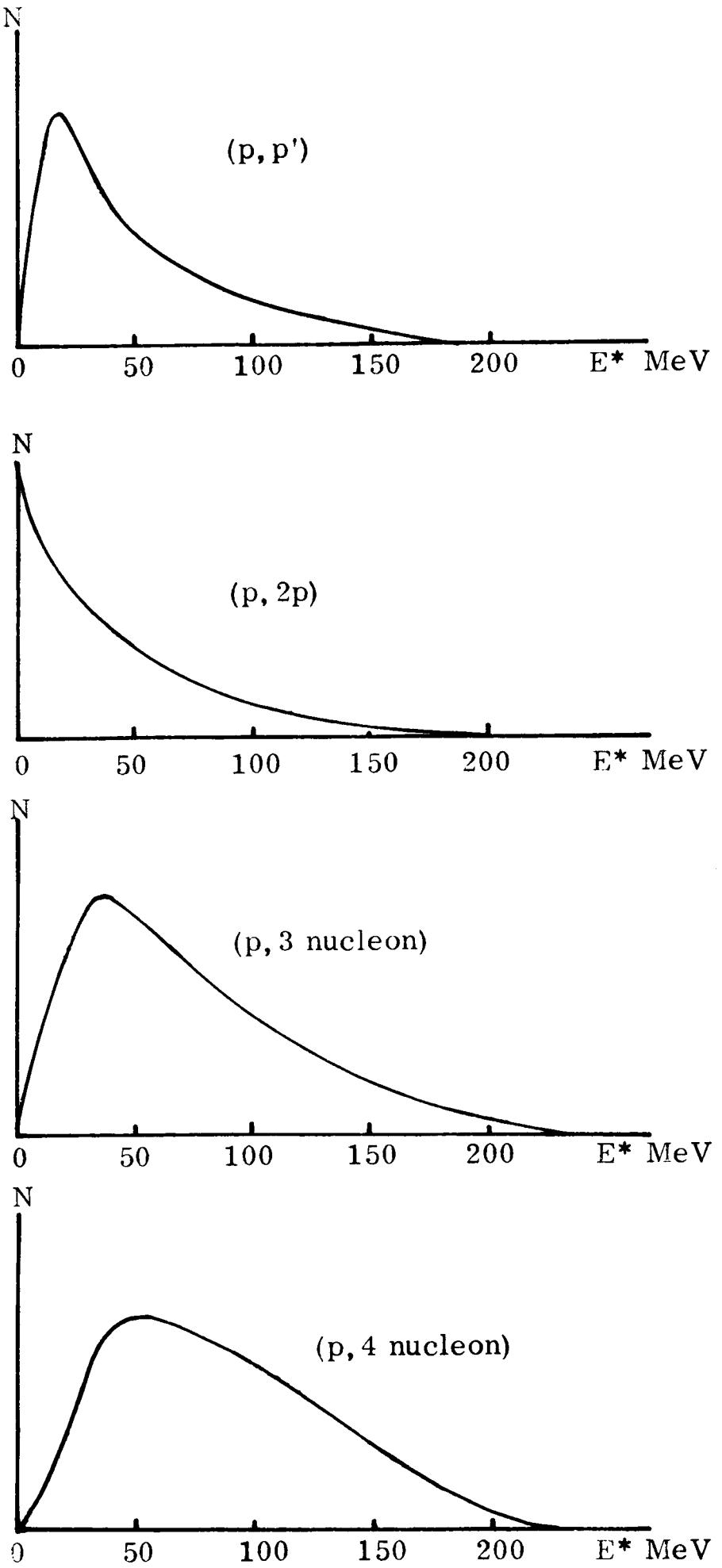

Fig. 1.1 Distributions of residual nucleus excitation energies (E*) calculated by Metropolis et al. for various nucleon cascades in Cu^{64} initiated by 286 MeV protons.

scattering experiments, and found that the main effect in going from a uniform to a non-uniform nucleon density was due to the increase in nuclear size when a diffuse edge is used. Generally, the results were similar to those of Metropolis. BERTINI (1964) has also calculated the following cross-sections for the various cascades in C^{12} (intranuclear clusters were not included in the calculations):

	Incident proton energy		
	50 MeV	100 MeV	150 MeV
p, 2p≠	41.2 mb	48.3 mb	42.7 mb
p, 2pn	13.9 mb	27.8 mb	26.3 mb
p, 2p2n	0.9 mb	4.0 mb	10.8 mb
p, 2p3n	-	0.6 mb	0.3 mb
p, 2p4n	-	0.3 mb	0.3 mb
p, 3p	2.5 mb	4.3 mb	7.4 mb
p, 3pn	0.3 mb	3.4 mb	9.3 mb
p, 3p2n	-	0.6 mb	2.2 mb
p, 3p3n	-	-	0.3 mb

≠ The probability of the residual nucleus being left with an excitation energy of less than 19 MeV was approximately 37% for the three incident energies considered.

Monte Carlo calculations on the residual nucleus decay stage of the reactions have been reported in detail only for nuclei much heavier than C^{12} (DOSTROVSKY et al. 1958) and because of the importance of the Coulomb barrier effect on the evaporation of particles, the results cannot be loosely applied to the lighter nuclei. However the general fact did emerge that decay

modes depend upon the nearness of the numbers of neutrons and protons in the residual nuclei to the closed-shell numbers. Also, the relationship between the number of evaporated particles and the mass number of the bombarded nucleus was seen to be very closely linear from A=4[illegible] to A=23[illegible]; if the information is extrapolated to A=12, a value is obtained of between 2 and 3 evaporated nucleons per reaction.

ZHDANOV & FEDOTOV (1[illegible], 1962, 1[illegible]) have reported a very interesting investigation of the proton-carbon reaction at [illegible] MeV. A nuclear emulsion was loaded with diamond dust (particles of 5-7μ in diameter) and by analysing those events occurring within the diamond particles a pure sample of proton-carbon reactions was obtained; thus two of the usual unsatisfactory aspects of emulsion experiments were eliminated, i.e. (a) the problem of separating the events from heavy and light nuclei and (b) the fact that events from the light emulsion nuclei (C, N, O) are inseparable and are presented together. The 54[illegible] disintegrations of C^{12} were attributed to the various reaction modes in the proportions shown in the second column of the table below.

The table shows that the most probable type of disintegration is that involving the break up of one α-particle substructure in C^{12} (i.e. modes p,3p2α and p,3pBe).

The reaction was analysed using a Monte Carlo method for the direct interaction cascade part of the interaction and a statistical model calculation for the decay of the residual nucleus. The cascade calculation was based upon that of Abate and it provided the distribution of residual nuclei, the cascade products and the residual nuclei excitation energies.

Type of disintegration	Percentage of total no. of disintegrations: Experimental	Theoretical
(p, pn) + (p, p2n)≠	13.1 ± 1.0	1[illegible]
(p, 2p) + (p, 2pn)≠	12.2 ± 1.[illegible]	11
p, 3p3α#	[illegible] ± [illegible]	28
p, 5pα	12.2 ± 2.2	15
p, p3α	7.[illegible] ± 2.0	11
p, 2pαLi	7.[illegible] ± 2.0	10
p, 3pBe	6.5 ± 2.0	5
p, 2p3απ⁻	3.2 ± 1.0	4
p, 7p	2.4 ± [illegible].8	1
p, 4pLi	1.7 ± 0.7	[illegible]
p, 6pαπ⁻	[illegible].6 ± 0.5	2

Protons are detected to energies below 1 MeV

The decay part of the calculation, made analytically, was based upon the hypothesis that the energy released within the nucleus is statistically distributed among the particles, so that the possible final states appear with frequencies proportional to their statistical weights. It was found that the probabilities for

---

≠ Taken by the authors from other authors' work

The neutrons from the break-up are not shown. The p is stated to stand collectively for the singly charged particles p, d, t and π^+, but from the discussion in the 1 64 paper it seems that the only important contribution comes from the protons; however this point is not made clear.

different decay modes were very sensitive to the excitation energy of the residual nucleus and to the binding energy corresponding to the given decay, and that the stability of the α-particle played a dominant role in determining the pattern of the decay (cf. Postrovsky's results). By combining the cascade calculation results with the decay mode results to form cross-sections of the type shown in the last section, the relative yields for the various overall reaction types were obtained; these are shown in the third column of the table. The agreement with the experimental results is very good and in particular the experimentally determined dominance of the p,3p2α (and p,3pBe) reactions is accounted for.

The weak dependence of the residual nucleus excitation energy on the energy of the incident nucleons (Metropolis results) suggests that the results of Zhdanov & Fedotov should be applicable, at least qualitatively, to the experimental results at 53-130 MeV of the present experiment.

1.4 The quasi-elastic $C^{12}(p,2p)B^{11}$ reaction

This reaction is an example of the simplest possible type of cascade reaction; the incoming nucleon collides with one target nucleon only and both nucleons leave the nucleus without any further interactions. This picture of the interaction has been formalized in the Impulse Approximation, and according to the Independent Particle Shell Model of the nucleus, in which each nucleon is pictured as moving independently in the average field created by the presence of all the other nucleons, the momentum of the recoiling residual nucleus will

be equal and opposite to the momentum that the target proton possesses when it is struck. This follows from the fact that the target nucleus as a whole is at rest. Therefore the recoil nucleus momentum distribution, when corrected for kinematical phase space effects should yield the nucleon momentum distribution for the target nucleus. Also, following from the Independent Particle picture, each nucleon of the nucleus lies in a discrete energy state in the nuclear potential well so that the energy loss in the reaction reflects the occupation of the various energy-states of the nucleus.

That these simple notions of the nucleus and the nucleon-nucleus interactions are broadly correct has been shown by many experimenters. For example, in the work of TYRÉN et al. (1958) at 185 MeV, GOODING & PUGH (1960) at 150 MeV, and GARRON et al. (1962) at 155 MeV, the energy loss distributions obtained from (p, 2p) reactions on nuclei from Li^7 to Ca^{40} showed quite distinctly the presence of discrete energy levels within the nucleus. It is found that the experimental peaks can be understood very well in terms of the extreme jj-coupling shell model[≠]; the peaks for nuclei of mass numbers (A) less than 12 correspond to the knockout of s-shell nucleons and $p_{3/2}$-shell nucleons, and for nuclei with A > 12, the knockout of $s_{1/2}$, $p_{3/2}$ and $p_{1/2}$ nucleons. Also, the nucleon momentum distributions derived from the recoil

---

≠ CLEGG (1963) has shown that, although a state of intermediate coupling midway between the jj-coupling model and the LS-coupling model prevails in the 1p-shell, some properties of the nucleus can be consistently close to what is expected from one of the extreme coupling schemes.

nucleus data by many authors, e.g. WATTENBERG et al. (1956), CLADIS et al. (1952), McEWEN et al. (1957), AZHGIREI et al. (1959), DOWELL et al. (1960), ANDERSON & McKENZIE (1960) are approximately the same as those expected from nucleons in a potential well of the harmonic oscillator type (in general, Gaussian momentum distributions with 1/e values corresponding to nucleon energies in the range 10–20 MeV were reported).

At first sight it is difficult to reconcile the success of the Independent Particle Model, which suggests the existence of weak long-range internucleon forces, with the well known experimental fact that the forces between nucleons are very strong short-range forces.≠ BRUECKNER and co-workers (1955) have greatly clarified this paradox by showing that, starting from the 2-body internucleon potentials, it is possible to introduce a mathematical transformation that allows a nuclear potential to be derived by self-consistent methods similar to those used for atomic electrons by HARTREE (1928). The derived potential is very similar to the refined shell model potentials; the parts of the internucleon potentials not incorporated into the nuclear potential representation give rise to second-order "residual interactions". The result is that the independent "particles" described by the model are very nucleon-like for a wide range of observations.

≠ The evidence for the persistence of the strong internucleon forces when the nucleons are within nuclear matter comes from deuteron pick-up reactions, from meson capture from low Bohr orbits in the atom, from the nuclear photo-effect at high energies, from nucleon-nucleon interactions (see BRUECKNER et al. 1955).

Because of the presence of the residual interactions in the nucleus itself, the quasi-elastic reactions do not lead exclusively to single-particle shell model states in the product nucleus: they also lead to other states close to the single-particle states. In the energy-loss distribution studies, the presence of these secondary transitions is usually masked by the resolution width of the dominant single-particle peak. However, CLEGG et al. (1961) and AUSTIN et al.(1962) have measured the relative feeding of excited states of the residual nuclei from $C^{12}(p, 2p)B^{11}$ and $C^{12}(p, pn)C^{11}$ reactions at 150 MeV by observing the gamma-radiation from their decays. They found that the ground state of the residual nucleus was produced only 80% of the time and that states of spin $3/2^-$, $5/2^-$ and $7/2^-$ were also produced; the cross-sections found for the feeding of these states in B^{11} are shown below:

State of B^{11}	Cross-section (mb) relative to $1/2^-$ state
$1/2^-$ at 2.14 MeV	0.98
$5/2^-$ at 4.46 MeV	0.54 ± 0.11
$3/2^-$ at 5.04 MeV	0.49 ± 0.13
$7/2^-$, $1/2^+$, $3/2^+$ at 6.48 and 6.34 MeV	0.36 ± 0.12
$5/2^-$ at 7.30 MeV	< 0.3
higher bound states	< 0.16

According to calculations by GOSWAMI & PAL (1963), admixtures into the pure shell model ground state of C^{12} from 2 particle-2 hole configurations might account for as much as 35% of the intensity of the state.

The branching ratios to states of B^{11}, fed in the quasi-elastic $C^{12}(p,2p)B^{11}$ reaction, give information about the details of the C^{12} ground state wavefunction. Using the fractional parentage concept as proposed by LANE & WILKINSON (1955), the C^{12} ground state wavefunction can be written in terms of the states of the parent nucleus (B^{11} in this case) and the knocked-out particle. When a proton is cleanly knocked out of C^{12}, the various states of B^{11} will be produced according to the extent to which they contribute to the C^{12} g.s. wavefunction expansion.

However, the interpretation of experimental results in terms of the parentage concept is beset with difficulties. For example, the excited states of the residual nucleus can also be produced via initial and final state interactions: in an initial state interaction, for example, an excited state of C^{12} could first be produced, and the subsequent feeding of the B^{11} excited states by the knock-out of one proton from the excited system will reflect the parentage expansion of the C^{12} excited state and not the C^{12} g.s.. These difficulties have been encountered in the present experiment and they are discussed in chapter 8 in relation to the experimental results.

The limitations of the Impulse Approximation are also met in the analysis of chapter 8. The high momentum component in the nucleon momentum distribution, associated with correlations within the nucleus, cannot be properly probed by the nucleon knock-out type of experiment (at least, not by an Impulse Approximation analysis of the results). The inadequacy of the Approximation has been discussed by GOTTFRIED (1963). In a qualitative approach he visualized the

nucleon motion within the nucleus as being something like that shown in the full-line trajectory below.

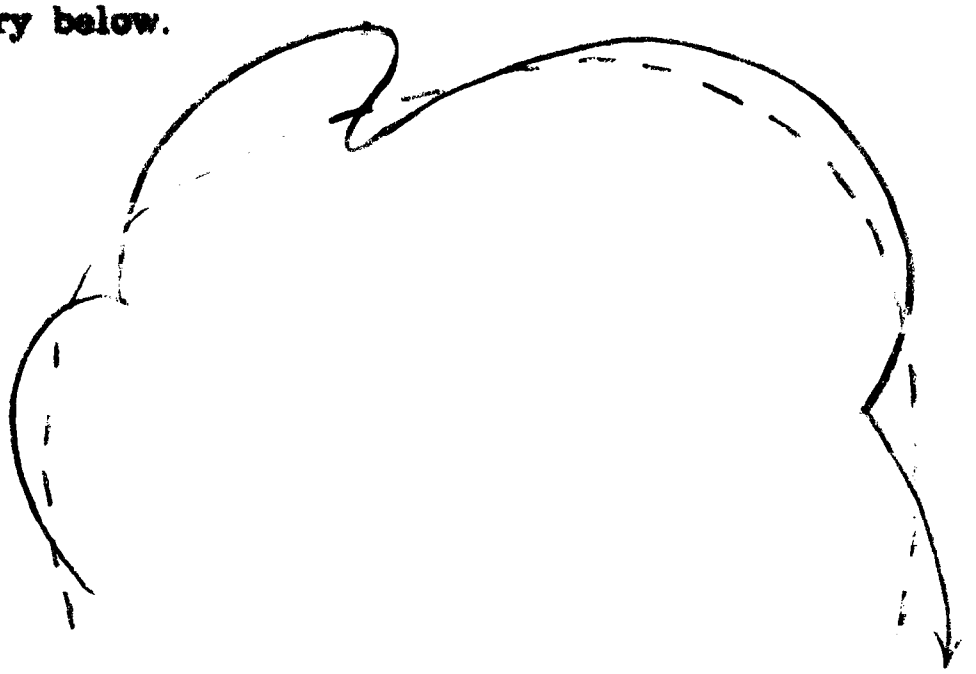

For most of the time the nucleon behaves according to the shell model picture and receives only small momentum transfers from the other nucleons: its trajectory is therefore smooth. Occasionally, however, the nucleon approaches another nucleon closely and undergoes a strong acceleration to a high momentum: these correlation effects are represented by the kinks on the trajectory drawn. In the shell model, the nucleon trajectory would be represented by the dotted curve, which is a good approximation to the slowly varying parts of the actual trajectory but a very poor approximation indeed to the kinked parts. The Impulse Approximation for a collision amounts to the replacement of the actual trajectory by its tangent at the time of collision, but in fact, because of the finite extent of the incident particle's de Broglie wavelength, the average behaviour of the target nucleon over the time of the reaction is observed. The difference between the nucleon motion represented by the tangent to the track and the motion represented by the average behaviour of the nucleon over

a finite path length is small for the smooth (shell model) parts of the trajectory but is large and arbitrary for the kinked parts of the trajectory. The Impulse Approximation analysis therefore ceases to be of use in probing the higher momentum components of the nucleon momentum distribution. However, it is to be expected that as the energy of the incident nucleon increases and its de Broglie wavelength decreases, it should be possible to detect more of any high momentum component present than at the lower incident energies. In the current experiment with an incident energy spread of 50-130 MeV this effect might be detectable.

1.5 Limitations of the apparatus

There are several important implications in the use of a propane bubble chamber for nuclear structure experiments; those relevant to the present study are summarized below.

1. The energy of the incident proton beam when it enters the illuminated region of the chamber is approximately 130 MeV, and when it leaves is approximately 25 MeV; the events recorded are therefore for this range of incident proton energies. Events in any energy range within these limits can be selected for analysis by considering events in the relevant part of the chamber. Ideally, sets of information should be collected for unique energies or at least for very limited ranges of energy. However, because the requirement for a limited energy range conflicts with the requirement for good statistics, it is necessary to analyse the data in as

large an energy slice as possible. This is determined by the range over which the mechanism being studied can be assumed not to undergo any radical change.

2. The uncertainty in the measured energy of the beam increases as the beam traverses the propane and loses energy. This arises from:

(a) the statistical nature of the slowing down process, and

(b) the magnification of any energy spread present in the original beam.

The former process is uncontrollable, but the effect of the latter can be minimized by giving careful attention to the optics of the proton beam between the cyclotron and the bubble chamber.

3. Although there are more neutrons than protons ejected from the C^{12} nucleus when it is bombarded with high energy protons, the bubble chamber does not detect the uncharged neutrons. The loss of information because of this is the major source of difficulty in the analysis of the non p-shell 2-prong carbon events and of all the 3-prong and 4-prong events.

4. A further complicating factor is that particles of different charge do not give rise to distinguishably different tracks in the propane. However the range-energy relationship for the particles in propane does depend upon their mass and their charge. The presence of deuterons, α-particles etc., can therefore only be inferred from kinematical fitting procedures, which are always complicated by the possible presence of neutrons.

5. The lowest energy particle that can be detected is that which produces one bubble in the propane, and even these particles will be difficult to detect because

of the difficulty of seeing short tracks. The minimum energies at which particles can be detected are:

p	~ 4.5 MeV
d	~ 6.2 MeV
t	~ 7.2 MeV
He^3	~ 15.7 MeV
α	~ 18.0 MeV

This source of loss is particularly serious in the case of α-particles and thus will strictly limit the observation of reactions involving them.

For all proton-carbon reactions, the residual nucleus, which can carry away a large proportion of the momentum of the final state system, is never seen.

6. The hydrogen in propane (C_3H_8) accounts for about 55% of all the 2-prong events. These hydrogen events cannot be separated from the carbon events by inspection of the film so they have to be measured together with the carbon events. On the one hand, this has the disadvantage of greatly increasing the data reduction effort, but, on the other hand, because the free proton-proton interaction has been extensively studied, it has the advantage of providing a set of data that can be used to detect systematic biases in the method of analysis. The hydrogen events also provide an easy method of measuring the resolution of the experiment.

Part 2 Experimental details and the data reduction processes

CHAPTER 2

THE TWELVE-INCH PROPANE BUBBLE CHAMBER

2.1 Bubble chambers

Development work on bubble chambers progressed very rapidly after the observation by GLASER (1952) that superheated liquids were sensitive to the passage of ionizing radiation. The chambers with dimensions of several metres, which are now being used for elementary particle physics, have been developed from the early chambers with dimensions of the order of centimetres only. A 12-inch propane chamber is large enough for nuclear structure experiments at 150 MeV. Glaser's own work, together with that of later developers, is now well documented in review articles, e.g. FRETTER (1955), DODD (1956), BUGG (1959) and BRADNER (1960).

In the present experiment the propane chamber provides both the carbon target and the means of detecting the charged reaction products. The description of the 12-inch chamber given in this chapter is not exhaustive, but emphasis has been placed on those aspects of the design that differ from the 4-inch chamber described by McKENZIE (1960) and ANDERSON (1960), and also on those aspects that gave rise to difficulties.

A general view of the chamber, from the beam-entry side, is shown in plate I, and a view of the optical system from the other side of the chamber can be seen in plate III.

Plate I

A general view of the bubble chamber.

The gas bottles in the background are not part of the apparatus.

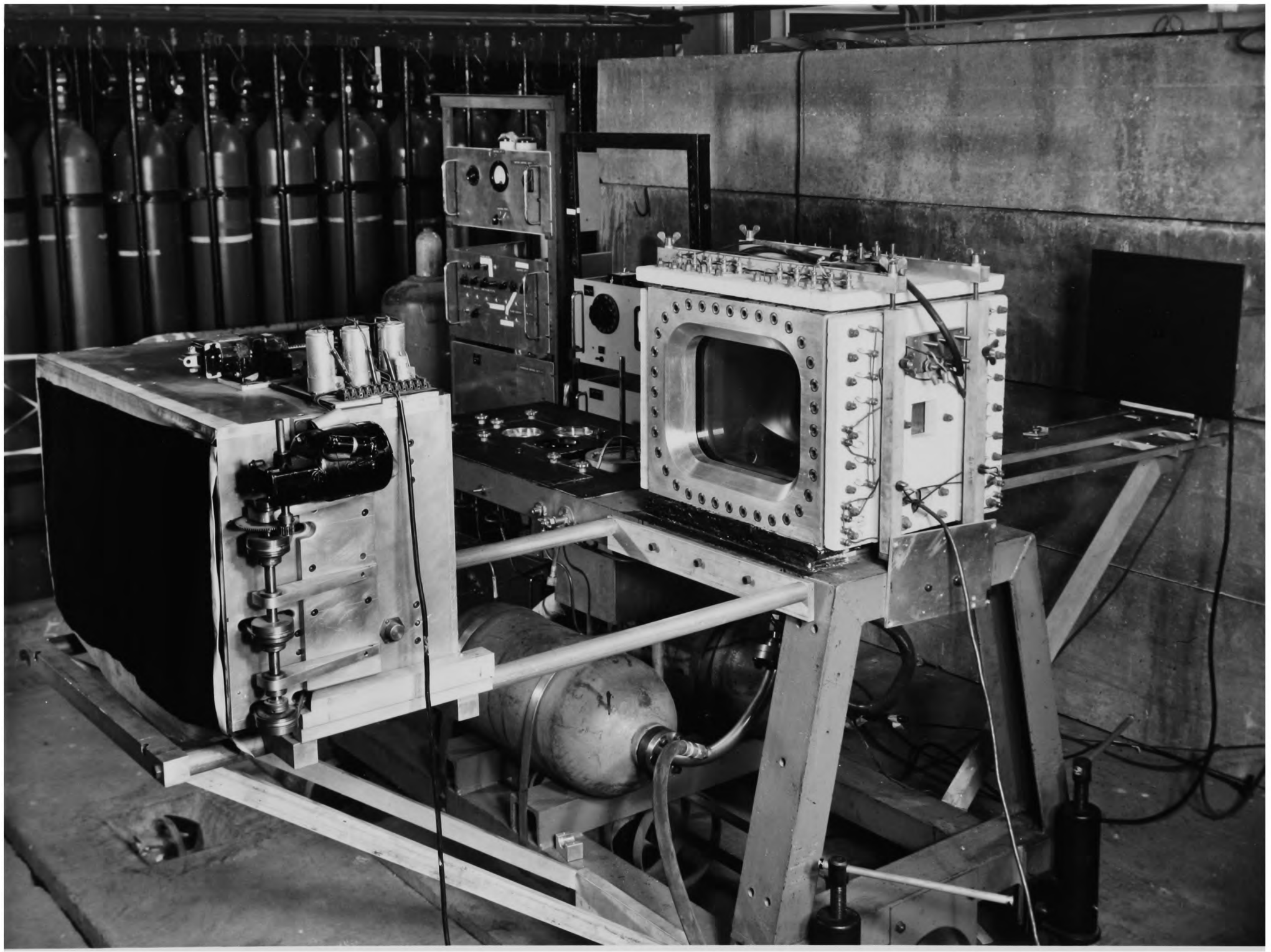

HK 14201

2.2 The chamber body

The proton energy of the beam extracted from the Harwell synchro-cyclotron is approximately 153 MeV; after the protons have passed through the dural beam entry window of the chamber their energy is 137 MeV. The window-volume of the chamber (12" x 9" x 9") was designed to allow all the charged reaction products from (p,H) and (p,C^{12}) reactions to be stopped by the propane.

Figure 2.1 shows a section through the chamber body*1 parallel to the wall containing the beam entry window. The latter, placed centrally in one of the 9" x 9" sides of the chamber, was made by machining down an area 2" x 2" from the nominal wall thickness of 3" to ½". To discourage turbulence and local boiling during the expansion of the chamber, the internal faces are polished and all edges smoothly rounded-off.

The windows are of 1½" 'armourplate' glass and are located in recesses in the 12" x 9" sides of the body; each window is clamped to the body by a 2" thick dural frame secured with 36 9/16" high tensile non-magnetic steel bolts. Sealing is effected by Gaco 'O' rings and the glass is further protected against any contact with metal by 1/16" neoprene strips. From the approximate design formula, quoted by Bugg, for toughened glass:-

$$84,000\ t^2 = p.A.f$$

---

* All asterisks in this chapter refer to appendix I, where more technical details are given.

Key to figure 2.1

H	heaters
T	thermistor
W	1½" armourplate glass windows
P	paraffin
L	condensing lens
C	window clamps
B	position of beam entry window
F	position of propane filling line
BP	composite base-plate
M	rayon reinforced rubber membrane
E	connection to expansion valve
Ch	chassis

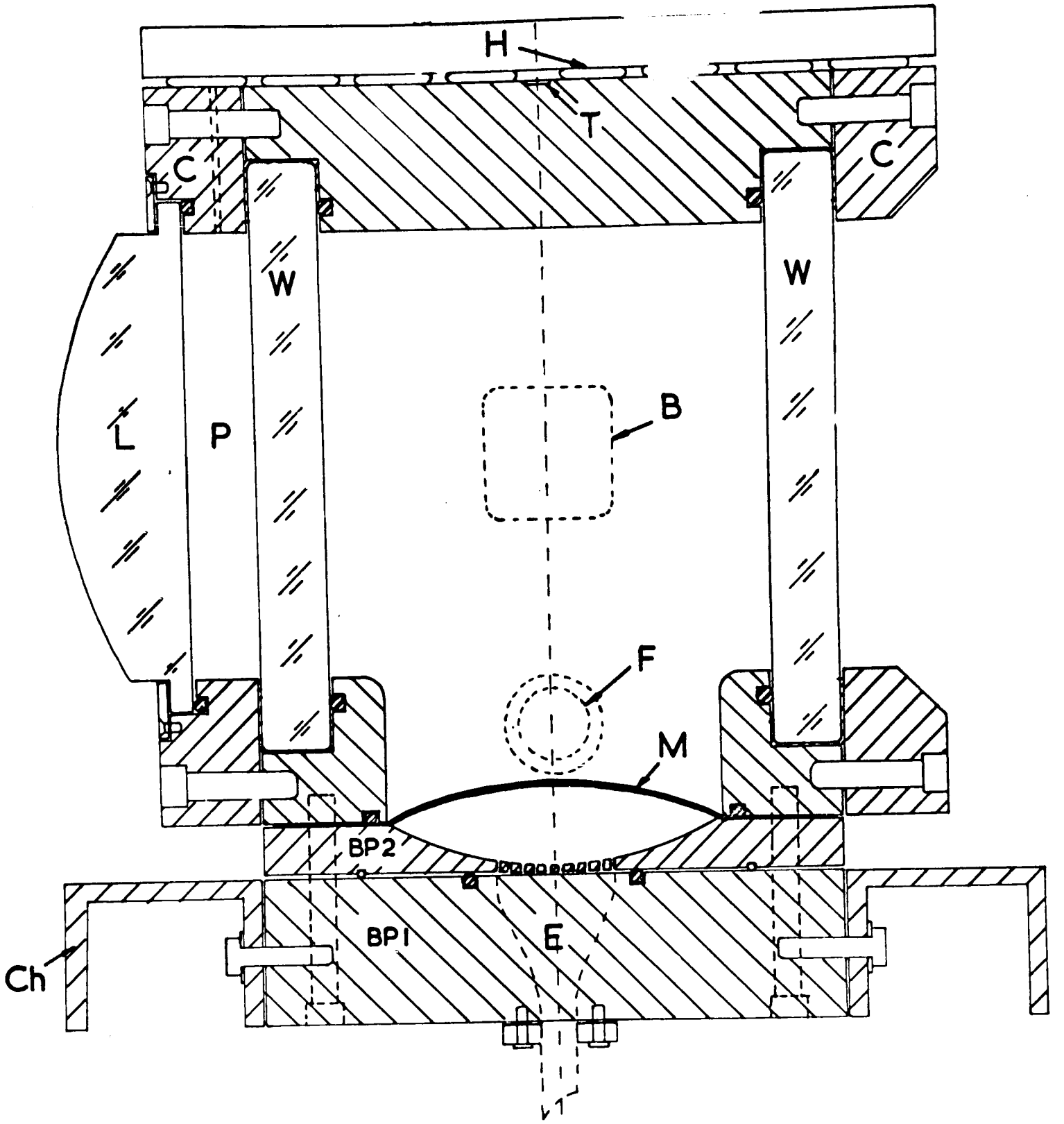

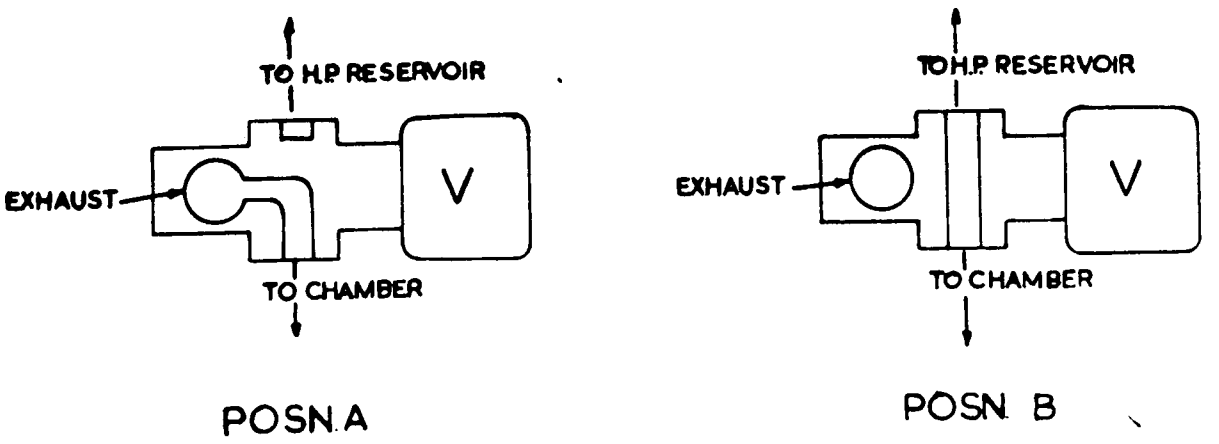

FIG.2.1 CROSS-SECTIONAL VIEW OF CHAMBER BODY

Where t = glass thickness (ins)

p = pressure difference across window (lbs/sq. in)

A = area over which pressure acts (sq. ins)

and f = factor of safety

it is seen that the design allows for a factor of safety of approximately 4.

Clamped into one of the window frames and sealed with an 'O' ring is a plano-convex polished perspex condensing lens. The space between the lens and the window is filled with paraffin, which, with a refractive index of 1.43 at 60°C, reduces optical discontinuities and leads to more efficient chamber illumination.

In the opposite wall from the beam entry window there is a hole mounted on the outside by a doubly sealing tap; this serves as a filling and evacuating line.

Twenty-four screws anchor the block to the baseplate which is, in turn, held rigidly to the mounting framework. Between the two, held by an 'O' ring seal, is the impervious membrane that isolates the propane from the high pressure air of the expansion system.

The total volume of propane in the chamber is 19 litres and the visible volume is 16 litres.

2.3 Temperature control

Sensitivity of superheated propane to ionizing radiation occurs at temperatures in the region of 60°C. To maintain the chamber at a fixed temperature in this region a surface of electrical heating elements is clamped

to three outside faces of the block (see plates I & III). To counterbalance the greater heat loss from the lower part of the chamber, caused by losses to the unheated base plates and the supporting framework, the lower elements of the side heaters are designed to dissipate more power than the upper elements.

The power to the heaters is supplied in two parts. A steady base-load power slightly less than that required to balance the heat lost to the air is supplied from the mains via a variac, and the remainder is supplied through a control unit operated by an A.C. bridge. A thermistor, located on the top of the chamber forms one arm of the bridge and the circuit is designed to switch the extra power to the heaters whenever the temperature at the thermistor drops below the predetermined control value.

To guard against any fault leading to overheating of the propane and consequent dangerous rise in pressure, a modified Bourdon pressure gauge is connected to the propane via the filling tap. This gauge is supplied with an electrical circuit designed to blow the heater fuses and give an audible alarm if the propane pressure rises above 550 p.s.i.g.

Comment on the performance of the heating unit

During the experimental run this part of the apparatus gave a considerable amount of trouble. Temperature oscillations were occasionally set up in the propane and these were sometimes large enough to cause a loss of sensitivity and a temporary halt in photography. These were usually initiated by large ambient temperature changes in the experimental area when,

due to the surface heating and control of the bubble chamber temperature, the propane conditions got out of phase with the surface conditions. Plate II shows an example of the phenomenon of foaming which occurred in one of these extreme oscillations.

A better method of temperature control for a chamber of this size has been indicated recently by the very successful scheme designed for the Oxford Freon Chamber. This used a water circuit within the walls of the chamber fed from a thermostatically controlled reservoir.

2.4 Expansion mechanism

With a chamber of the present dimensions an expansion mechanism of very small intrinsic inertia is required to ensure the rapid expansion and recompression of the propane. Rapid expansion is required to prevent the chamber from partially recompressing itself by gasket boiling etc. which would prevent the achievement of sensitivity. Rapid recompression is needed to squash-out all the gas bubbles formed, before they have time to coalesce and collect at the top of the chamber. A large bubble at the top takes a few seconds to condense due to the absence of an efficient thermal sink and it also leads to a concentration of heat at the top of the chamber; these effects would result in an interruption of the continuous operation of the chamber. A piston-operated expansion mechanism of the type used in the 1" chamber has too high an inertia.

By using a strong membrane to seal off the propane and by connecting a high pressure air supply through a rapid action 3-port valve to a supply port

Plate II

An example of foaming in the chamber.

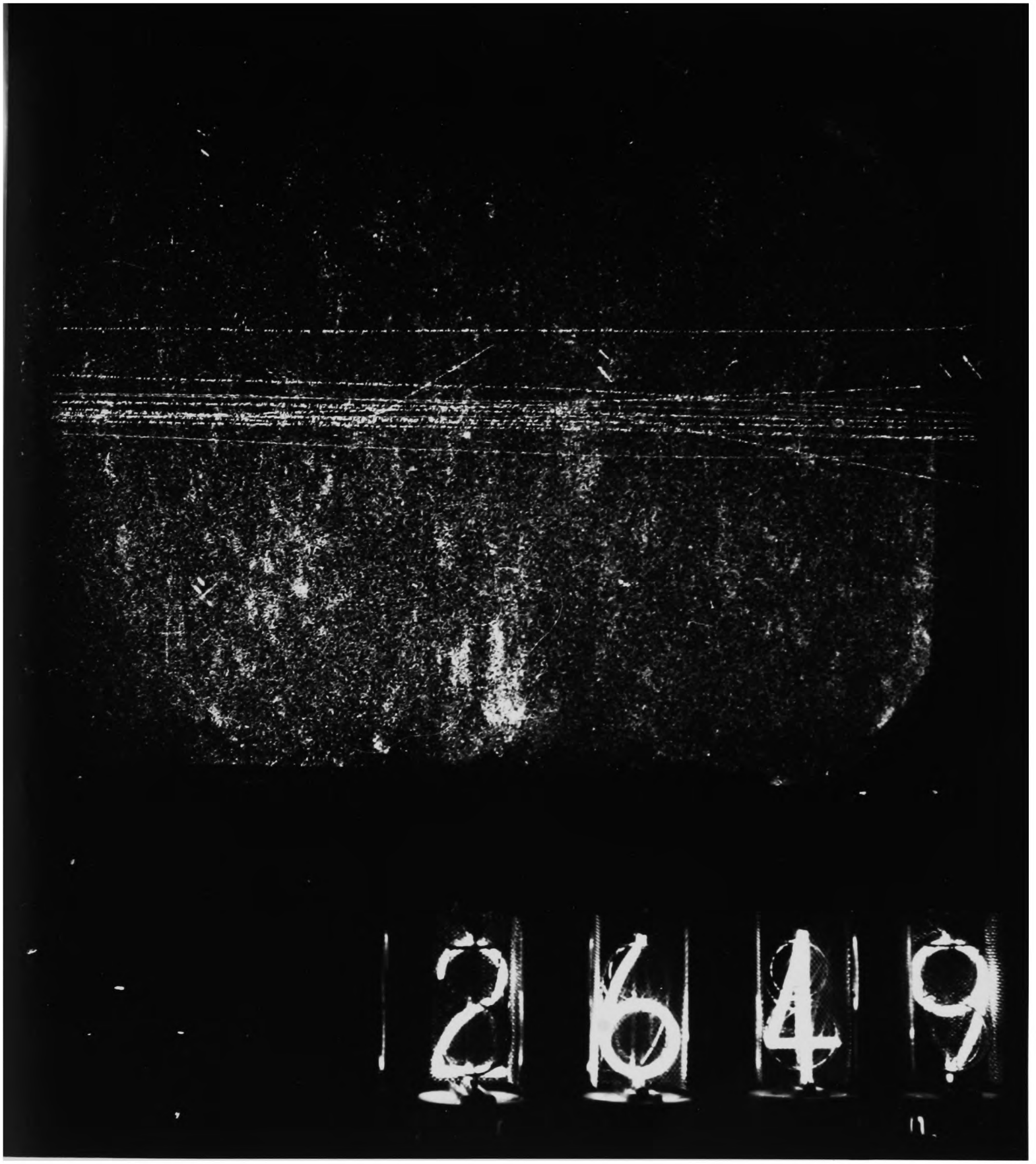
26449

beneath the membrane, a very low inertia system is obtained. The two positions of the valve are shown at the bottom of figure 2.1. The normal de-energised state of the valve (position B) keeps the propane at the air reservoir pressure (about 100 p.s.i. above its s.v.p.). For the duration of the expansion pulse the valve is energised and switched to position A which isolates the gas reservoir and releases the high pressure air pocket under the diaphragm to the atmosphere. The propane expansion speed is limited only by the inertia of the propane-membrane-air system which is negligible; the membrane very rapidly hits the base-plate and the expanded propane is in its superheated sensitive state. After about 5 msecs the chamber starts to recompress itself, relatively slowly, by gasket boiling etc. until the valve is de-energised to position B again and the propane is very rapidly recompressed to the air reservoir pressure. The total sensitive time can be controlled very easily from zero up to approx. 10 msecs by varying a resistor in the expansion pulse-width control unit (see section 2.8).

Compressed air is supplied by a two-stage heavy-duty compressor[*2] fitted with a blow-off valve[*3] which is operated by a pressure controlling device[*4] connected to the air reservoir on the bubble chamber assembly. To vary the overpressure in the chamber it is only necessary to change the setting of the control meter. Because of the extremely loud report made by the expanding gas when it escapes freely from the valve, the exhaust port of the valve is connected to a silencing system comprising a gas bottle and a lorry silencer.

The valve used is a magnetic Barksdale valve[*5]. In order to obtain a very rapid action from this valve, which has a specified running voltage of 250 volts, an initial power surge of 860 volts is used for the switching operation.

The membrane consists of two parts: a 5 thou melinex sheet and a 1/8" doubly rayon reinforced butyl rubber[*6] sheet. In the first design this was clamped between the body of the chamber and a flat base-plate (BP1 in fig. 2.1) but during a prolonged test of the chamber the membrane fractured after some 10,000 expansions. The probable cause for this was the inelasticity of the melinex; thus, after the first few expansions it maintained its bowed-up surface area so that on each subsequent expansion it folded up on hitting the base-plate (when the chamber was dismantled the membrane was found to be split along a very pronounced crease). To increase this unacceptably short maintenance-free running time the base-plate was modified by the addition of a hollowed-out slab of dural (BP2 in fig. 2.1) with a surface area equal approximately to the bowed-up area of the membrane. On expansion of the chamber the membrane then lay smoothly in contact with the base-plate. This system underwent some 60,000 expansions without showing any sign of deterioration.

2.5 Optical design

Following the successful photography of the 4" chamber, a similar but scaled-up version of its dark field illumination system was designed for the 12" chamber. Plate III shows the components of the optical system and

Plate III

Components of the optical system

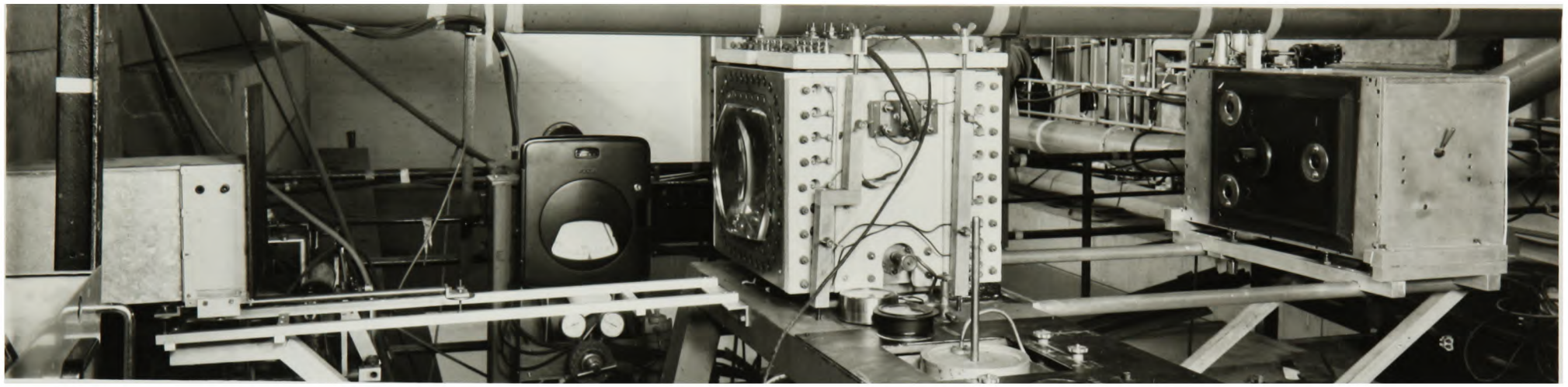

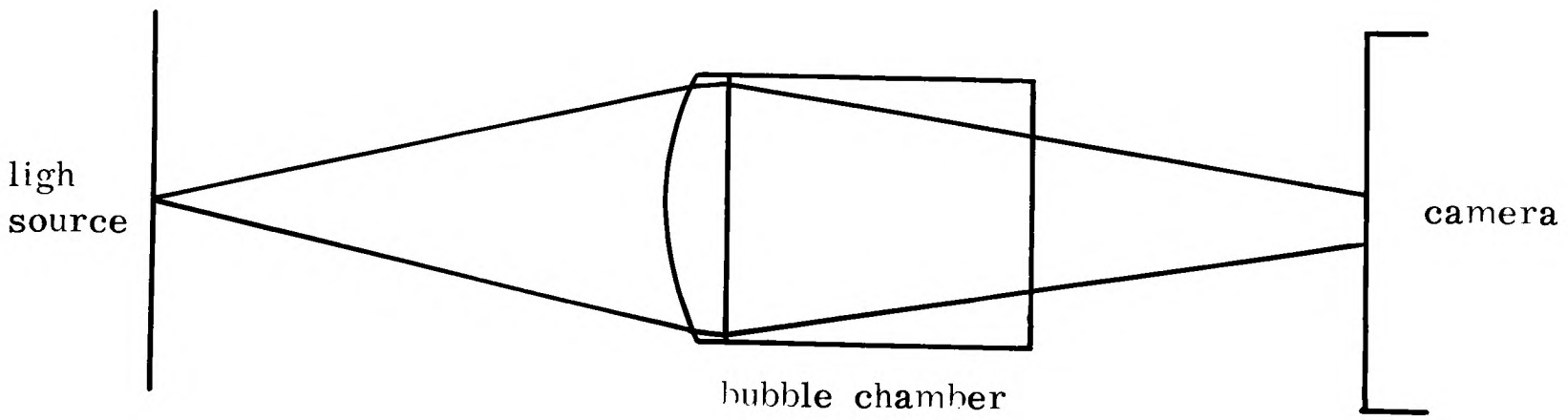

Fig 2.2

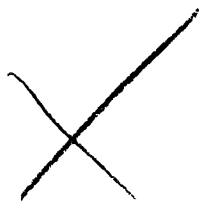

LL14200

figure 2.2 shows diagrammatically the marginal rays from the light source to the camera front. The position of the camera assembly is dictated by the need for a demagnification of approximately 15 from the object space to the film. The position of the flash box on the principal axis of the condensing lens is determined by the need to illuminate as much of the window volume of the chamber as possible and yet to inhibit the entry of stray light into the cameras. With an ideal optical system the image of the flash could lie only just within the lenses on the camera front, but because of the distortion in the very thick condensing lens and reflection from the cut-away sides of the lens it was found that the maximum permissible image radius was 2" compared with the ideal radius of 6.3". Under these conditions the central plane of the chamber, parallel to the windows, has an unilluminated peripheral region of ½" wide at the top and bottom and 3/4" wide at the two sides. The condensing lens was highly polished and the windows were kept clean and free of abrasions. On the outside faces of the windows sets of fiducial marks were etched with hydrofluoric acid: Andrew Crosses on the window nearest to the cameras and George Crosses on the other window. The relative positions of these were carefully measured when the chamber was assembled and their images are used in the geometrical reconstruction of the events photographed in the chamber (see chapter 5).

There are no shutters on the cameras and during operation an intense flash of light is timed to occur shortly after the nucleation of boiling along the paths of the charged particles; the time delay between the pulse of protons

from the cyclotron and the flash is variable so that optimum quality tracks can be obtained and maintained. Ideally, the cameras should record only the images of the bubble tracks and the fiducial marks both of which scatter light out of the main cone of light shown in figure 2.2, but a certain amount of stray light also enters the cameras. It was discovered that much of this stray light was due to double reflection from the camera front and the bubble chamber window. Liberal use of black non-reflecting paint reduced the background light to an acceptably low value.

The light source used is a G.E.C. high duty flash tube[*7] which gives a good point source of light and is mounted at the centre of curvature of a small concave mirror. To obtain a sufficiently intense beam of light from this arrangement it is found necessary to discharge through the tube a 60μF capacitance charged to 2.5 KV. At this rating the useful life of each tube is 10,000 cycles. The condensers making up the 60μF cannot be mounted with the remainder of the flash tube circuitry because the voltage drop in the connecting cable then dissipates most of the available power; they are mounted behind the flash tube in the box that can be seen in plate III. The flash is produced by the breakdown of the tube resistance, effected by a 100 KV pulse fed from a pulse transformer onto a tickler electrode coiled around the tube.

The camera is mounted on a supporting framework (see plate I) and is provided with three levelling screws to allow the front of it to be set accurately parallel to the windows of the bubble chamber. Three lenses[*8] are carried on the front plate which can be moved with respect to the main

assembly for focussing purposes. Behind each lens is mounted a cassette which can hold a 200 ft reel of 35 mm film[*9], enough for 2,400 exposures. A mechanism is provided for winding-on the film and for clamping it in the focal plane of the lens before each exposure. The operation of the camera is controlled by a square wave pulse from a relay in the control unit.

Approximate focussing was performed by viewing the chamber through the back of a dummy cassette and more accurate focussing was then achieved by a series of photographs. The focus condition chosen was that with back and front fiducial marks out of focus to approximately the same degree.

The lens aperture was set at f20; this was determined by the usual process of compromise between depth of focus limitations and diffraction limitations. The calculation is shown in Appendix II.

2.6 Frame numbering counter

The use of an illuminated post office counter mounted adjacent to the front window of the chamber proved unsuccessful in giving discernible images on the films. Since the camera had not been designed for a back projection system in which the image of a small counter is projected directly onto the films through the backs of the cassettes, it was decided to build a self-illuminating electrical counter with a separable display unit of large digits which could be mounted immediately above the chamber window.

The basic unit of the display panel is a digitron tube[*10]. Five tubes are shown mounted in the display unit in plate IVa. Each tube has ten separately insulated one-inch high wire cathodes in the shape of the digits

Plate IV

The frame numbering counter

(a) the display panel

(b) the uniselector counting circuit

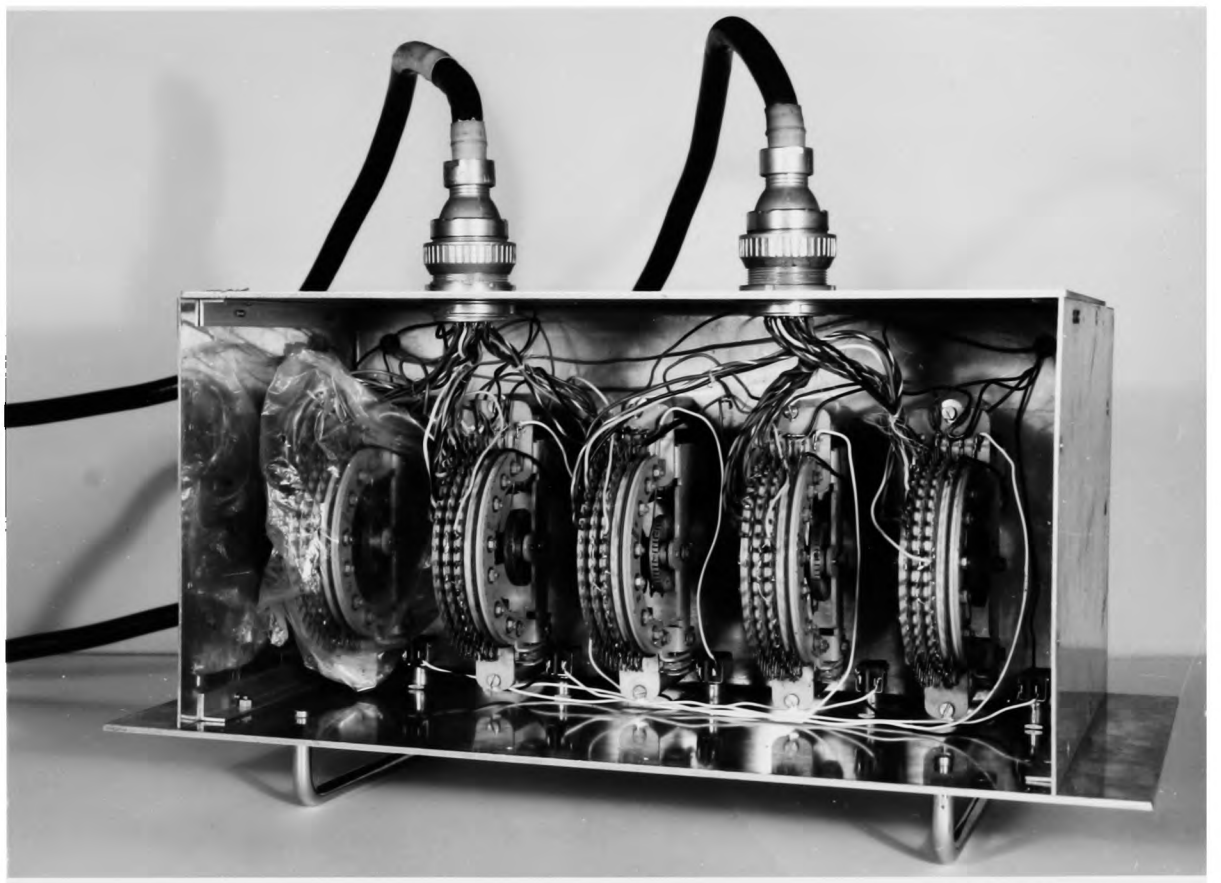

IVb

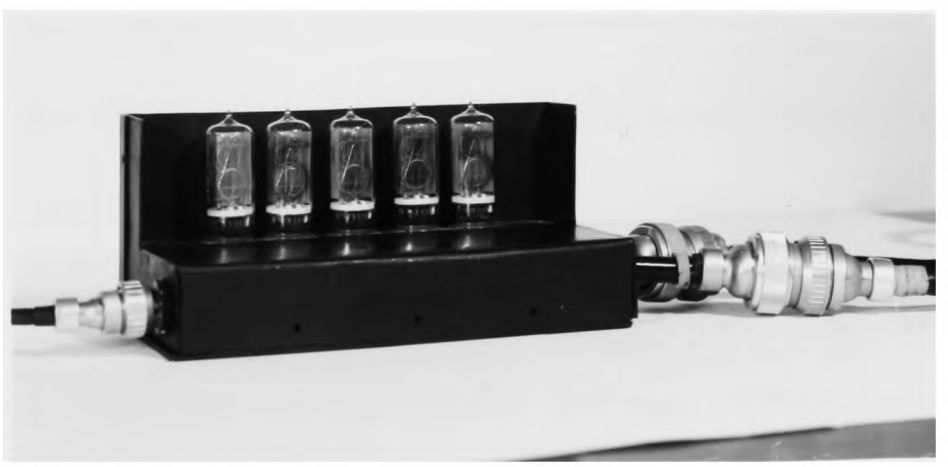

IVa

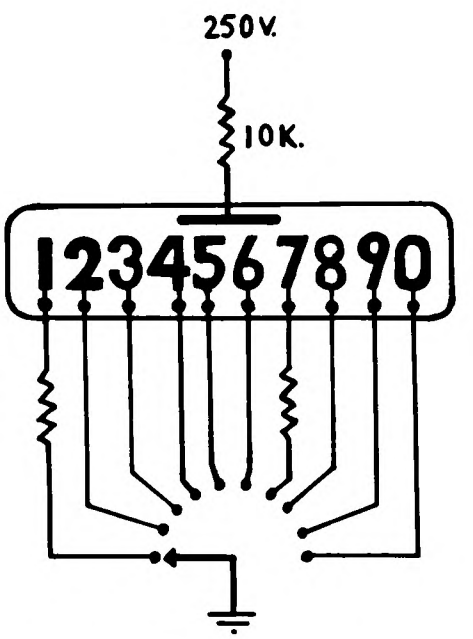

Fig. 2. 3

0 to 9 surrounded by a wire mesh anode. The cathodes are connected via two 25-cored cables to the counting unit and the anodes are supplied from an unsmoothed 250 volt power pack. An earthed cathode glows red due to a cold discharge in the tube. Figure 2.3 shows diagrammatically how one unit can be made to "count" from 0 to 9.

The counting circuit itself comprises five 25-way, 4-bank uniselectors, each operated through two parallel 37 ohm coils from an unsmoothed 30 volt supply. It is shown in plate IVb. The circuit diagram is shown in figure 2.4.

A square-wave pulse from the camera coincides exactly with the film wind-on. The leading edge of this pulse closes relay R, disconnecting the digitron cathodes from earth (via bank 1 - the outside bank in diagram), and the illumination ceases. When the film has wound-on the trailing edge of the pulse moves on the first uniselector arm by one position and simultaneously re-earths the cathodes; the display is now re-illuminated and shows the new number. On receipt of each tenth pulse, the arms sweep around to the zero position due to the action through the second bank; as they do this a pulse is fed, via bank 3, to the next uniselector, which then moves on one position. On receipt of every hundredth pulse, both the first and second selectors return to zero and the third moves on one position; and so on. The continuous bank (number 4) allows for the manual reset of each decade to zero.

The quality of the image can be seen in plate III; it facilitates quick recognition of frames and in this respect is superior to any other frame numbering seen by the author.

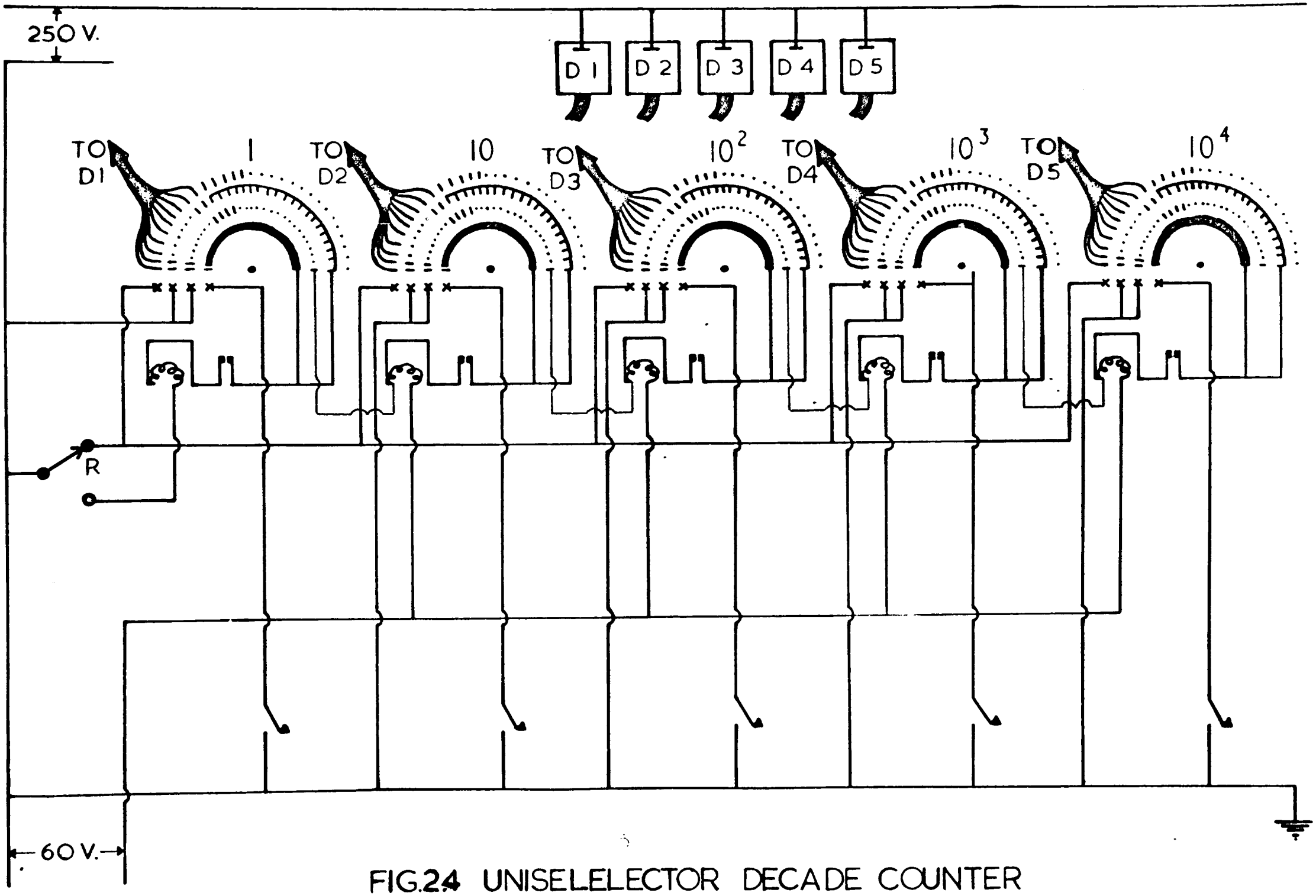

FIG.24 UNISELELECTOR DECADE COUNTER

2.7 The chassis

All the components described, with the exception of the compressed air supply and control units, are mounted on a welded steel trolley, which also carries the pipe and tap system necessary for the various air and propane transfer operations. It is 39" high, has base dimensions of 30" x 63" tapering to top dimensions of 19" x 57" and is constructed from 3/8", 4" x 3" angled steel. It can quite easily be lifted in and out of the experimental area by crane, which enables all preparatory work to be done in a radiation-free zone while the cyclotron is in operation.

2.8 Electronic control unit

For the successful operation of the bubble chamber assembly, the propane must be in a superheated state at the precise time that a proton pulse is delivered from the cyclotron, the illuminating flash (which acts as the camera shutter) must occur when the bubbles of the proton tracks are at a suitable size, the propane must then be recompressed before much spurious boiling can take place, the cameras must wind-on the films ready for the next exposure, and finally the frame numbering device must be advanced by one unit. The organisation of this cycle of operations is carried out by the transistorized control unit, which consists essentially of a collection of pulse generating circuits and variable delay circuits. Figure 2.5 shows a block diagram of the unit and figure 2.6 shows the time sequence of the more important pulses from the unit in relation to the sensitive period of the chamber.

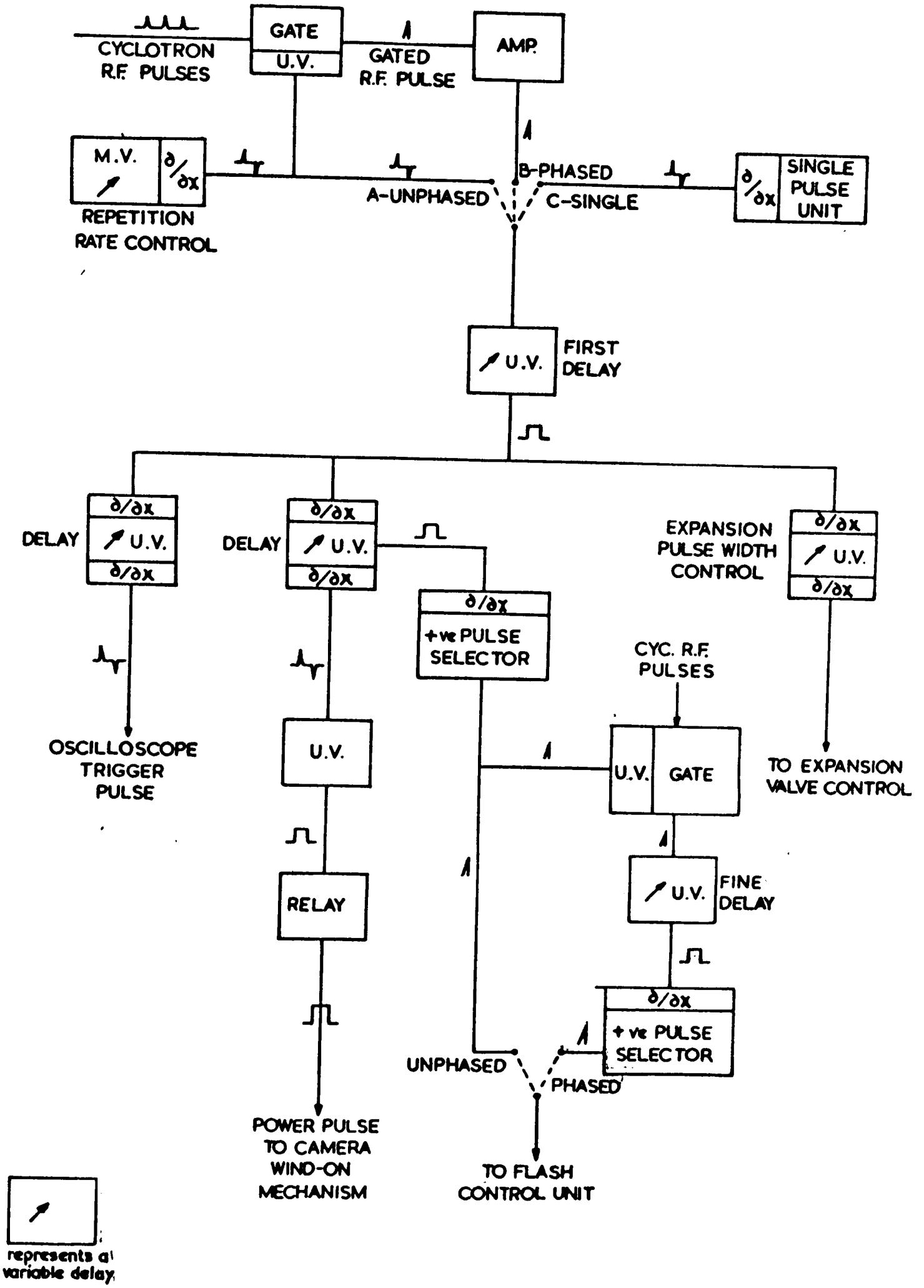

FIG.2·5 BLOCK DIAGRAM OF CONTROL UNIT

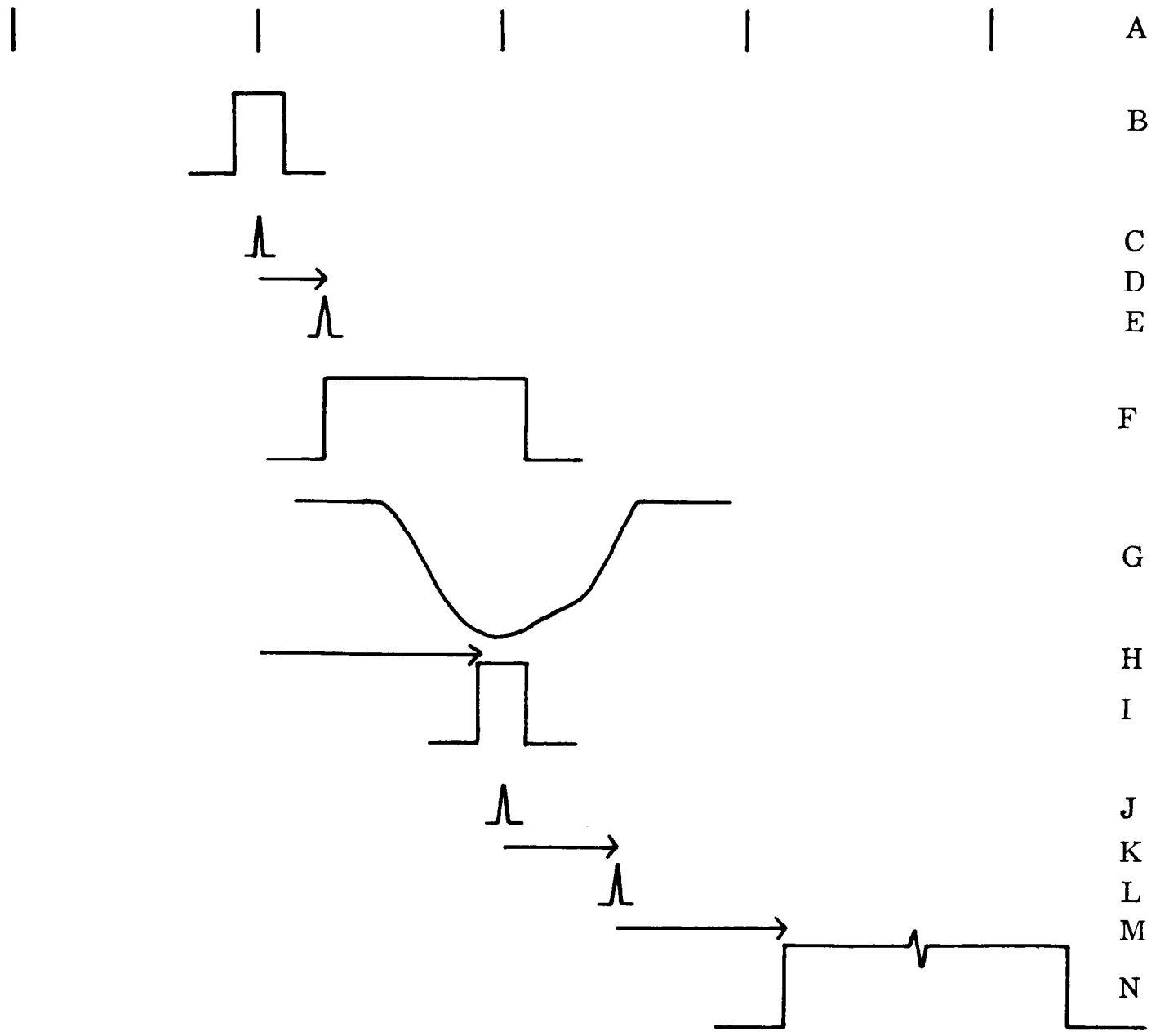

KEY

A Cyclotron R. F. pulses
B Gate to accept a pulse to initiate B. C. cycle
C Accepted and amplified pulse
D First delay
E Trigger to expansion pulse-width circuit
F Pulse to expansion valve
G Propane pressure pulse
H Flash gate delay
I Gate in the sensitive period of B. C.
J Pulse coincident with the required proton pulse
K Flashdelay
L Trigger to flash control unit
M Fixed delay to camera-control relay
N Camera wind-on pulse

Fig. 2. 6 Schematic sequence of pulses and delays for operating the bubble chamber in the proton beam.

There are three possible modes of operation of the unit, corresponding to the positions A, B and C of the switch shown above the first delay unit in figure 2.5. For operation in phase with the cyclotron, pulses from the latter's radio frequency generator, in phase with the proton pulses, are accepted through position B. For testing purposes it is possible to cycle the unit either continuously with pulses from the pulse generating multivibrator unit through position A, or singly by push-button in an univibrator circuit through position C. For both phased and unphased continuous operation the repetition rate of the cycle is controlled by a setting on the multivibrator circuit.

Because of the instabilities in the propane temperature (discussed in section 2.3) the bubble growth rate tended to vary during the experimental run and in order to photograph the tracks at their optimum quality, the time delay between the proton pulse and the light flash (delay (K) in fig. 2.6) had to be adjusted occasionally.

2.9 Preparation and operation of the bubble chamber

On assembling the chamber body, great care was taken to clean thoroughly all internal surfaces. Any dust and grease left in the chamber would give rise to scattered light, which would decrease the quality of the photographs. Before filling the chamber with propane, a water pressure test was performed up to 900 p.s.i., twice the pressure to be applied to the propane. This tested the safety of the apparatus and the sealing at all of the 'O' rings.

Propane reacts with water to form the insoluble hydrate, the presence

of this would destroy, or at least reduce, the transparency of the liquid. Therefore when the chamber had been drained after the pressure test it was vacuum-pumped to remove all traces of water. When the chamber was dry, a propane[*11] reservoir was connected to the filling tap via a drying bottle containing silica gel; the chamber was kept at room temperature and the reservoir was heated to distil the propane into the chamber. The filling tap was closed when the liquid level was within 1" of the top of the chamber and the propane was heated to its controlling temperature.

The optimum running conditions were found to be:

temperature	62°C (S. V. P. 330 p. s. i.)
over pressure	90 p. s. i.
volume expansion ratio	~ 3%
repetition rate	15 expansions/min.
expansion pulse width	30 msecs.
flash delay time	1 msec.

A bubble density of 24 to 25 bubbles/cm was obtained under these conditions.

CHAPTER 3

THE HARWELL SYNCHROCYCLOTRON, THE PROTON BEAM, AND THE EXPOSURE OF THE BUBBLE CHAMBER

3.1 The synchrocyclotron

The Harwell synchrocyclotron, built in 1949, is of conventional design; it has been described in detail by ADAMS & EDMUNDS (1950) and by PICKAVANCE & CASSELS (1952). Protons, produced by a pulsed hydrogen gas discharge at the centre of the dees, are accelerated by a 6 kv radio frequency voltage until they strike a tungsten target at a radius of 49 inches. The extracted beam comprises those protons that scatter from the target into the magnetically shielded extraction channel.

At the extraction radius the circulating beam has 1 inch radial oscillations about its stable orbit, and therefore the energy of the protons that strike the target is the cyclotron energy corresponding to a stable orbit radius of 48 inches.

This is given by

$$T^2 + 2E_0T - e^2H^2r^2c^2 = 0$$

where r is the radius of extraction

H is the magnetic field at this radius

E_0 is the rest mass energy of the proton

and T is the kinetic energy of the protons at the radius r.

At a radius of 48 inches the cyclotron magnetic field is 15,800 gauss

giving the energy of the circulating proton beam as 164 MeV. The tungsten target degrades the energy to 154 MeV and a further 0.5 MeV is lost along the transport system because of the presence of mylar windows and air gaps. A beam energy in the region of 153.6 MeV is therefore expected at the bubble chamber. In fact, a value of 154±0.1 MeV was deduced from the range telescope measurement, reported in section 5.4, and a value of 152±1.5 MeV was deduced from the measurements on stopping tracks, reported in section 5.5.

The internal beam strength of 6×10^{12} protons/sec (1μA) is reduced to 10^{8} protons/sec by the extraction process. This full beam strength was used for all the experiments on the beam, but for the bubble chamber run the beam strength was reduced to approximately 10^{3} protons/sec (~6 protons/pulse).

3.2 The external proton beam

There are four important conditions that the beam must meet.

1. The proton flux must be stable at a level giving 5 to 10 protons per pulse.
2. The proton pulses must be short compared with the growth time of the bubbles in the propane.
3. At the entry plane to the bubble chamber the beam must be collimated so that the protons are well spread out in the plane parallel to the chamber windows. This makes it possible to see from the photographs exactly what happens to each proton as it traverses the chamber.
4. There must be a small energy spread in the beam.

Condition 3 is dealt with in the next section, and conditions 1 and 2 in

section 3.4. Here the requirements on the spread of proton energies in the beam are discussed.

The beam energy sp read

The successful separation of the events representing proton-hydrogen interactions from those representing proton-carbon interactions, and the subsequent separation of carbon events representing the direct knock-out of a p-shell proton from the other carbon events is of extreme importance. For example, even a small contamination of the p-shell events by hydrogen events would seriously distort the measured p-shell nucleon momentum distribution.

The classification of an event into one of the various reaction hypotheses is based upon the energy-loss (E_L) measured for the reaction. This is given by:

$$E_L = E_o - \sum_i E_i - E_R$$

where E_o is the energy of the incoming proton

E_i is the energy of the i^{th} outgoing proton

and E_R is the energy carried away by the residual nucleus (calculated from the momentum unbalance in the reaction)

The energies E_o and E_i are calculated from the measured residual ranges of the particles; the uncertainties in these energies determine the resolution obtainable for E_L. There is an intrinsic limit to the accuracy of energy measurement by this method, due to the statistical nature of the slowing-down process, and this determines the best possible resolution that can be obtained

for E_L. Added quadratically into the intrinsic uncertainty in E_o is the uncertainty arising from the spread of energies in the incident beam; it is desirable that this be small enough to make an insignificant contribution to the overall energy resolution. Errors of measurement on the film contribute, in most cases, only very small errors to E_L.

Let us now consider the precise beam energy spread requirements.

As a consequence of the non-linear relationship between the energy of a proton and its residual range ($E \sim AR^B$; $B \sim 0.5$), an energy spread in the proton beam delivered to the bubble chamber by the beam transport system is magnified as the protons traverse the chamber. It is shown in appendix III that for a proton beam of energy E and RMS energy spread dE, the RMS energy spread in the beam after the protons have traversed a thickness L is given, to a first approximation, by

$$dE_{o1} = \frac{EdE}{A\sqrt{R-L}}$$

where A is the range constant

and R is the range of a proton of energy E

STERNHEIMER (1960) has determined the straggle in the residual range due to the statistical nature of the slowing-down process for protons of various energies. From this information an estimate can be obtained for the intrinsic energy uncertainty in the proton beam at each point along its path. In appendix IV the energy spread due to straggling in the beam at a depth L is shown to be, to a first approximation,

$$dE_{o2} = \frac{kA}{2}\sqrt{\frac{2RL-L^2}{R-L}}$$

where k is the straggle coefficient as determined by Sternheimer

R and A are as before.

These two first order equations can be used to obtain some idea of the requirements on the incident beam energy spread. If, for example, we make the specification that the beam spread must contribute an energy uncertainty in E_o less than that contributed by the straggle spread at, say, a distance of 12 cms in the chamber (where the energy is approx. 100 MeV) we get from

$$\frac{dE_{o1}}{dE_{o2}} = \frac{2dE}{kA}\sqrt{\frac{R}{2RL-L^2}}$$

with $dE_{o1} \leqslant dE_{o2}$

that the RMS energy spread in the incident beam (dE) must be less than 0.6 MeV.

In figure 3.1 the energy uncertainty in E_L for a 2-prong event arising from the combined straggling effects on the incident proton and the two product protons is shown as a function of the distance traversed by the incident proton before it interacts. Also shown are the independent energy uncertainties that would be produced by incident beams with initial RMS energy spreads of 0.5 MeV, 1.0 MeV and 1.5 MeV.

In figure 3.2 the energy resolution in E_L, for $E_o \sim 100$ MeV, is shown as a function of the incident beam energy spread. Since the straggling error cannot be removed, undue effort to reduce the incident beam energy spread below 0.5 MeV pays very little dividend.

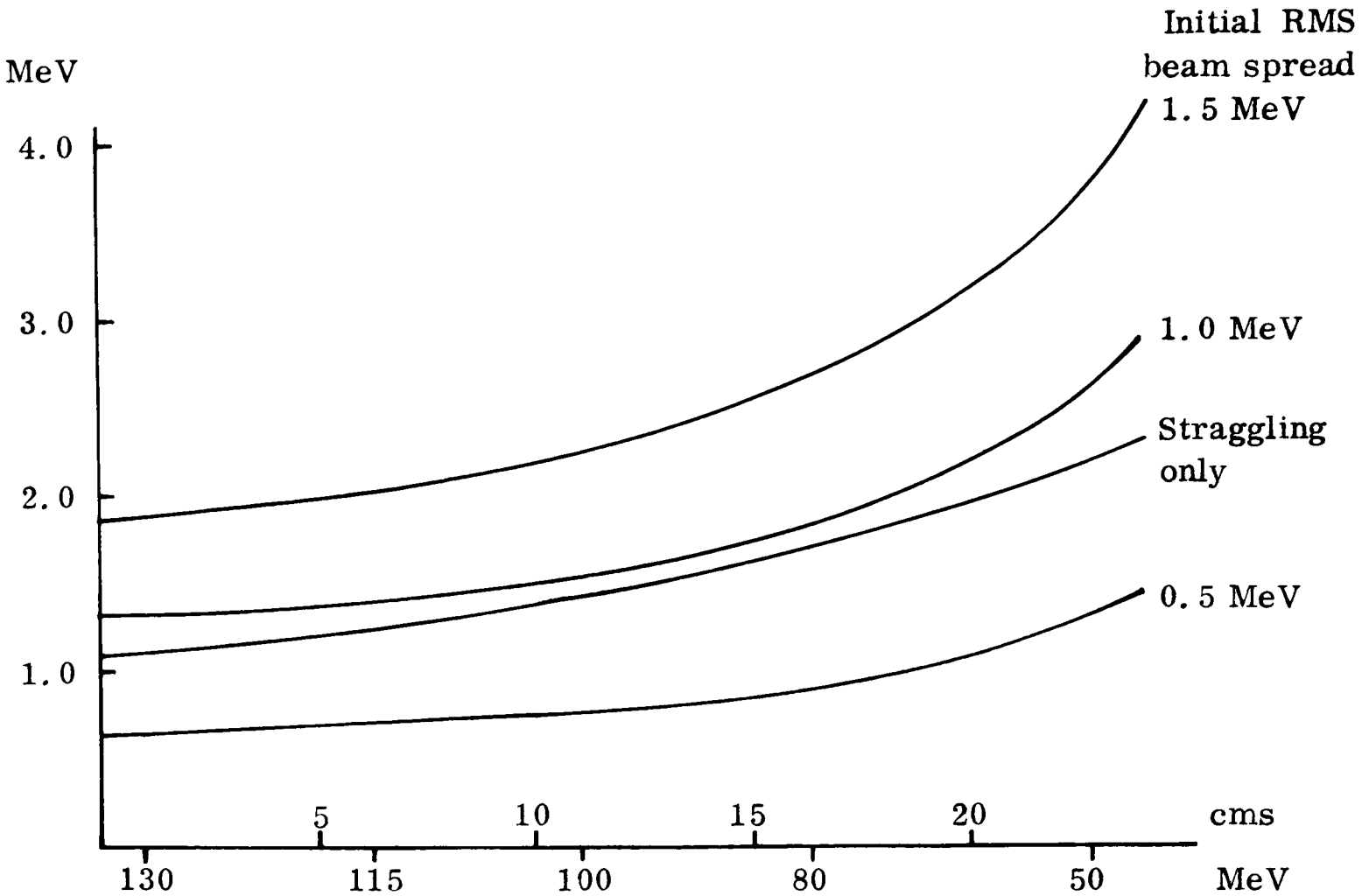

Fig. 3.1 Uncertainty in the measured energy-loss at various depths in the chamber, produced by straggling and by energy spread in the incident beam.

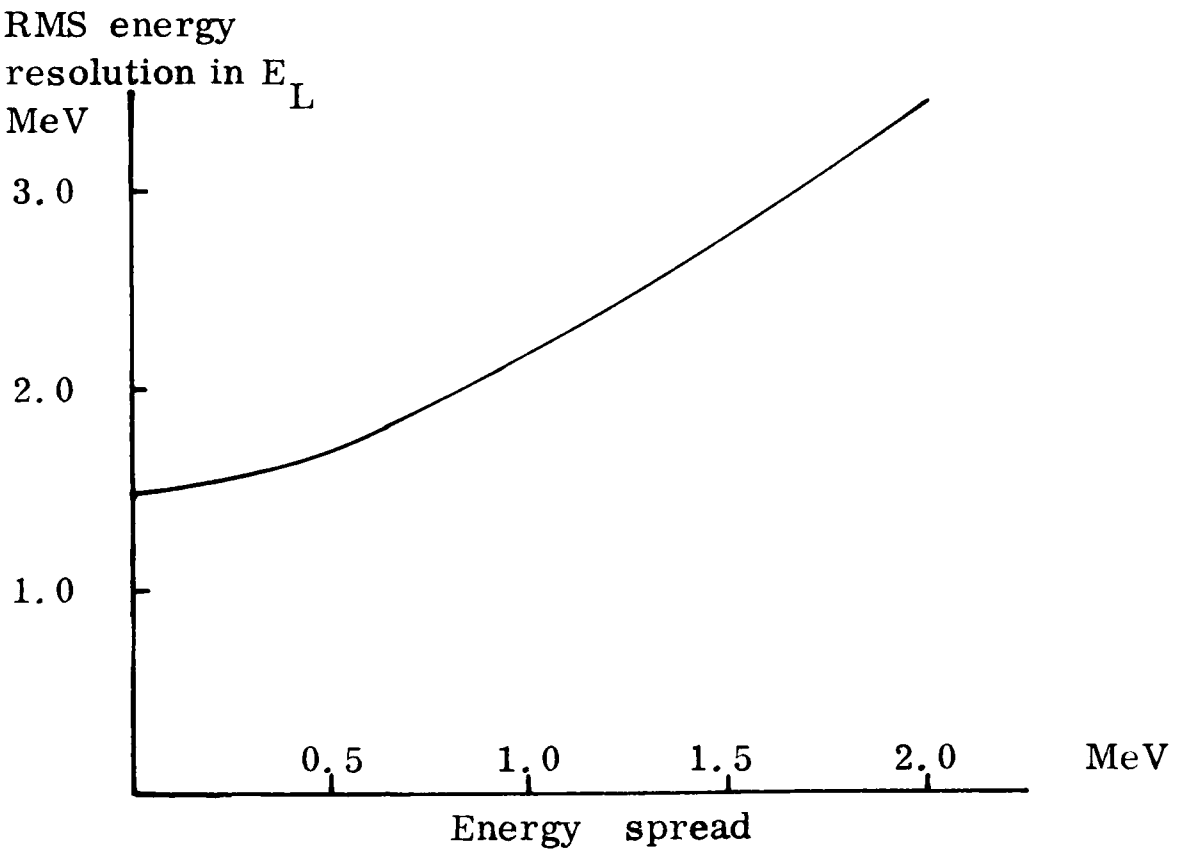

Fig. 3.2 Total RMS energy resolution for various incident energy spreads, produced at a depth of penetration of 12 cms ($E_o \sim 100$ MeV).

3.3 Experiments with the beam

The proton beam that emerges from the cyclotron extraction channel has an energy spread of approximately $\pm$ 5 MeV. The beam transport system has to reduce this to less than 0.5 MeV and at the same time produce a geometrical beam profile at the bubble chamber that is well spread-out in the vertical direction and closely confined in the horizontal direction. There was little experience of setting-up a beam of this type and it was necessary to experiment with the beam transport system before performing the bubble chamber experiment.

Three measuring techniques were used in these experiments:

(1) The beam flux levels were measured with an ionization chamber.

(2) Geometrical profiles were recorded on X-ray plates inserted in the full flux beam. Plate V shows a selection from the beam profiles obtained during the evolution of the required form.

(3) Energy measurements were made with a range telescope. This consisted of three scintillation counters lined up along the beam path, and a set of aluminium plates of uniform and accurately known thicknesses - see figure 3.3.

To determine the spread of energies in the beam, the ratio of coincidences for counters 1, 2 and 3 to the coincidences for counters 1 and 2 only is measured for various thicknesses of aluminium between counters 2 and 3. When allowance is made for nuclear scattering in the aluminium this ratio gives the number of protons stopped by each thickness of aluminium and

hence the number of protons in the beam of energy greater than E, given by

$$E \sim AR^B$$

where R is the thickness of aluminium

A and B are the range constants for aluminium.

Very small increments in the aluminium thicknesses are made when the coincidence ratio begins to fall off rapidly, i.e. as the thickness corresponding to the mean energy of the beam is approached.

A typical range curve from such a measurement is shown in figure 3.4.

The measured energy spread is obtained from this by eliminating the nuclear scattering component, which can be determined from the slope of the curve at the low aluminium thicknesses, and differentiating the resultant curve.

An energy spread is introduced by the aluminium itself because of straggling effects and it is the spread due to the combination of the incident beam energy and the straggling spread that is actually measured. To separate them it is essential to have an accurately measured range curve.

The curves of figure 3.5 show the differentiated range curves which would be obtained from measurements on beams of various initial RMS energy spreads. The straggling component for these curves was obtained from the results of Sternheimer who showed that for a mono-energetic beam the probability of a proton stopping within the distance R to R+dR is given by

$$P(R)dR = \frac{1}{\sqrt{2\pi}} \exp-\left[\frac{(R-R_0)^2}{2\sigma^2}\right] dR$$

where R_0 is the mean range of the protons

σ is the RMS spread of ranges.

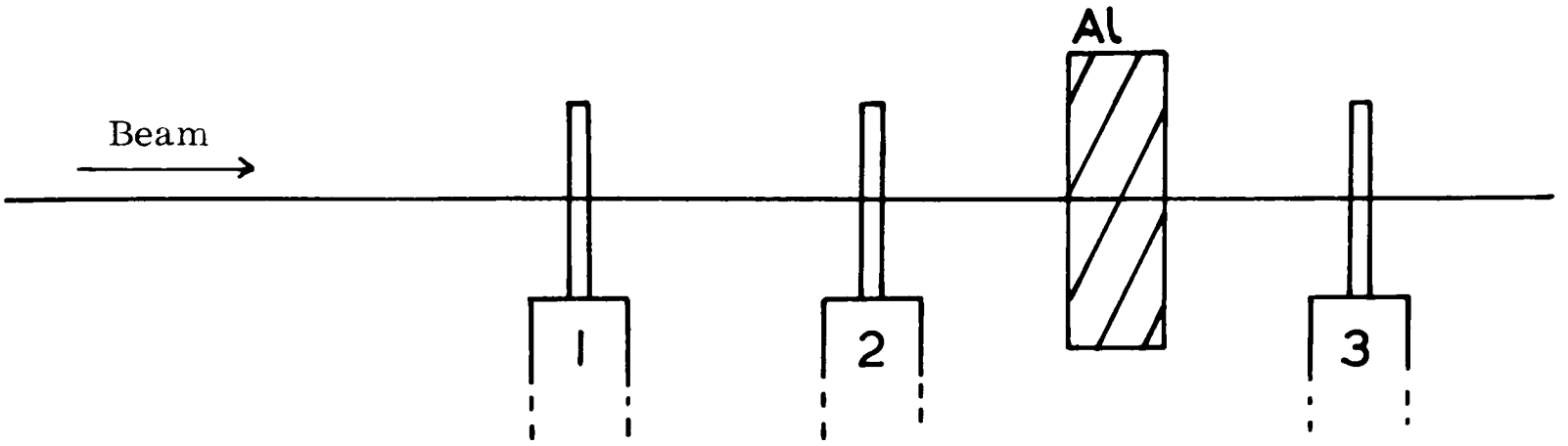

Fig. 3.3 Range telescope.

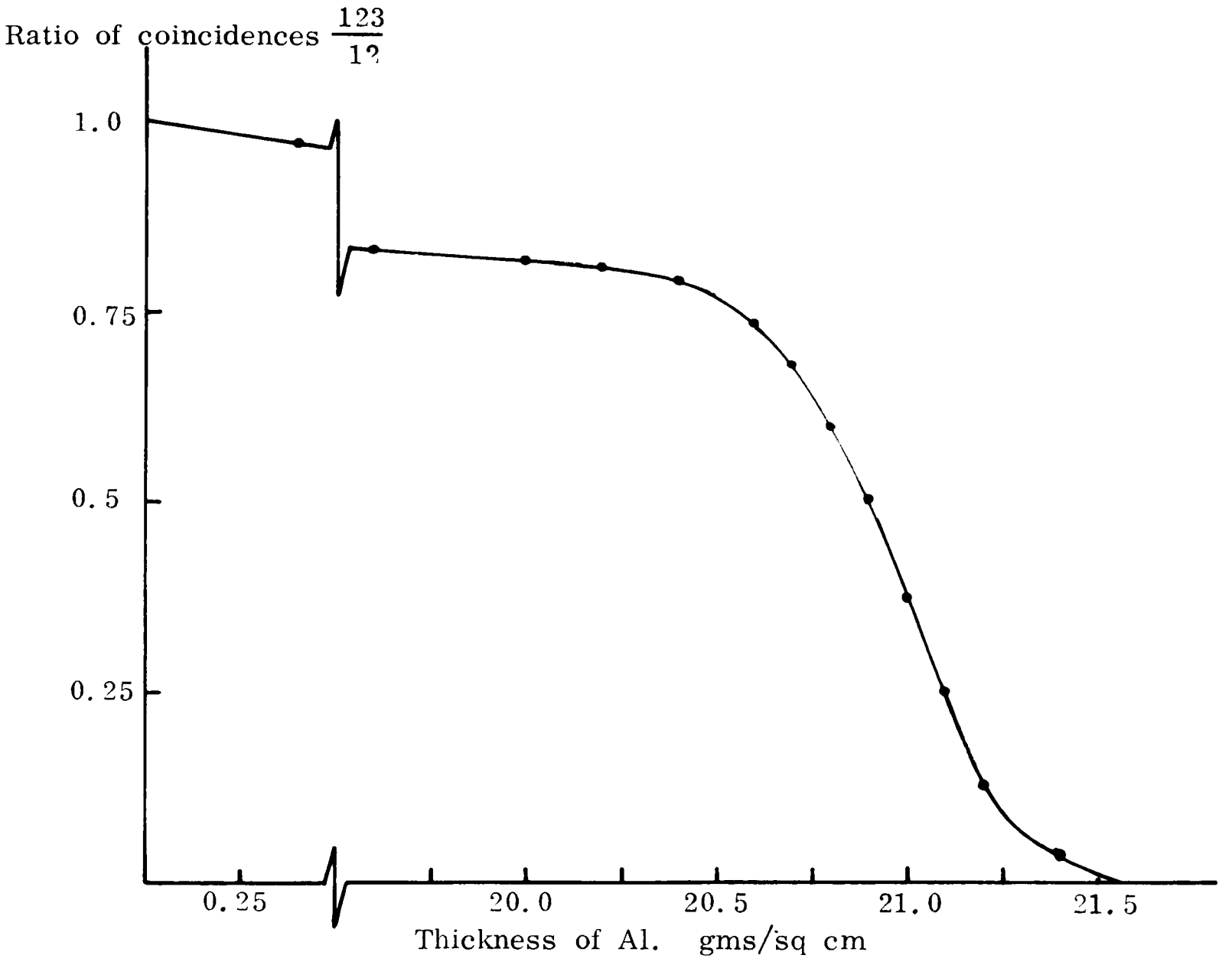

Fig. 3.4 A typical range curve.

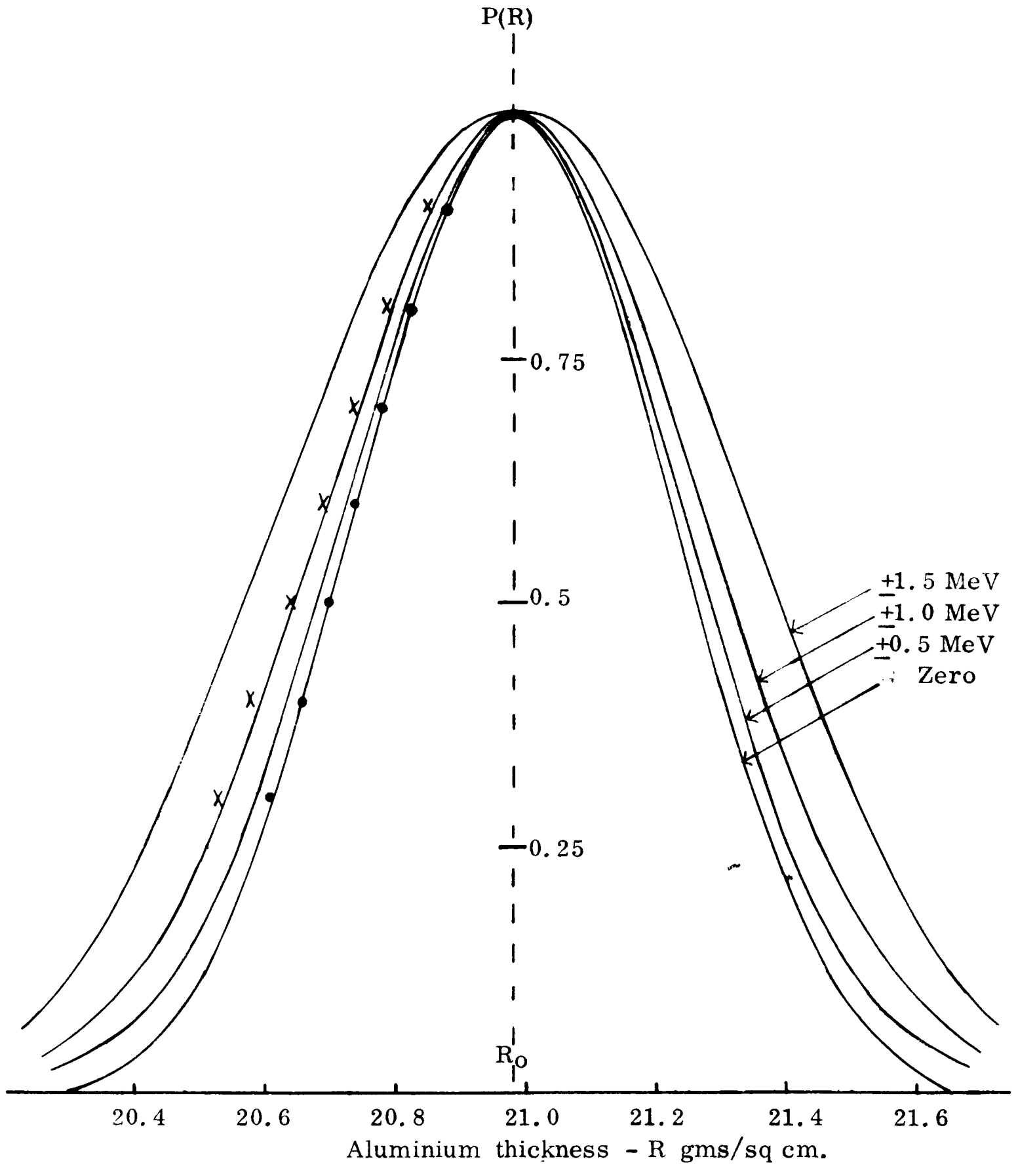

Fig. 3.5 The curves show the differentiated range curves expected from beams with various RMS incident energy spreads; the points show the two sets of experimental results obtained.

For 153 MeV protons in aluminium Sternheimer gives $\frac{\sigma}{R_o} = 0.01146$. By comparing the measured beam energy spreads with these curves the spread in the beam itself can be determined.

Figure 3.6 shows a plan of the beam path between the cyclotron and the bubble chamber. Components C_1, BM_1, C_3 and Q were available when the beam experiments commenced. When all these components were set at the values normally used for counter experiments, the geometrical beam profile obtained at position A was that shown under label A in plate V. With the quadrupole focussing magnets (Q) switched off, profile B was obtained; this was changed to profile C by collimating at C_1 and C_3. The differentiated range curve obtained from a section of this profile is shown by the crosses in figure 3.5. Evidently a RMS beam spread in excess of 1 MeV was present.

To improve the beam two additions were made to the transport system:

(1) The collimator C_2 was inserted to limit the angular spread of the protons entering BM1. Because of the fringe field of the cyclotron there is an angle-energy correlation in the beam as it emerges and close collimation at C_2 can select part of the energy spectrum.

(2) A second bending magnet (BM2), which became available at this time, was inserted in front of the bubble chamber to sweep away any low energy component in the beam arising from slit scattering at C_3.

By suitably setting all components in the new beam line, the profile E was obtained (profile D shows an intermediate stage). The collimator settings

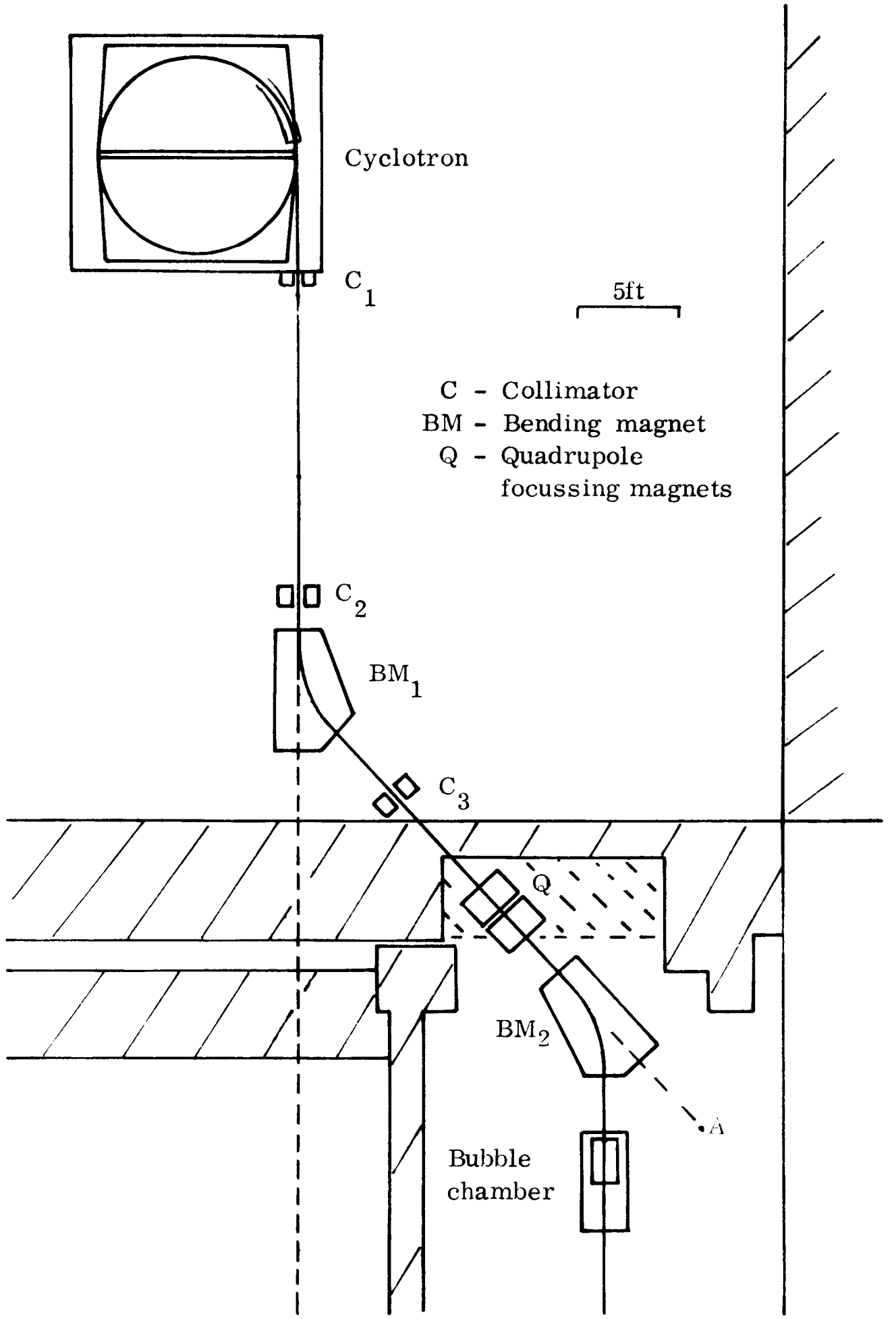

Fig. 3.6 The beam path.

Plate V

X-ray exposures taken at various stages during the setting-up of the beam; they show the beam profiles at the position of the bubble chamber beam entry window.

A

B

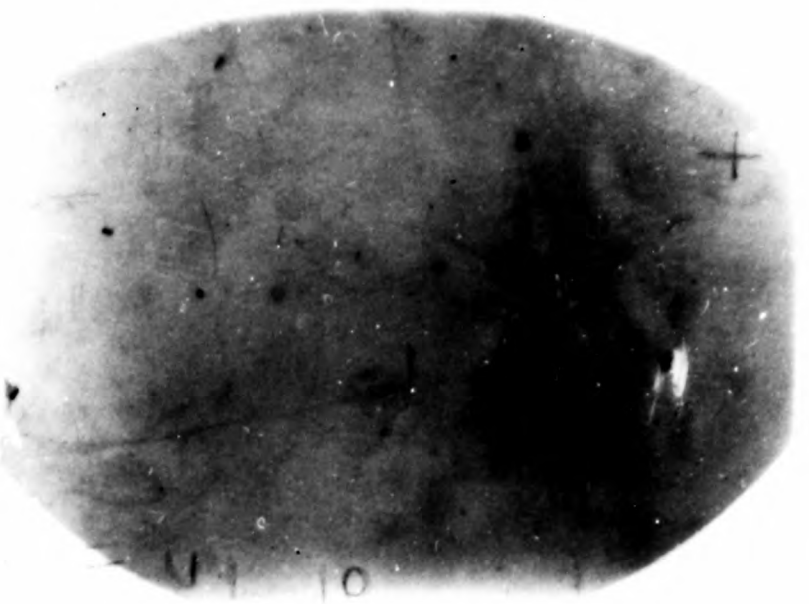

C

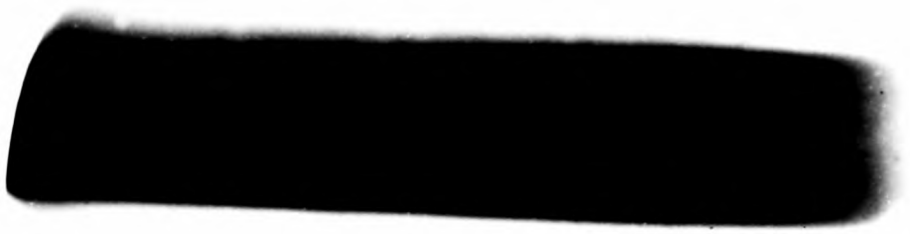

D

E

V

for this beam were as follows:

C_1 $x = 1.1 \pm 0.2$ cms

y no collimation provided

C_2 $x = 1.35 \pm 0.15$ cms

$y = 0 \pm 1$ cm

C_3 $x = -0.7 \pm 0.1$ cms

$y = 0 \pm 5$ cms

The sense of the co-ordinates can be seen from the sketch.

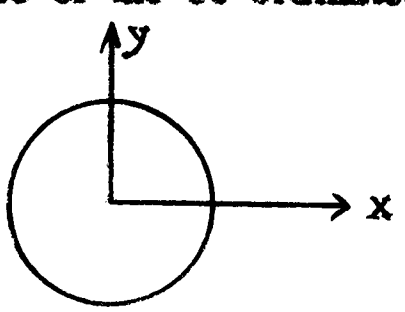

Looking up the beam tube towards the cyclotron

The differentiated range curve obtained from profile E is shown by the circles in figure 3.5 (the range curve itself is the one shown in figure 3.4). Therefore this beam has a RMS energy spread consistent with zero and certainly below 0.5 MeV. The resolution in the energy loss spectrum for the p-hydrogen events, discussed in section 6.6, confirms this result.

The mean thickness of aluminium required in the beam to stop the protons was 20.98 ± 0.01 gms; this corresponds to a mean beam energy of 153.04 ± 0.05 MeV.

3.4 The bubble chamber experiment

The preliminary testing and filling operations were made as described in section 2.9. The chassis was lowered into the experimental area and lined up with the beam path in the position shown in figure 3.6, so that the beam profile E (plate V) was in the centre of the beam entry window.

Beam condition 2 of section 2 was automatically satisfied because the proton pulse supplied by the cyclotron is of only 600 μsecs duration. However, the magnitude of the flux had to be reduced to the extremely low level of 5 to 10 protons per pulse; this was done by inserting the "chopper" (a block of lead) into the circulating beam within the cyclotron tank. Because the chopper had to be almost fully inserted to reduce the flux sufficiently, it tended to give rise to seriously varying flux levels when the cyclotron was not completely stable. For example, whenever the cyclotron tripped off, the chopper would cool and contract and on the subsequent restart of the machine would allow too much beam to pass. The beam flux was therefore continuously monitored by an observer with binoculars situated at a vantage point in a radiation-free zone above the experimental area. It was found that, despite the very short duration of the illuminating flash, an experienced observer was able to detect serious fluctuations in both the flux level and the quality of the tracks. When each cassette was changed, a strip of film from the end of the roll was developed to check directly the flux level and quality of the tracks.

For the last hundred frames of each roll, aluminium absorber was placed in the beam path; 2.04 gms for 50 frames and 8.22 gms for 50 frames. The protons stopped approximately two-thirds the way across the visible region for the first set of frames and approximately half-way across for the second set. From these, the range constants for the propane under the operating conditions could be found and also a measurement of the beam

energy could be made (see section 5.5).

28,000 photographs were taken and these yielded approximately 9,500 2-prong events; this was the limit to the number that could be analysed on the measuring-machines in the machine time made available for this experiment. It had been hoped that another 10,000 photographs would be taken to obtain better statistics for the 3-prong events, the analysis of which required mainly scanning-machine time, on which there was no limit of availability. However, the run was brought to an end before these additional photographs could be taken because of the temperature controlling difficulties discussed in section 2.3.

Plate VI shows a typical frame.

Plate VI

A typical exposure showing a 2-prong event and the fiducial marks on the windows of the bubble chamber.

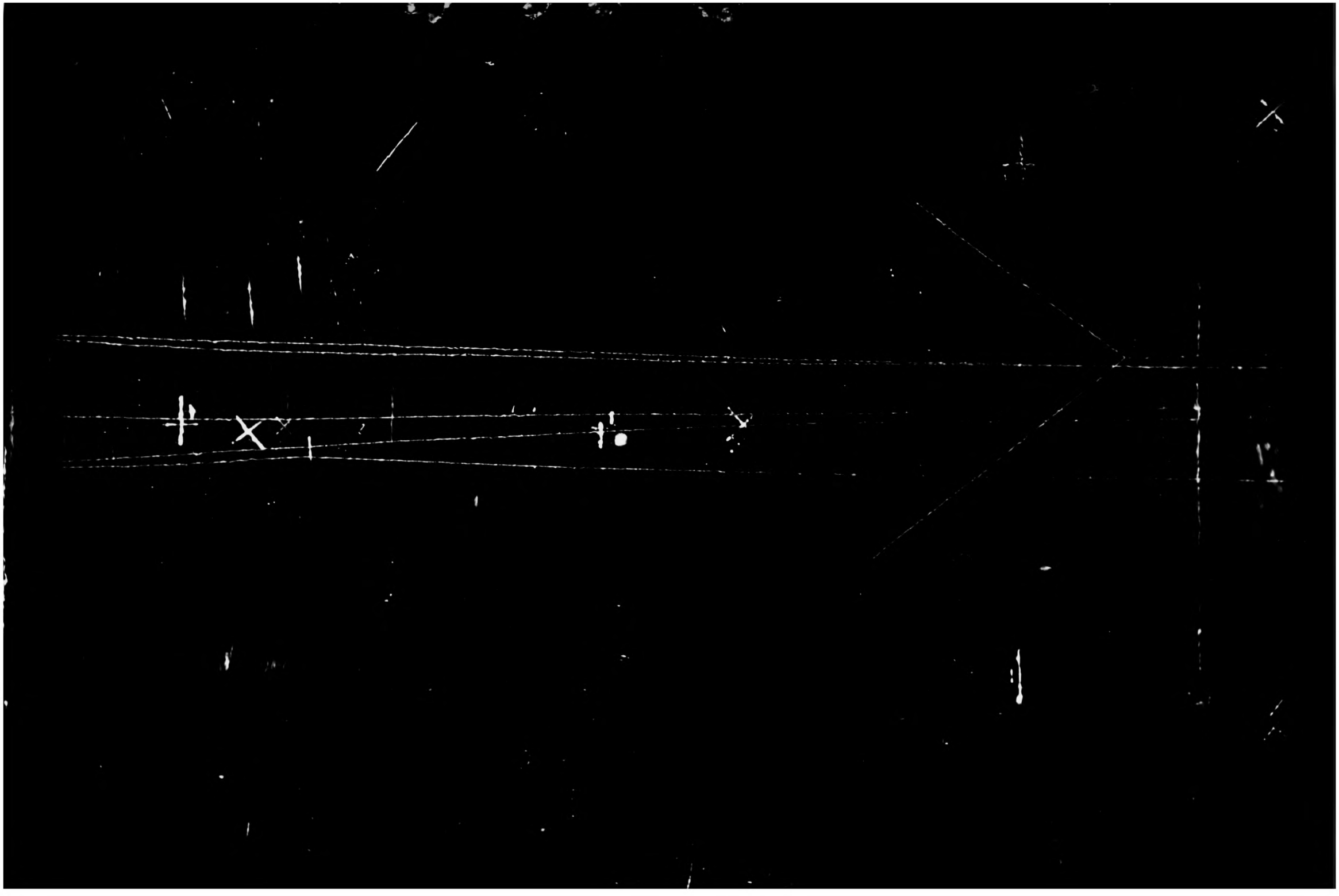

CHAPTER 4

EXTRACTION OF INFORMATION FROM THE FILM

4.1 Introduction

The collection of the experimental data was completed in approximately two weeks but the subsequent extraction of this data from the film took almost eighteen months. Some 27,600 expansions with the full energy proton beam were recorded but, for various reasons, such as flash tube failure and foaming, 1,200 frames were unusable.

The film was first scanned, when all the relevant information on each frame was noted, and then each 2-prong, 3-prong and 4-prong event was measured; the measurement consolidated , in a coded form on punched paper tape, all the information needed for the geometrical reconstruction of each event. The paper tape was processed by a Ferranti "Mercury" computer to give all the relevant geometrical and kinematical quantities for each event.

Appendix V gives the actual instructions followed in the routine analysis work. The remaining sections of this chapter are concerned with some of the details of the procedures followed, the discussion of which highlights the difficulties encountered in the collection of data by the bubble chamber method.

Scanning and measuring were kept quite independent of each other and they were, in fact, performed on different types of machines. The explanation for this is that the measurement of events on the film requires much more complex equipment than the basic projection and wind-on mechanisms required

for the scanning of the frames. It is therefore not an economical proposition to use more time on the measuring machine than is essential for the actual measurement of the events.

Because of the repetitive nature of the scanning process and because of the difficulties of the interpretation of the scanning instructions in border-line cases, the data collected depends to some extent upon the person scanning and also upon his or her mental alertness at the time of the scan. For this reason two completely independent scans were made of all the frames and from them a master-list was compiled. This master-list was used to find the events at the measuring stage of the analysis and whenever the list showed a discrepancy between the two scans an adjudicating decision was made by the measurer or, in cases of difficulty, by a physicist.

4.2 Scanning

This was performed on "British National Scanning Machines" with a magnification from film to projected image of 20; a description of these machines has been given by CRENNELL (1964).

Scanning is essentially a process of finding and tabulating all the events of interest on the film, in this case, the events with two or more prongs. However, to prevent inaccuracies in the cross-sections and the various angular and energy distributions obtained from the analysis, it is important that as much systematic bias as possible is avoided in the collection of the data.

Systematic biases arise because some classes of events are more easily

overlooked than others. Thus, for example, those 2-prong events with one very short prong are more likely to be overlooked than those with two long prongs, and since the proton energies decrease as the beam traverses the bubble chamber, the effect becomes more marked. Figure 4.1 shows a good example of such a loss. The distribution of proton energies is shown for all proton-hydrogen interactions for which the interacting proton energy is greater than 50 MeV. In the absence of any loss of events the known isotropy of the (p,H) cross-section in the centre of mass of the system dictates that the distribution should be uniform from zero up to 50 MeV; in fact, it is seen that there is a complete loss of events that have one proton of energy less than 4 MeV, and a gradually decreasing loss for events that have one proton energy between 4 MeV and 12 MeV (one bubble diameter corresponds to an energy of approximately 4.5 MeV).

A big reduction can be made in scanning biases if those frames on which it is very difficult or impossible to follow right through the bubble chamber the path of each incident proton are excluded from the analysis. Thus, for example, a frame was excluded from the analysis if:

(a) all the beam protons entered very close to each other

or (b) there was a very large number of tracks on the frame

or (c) the tracks were too faint for efficient detection; this occurred occasionally when the flash tube deteriorated more quickly than expected or when the propane drifted from its ideal working temperature.

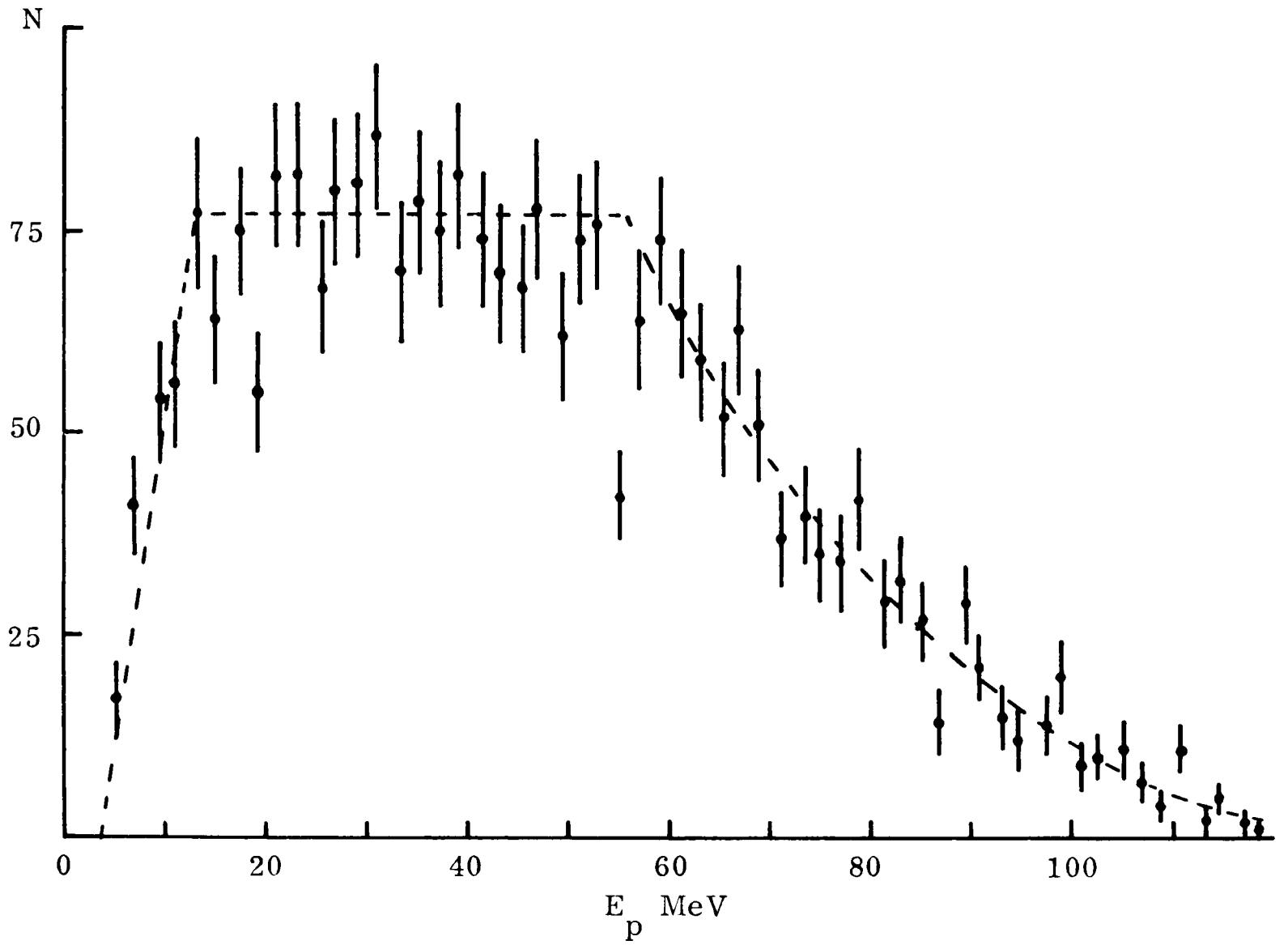

Fig. 4.1 Distribution of prong lengths for hydrogen events.
$E_o > 50$ MeV ; -5 MeV $< E_L <$ 5 MeV

Because very strict acceptance criteria were imposed, approximately 25% of the original frames were rejected (see chapter 7 and the table on page 55 for details).

Although all 2-prong events on rejected frames were completely ignored, it was decided that 3-prong and 4-prong events seen on these frames would be included in the lists - but their origin was noted so that they could be excluded from absolute cross-section measurements. These events were included for two reasons: firstly, because of the failure to accumulate, as planned, extra exposures to improve the statistics of the 3-prong and 4-prong events; and secondly, because, due to the large loss of 3-prong and 4-prong events even under ideal conditions (because of their very short prongs), any additional bias introduced by including the events on rejected frames would be small in any case.

When a frame was accepted, it was systematically examined for the presence of events with two or more prongs. All three views were examined because sometimes an event is clearly visible on one view only. Events with more than two prongs are confined to the first half of the chamber where the energy of the interacting protons is high. Also they proved to be easy to detect because they are characterized by the absence of long prongs. For these reasons the scanning of the rejected frames for the multi-prong events was not as difficult as might have been expected. This fact, reported in the next section, is reflected in the high scanning efficiencies achieved for these events.

There are several reasons for not recording some events which at first sight might appear quite acceptable. The application of the following tests removed some of the unwanted events before the measuring stage was reached.

(a) If the angle of entry of the incident proton, as seen on any of the views, was more than 3° from the mean entry angle, the event was not accepted. Protons entering at large angles must have scattered either in the beam entry window or in the unilluminated part of the propane, and, since nothing is known about these scatters, the protons have undeterminable energies.

Figure 4.2 shows the distribution of the angle between the incident proton direction projected on to the front window of the chamber and the horizontal.

(b) If the incident proton track, when projected backwards, fell outside the vertical limits of the beam entry window the event was again not accepted. The beam entry window limits drawn on the test template lie just within the actual window limits to allow for the rounding off of the corners of the window. Any proton outside these limits will have been degraded by an unknown amount.

Figure 4.3 shows the vertical distribution of the tracks entering the chamber.

(c) The incident proton track of an event was carefully examined and if it had a scatter on it the event was ignored. In this case the incident proton must be considered to have given rise to a one-prong event and

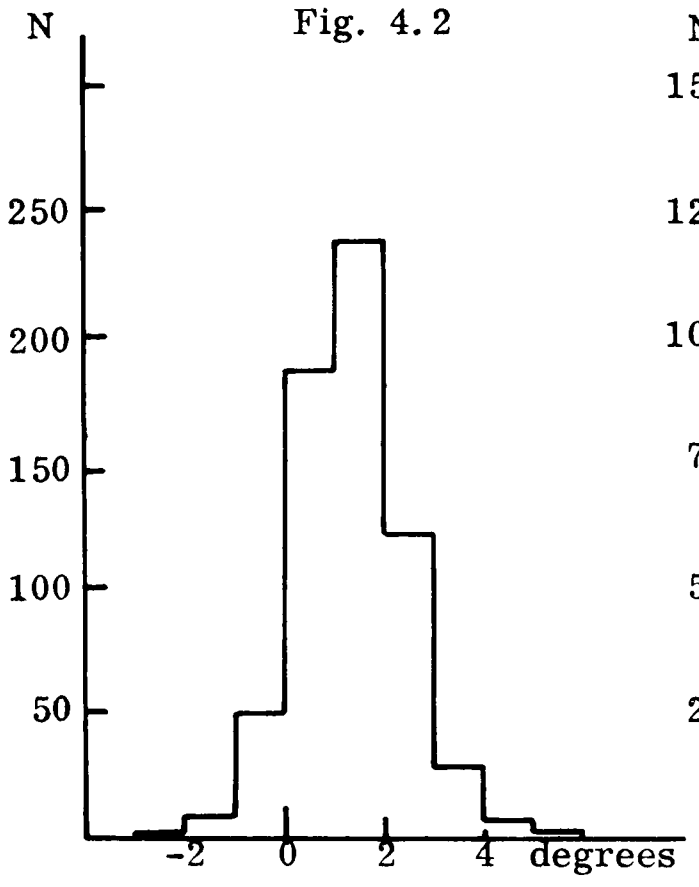

Fig. 4.2

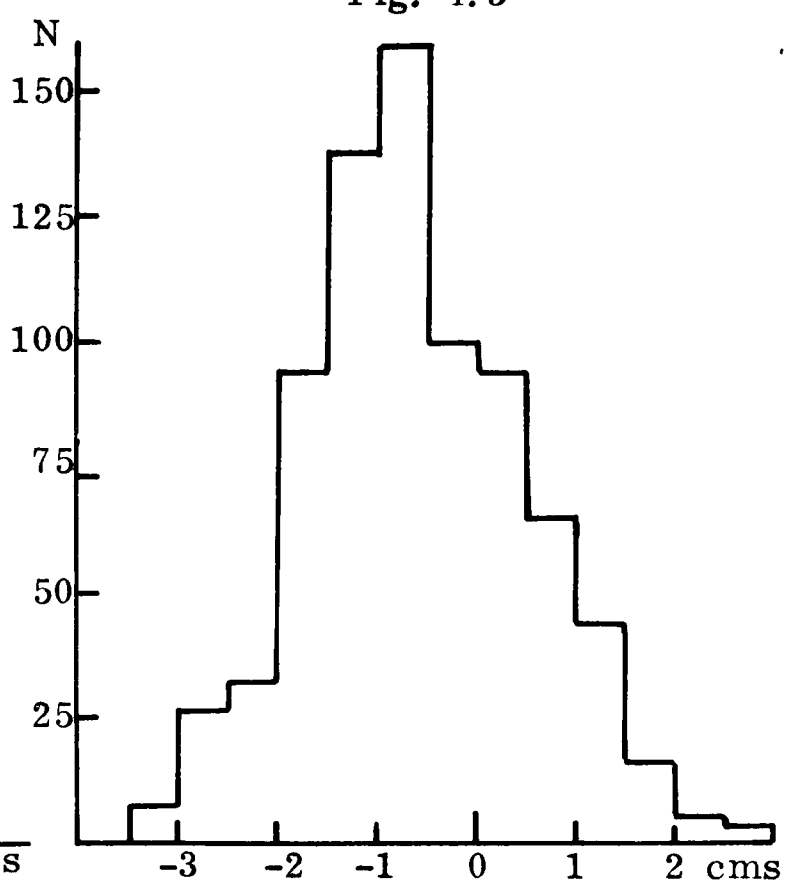

Fig. 4.3

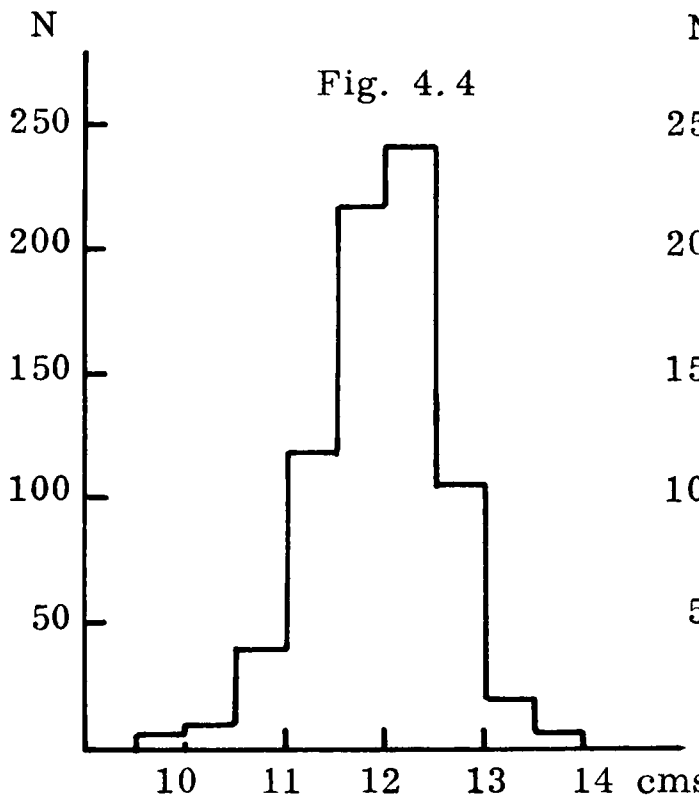

Fig. 4.4

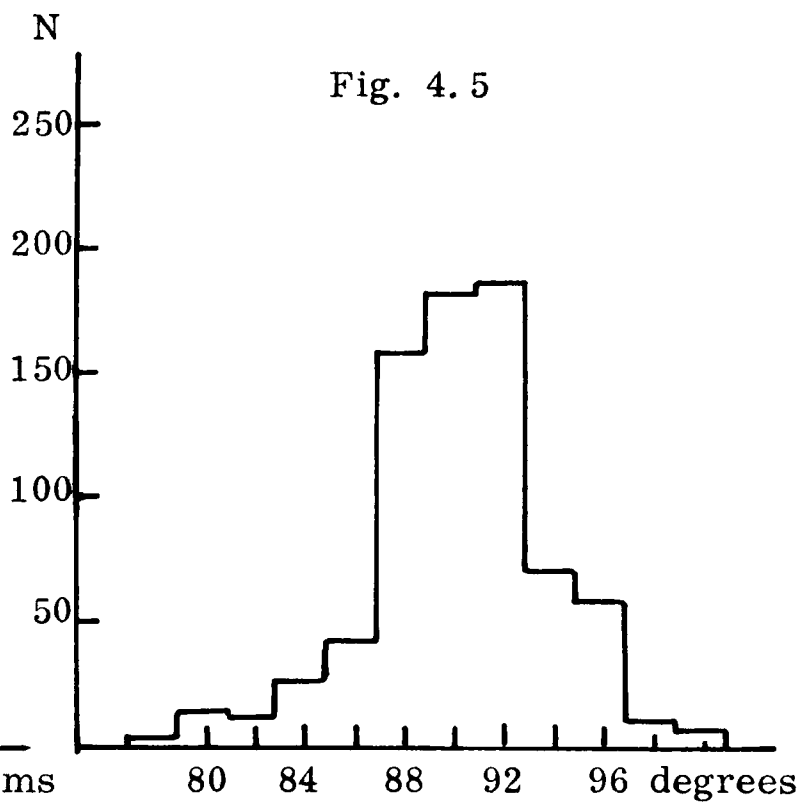

Fig. 4.5

Fig. 4.2 Angle between incident track and a line normal to beam entry window projected onto vertical plane

Fig. 4.3 Vertical distribution of incident tracks at point of entry to bubble chamber

Fig. 4.4 Distribution in depth of incident tracks at point of entry to bubble chamber

Fig. 4.5 Angle between incident track and a line normal to the beam entry window projected onto horizontal plane.

so contributes to the elastic or (p,p') cross-section and not to the multi-prong cross-section. (A multi-prong event with a further interaction on one of its prongs must, of course, be included; although a full analysis cannot be made of such events, they must be allowed for in the calculation of cross-sections.)

These criteria were also applied when the number of tracks on the frame was counted; this was done on every tenth frame.

The three tests given above eliminate most of the unwanted events, but, due to the fact that a two dimensional projection of the bubble chamber space is observed on the films, large angles and displacements in a direction away from the camera plane cannot be detected on the projected images. Another test was therefore made in the reconstruction program to remove any such events.

Figure 4.4 shows the distribution in depth of the apices of events and figure 4.5 shows the distribution of the angle, projected on to a horizontal plane, between the incident proton direction and a horizontal line normal to the plane of the beam entry window.

4.3 Comparison of the two independent scans

The table below summarizes the data obtained from the two scans. The number of frames examined was 27,584

	Seen on 1st scan but not 2nd	Seen on 2nd scan but not 1st	Seen on both scans
No. of rejected frames	2704	2124	6037
No. of 2-prong events	1239 + 771R	966 + 980R	5544
No. of 3-prong events	47 + 24R	36 + 18R	623 *1
No. of 4-prong events	2 + 1R	-	23 *2

R denotes the events seen on one scan which fell on frames rejected on the other scan.
*1 623 includes 135 events on frames rejected on both scans
*2 23 includes 8 events on frames rejected on both scans
The number of 4-prong events is considerably less than the total number of 4-prong events actually measured because a comparatively large number of 4-prong events was discovered when the classified 3-prong events were examined closely under a microscope at the measuring stage.

Scanning efficiencies can be deduced from the figures in the table.

To obtain an expression for the efficiencies of the two scans and of the combined scan, it is assumed that the events not seen on each scan form a random sample of the events actually present.

Therefore if

N_0 = number of events seen on both scans

N_1 = no. of events seen on the 1st scan but not on the 2nd

N_2 = no. of events seen on the 2nd scan but not on the 1st

N = the unknown total number of events present

e_1 = the efficiency of the 1st scan

e_2 = the efficiency of the 2nd scan

e = the efficiency of the combined scan

then

No. of events seen on the 1st scan = $e_1 N$

No. of events seen on the 2nd scan that were not seen on the first scan

= e_2 x the no. of events <u>not</u> seen on the first scan

= $e_2 (N - e_1 N)$

The total no. of events seen by both scans is therefore

$$eN = e_1 N + e_2 N - e_1 e_2 N$$

$$e = e_1 + e_2 - e_1 e_2 \qquad (1)$$

and the individual efficiencies are

$$e_1 = \frac{e (N_o + N_1)}{N_o + N_1 + N_2} \qquad (2)$$

and $$e_2 = \frac{e (N_o + N_2)}{N_o + N_1 + N_2} \qquad (3)$$

Equations (1), (2) and (3) can be solved for e_1, e_2 and e.

It must be remembered that these expressions do not include systematic losses.

Using the equations and the values given for the 2-prong events in the table (and ignoring those events on rejected frames), the efficiencies derived are

$$e_1 = 85.2\%$$

$$e_2 = 81.9\%$$

$$e = 97.3\%$$

These figures give a lower-limit estimate for the efficiencies because the first two columns of figures in the table for the 2-prong events reflect, to a large extent, those cases where a scanner was in doubt as to whether or not an observed phenomenon was a 2-prong event. Different decisions on the two scans for the same phenomena therefore give rise to a large proportion of the events in these columns. It can be seen in appendix VII that about a half of these phenomena proved not to be 2-prong events when studied more closely at the measuring stage. This reflects a tendency on the part of scanners, especially when tired, to record a doubtful phenomenon rather than to examine it carefully on all three views. This is inclined to make the scanning efficiencies, as defined appear rather low.

An upper limit for the efficiencies can be obtained by analysing those 2-prong events that have both prongs of length greater than, say, 2.5 mms (corresponding to a proton energy of approx. 10 MeV). This category of events excludes most of the doubtful phenomena described above, although it also excludes the event types particularly prone to loss at the scanning stage. From these events the following upper-limit efficiencies were obtained

$$e_1 = 95.6\%$$

$$e_2 = 95.1\%$$

$$e = 99.8\%$$

It is interesting to note that, despite the short prongs always associated with 3-prong events, the detection efficiencies for these events are of approximately the same magnitude as those for the 2-prong events. From the

figures in the table (excluding the events on rejected frames), the efficiencies are calculated as

$$e_1 = 93.1\%$$

$$e_2 = 91.3\%$$

$$e = 99.4\%$$

4.4 Measurement of events

The 2-prong events were measured on a machine constructed at the Nuclear Physics Laboratory by the bubble chamber analysis group. On this machine (which differed in this respect from most of the machines in use at the laboratory), the measurements were performed on the projected image and not on the film itself. A co-ordinate measuring apparatus, previously used and described by HOPKINS (1961), was provided with an automatic digitizer, coupled to a paper-tape punch, and set over the horizontal screen on to which the image of the film was projected with a magnification of approximately 20. To record the co-ordinates of a point a reference cross-wire, carried on the co-ordinate arms, was set in coincidence with the relevant point and a foot-pedal switch was operated to transfer the x and y co-ordinates of the point on to 5-hole paper tape. The sequence of points measured and the facilities for correcting errors are shown in detail on the "Measuring Procedure" given in appendix V. The measurement of fiducials on the chamber window provides the link between the co-ordinate system of the measuring machine and that of the bubble chamber.

Accuracy of measurement was checked in the geometrical reconstruction

program and all events that failed to meet the tight tolerances imposed on the measured points were separated out. These events, with certain exceptions, were remeasured until they were accepted by the program. The exceptions referred to were those events that only just failed to meet the accuracy requirements and which were recognized from the computer output to be due, unambiguously, to proton-hydrogen interactions. Because no detailed analysis of these interactions was to be made, a set of less accurately measured events was quite acceptable.

The 3-prong events were measured on a "Cooke series 400" microscope at a magnification of 150. The need for a microscope measurement was clearly indicated when an initial measurement showed that only 50% of the events could be measured on the measuring machine because of the small relative size of the event compared with the reference fiducial. With the microscope 85% of the events were measured. Also, with the microscope a much more accurate setting could be made on end points and apices, and this is important in the case of 3-prong events because of the large number of associated short tracks. Plate VII gives a good indication of the improvement obtained by using the microscope; the two photographs show the same 3-prong event* as it appeared on the measuring machine and under the microscope.

---

* The frame shown was actually rejected on the criteria set out in section 4.2.

Plate VII

A 3-prong event as it appeared on a measuring machine and as it appeared under the microscope

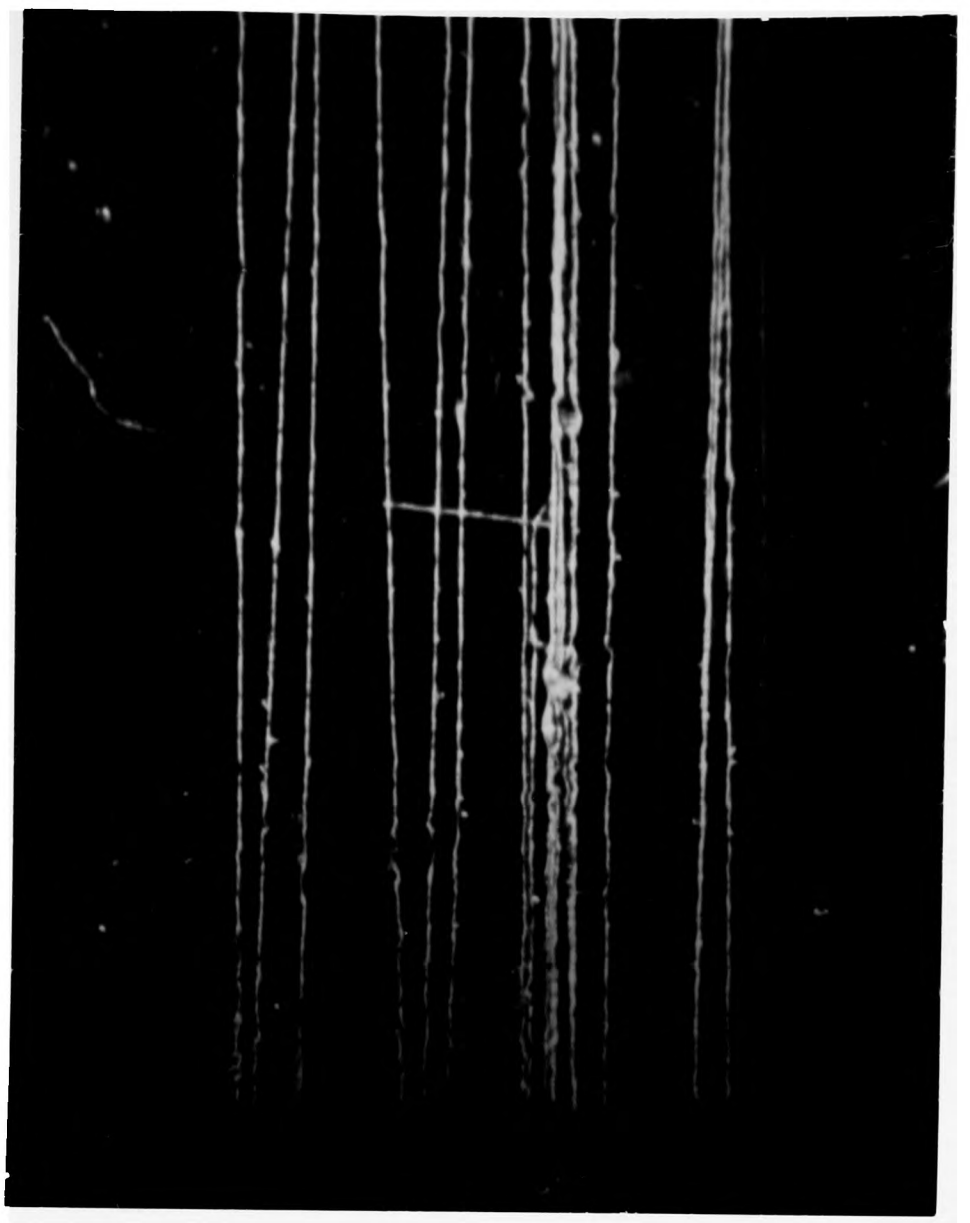

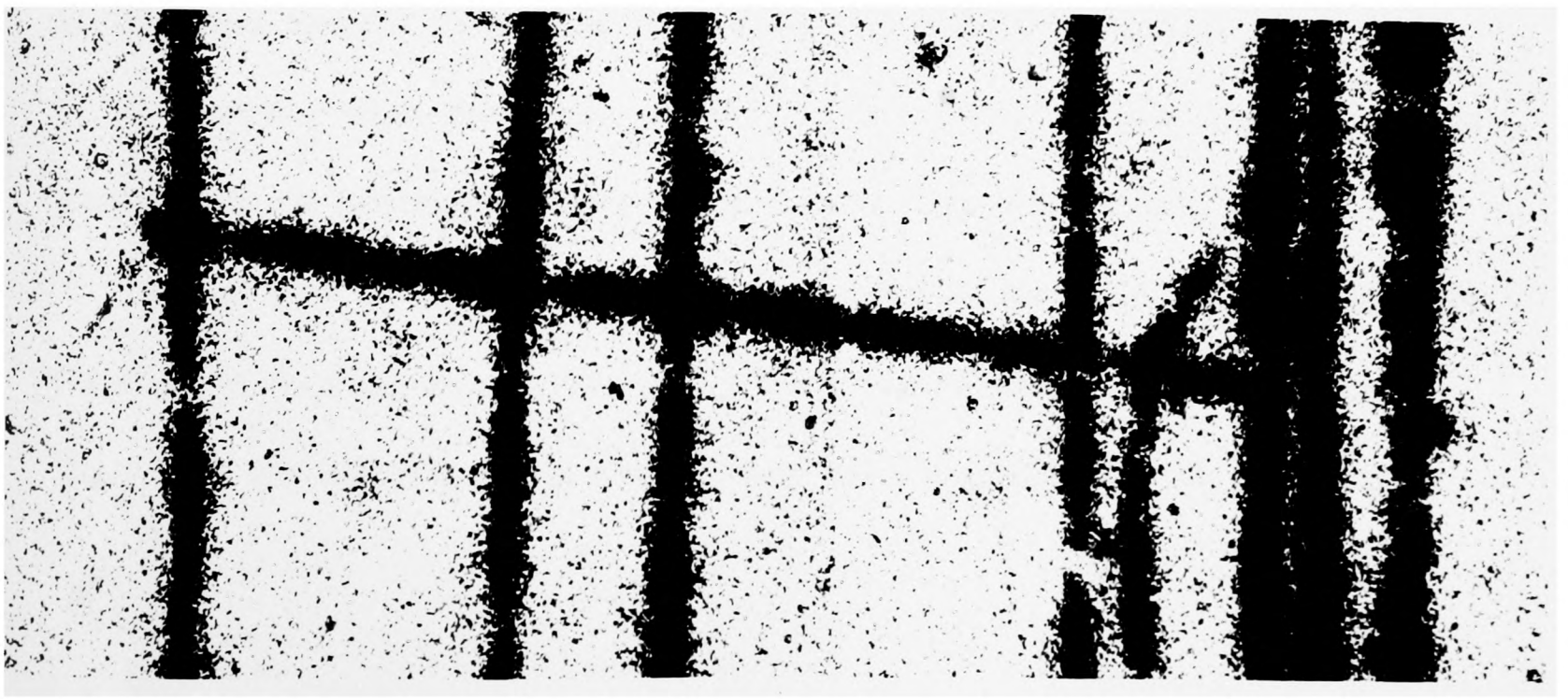

Whenever possible the events were measured on all three views and the reconstruction was performed for all pairs of views that met the accuracy tolerances: the results from these reconstructions were then averaged. The presence of distortions or of other tracks sometimes prevented measurement on one or more views. An example of distortion is shown in plate VIII in which view B is undistorted and view A has a distortion on one prong.

Because the microscope was not supplied with an automatic digitizer, the following operations were necessary to transfer the information from the microscope to paper-tape:

(a) x and y co-ordinates were read from the micrometer screw gauges on the microscope.

(b) the numbers were written on specially prepared forms

(c) the numbers were teleprinted on to 5-hole paper-tape.

Each operation involved 42 numbers per event and the cumulative errors of the three manual processes were such that 5 % of the events were found to have errors when they were checked in the reconstruction program. This meant that, on average, each event had to be measured twice.

About 10% of the 3-prong events recorded in the scanning process were found to be 4-prong events when they were examined under the microscope. These and the other 4-prong events were also measured on the microscope.

Plate VIII

Two views of a 4-prong event under the microscope, indicating the type of difficulty that occurred as a result of optical distortions in the propane.

A

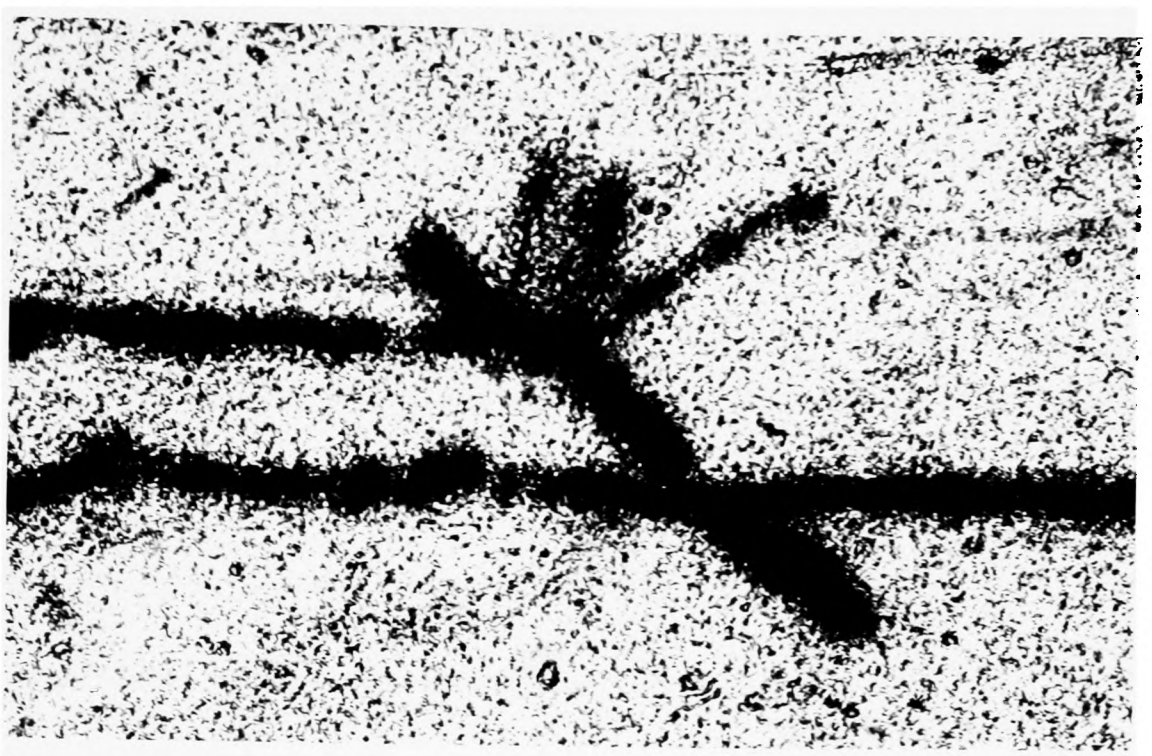

B

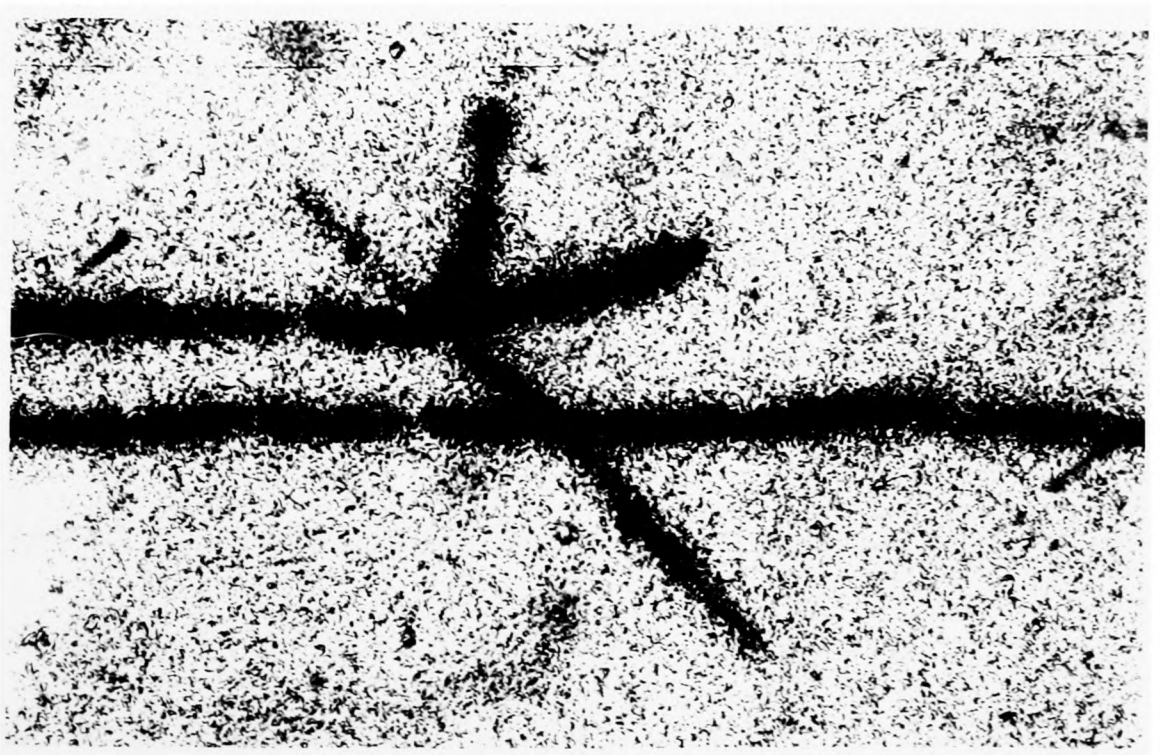

CHAPTER 5

FROM MEASUREMENTS TO PHYSICS

5.1 Introduction

The paper-tape output from the measuring machine contains all the information necessary for the identification and reconstruction of each event. It was processed on "Mercury" computers at AERE, Harwell and at the Computing Laboratory of the University. The program for the analysis of the events was written mainly in "Autocode" and its main functions were to read and decode the co-ordinates of the measured points, to check on the accuracy of the measurements, to reconstruct the events in three dimensions from the information provided by two stereoscopic views, and finally to calculate the necessary geometrical and kinematical quantities.

This chapter

(a) shows the derivation of the equations used for the reconstruction, with emphasis upon their use in practice;

(b) describes in detail the program written for the analysis of the 2-prong events;

(c) indicates the modifications to the basic program necessary for the analysis of the 3-prong and 4-prong events;

and (d) deals in some detail with the determination of the parameters needed for the analysis.

5.2 Reconstruction of an event from measurements on two stereoscopic views

For the sake of the discussion, 2-prong events are considered.

For all 2-prong events the points x_1y_1 to x_5y_5 were measured and for some events either or both of the points x_6y_6 and x_7y_7 were also measured (see appendix V). These latter two points, when measured, were used only for measurement accuracy checks.

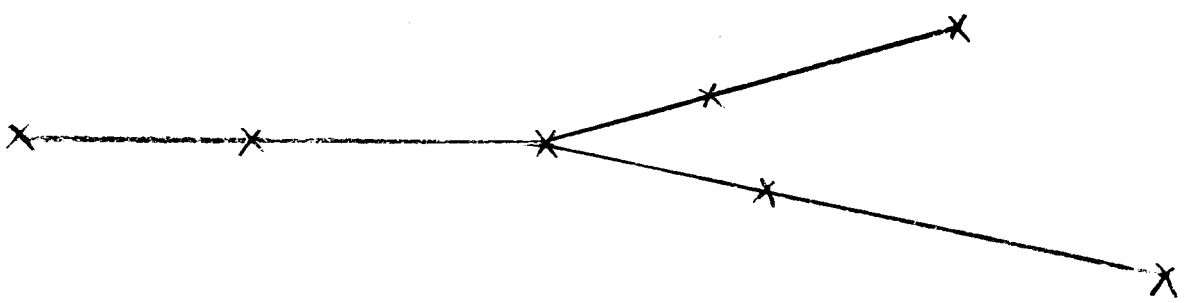

The apex and the end points of the two prongs could be unambiguously identified and measured on the two separate views, but the point of entry of the incident proton to the illuminated region of the chamber was usually indistinct because of a slight diffuseness at the edge of the illuminating light-cone; non-corresponding points were measured therefore on the incident track. Because of this, the method used for reconstructing the two prongs was different from that used for reconstructing the incident track; these two methods are discussed below.

The co-ordinate axes (XYZ), (x'y'z') and (x''y''z'') all refer to a system using the base line of the cameras, projected on to the bubble chamber window, as the abscissa It is assumed that the transformations through the co-ordinate systems defined by the measuring machine and by the fiducials etched on the bubble chamber window have been made. The co-ordinate axes are shown in appendix VI and the series of co-ordinate transformations made in the analysis

program can be seen in figures 5.1 and 5.2.

Reconstruction of the corresponding points of the prongs

In appendix VI the equations are derived which relate the spatial co-ordinates (XYZ) to the film co-ordinates of a corresponding point; they are:

$$X = \frac{\ell/2\,(y'x'' + x'y'')}{(y''x' - y'x'')}$$

$$Y = \frac{\ell y'y''}{(y''x' - y'x'')}$$

$$Z = \left[\frac{\ell y''}{y'x''-y''x'} - \frac{d}{f} - \delta\left\{n^{*2}f^2+(x'^2+y'^2)(n^{*2}-1)\right\}^{-\frac{1}{2}}\right]\left[n^2f^2+(x'^2+y'^2)(n^2-1)\right]^{\frac{1}{2}}$$

where

x'y' are the co-ordinates of the point on one view, scaled-up to bubble chamber dimensions
x''y'' are the co-ordinates of the same point on the other view, also scaled-up
ℓ is the distance between the cameras
d is the perpendicular distance between the camera lenses and the front window of the chamber
f is the distance between the lens and the film within the cameras
δ is the thickness of the front window
n* is the refractive index of the front window
n is the refractive index of the propane.

Because the co-ordinate system is tied to the two camera positions, as described above, y' is approximately equal to y'' (see appendix VI). This property is used as a check on the accuracy of the measurement of corresponding points.

If the co-ordinates y' and y'' are replaced by $y = \frac{y'+y''}{2}$ the above equations reduce to

$$X = \frac{\ell/2\,(x' + x'')}{x' - x''}$$

$$Y = \frac{fy}{y''-x''}$$

$$Z = \left[\frac{f}{x''-x'} - \frac{d}{f} - \left\{n^{*}d^{2}+(x'^{2}+y'^{2})(n^{*2}-1)\right\}^{-\frac{1}{2}}\right]\left[n^{2}d^{2}+(x'^{2}+y'^{2})(n^{2}-1)\right]^{\frac{1}{2}}$$

It is shown below that the errors arising from this approximation are very small and that, paradoxically, it is essential to use the "approximate" equations in order to achieve accurate reconstruction.

The approximation $y' \approx y''$

It can be shown, by manipulating the equations of appendix VI, that

$$y''-y' \sim \frac{Yf(r''^{2}-r'^{2})}{2d^{4}}\left[\frac{Z(n^{2}-1)}{n^{2}} + \frac{\delta(n^{*2}-1)}{n^{*3}}\right]$$

where $r'^{2} = (x'^{2}+y'^{2})$

and the other symbols are the same as before.

If the worst combination possible within the bubble chamber for the values of Y, Z, r' and r'' is used,

$$y''-y' \sim 0.15 \text{ mm}$$

this is of the same order as the measuring errors. In general, therefore, the error arising from the approximation is much smaller than the measuring error and it can be neglected.

Because of the presence of measuring errors, the exact equations can, under certain circumstances, lead to very large errors in the reconstructed points. For example, consider the first term in the exact equation for Z. The error in this due to measurement errors in y' and y'' is

$$\frac{\delta x''}{y\,(x''-x')}\,\Delta y' + \frac{\delta x''}{y''(x''-x')}\,\Delta y''$$

Therefore for points close to the camera base line (y' and y'' →), the error in Z can become very large.

The reconstruction of the fiducials on the back window of the bubble chamber illustrates this point very well, because for each view pair two fiducials lie close to the camera base line, as can be seen from the following diagram:

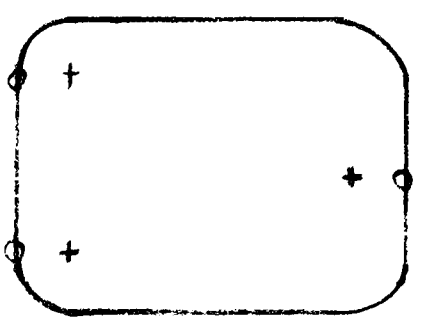

The circles show the intersections of the optic axes of the cameras with the window, and the crosses show the approximate positions of the fiducials measured.

The 7 co-ordinates of the fiducials, as reconstructed from the exact and approximate equations, are shown in the table (in centimetres).

		views 1 and 3	views 2 and 3	views 1 and 2
EXACT	F_1	13.9	22.9	27.4
	F_2	23.2	26.8	25.2
	F_3	18.9	23.6	23.9
APPROX	F_1	22.9	22.7	23.2
	F_2	23.1	23.2	23.3
	F_3	22.6	23.0	23.6

The measured depth of the chamber is 22.97 cms.*

It is seen that in each case the two fiducials lying close to the base line were very badly reconstructed by the exact equations. The "approximate" equations were, therefore, used throughout the analysis.

Reconstruction of the incident track

A reconstruction method based on the construction of corresponding points on the incident tracks was found to lead to errors of up to 2 to 3 MeV in the calculated incident energy. The following method, using the angles of the track, as measured on the two views, gave an order of magnitude improvement in accuracy.

It is shown in appendix VI that the spatial angles of the incident track (α and β) are related to the angles of the track measured on the film (θ' and θ'') through the equations

$$\Phi = \tan^{-1}\left(\frac{\tan\Phi}{\tan\Theta}\right)$$

$$\alpha = \tan^{-1}\left(\frac{\tan\Phi}{\sin\beta}\right)$$

where
$$\tan\Phi = \frac{(Y_o - \ell/2)\tan\theta'' - (Y_o + \ell/2)\tan\theta'}{(Z_o + nd + n\delta/n^*)(\tan\theta'' - \tan\theta')}$$

and
$$\tan\Theta = \frac{X_o}{(Z_o + nd + n\delta/n^*)} - \frac{\ell\tan\theta'\tan\theta''}{(Z_o + nd + n\delta/n^*)(\tan\theta'' - \tan\theta')}$$

$X_o Y_o Z_o$ are the co-ordinates of the apex.

---

* The discrepancies between this value and those given in the table are due mainly to the fact that these numbers were obtained before the camera positions had been finally determined.

From α, β, X_o, Y_o, and Z_o, the point of intersection of the incident track with the inside of the beam entry window was calculated.

The angles θ' and θ'' were obtained from least squares fits to the three points measured on the incident track.

5.3 The computer program for the analysis of the 2-prong events

This was written mainly in "Autocode", but basic machine language was used for decoding the co-ordinates punched out by the measuring machine. Figures 5.1 to 5.3 show, together, a macroscopic flow diagram for the whole program, which can conveniently be divided into three sections. The first section, shown in figure 5.1 and the upper part of figure 5.2, deals with the reading of the measuring machine tape; the checking for format errors on the tape and for inaccurate measurements; the decoding of the co-ordinates to decimal form, and the transformation into the camera-co-ordinate system of all the event co-ordinates. The second section, shown in the lower part of figure 5.2, deals with: the reconstruction of corresponding points and the incident track; the transformation of points and angles back to the fiducial co-ordinate system; and checking that the tracks do not leave the illuminated region of the propane or pass through the bubble chamber windows. Finally, in the third section, shown in figure 5.3, the geometrical and kinematical quantities are calculated and printed on to the output tape.

More details concerning some of the operations and calculations shown in the flow diagrams are set out in the following notes:

1. The point measured first and last on each view was the fiducial at the

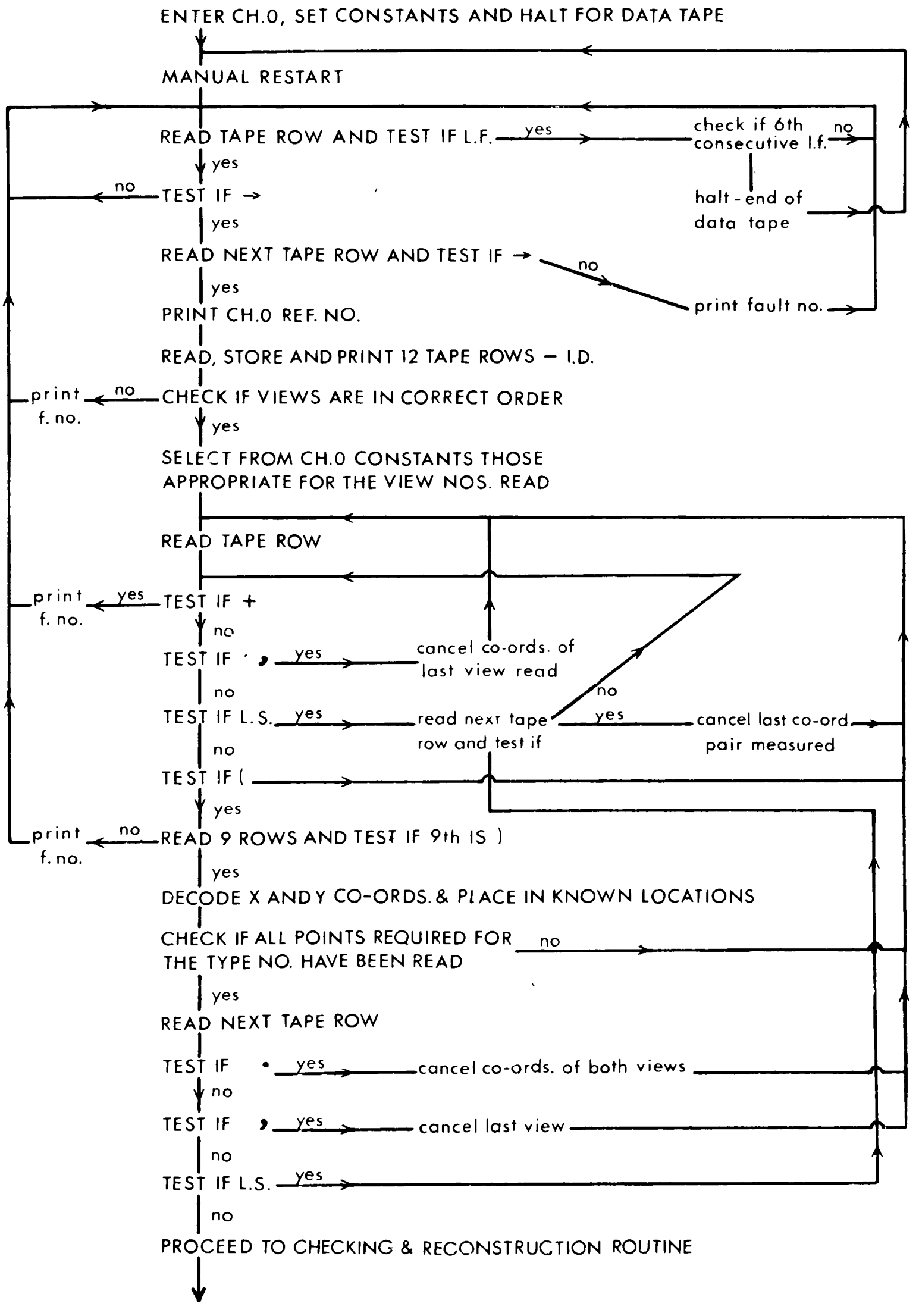

FIG.5·1 INPUT ROUTINE

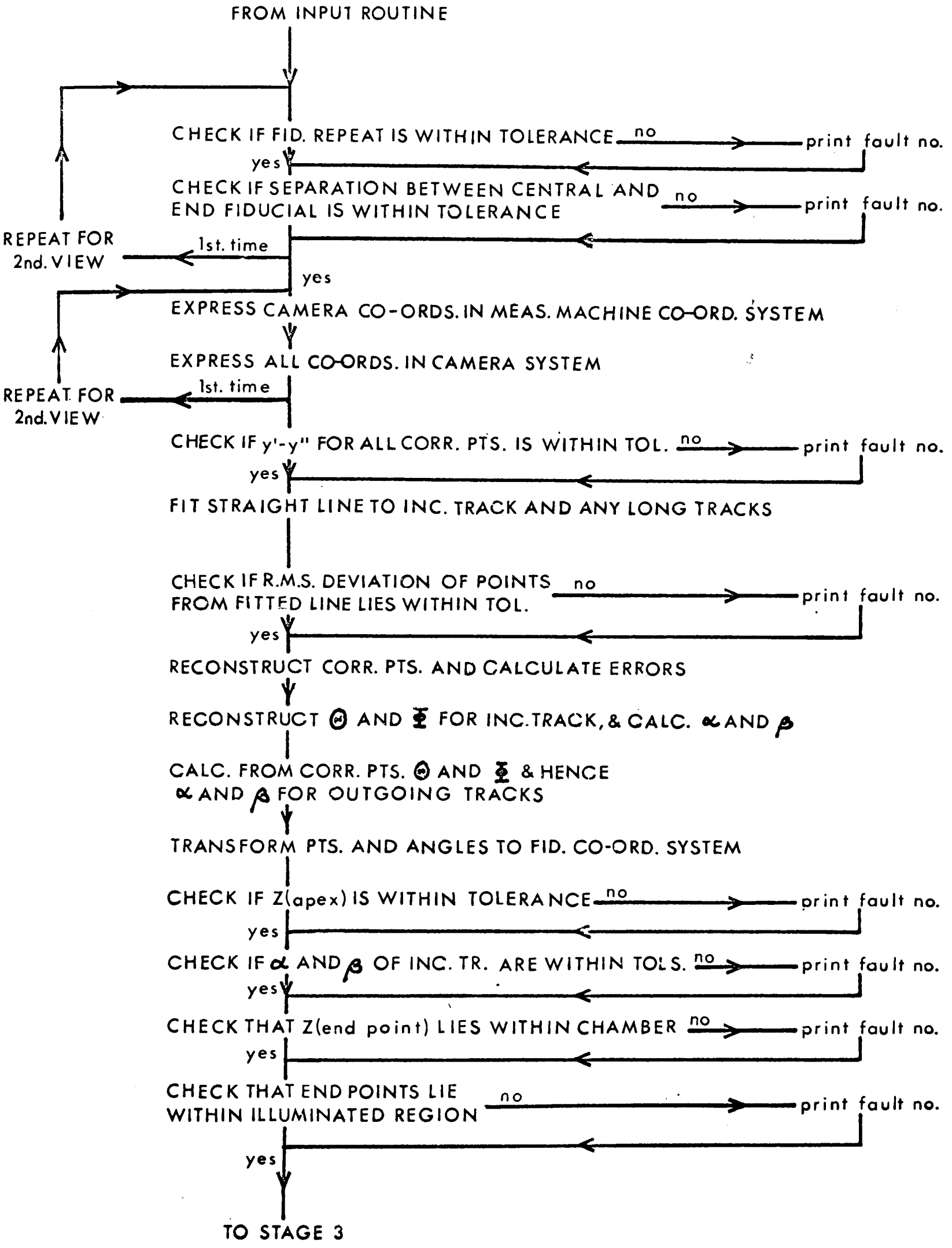

FIG. 5.2 CHECKING AND RECONSTRUCTION ROUTINE

CALCULATE AZIMUTHAL ANGLE

CALCULATE COPLANARITY

CALCULATE $\theta_1, \theta_2, \theta_3$

CALCULATE l_0, l_1, l_2, AND HENCE E_0, E_1, E_2

CALCULATE MOMENTUM & ENERGY OF RECOIL NUCLEUS

$E_0 - E_1 - E_2$

CHECK IF > 5 Mev — no

yes

SUBTRACT E_R

PRINT ROUTINE

JUMP TO INPUT ROUTINE AND PROCEED TO NEXT EVENT

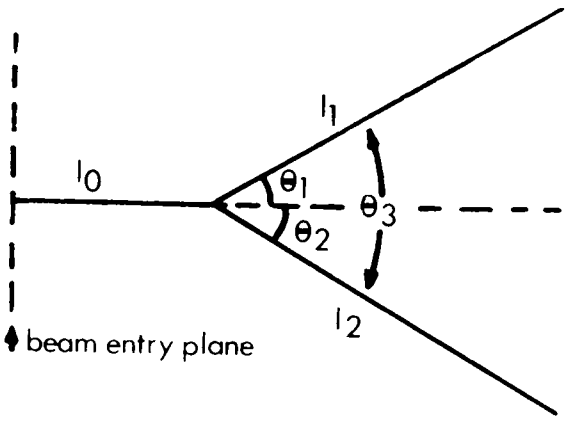

FIG. 5·3 EVENT KINEMATICS

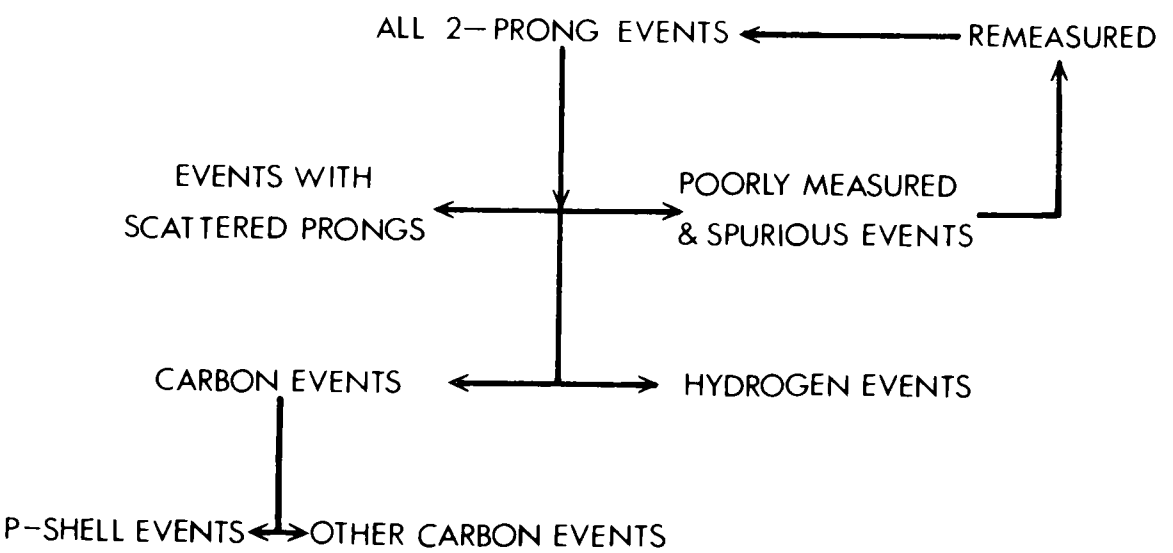

FIG. 5·4 2-PRONG EVENT SORTING

centre of the front window of the chamber. Any inconsistent behaviour of the measuring machine can be detected by comparing these measurements.

2. The parameters of the straight line fitted to the incident track on each view are given by:

$$m = \frac{\begin{vmatrix} \sum x_i y_i & \sum x_i \\ \sum y_i & 3 \end{vmatrix}}{\begin{vmatrix} \sum x_i^2 & \sum x_i \\ \sum x_i & 3 \end{vmatrix}} \quad \text{and} \quad c = \frac{\begin{vmatrix} \sum x_i^2 & \sum x_i y_i \\ \sum x_i & \sum y_i \end{vmatrix}}{\begin{vmatrix} \sum x_i^2 & \sum x_i \\ \sum x_i & 3 \end{vmatrix}}$$

$$i = 1 \rightarrow 3.$$

3. The illuminated region of the propane is conical, with a cross-section of the same shape as the condensing lens (see plate III). A set of equations defining four planes and four conic segments gave a good fit to surface of the region. The distance of each point from the surface was calculated and it was found that, with the exception of those points associated with events at the very end of the chamber, all the end points lay well within the illuminated region. The same result applied for the distances of the end points from the windows of the chamber. Since events at the very end of the chamber were excluded from the analysis (see section 6.1), all reaction products of interest stop within the visible region of the chamber.

4 The azimuthal angle (λ) is defined as the angle between the plane of the front window of the bubble chamber and the plane containing the incident track and the longer of the two prongs. In the program it was calculated

from

$$\lambda = \frac{\underline{\ell}_0 \, \underline{\ell}_1 \cdot \underline{Z}}{|\ell_0 \ell_1 Z| \sin\theta_{01}}$$

where $\underline{\ell}_0$ is the incident track length vector

$\underline{\ell}_1$ is the length vector of the longer prong

$\underline{Z}$ is the unit vector perpendicular to the chamber window

and θ_{01} is the angle between the incident track and the longer prong.

5. The coplanarity (γ) of the event is defined as the volume of the parallelepiped whose sides are the unit vectors along the incident track and the two prongs.

$$\gamma = \frac{\underline{\ell}_0 \wedge \underline{\ell}_1 \cdot \underline{\ell}_2}{|\ell_0 \ell_1 \ell_2|}$$

6. Energies were calculated from the ranges of the particles (or, in the case of the incident proton, the residual range). For protons the range-energy relationship used was:

$$\log_e E = 3.0446 + 0.5427 \log_e R + 0.0245 (\log_e R)^2$$

(E in MeV and R in cms)

7. In the initial analysis all the observed tracks were assumed to represent protons and the 2-prong events were analysed either as (p, H) reactions or $C^{12}(p, 2p)B^{11}$ reactions. To establish the energy loss in each reaction the quantity $E_0 - E_1 - E_2$ was first calculated

where E_0 is the energy of the interacting proton

and E_1 and E_2 are the energies of the two "protons" produced by the interaction.

If $E_o - E_1 - E_2$ is in the range 0 ± 5 MeV the event must represent a (p, H) reaction, but if it is greater than 5 MeV the event almost certainly represents a (p, C^{12}) reaction. The good energy resolution obtained for the energy-loss distribution for the 2-prong events, as shown in chapter 6, makes this unambiguous separation possible.

For hydrogen events $E_o - E_1 - E_2$ was printed as the energy loss, but for carbon events the energy of the recoiling nucleus (E_R) was calculated from the momentum balance, assuming a $C^{12}(p, 2p)B^{11}$ reaction, and $E_o - E_1 - E_2 - E_R$ was printed as the energy loss in the reaction.

A subsidiary program was written for reconstructing the carbon events on the assumption that they represented various reactions involving heavy particles, for example (p, pα), (p, pd) etc.

A book-keeping program was used to sort out the events into various categories. The operations of this program are summarized in figure 5.4.

5.4 Computer programs for the analysis of the 3-prong and 4-prong events

These programs were basically the same as the 2-prong program. The main differences were as follows:

1. The decimal co-ordinates from the microscope measurements were read into the computer by the standard "Autocode" fast read routine and they required no decoding.
2. Measurement from either two or three views could be read in; the relevant directive was stored in the event identification number.
3. For the 3-prong events the initial analysis was made in terms of the

$C^{12}(p, 3p)Be^{11}$ reaction, and for the 4-prong events in terms of the $C^{12}(p, 4p)Li^{9}$ reaction. Later, a whole range of reaction hypotheses, involving one or two of the particles d, t, He^3 or He^4, were investigated for the 3-prong events, and the reaction hypothesis $C^{12}(p, p3\alpha)$ was investigated for the 4-prong events.

The range-energy relationship used for the heavy particles was:

$$\log_e\left(\frac{E}{m}\right) = 3.0446 + 0.5427 \log_e\left(\frac{Z^2}{m}R\right) + 0.00345 \left(\log_e\left(\frac{Z^2}{m}R\right)\right)^2$$

where R is the range in centimetres

m is the mass of the particle in units of the proton mass

Z is the charge of the particle.

4. When three views had been measured for an event, the event was reconstructed on each of the three possible view pairs in turn.

5. After all events had been measured, and, where necessary, remeasured, the results from all the acceptable reconstructions for each event were averaged.

5.5 Bubble chamber constants

Numerical values for several parameters of the apparatus were required for the analysis of the events. The methods that were used to determine these are discussed below:

1 Thickness and refractive index of the front window of the chamber.

These were determined by direct measurement on the window

thickness = 3.89 cms

refractive index = 1.53.

2. Co-ordinates of the camera principal axes in the fiducial co-ordinate system.

A standard program, written by BÖCK (1960) was available for the determination of the camera co-ordinates. It assumes that the two windows of the bubble chamber and the plane in which the camera lenses lie are parallel to each other, and it requires the following input information:

(i) Refractive index and thickness of the front window

(ii) Depth of the chamber and the refractive index of its contents; the former was obtained directly with a copper spacer-bar (=22.97 cms), and the latter was unity because the measurements were made on photographs of an empty chamber.

(iii) Distance between the camera plane and the chamber window; found by direct measurement (=85.13 cms).

(iv) Co-ordinates of the fiducial marks on the front and back windows, found by theodolite measurement during the assembly of the chamber.

(v) Approximate co-ordinates of the cameras in the fiducial co-ordinate system. Found by direct measurement.

(vi) Distances between the three pairs of camera lenses. Found by direct measurement.

(vii) Measurements on the film from each camera, taken in the same order as in (v), of each of the fiducial marks, taken in the same order as in (iv).

The co-ordinates of the camera principal axes calculated by the program were:

	camera 1	camera 2	camera 3
x(cms)	-13.64	14.55	14.73
y(cms)	- 0.61	-10.66	8.69

3. Refractive index of the propane under operating conditions.

An iterative method was used to determine the refractive index. Its value in the analysis program was varied until the reconstructed values of the Z co-ordinates of the fiducial marks on the back window of the chamber best fitted the known depth of the chamber. The best fit was obtained for a refractive index of $1.22 \pm .01$.

4. The position of the beam-entry plane in the fiducial co-ordinate system.

This was found, by theodolite measurement, to be in the yz plane at x = 15.45 cms.

5. Parameters of the range-energy relationship in propane and the incident proton energy.

The range-energy relationship was determined by numerical integration from the energy-loss formula of LIVINGSTONE and BETHE (1937), which for protons is:

$$-\frac{dE}{dx} = \frac{4\pi e^4}{mv^2} NZ \left[\log_e \left(\frac{2mv^2}{I}\right) - \log_e (1-\beta^2) - \beta^2 \right]$$

where e is the electronic charge
m is the mass of the electron
v is the velocity of the incident proton
NZ is the electron density in the target
$\beta = v/c$

and I is the mean excitation potential; the values used were $I_H = 17.5$ eV and $I_C = 69$ eV.

On integration the above equation has the form

$$E = \frac{4\pi e^4}{m} NZ\, f(R)$$

and a quadratic function of the form

$$\log_e E = A + B \log_e R + C(\log_e R)^2$$

was found to fit the tabulated values of E and R to within 0.15 MeV over the energy range 1 MeV to 130 MeV.

Because the density of propane under the operating conditions was not precisely known, an approximate value (0.434 gms/cc) was used to determine B and C (it can be seen from the equations above that the density, which determines NZ, is contained in the parameter A only). With the approximate density the parameter values were A = 3.0848, B = 0.5427, and C = 0.00345. Information from protons stopped in the propane by known thicknesses of aluminium was then used to determine the correct value of A, as indicated below:

Let E_o = energy of the protons delivered by the beam transport system

E_L = energy of the protons after passage through L gms of Al absorber

E_M = energy of the protons after passage through M gms of Al absorber

r_L = residual range in propane of protons of energy E_L

r_M = residual range in propane of protons of energy E_M

r_{oAl} = range in aluminium of protons of energy E_o

Assuming a range-energy relationship for protons in aluminium of the form:

$$E = A_{Al}\, r^{B_{Al}}$$

the energies E_L and E_M can be expressed in terms of ranges in aluminium as

$$E_L = A_{Al}\,(R_{oAl}-L)^{B_{Al}}$$

and $$E_M = A_{Al}\,(R_{oAl}-M)^{B_{Al}}$$

From the measured ranges in propane r_L and r_M (see section 3.4)

$$\log_e E_L = A + B\log_e r_L + C(\log_e r_L)^2$$

$$\log_e E_M = A + B\log_e r_M + C(\log_e r_M)^2$$

Using the values:

$A_{Al} = 26.829$ $B_{Al} = 0.5715$ RICH and MADEY (1954)

$r_L = 26.1$ cms $r_M = 15.5$ cms

$B = 0.5427$ $C = 0.00345$

$L = 5.47$ gms/cm^2 $M = 11.65$ gms/cm^2

and solving for A and R_o (hence E_o) the following values are obtained

$A = 3.0446$

$E_o = 152 \pm 1.5$ MeV.

The range-energy relationship for protons in the bubble chamber is, therefore

$$\log_e E = 3.0446 + 0.5427 \log_e R + 0.00345 (\log_e R)^2$$

6. Demagnification from bubble chamber to film.

This was slightly different from view to view and from roll to roll,

because of inconsistent positioning of the cassettes in the camera housing. For each roll of film the demagnification was obtained by comparing the measured separation of a given pair of fiducial marks with the mean value obtained from all the measurements available from the film. The demagnifications were all within about 1% of 13.0.

Part 3 The analysis of the results

CHAPTER 6

INTRODUCTION TO THE EXPERIMENTAL RESULTS

6 1 The incident energy spectra for the analysed events

The incident protons enter the illuminated region of the propane with an energy of approximately 192 MeV and leave it with approximately 25 MeV. Figure 6 1 shows the distribution in incident energy of the measured 2-prong, 3-prong, and 4-prong events

The propane bubble chamber method is not very suitable for investigating proton-carbon reactions for low energy protons In figure 6 2 the measured angular correlation between the two prongs of a random selection of hydrogen events is shown plotted against the energy of the shorter prong; it can be seen that the reconstruction errors become very large for events with a prong energy below about 15 MeV All carbon events with incident proton energies less than 50 MeV have one prong of proton energy≠ less than 15 MeV. Also, as was pointed out in section 4 2, there is a serious loss of events in which low energy protons are produced Furthermore, in the present experiment, the energy errors due to straggling and spread of any initial beam energy spread increase rapidly at the low proton energies; this was shown in figure 3 1. Therefore, events initiated by protons of energy less than 50 MeV are excluded from the analysis

---

≠ i.e. the energy calculated for the particle assuming it to be a proton

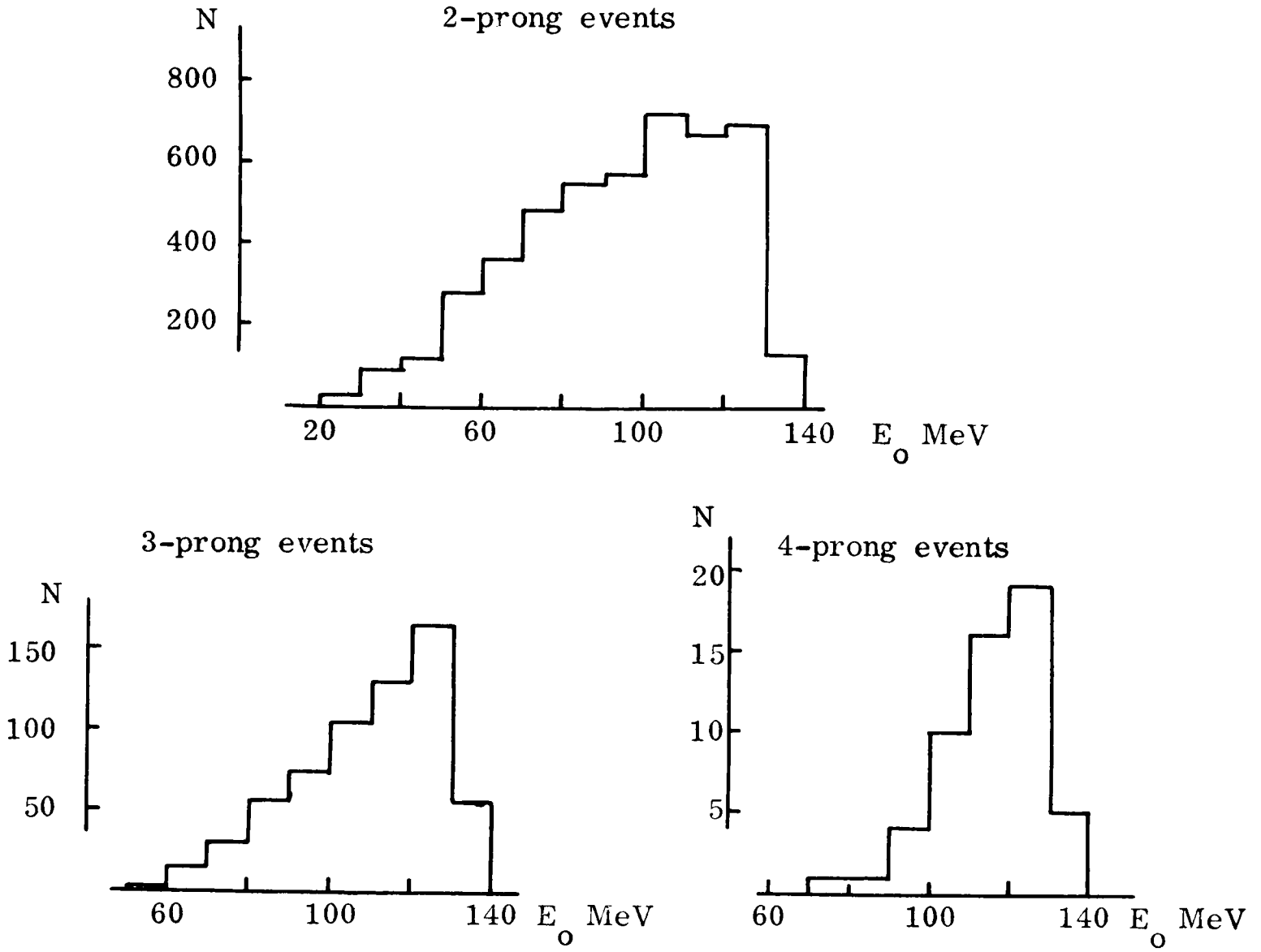

Fig. 6.1 Distribution in incident energy of the measured events.

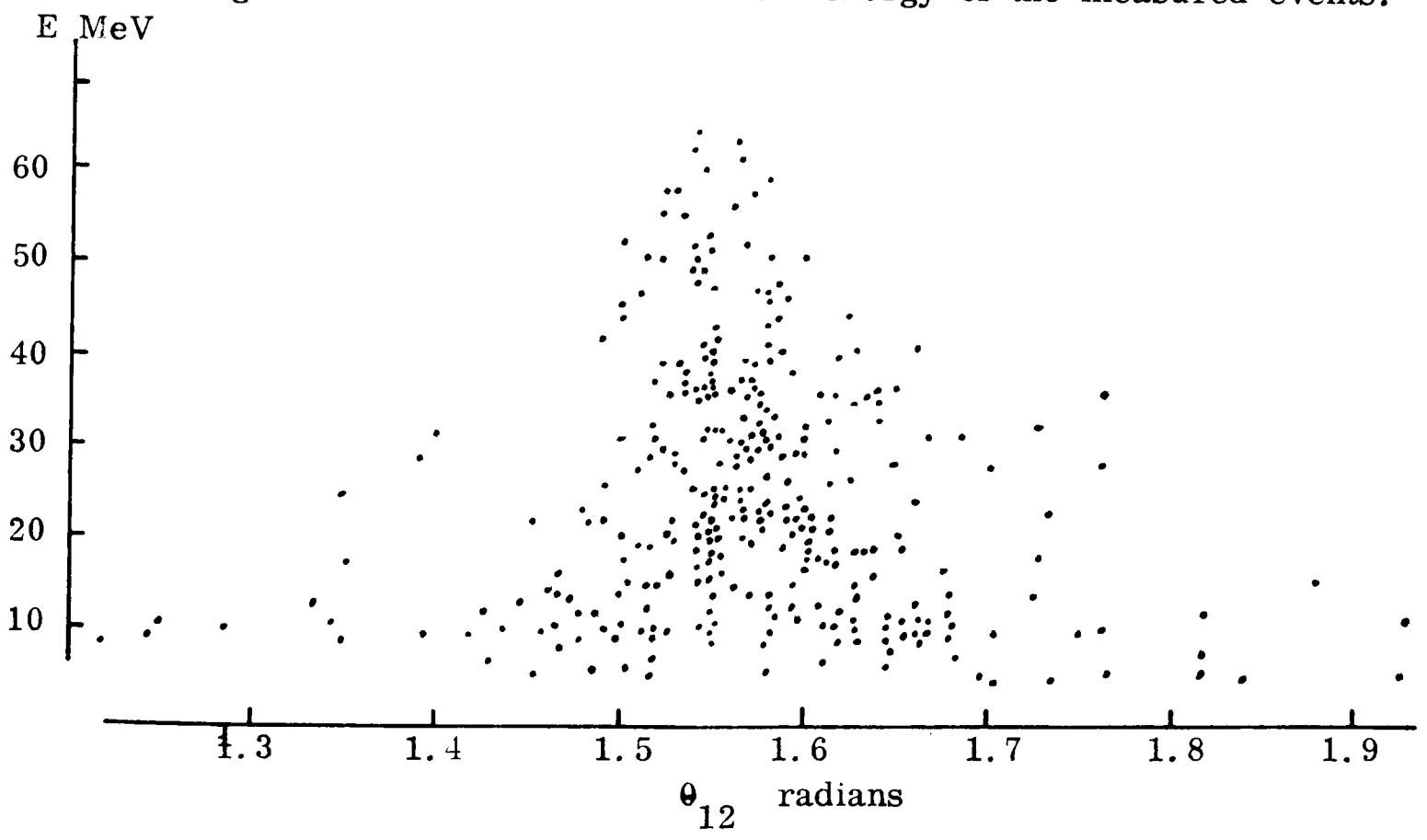

Fig. 6.2 Effect of prong length on resolution.

6.2 Reactions represented by the 2-prong, 3-prong and 4-prong events

The 2-prong events can represent proton-hydrogen reactions or proton-carbon reactions, but the 3-prong and 4-prong events must represent proton-carbon reactions. For a hydrogen event the incident track and the two prongs show the complete reaction, but for a carbon event the recoiling residual nucleus is never seen. However, when the residual nucleus is the only unobserved product from a proton-carbon reaction, the latter is still completely kinematically defined by the momentum and energy balances for the system.

Hydrogen events can be completely separated from carbon events, and they can be analysed without any difficulty. But for carbon events, there are two factors that complicate the determination of the nature of the causal reactions. Firstly, the prongs of an event can represent protons or heavier particles such as d, t, He^3 and He^4, and it is not possible to distinguish between these by looking at the tracks. Secondly, an event does not always show all the product particles of the reaction; there can be neutrons present or charged particles with insufficient energy to produce the minimum observable prong length of one bubble diameter; the latter loss is particularly serious in the case of α-particles.

Various reactions that can contribute to 2-prong, 3-prong and 4-prong events are listed below:

2-prong events: $H^1(p, p)H^1$

$C^{12}(p, 2p)B^{11}$

$C^{12}(p, pd)B^{10}$; $C^{12}(p, pt)B^9$; $C^{12}(p, pHe^3)Be^9$; $C^{12}(p, p\alpha)Be^8$

$C^{12}(p, 2pxn)B^{11-x}$ $\quad x = 1, 2, 3,$

3-prong events: $C^{12}(p, 3p)Be^{10}$

$C^{12}(p, 2pd)Be^{9}$; $C^{12}(p, 2pt)Be^{8}$; $C^{12}(p, 2pHe^{3})Li^{8}$; $C^{12}(p, 2p\alpha)Li^{7}$

$C^{12}(p, p2d)Be^{8}$; etc

$C^{12}(p, 3pxn)Be^{10-x}$ $x = 1, 2, 3,$

4-prong events: $C^{12}(p, 4p)Li^{9}$

$C^{12}(p, p3\alpha)$

$C^{12}(p, 4pxn)Li^{9-x}$ $x = 1, 2, 3, \ldots$

Possible radiative decays of low-lying excited states of residual nuclei are not represented and the residual nuclei shown are not necessarily in their ground states. Also, because of the second cause of complication mentioned above, any of the reactions listed under 3-prong events can contribute to the 2-prong events if one of the charged particles has too low an energy to be detected. Similarly, any of the reactions listed under 4-prong events can contribute to the 3-prong events or to the 2-prong events.

A first picture of the importance of the various contributing reactions can be obtained by examining the energyloss distributions that arise by hypothesizing that all of the events are of the simplest possible form, i.e., that protons only are produced and that all the reaction products (except the residual nuclei) are observed. Thus, for example, if the hypothesis were a correct one we could expect to find very simple energy-loss distributions with peaks at, or just above, the energies corresponding to the Q-values for the (p,xp) reactions (x=1, 2, 3, ...)

The energy-loss (E_L) for a reaction can be obtained from the momentum, and energy balance equations for the reaction.

If $E_o, \underline{k}_o$ = incident proton energy and momentum,

$E_i, \underline{k}_i$ = energy and momentum of the i^{th} product proton,

$E_R, \underline{k}_R$ = energy and momentum of the unseen recoiling nucleus,

and E_L = energy-loss in the interaction = binding energy of the knocked-out particles + the residual nucleus excitation energy (if the correct reaction hypothesis is used),

then the momentum balance equations give the momentum of the recoiling nucleus:

$$\underline{k}_R = \underline{k}_o - \sum_i \underline{k}_i ;$$

this gives E_R, and then the energy balance equation gives the energy-loss:

$$E_L = E_o - \sum_i E_i - E_R .$$

The energies E_o and E_i, and the vector momenta $\underline{k}_o$ and $\underline{k}_i$ are fully determined from the event reconstruction procedure.

6.3 The energy-loss distribution for the 2-prong events

The energy-loss distribution for all the 2-prong events with incident energies above 50 MeV, obtained on the assumption that the events represent either $C^{12}(p, 2p)B^{11}$ reactions or $H^1(p, p)H^1$ reactions (hereafter referred to as the (p, 2p) energy-loss distribution), is shown in figure 6 3

It is seen that the energy resolution is good enough to isolate completely the hydrogen events, which are elastic and so lie in the peak centred at zero.≠

≠ A systematic error of approximately 0.5 MeV is present in all incident energies calculated for the 2-prong events This is not a serious error but it accounts for the fact that both the hydrogen peak and the p-shell peak are not centred exactly at the expected energies

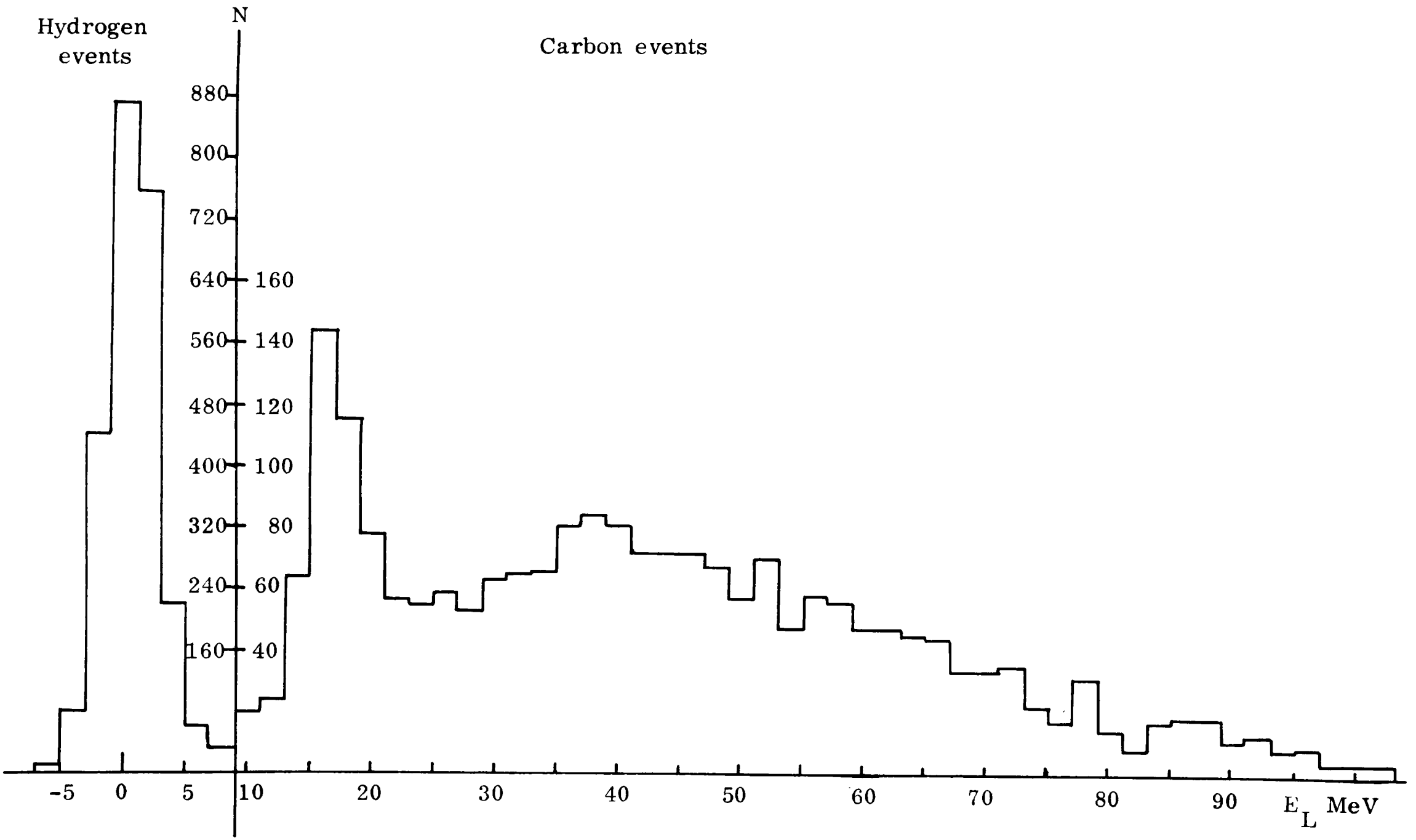

Fig. 6.3 The (p, 2p) energy-loss distribution.

from the carbon events The width of the hydrogen peak gives a measure of the energy resolution achieved; this is discussed in section 6.5 Two peaks can be recognized in the distribution for the carbon events, one at 18 MeV with a width close to the resolution width, and a much broader one centred at about 38 MeV. The distribution is very similar to those obtained from the coplanar carbon events analysed by several experimenters with counter telescope methods (see section 1.4). The peak at 18 MeV is recognized as being due to the quasi-elastic knock-out of p-shell protons from C^{12}, and the peak at 38 MeV occurs at an energy-loss close to that predicted for the quasi-elastic knock-out of s-shell protons; it has usually been attributed to such interactions by other authors

The p-shell peak is fairly sharply defined at its lower limit but it merges into a general background of events at its upper limit; it is also asymmetric Because of the energy resolution limit, caused mainly by straggling, it is not possible to see directly whether or not the low excited states in B^{11} (at excitation energies of 2.14 MeV; 4.46 MeV 5.04 MeV, etc) are being fed, but it is evident that the predominant interaction is feeding the B^{11} ground state (the $C^{12}(p, 2p)B^{11}$ Q-value is 15.96 MeV). Of the other reactions that can contribute to the 2-prong events, only the (p, pα) reaction can give events in the region of the peak; this can be seen from the third column of the table shown below:

Reaction	Q-value	Minimum energy at which events can appear in fig. C 3 ≠
(p, pd)	25.2 MeV	27 MeV
(p, pt)	27.4	30
(p, pHe^3)	26.3	38
(p, pα)	7.4	21
(p, 2pn)	27.4	28
(p, 2p2n)	35.9	36

The events causing the asymmetry of the peak and the events in the energy-loss region below 27 MeV must, then, be due either to (p, pα) reactions or to the production of the excited states of B^{11} by (p, 2p) reactions In section 8 4, it will be seen that the (p, pα) reaction does not contribute many events, and that some information can be obtained from the asymmetry about the reaction mechanisms leading to the B^{11} excited states

There are two intrinsic nuclear effects that make it more difficult to observe the s-shell reactions than it is to observe the p-shell reactions in this type of experiment, these are:

≠ The differences between columns 2 and 3 are the direct result of treating all particles as protons For example, the minimum observable energy of an α-particle is 18 MeV (section 1 5) and if the track of such a particle is assumed to be a proton its calculated energy becomes 4.5 MeV Therefore 13.5 MeV of energy is "lost" in the reconstruction: this is the difference between the Q-value for the reaction and the minimum energy at which it can be observed on the (p, 2p) energy-loss distribution

(a) that the s-shell nucleons lie more deeply in the nucleus than the p-shell nucleons; the spatial wavefunction for the s-state peaks at zero radius while the p-state wavefunction falls to zero at zero radius. Nuclear absorption effects will therefore reduce the probability of quasi-elastic s-shell reactions,

and (b) that the s-state has a natural width of 5-7 MeV; the consequent broadening of the peak makes it merge more into the background of the non-(p, 2p) events that are present in this region of energy-loss ≠

These factors might account for the fact that the s-shell peak is only just observed. However, in section 10.8, evidence is presented which points to the fact that even the observed peak might not be due to s-shell events but due to background events from the reaction $C^{12}(p, 2pn)B^{10}$.

No analysis of the s-shell events is possible, therefore, and there must be some doubt as to whether the quasi-elastic knock-out of s-shell protons is being observed at all in this experiment.

≠ Although at first sight it might be thought that a third effect enters because there are only half as many s-shell protons in C^{12} as p-shell protons, CLEGG (1963) has pointed out that, since the collision cross-section is determined by a matrix element whose value is partly dependent on the form of the target nucleon wavefunction, the relative cross-sections for the knock-out of nucleons from different nuclear states is not necessarily proportional to the number of nucleons in these states. In fact, evidence is presented from the $Ca^{40}(p, 2p)$ reaction to suggest that, for this nucleus at least, reactions in the s-state are considerably enhanced over those in the p-state.

6.4 The energy-loss distributions for the 3-prong and 4-prong events

The most noticeable feature of the (p, 3p) and (p, 4p) energy-loss distributions, which are shown in figures 6.4 and 6.5 respectively, is the complete absence of peaks at energy-losses corresponding to the threshold energies (or low residual nucleus excited state energies) for the reactions $C^{12}(p, 3p)Be^{9}$ and $C^{12}(p, 4p)Li^{9}$. In this respect they differ from the (p, 2p) energy-loss distribution shown in figure 6.3, but in their general forms they are very similar to that part of the (p, 2p) distribution which lies above the p-shell peak.

It is evident that the simple (p, xp) descriptions cannot apply to these events but the similarities of the three distributions does suggest that the three sets of events are produced by similar reaction mechanisms. It is interesting to note that the distributions are similar to the excitation functions obtained by Metropolis (see section 1.3) from his calculations for intranuclear cascade reactions on Cu^{64} at 286 MeV.

6.5 The experimental resolution

The events in the hydrogen peak of figure 6.3 provide an excellent means of determining the purely experimental resolution for the various measurements made on the events. The events represent elastic proton-proton interactions which have the following unique properties:

(a) no energy is lost in the interaction; $E_0 - E_1 - E_2 = 0$,

(b) the summed momenta of the product protons is equal to the incident

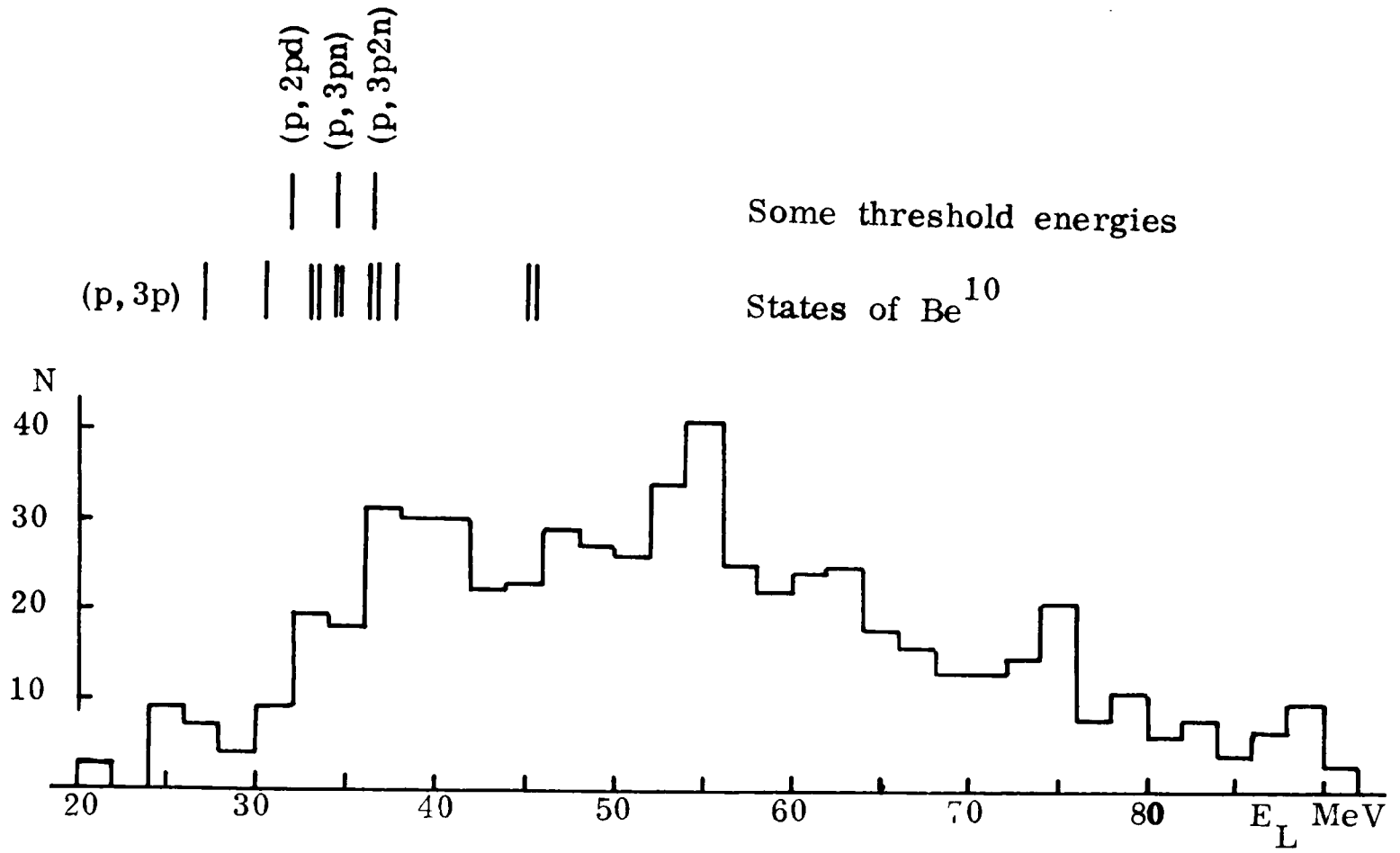

Fig. 6.4 (p, 3p) energy-loss distribution.

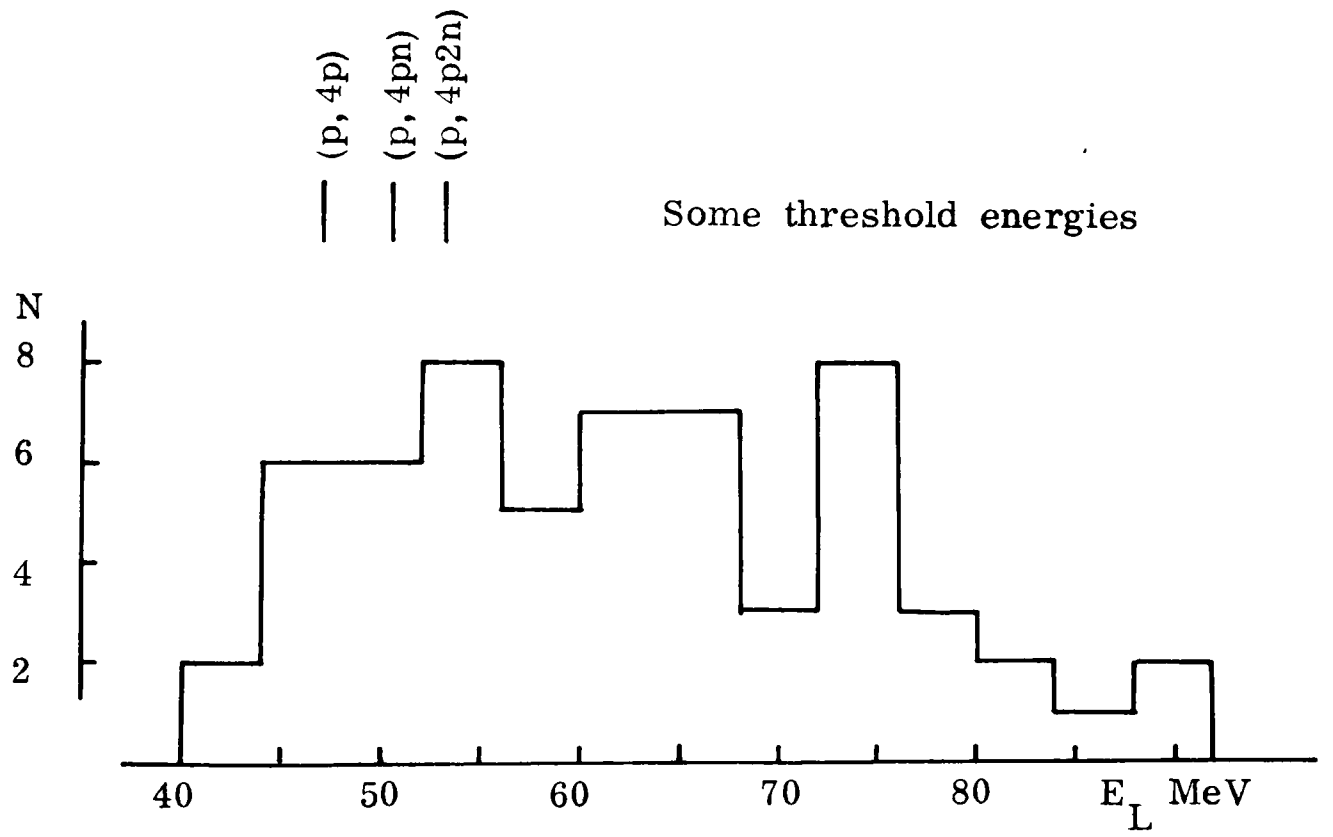

Fig. 6.5 (p, 4p) energy-loss distribution.

momentum: $\underline{k}_o - \underline{k}_1 - \underline{k}_2 = 0$,

(c) the angle between the two protons is always between 88° and 90° (=90° in the non-relativistic limit),

and (d) the incident proton and the product protons lie in the same plane;

$$\gamma = \frac{\underline{k}_o \wedge \underline{k}_1 \cdot \underline{k}_2}{k_o k_1 k_2} = 0$$

The width of the experimental distribution for each quantity, shown in figures 6.6 to 6.9, gives directly its experimental resolution.

Of particular interest are the distributions of the energy-losses; for events with incident energies below 100 MeV (mean $E_o \sim 85$ MeV), the RMS deviation is 2.0 MeV and for events with incident energies above 100 MeV (mean $E_o \sim 115$ MeV), the RMS deviation is 1.2 MeV. In chapter 3 the calculated RMS energy spreads produced by straggling and by energy spreads in the incident beam were shown. Referring to figure 3.1 it can be seen that the RMS deviations quoted above are consistent with an RMS energy spread of less than 0.5 MeV in the beam incident upon the chamber. This result confirms the result obtained by the range-telescope method of measurement made before the commencement of the bubble chamber run (see section 3.3). It was pointed out in chapter 3 that once the beam energy spread has been reduced to about 0.5 MeV, further reduction makes very little difference to the energy resolution obtained in the bubble chamber measurements. It follows, therefore, that in this experiment the bubble chamber is being used at the limit of its resolving power.

The RMS errors in quantities (b), (c) and (d) are very much smaller than any structural features in the distributions for these quantities for the carbon events (see chapter 8), so that the errors place no limit on the analysis.

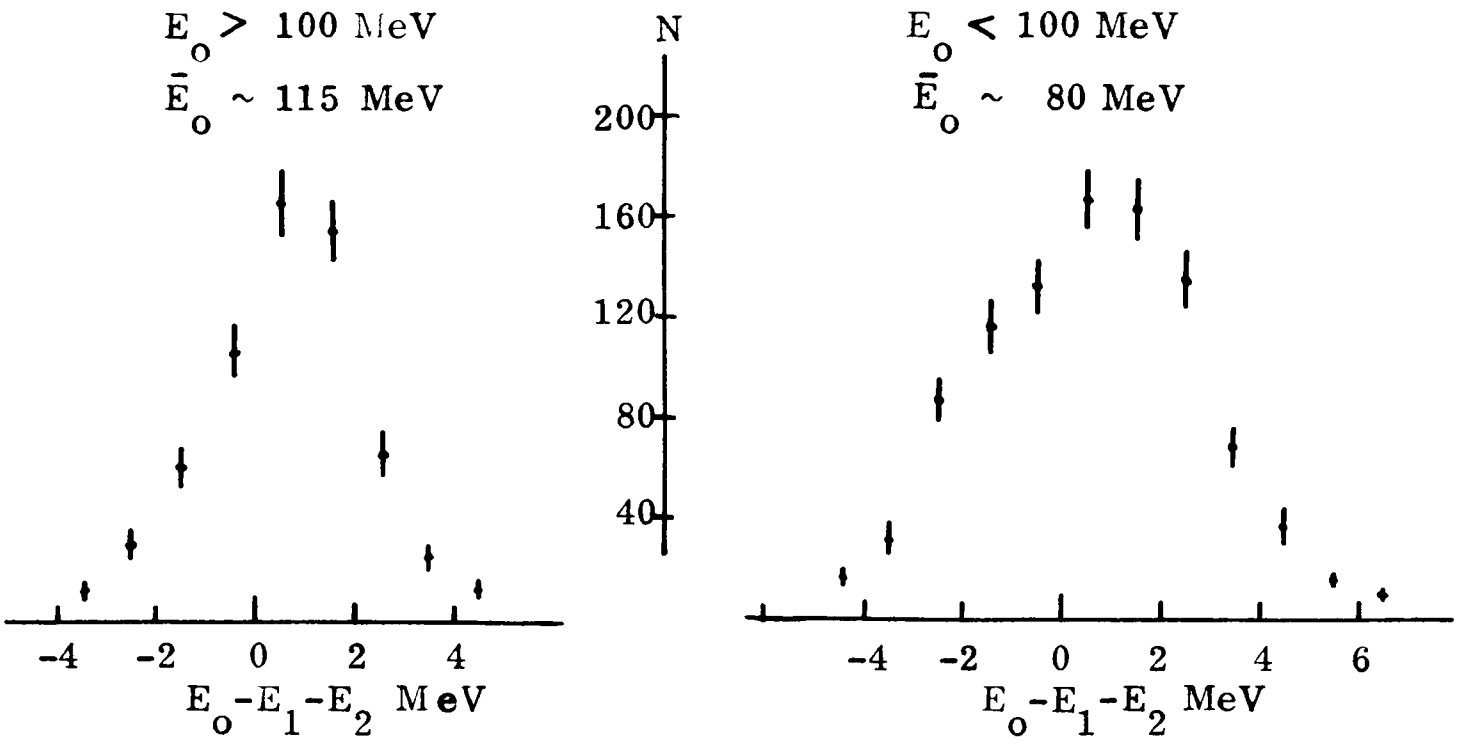

Fig. 6.6 Energy-loss distributions for hydrogen events.

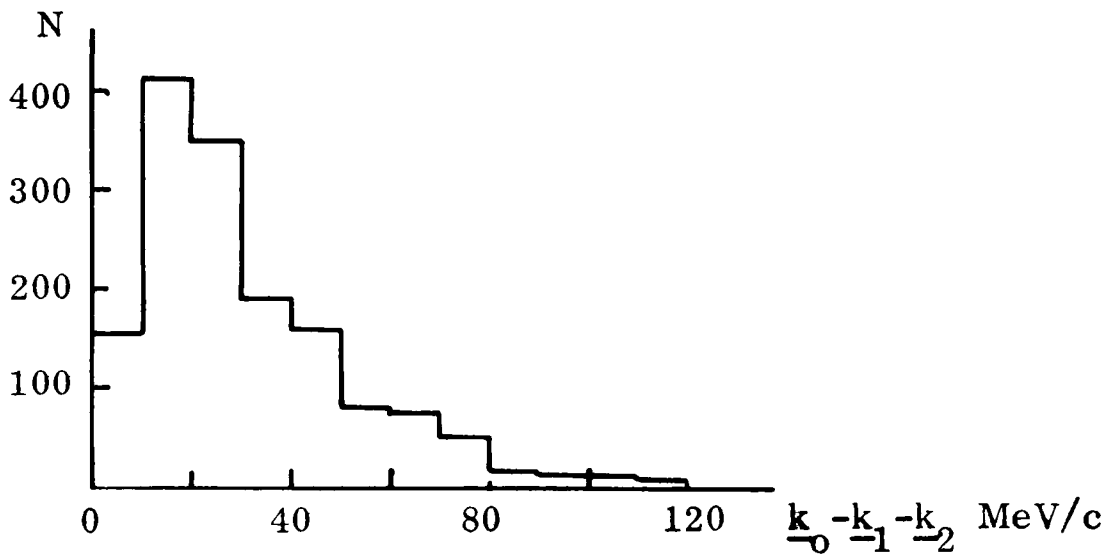

Fig. 6.7 Momentum unbalance for hydrogen events.

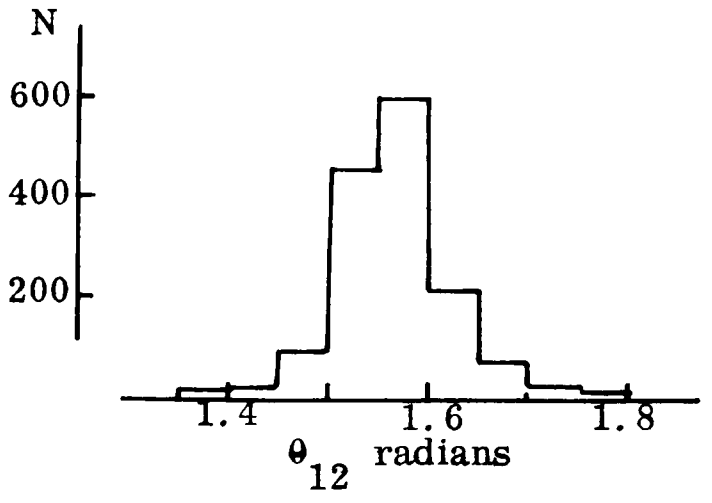

Fig. 6.8 Angular correlation for hydrogen events.

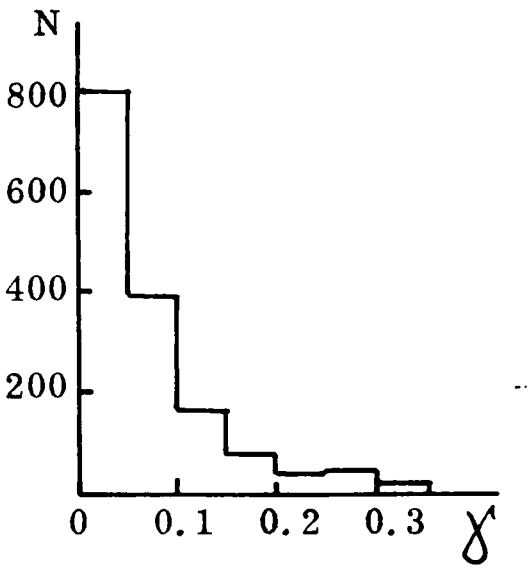

Fig. 6.9 Coplanarity for hydrogen events.

CHAPTER 7

THE CROSS-SECTIONS

7.1 The measurable cross-sections

In chapter 10, evidence is given to show that events from the reaction $C^{12}(p,3p)Be^{10}$ can be separated, at least approximately, from the other 3-prong events. This categorization of events is the only improvement made upon that which is given in chapter 6 on the basis of the (p,xp) energy-loss distributions. Six categories of events can therefore be recognized:

p-shell events

hydrogen events

other 2-prong events

(p,3p) events

other 3-prong events

4-prong events.

If the cross-sections for the production of the ground state and of each of the excited states of B^{11} could be measured, information could be obtained on the parentage coefficients of the C^{12} g.s., in terms of B^{11} states (see section 1.4). However, it was seen in chapter 6 that the energy resolution in the experiment, coupled with the fact that none of the B^{11} excited states is produced very strongly, makes it impossible to resolve individual states. Despite this, the extent to which the C^{12} g.s. wavefunction deviates from a pure shell model wavefunction could be measured by comparing the frequency of

production of the B^{11} g.s. with that of all the excited states taken together.

Unfortunately, the B^{11} excited states can be produced by mechanisms other than the direct knock-out of a nucleon; for example:

(a) by initial and final state interactions; these reflect the parentage of some intermediate state of C^{12} or B^{11} and not that of the C^{12} g.s. (see section 1.4). The final state interactions, in which outgoing protons suffer inelastic scattering off other nucleons or groups of nucleons in the nucleus, are likely to be more important than the initial state interactions because there are, after the knock-out reaction, two product protons both with energies much lower than the incident energy ($\frac{E_0-16}{2}$, on average), and the nucleon-nucleon cross-section increases rapidly with decreasing energy below 100 MeV.

and (b) by the decay to B^{11} of a C^{12} excited state produced in the reaction $C^{12}(p,p')C^{12*}$. GROVER & CARETTO (1964) have pointed out that for 93 MeV protons, the production of the C^{12} states with excitation energies between 19 MeV and 30 MeV (those likely to decay by the emission of a single nucleon) is 26 mb and that the branching ratio for proton emission is somewhere in the region of 0.3 to 0.4.

It is not possible to disentangle the events due to these other mechanisms from those due to the clean knock-out mechanism and so to obtain the ground state to excited state parentage ratio. An analysis of the events just above the ground state peak is given in chapter 8. Here the cross-section determination has been limited to the reaction $C^{12}(p,2p)B^{11}$ g.s. (p-shell events).

Several incident-energy-dependent correction factors enter into the calculation of the (p, 2p) cross-section and also, because of difficulties in determining the total incident proton flux, there is an uncertainty in the absolute value of the calculated cross-section of about 10%. The proton-proton interaction cross-section is, however, well known and strongly energy dependent in the energy interval 50 MeV$< E_o <$ 130 MeV; a summary of the published experimental results is given by HESS (1958). Therefore, by first calculating this cross-section from the hydrogen events (which are subject to very similar correction factors to those used for the p-shell events), it is possible to check, from the energy dependence, the validity of the correction factors, and to obtain, from the absolute magnitude, the flux normalization factor required to give an absolute value to the cross-section for the $C^{12}(p, 2p)B^{11}$ g.s. reaction.

Cross-sections for the observation in the bubble chamber (i.e. uncorrected) of the other categories of events are also calculated.

7.2 The calculation of cross-sections

To calculate from the bubble chamber data the cross-section for a reaction of the type R at energy E, the following relationship is used:

$$\sigma_E(R) = \frac{Wn_E(\Delta E)10^{27}}{\ell_E(\Delta E) x N d F_E} \quad \text{millibarns}$$

where N = Avogadro's Number = 6.064×10^{23}
W = the molecular weight of propane = 44.09
x = 3 for carbon cross-sections and 8 for the hydrogen cross-section
$\ell_E(\Delta E)$ = path length in centimetres corresponding to the degradation in the beam energy from E+ΔE to E-ΔE

$n_{E}(\Delta E)$ = the number of reactions of the type R in the energy interval $E \pm \Delta E$

d = the density of propane at the operating conditions

I_{E} = the proton flux at the energy E.

A summary is given below of the methods used to obtain the propane density and the proton flux.

Propane density. In section 5.5 the range-energy relationship was obtained for protons in propane under the operating conditions of the experiment, w thout use of the exact proton density. A density of 0.434 gms/cc was assumed and the computed range-energy data was fitted with a quadratic equation of the type:

$$\log_e E = \alpha + \beta \log_e R + \gamma (\log_e R)^2.$$

Using the values of β and γ so obtained, the parameter α was optimized to fit the data available from the measurement of the tracks of protons stopped in the chamber. The density can be determined from this value of α.

If R is measured in gms/cm^2, the relationship is independent of the density of the propane. For measurements taken in centimetres it becomes:

$$\log_e E = \alpha + \beta \log_e Rd + \gamma (\log_e Rd)^2$$

where d is the propane density and R is in cms.

An error of less than 0.1% arises if the last two terms in the expansion of the γ term are omitted, so the relationship can be written to a good approximation as:

$$\log_e E = \alpha + \beta \log_e d + \beta \log_e R + \gamma (\log_e R)^2.$$

It was shown in section 5.5 that the constant term, $(\alpha + \beta \log_e d)$, is 3.0446 for the operating conditions of the propane. It was also seen that for a propane density of 0.434 gms/cc, the relevant constant term is 3.0848. Since β and γ

are independent of changes in density (see section 5.5) the density corresponding to the operating conditions of the propane can be determined from the two equations:

$$3.0446 = \alpha + \beta \log_e d$$

$$3.0848 = \alpha + \beta \log_e 0.434$$

using $\beta = 0.5427$ and solving for d

$$\underline{d = 0.404 \text{ gms/cc.}}$$

Proton flux. In order that the cross-section may be correctly determined the proton flux in each energy interval and the number of events in this same interval must be consistent with each other. This is not an easy specification to meet and, as soon as frame and event acceptance criteria of the type discussed in section 4.2 are introduced into the analysis, different biases tend to operate when the film is scanned for different information. It will, in fact, be seen in section 7.3 that the cross-sections calculated are systematically high and in retrospect it is possible to recognize the origin of the error; this is done below for the factors that make up the total proton flux, F_E.

F_E = (no. of frames included in the analysis) x (average no. of tracks/frame) x $(1-f_E)$

where f_E is the attenuation of the incident beam flux at the energy E.

(i) Number of frames The total number of frames examined was 27,584 and of these 6,037 were rejected on both scans (see section 4.3). Of the frames that were accepted on one scan but not on the other, 734 were rejected at the measuring stage. The number of frames consistent with the events measured is, therefore, 21,813.

Source of error: there is some evidence to show that a bad frame was less likely to be eliminated if it had a very clear event on it. This bias would increase the calculated cross-section.

(ii) Number of tracks per frame. At the scanning stage the number of protons entering the chamber was counted on every tenth frame. Figure 7.1 shows the frequency distribution obtained; the mean value with its statistical error is 6.56 ± 0.06.

Source of error: a systematic bias operated here similar to that of (i) above. A frame with a large number of tracks was more likely to be rejected if the tracks on it had to be counted than if they had not to be. This bias again would increase the calculated cross-section.

(iii) Attenuation. This was determined by scanning the best frames of several rolls of film. The 0, 1, 2, 3 and 4-prong events were recorded in intervals corresponding to 5 MeV incident energy steps. The attenuation at any point in the chamber is the fraction of the incident beam lost up to that point. The result is shown in figure 7.2.

The proton flux at an energy E is, therefore: $136533.28\,(1-f_E)$.

7.3 The elastic proton-proton cross-section

Not all of the 2-prong events listed at the scanning stage could be straightforwardly measured and categorized by energy-loss into hydrogen events etc. For example: some events could not be measured at all; some had scatters on their prongs; etc. In appendix VII the categorization accomplished at the measuring

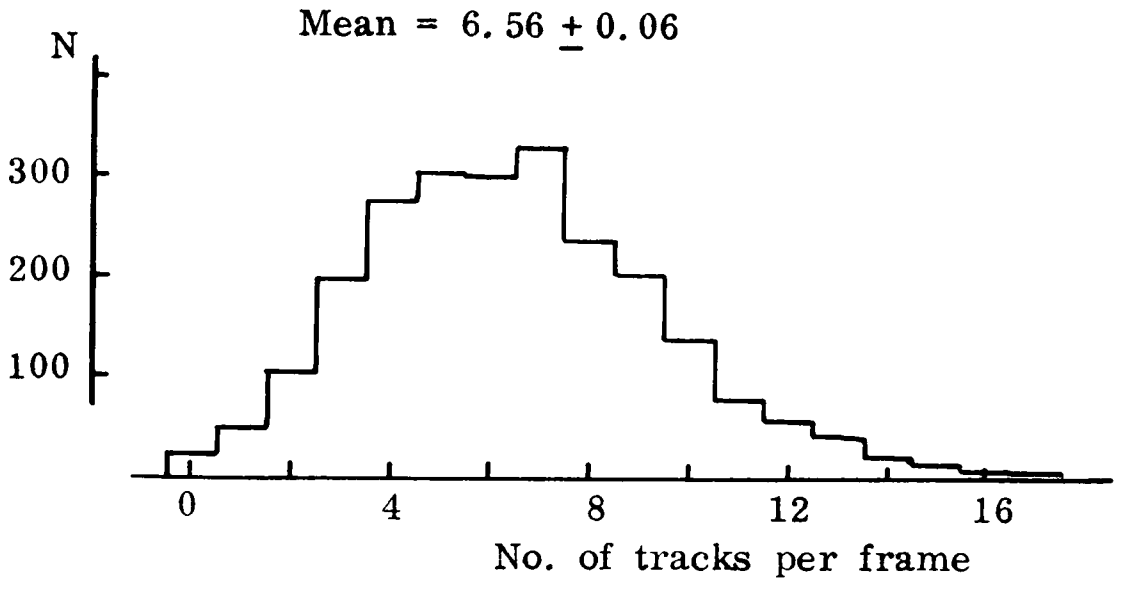

Fig. 7.1 **Number** of incident protons per frame.

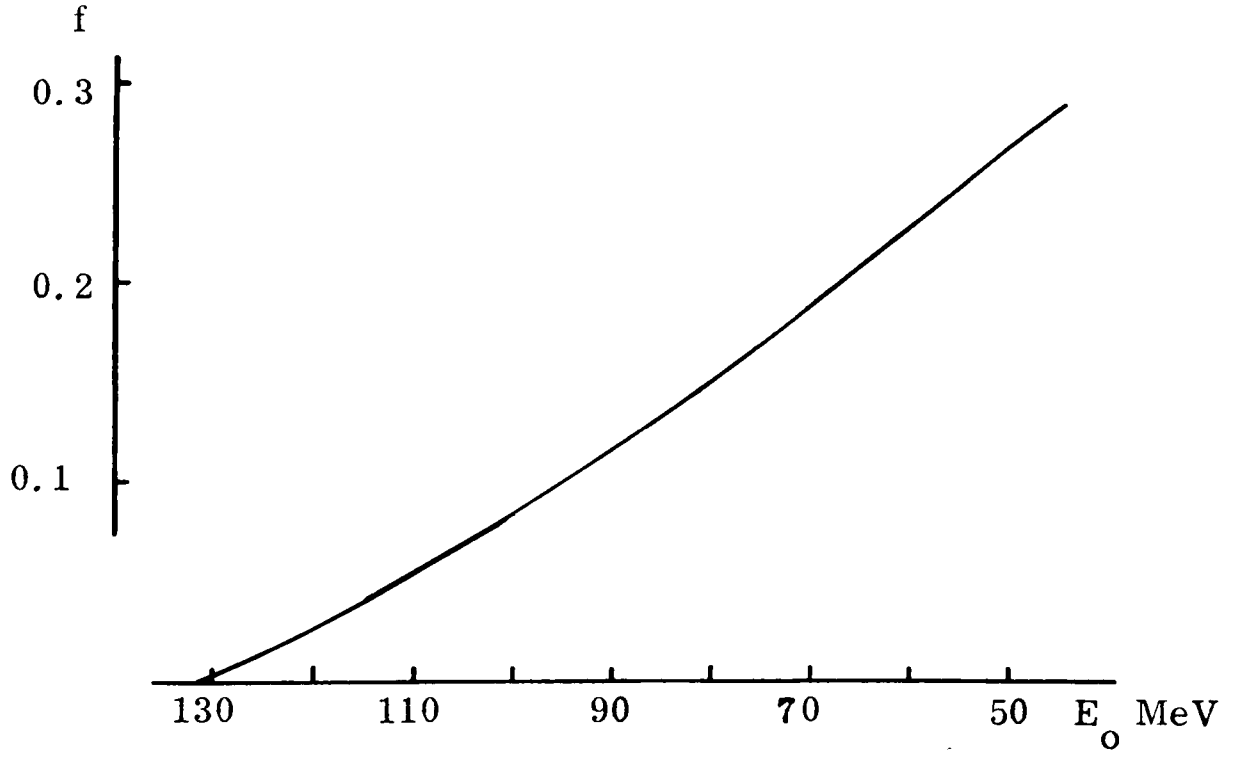

Fig. 7.2 Beam attenuation.

stage of the analysis for all the 2-prong events that appeared in the combined scanning list (see chapter 4) is given; this is the starting point for the calculation of the p-shell cross-section and hydrogen cross-sections.

Column II of table A shows, for each 5 MeV incident energy interval, the results collected from the following categories (see appendix VII): the successfully measured hydrogen events; the hydrogen events not remeasured; and that component of the events not measured that were classed as hydrogen events. The first correction factor is applied to these events to allow for the events not observed because of the azimuth effect.

The azimuthal correction. For unpolarized protons and an unpolarized target, the plane of an elastic event is arbitrarily oriented with respect to any fixed plane containing the incident track. However, if the plane of the event passes through, or close to, the camera through which the event is being observed, the event image will appear as a straight line only and it will not be recorded. The distribution of the azimuthal angle, measured with respect to a plane parallel to the glass windows of the chamber, is shown in figure 7.3 for the hydrogen events in the various incident energy regions of the chamber. To avoid any overlap with the short-prong correction, only events with both protons of energy greater than 12 MeV are included. From the distributions of figure 7.3, an energy dependent correction factor is determined; this is shown in figure 7.4. Column III of table A shows the corrected numbers of events.

The correction is not applied to the events with scatters because a scatter on one of two nearly coincident tracks immediately resolves them. The hydrogen

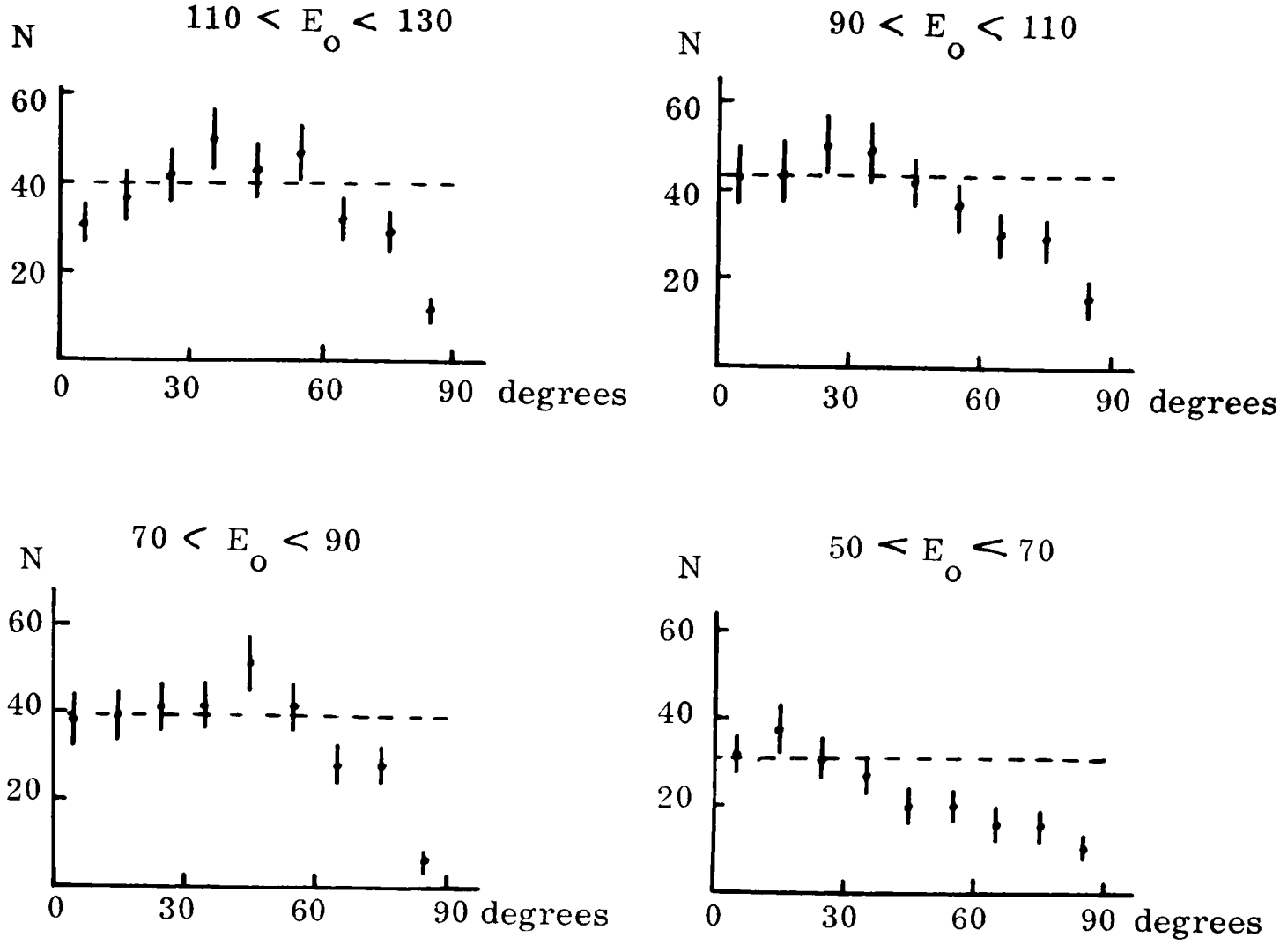

Fig. 7.3 Distribution with azimuthal angle of the hydrogen events.

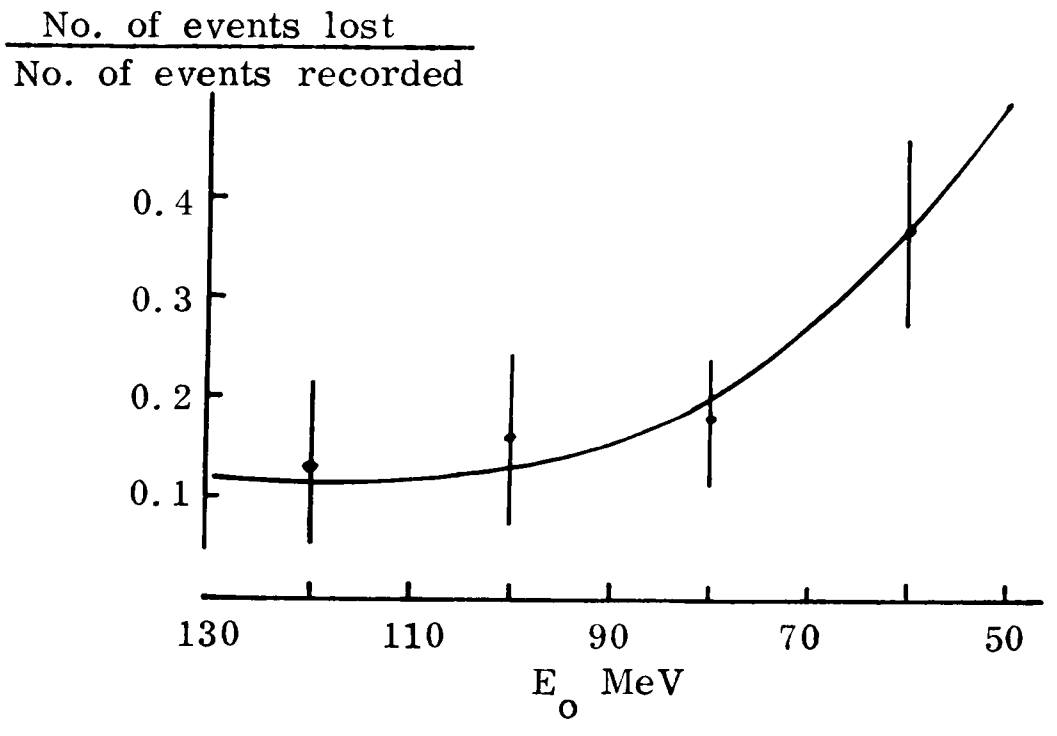

Fig. 7.4 Azimuthal correction factor.

events with scatters are added in column IV; these numbers must now be corrected for the events lost in the analysis because of their very short prongs.

The short-prong correction. Events in which the incident energy is shared very unequally between the two protons can easily be overlooked; the small angle of scatter of the high energy proton and the very short (or non-existent) track of the low energy proton make it difficult (or impossible) to detect such events. The distribution of the energies of the protons from all the events with $E_o > 50$ MeV is shown in figure 7.5; there is a noticeable absence of low energy protons.

The proton-proton cross-section is closely isotropic in the centre of mass system and it follows from this that in the laboratory frame of reference the distribution of the energies of the scattered protons (from a mono-energetic beam of E_o MeV) is uniform from zero to E_o MeV. If all protons with an energy less than x MeV are not detected, the ratio

$$\frac{\text{events lost}}{\text{events recorded}} = \frac{2x}{E_o - 2x}$$

From the distribution of figure 7.5, which without loss would be uniform from zero to 50 MeV, the equivalent complete cut-off energy is taken as 8 MeV; the correction factor for the hydrogen events is, therefore:

$$\frac{16}{E_o - 16}$$

Column V of table A shows the numbers of events after this correction factor has been applied. These numbers are used to calculate the proton-proton cross-section.

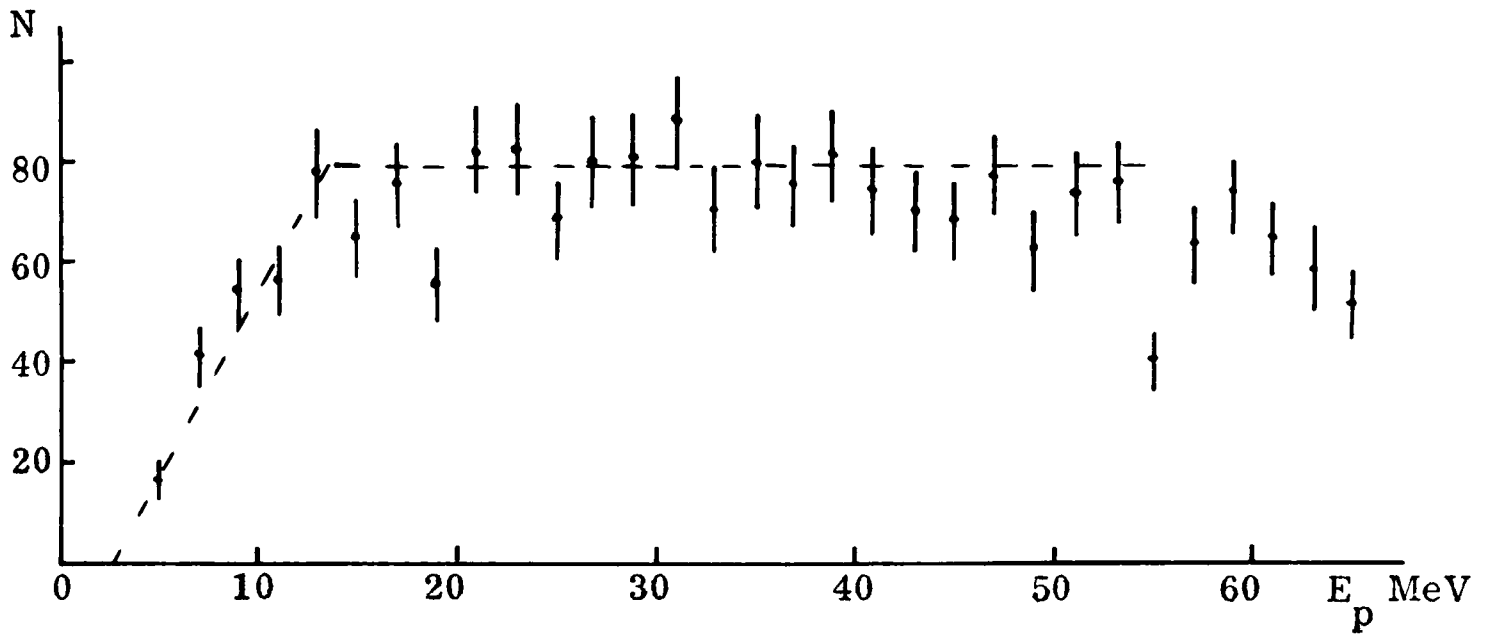

Fig. 7.5 Distribution of proton energies for hydrogen events.

I	II	III	IV	V	VI	VII
$\bar{E}_o$	No. without scatter	Corrected Az. Loss	Plus events with scatter	Corrected for sh. pr.	σ mb	σ mb
52.5	100	145	170	244	58.8	
57.5	126	178	189	262	57.7	51.4
62.5	105	141	156	210	43.1	
67.5	137	175	193	253	46.2	
72.5	156	193	221	283	48.3	
77.5	134	163	195	246	38.4	40.2
82.5	140	167	206	256	37.6	
87.5	153	179	217	266	36.5	
92.5	135	155	215	260	33.8	
97.5	139	158	194	232	28.5	31.5
102.5	151	172	220	261	30.5	
107.5	177	200	260	305	33.4	
112.5	150	170	247	288	30.0	
117.5	166	186	260	301	29.8	30.5
122.5	170	190	287	320	31.5	
127.5	179	200	293	335	30.7	

Table A - The hydrogen events.

In figure 7.6, the curve shows the proton-proton cross-section taken from the paper by HESS (1958) and the circles show the experimental results derived in table A. The energy dependence of the cross-section is very well reproduced but the absolute values are high; a normalization factor of 0.9 is needed to bring the points on to the curve. The normalized values are shown by the crosses in the figure; the error bars represent statistical errors only.

It is concluded that the method of determining the cross-sections is sound but that the proton flux measurement was inaccurate; the sources of this inaccuracy were indicated in the preceding section.

7.4 The cross-section for the reaction $C^{12}(p, 2p)B^{11}$ g.s.

It was seen in section 6.3 that reactions other than $C^{12}(p, 2p)B^{11}$ g.s. can contribute events to the (p, 2p) energy-loss distribution above 18 MeV. To obtain the extent of the basic ground state peak, therefore, the lower half of the peak is reflected about the reaction threshold energy[#]; this operation shows that the p-shell (or ground state) events have energy-losses within the range 12 MeV to 21 MeV.

In column II of table B, all the events without scatters and with energy-losses in the range 12 MeV to 21 MeV are listed for 5 MeV incident energy intervals. The table is constructed for the derivation of the p-shell cross-section in the same way as table A was constructed in the preceding section

---

[#] Actually, about 16.5 MeV because of the 0.5 MeV systematic error in the (p, 2p) energy-loss calculation.

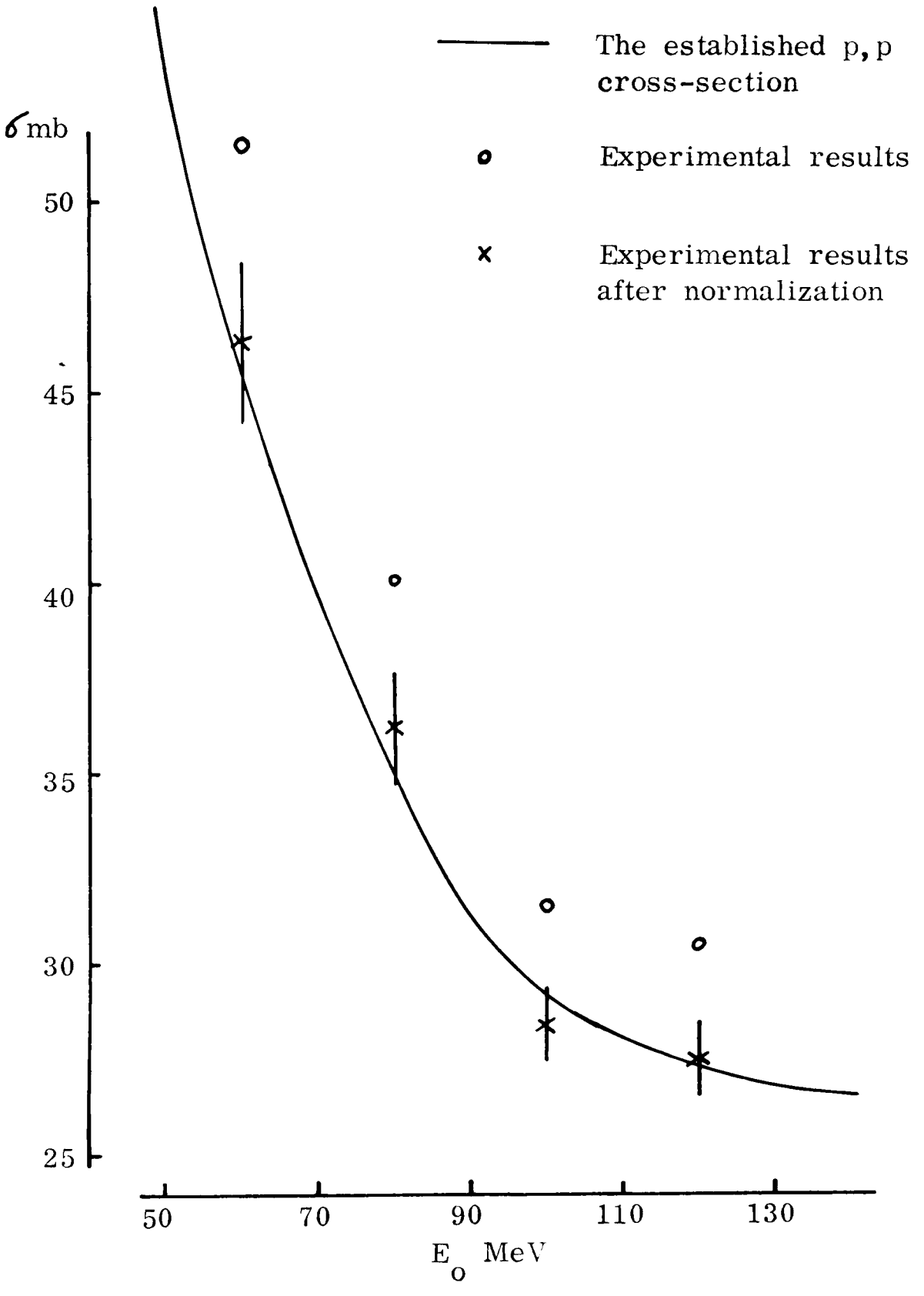

Fig. 7.6 The elastic proton-proton cross-section.

for the hydrogen events. Three correction factors are applied: a correction to allow for the non-ground-state events included in column II; the azimuthal correction, and the short prong correction; these are discussed below.

Non-ground-state correction. If there are n events, from any given incident energy interval, in the lower half of the p-shell peak ($12 < E_L < 16.5$), and N events, from the same incident energy interval, in the region covered by the complete peak ($12 < E_L < 21$), the normalization factor to be applied to the total number N to obtain the number of p-shell events is $\frac{2n}{N}$. However, this assumes perfect symmetry in the fundamental peak and this will only apply if the reconstruction procedure is completely free of any incident energy dependent bias. An easy way of allowing for the possible presence of such a bias is to weight the above correction factor by a term $\frac{N_H}{2n_H}$, which measures the asymmetry of the hydrogen peak.

From a breakdown of the hydrogen, and p-shell, events, the two quotients, $\frac{2n}{N}$ and $\frac{N_H}{2n_H}$, were obtained as functions of the incident energy. These are shown in figure 7.7, together with their product, which is the correction factor applied to column II of table B to allow for the presence of the non-ground-state events.

The azimuthal correction. Although p-shell events are not, in general, coplanar, the reconstruction program calculates the azimuth of the plane containing the incident proton and the longer of the two prongs of each event, so that the same method of correction can be used for the p-shell events as was used for the hydrogen events. The relatively small number of p-shell events prevents the determination of the azimuthal correction as a function of incident energy, but

I	II	III	IV	V	VI	VII
$\bar{E}_o$	No. without scatter	Non-g. s. corrected	Corrected Az. Loss	Plus events with scatter	Corrected for sh. pr.	$\sigma_{mb}^{\neq}$
52.5	11	11	14	14	24	
57.5	20	20	24	24	39	
62.5	20	20	23	23	35	16.4
67.5	18	18	21	22	32	
72.5	29	28	31	34	47	
77.5	23	22	24	27	37	
82.5	27	26	28	30	40	15.6
87.5	28	27	29	32	42	
92.5	23	21	23	28	35	
97.5	29	27	29	34	42	
102.5	55	50	53	63	78	15.8
107.5	47	43	45	56	68	
112.5	43	38	40	53	64	
117.5	35	31	33	50	60	
122.5	40	35	37	53	62	15.5
127.5	53	46	48	68	80	

$\neq$ normalized to the hydrogen cross-section

Table B - The p-shell events.

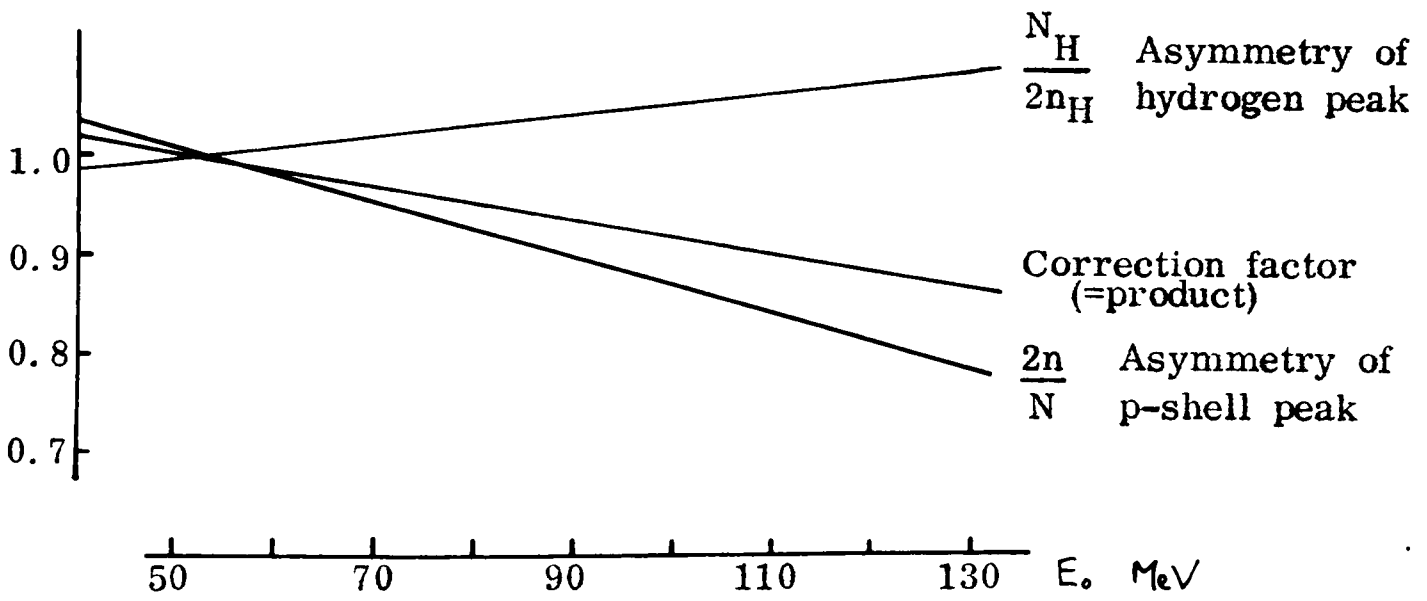

Fig. 7.7 Correction factor to allow for non-ground state events.

an average correction factor (i.e. no. of events lost/no. of events recorded) of 0.09 is obtained by taking together all the events with both proton energies greater than 12 MeV; the distribution of the azimuthal angles is shown in figure 7.8. The corresponding average correction factor for the hydrogen events is 0.18. The p-shell azimuthal correction factor is, therefore, assumed to have the same energy dependence as (but half the value of) the correction factor calculated for the hydrogen events.

The short-prong correction Figure 7.9 shows the distribution of proton energies for all the events with $E_o > 50$ MeV and 12 MeV$< E_L <$ 21 MeV. The equivalent complete cut-off energy is at 8 MeV, as it was for the hydrogen events. Assuming, on the strength of the quasi-elastic hypothesis, that the distribution should be uniform from zero up to the total available energy (E_o-16 MeV in this case), the short-prong correction factor is: $\frac{16}{E_o - 32}$.

Column VII of table B shows the cross-sections after they have been normalized to allow for the incident flux discrepancy detected by calculating the proton-proton cross-section. The values are shown graphically in figure 7.10; the error bars represent the statistical errors only.

7.5 Discussion of the $C^{12}(p,2p)B^{11}$ g.s. cross-section

To within the statistical errors, the measured cross-section is independent of the incident energy from 50 MeV to 130 MeV.

YUASA & POULET (1963) have measured the C^{12} p-shell cross-section with a propane bubble chamber but they used different energy-loss limits to

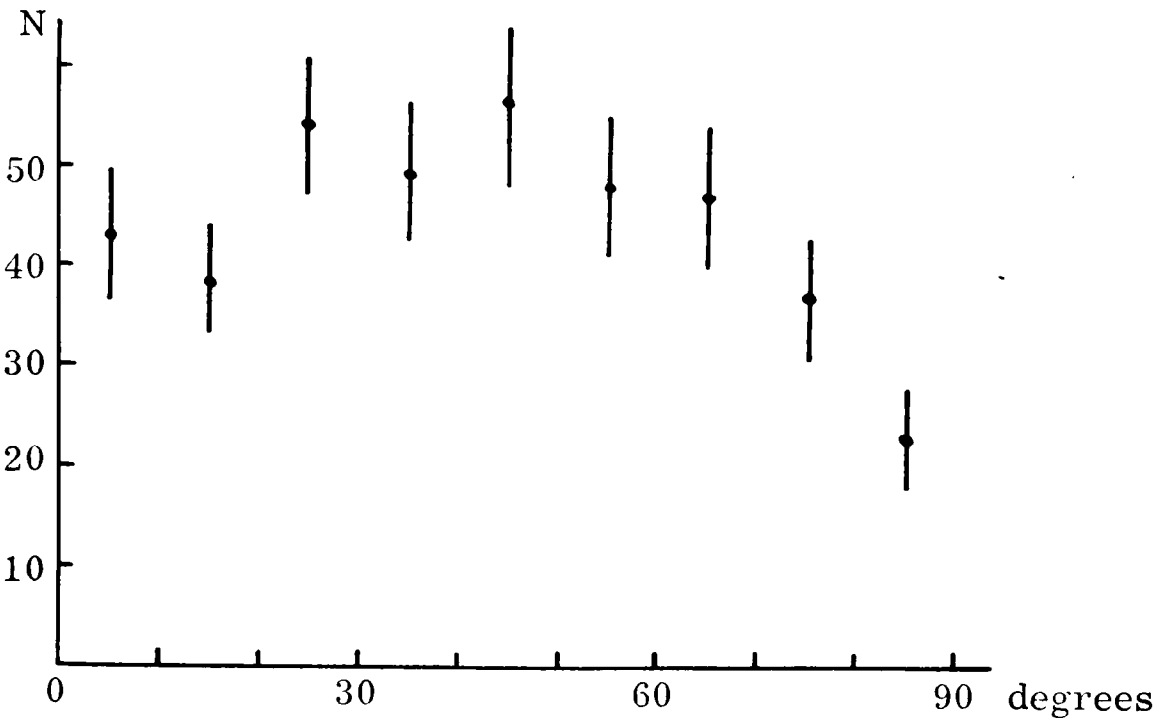

Fig. 7.8 Distribution with azimuthal angle of p-shell events.

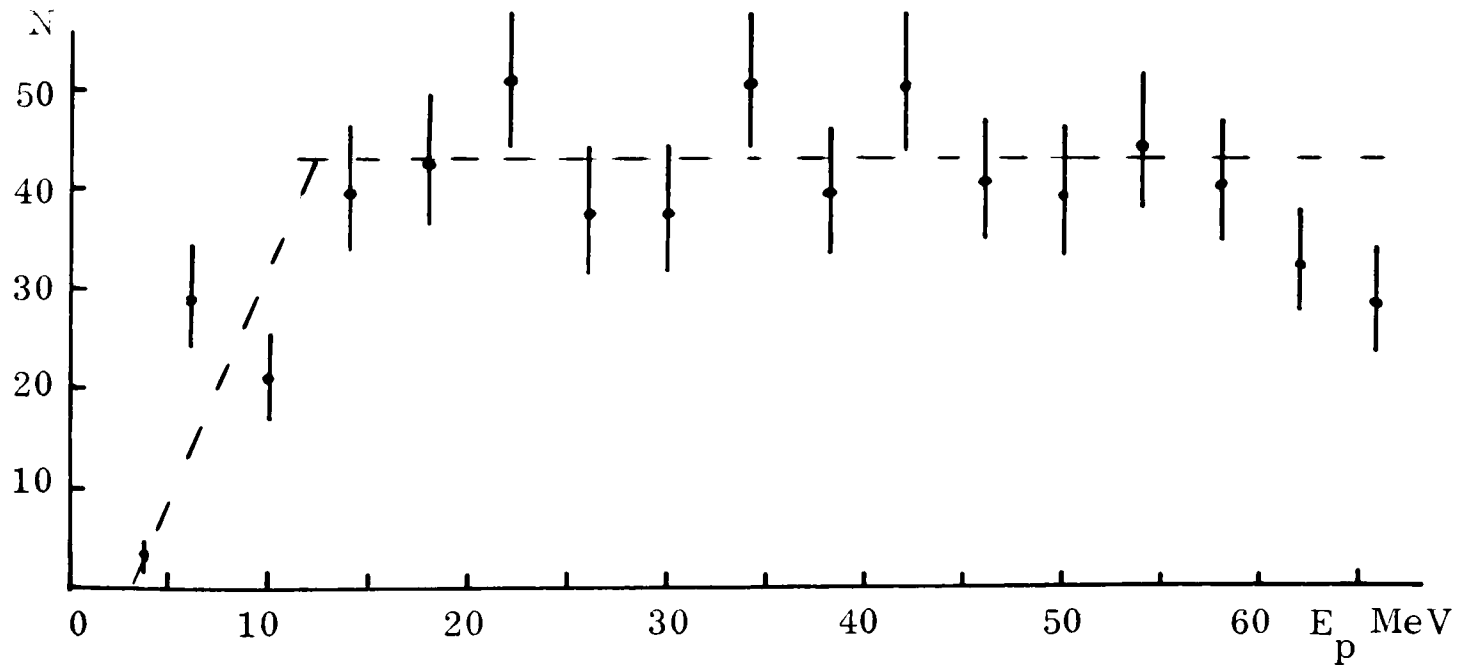

Fig. 7.9 Distribution of proton energies for p-shell events.

define the p-shell events; their results are summarized below. In the last column, the cross-sections from the present experiment, calculated for the same energy-loss limits, are shown.

Incident energy (MeV)	Energy-loss (MeV)	Cross-section (mb)	Comparable[6] from present results (mb)
$70 < E_o < 90$	$12 < E_L < 22$	16.3 ± 3.9	17.4 ± 1.9
	$12 < E_L < 28$	25.9 ± 3.9	24.5 ± 2
$90 < E_o < 110$	$12 < E_L < 22$	15.9 ± 3.0	17.6 ± 1.6
	$12 < E_L < 28$	23.7 ± 3.0	23.0 ± 1.7

There is excellent agreement between the two sets of results.

GOODING & PUGH (1960) measured the C^{12} p-shell cross-section at 153 MeV using the counter telescope method and they obtained a value of 16 ± 4 mb; the energy-loss limits used were 8 MeV and 27 MeV. The corresponding result[≠] from the present experiment is 16.5 ± 2 MeV, which agrees within the statistical errors with the quoted result. This is a more interesting agreement than the one above because the bubble chamber method, and the counter telescope method, of measuring cross-sections involve different experimental difficulties, so that undetected systematic biases would be more likely to show in a comparison of these results than in a comparison of results from two bubble chamber experiments.

≠ Energy-loss limits of 10 MeV and 27 MeV were used because the events below 10 MeV in the energy-loss distribution (fig. 6.3) are hydrogen events. The experimental results were extrapolated to 153 MeV.

MORRISON & CARETTO (1962), in radiochemical experiments, have also found that (p, 2p) cross-sections are approximately energy independent; they measured the cross-sections for Si^{30}, Zn^{66} and W^{186} in the incident proton energy range 150 MeV to 450 MeV.

Assuming that the nucleon-nucleon interactions within nuclear matter resemble interactions between free nucleons (i.e. accepting the Impulse Approximation), the energy independence of the (p, 2p) cross-section can, in fact, be accounted for.

GOLDBERGER (1948) has shown that, within nuclear matter, free nucleon-nucleon cross-sections are decreased by the operation of the Pauli principle; he showed that the intranuclear nucleon-nucleon cross-sections are related to the free nucleon-nucleon cross-sections by the following formula:

$$\sigma_I = \sigma\left(1 - \frac{7E_F}{5(E_o + V_o)}\right)$$

where σ_I = nucleon-nucleon cross-section within the nucleus
σ = free nucleon-nucleon cross-section at the energy $(E_o + V_o)$
E_F = Fermi energy
E_o = incident nucleon energy
V_o = depth of the nuclear potential well

The energy dependence of the quasi-elastic (p, 2p) reaction depends upon:

(a) the intranuclear proton-proton cross-section for the incident protons, and

(b) the intranuclear proton-nucleon cross-section for the protons produced by the initial quasi-elastic reaction (because a final state interaction destroys the quasi-elastic nature of the reaction).

Using the values: E_F = 30 MeV; V_o = 40 MeV; and values of σ from HESS (1958), σ_I for the incident protons is found to be independent of the incident energy in the range 50 MeV $< E_o <$ 130 MeV, and equal to 17 mb.

For incident proton energies of 50 MeV and 130 MeV, the average proton energies in the final state within the B^{11} nucleus, $(E+V_o)$, are 55 MeV and 95 MeV respectively. Using these values for (E_o+V_o), and an appropriately weighted average proton-nucleon cross-section ($\sigma = 5\sigma_{pp}/11 + 6\sigma_{pn}/11$), in the Goldberger formula, the cross-section for proton interactions in the final state is found to be approximately energy independent: σ_I(50 MeV) = 23.5 mb and σ_I(130 MeV) = 25 mb.

The energy independence of the two factors affecting the quasi-elastic (p, 2p) reaction can account for the energy independence of the measured cross-section. The agreement also lends support to the validity of the Impulse Approximation picture of nuclear reactions.

The above effects are implicit in Monte Carlo calculations, in which they receive a more detailed treatment, and the Monte Carlo calculated cross-sections do, in fact, turn out to be energy independent. For example, it was seen in section 1.3 that the $C^{12}(p, 2p)B^{11}$ cross-section calculated by Bertini is approximately constant from 50 MeV to 150 MeV. Although the value of the cross-section quoted is approximately 44 mb, it refers to reactions leaving the B^{11} nucleus with all possible excitation energies, and if the cross-section for the production of B^{11} with an excitation energy of less than 10 MeV is taken,*

---

* The Monte Carlo calculation does not produce a body of ground state events because the shell structure of the nucleus is not built into the nuclear model used.

it is found to be equal to 16 mb., i.e. in good agreement with the value measured in the present experiment.

Another example from Monte Carlo calculations comes from the calculation of the cross-section for the reaction $Cu^{65}(p,pn)Cu^{64}$ by METROPOLIS et al (1958). They showed that the experimentally measured strong energy dependence for this cross-section, in the incident energy range 50 MeV $< E_o <$ 150 MeV, is due entirely to the composite reaction: $p + Cu^{65} \rightarrow p' + Cu^{65*}$; $Cu^{65*} \rightarrow Cu^{64} + n$, and that the cross-section for the direct knock-out of a neutron is approximately energy independent. It seems probable that the experimental results of CRANDALL et al (1956) for C^{12}:

$$\sigma\,(p,pn) \text{ at } 130 \text{ MeV} = 51 \text{ mb}$$

$$\sigma\,(p,pn) \text{ at } 50 \text{ MeV} = 87 \text{ mb}$$

can also be explained by the same composite reaction and that the cross-section for the quasi-elastic (p,pn) reaction is energy independent like that of the quasi-elastic (p,2p) reaction.

7.6 Other cross-sections

Figure 7.11 shows the cross-sections corresponding to the numbers of events actually observed in the bubble chamber for all the 2-prong events with energy-losses above 30 MeV, for all the 3-prong events, and for all the 4-prong events.[#] No correction factors have been applied to the results except for the flux normalization; the error bars show the statistical errors only. The most

---

[#] The events on rejected frames (see section 4.2) were excluded from the cross-section determination.

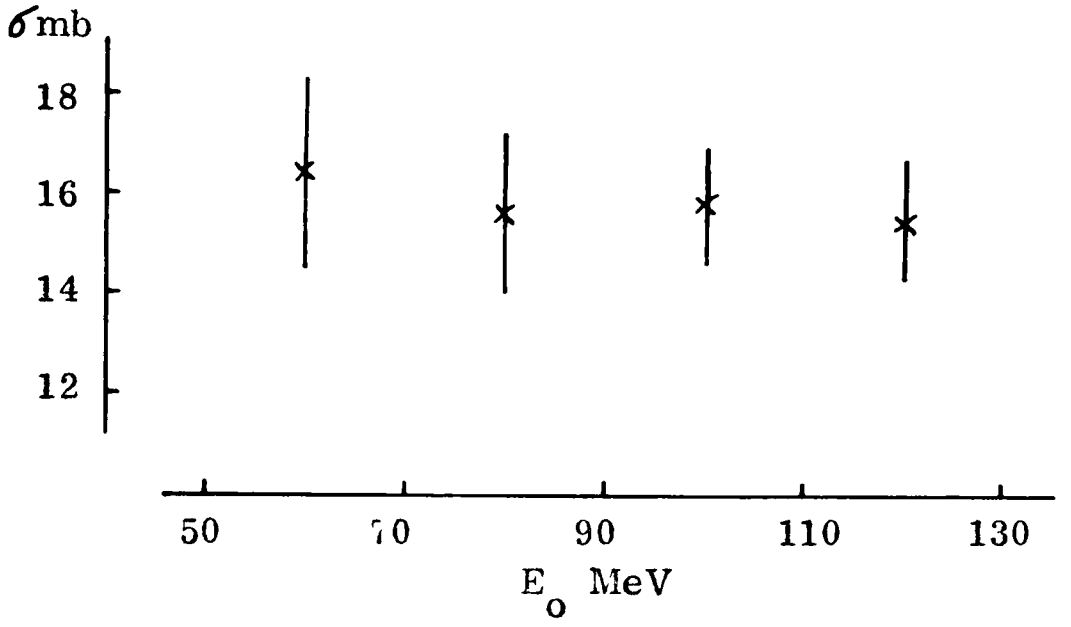

Fig. 7.10 The cross-section for the reaction $C^{12}(p, 2p)B^{11}$ g.s.

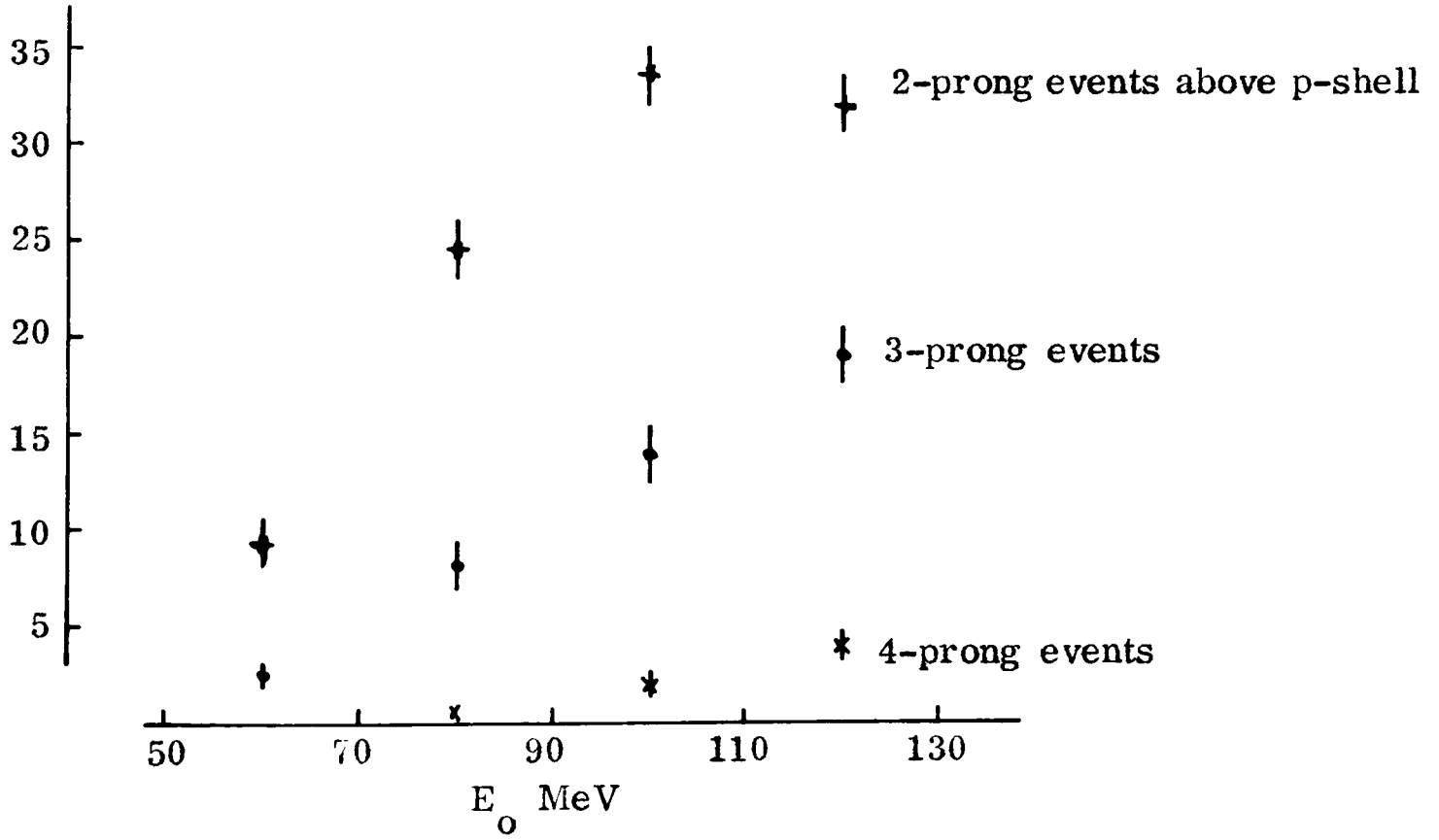

Fig. 7.11 Cross-sections for the categories of events shown.

important correction would be for the non-observation of short prongs, but because the contributions to the events from the various reaction mechanisms are not fully understood, especially for those events with short prongs (i.e. reactions for which nucleon evaporation and heavy particle ejection are important), no meaningful correction can be given.

It is interesting to note that even the uncorrected cross-section for the 3-prong events is 50% above the value for the nucleon cascade reactions $\sum_x$ (p,3pxn) given by Bertini (see section 1.3).

In chapter 10, it is shown that there is evidence to support the hypothesis that a large proportion of the events with (p,3p) energy-losses below 40 MeV are consistent with the reaction $C^{12}(p,3p)Be^{10}$. The uncorrected cross-section for these events is independent of the incident energy and is equal to 2.6 ± 0.5 mb.

CHAPTER 8

THE $C^{12}(p, 2p)B^{11}$ REACTION FOR ZERO AND LOW EXCITATION ENERGIES OF B^{11}

8.1 Nomenclature

The diagram shows the nomenclature used in describing the (p, 2p) reaction.

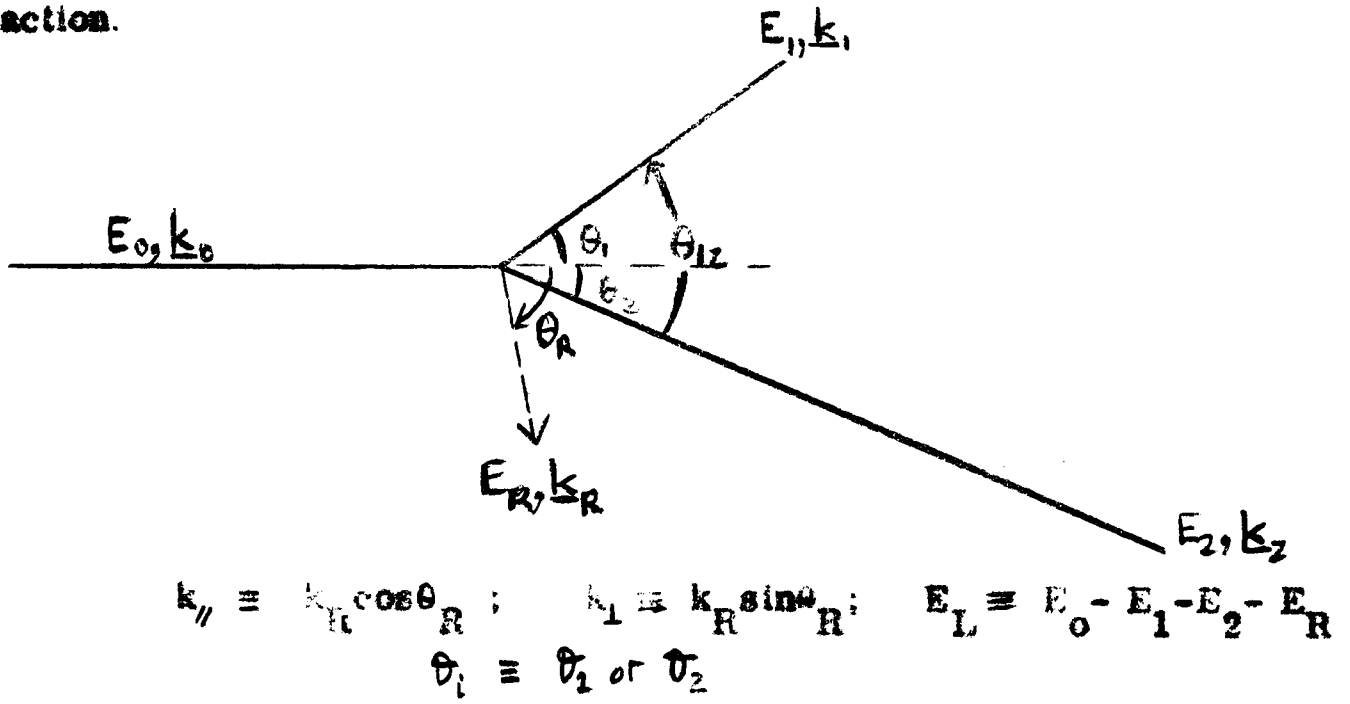

$$k_{//} \equiv k_R \cos\theta_R \; ; \quad k_\perp \equiv k_R \sin\theta_R ; \quad E_L \equiv E_0 - E_1 - E_2 - E_R$$

$$\vartheta_i \equiv \vartheta_1 \text{ or } \vartheta_2$$

8.2 The quasi-elastic nature of the reaction

The recoil nucleus momentum distribution data for events with energy-losses in the range of 12 MeV to 21 MeV, shown in figure 8.1, give direct evidence in support of the quasi-elastic reaction hypothesis.

If the reaction were due to a compound nucleus mechanism, the distribution of the recoil nucleus momentum would be determined only by the available phase space (including the energy and momentum conservation laws for the system). This phase space factor has been determined for incident protons of energy

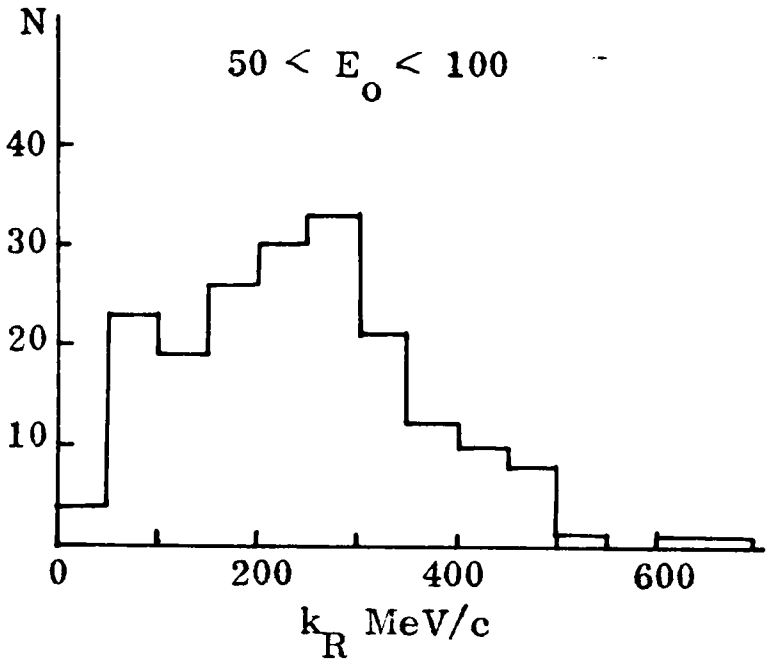

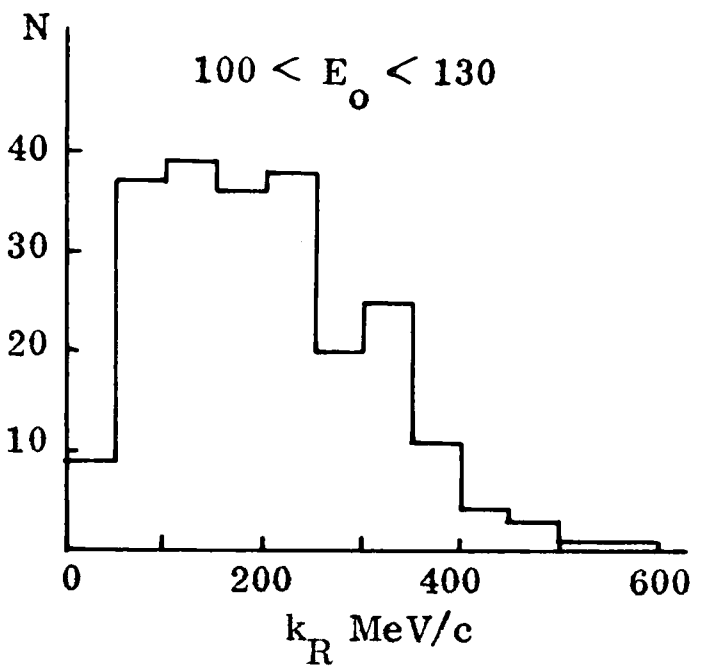

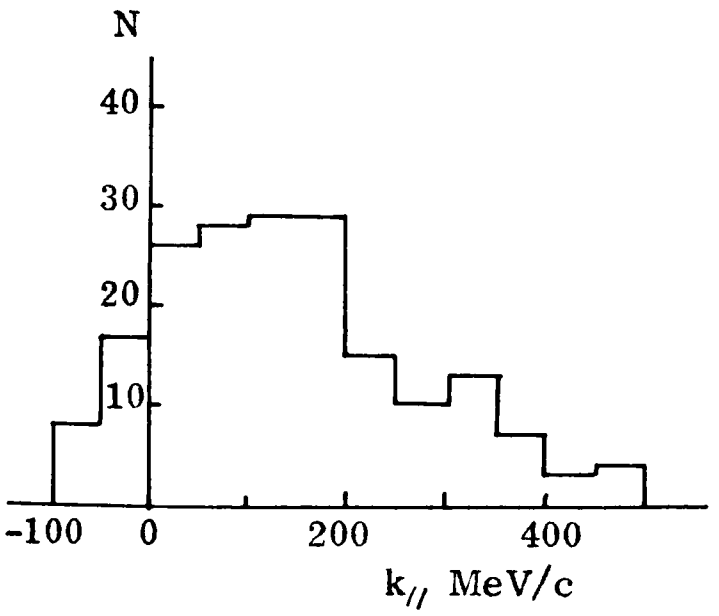

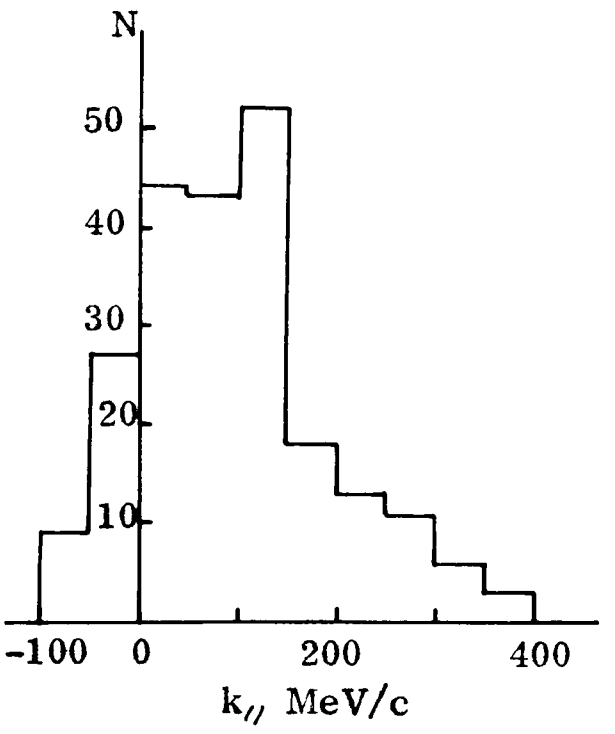

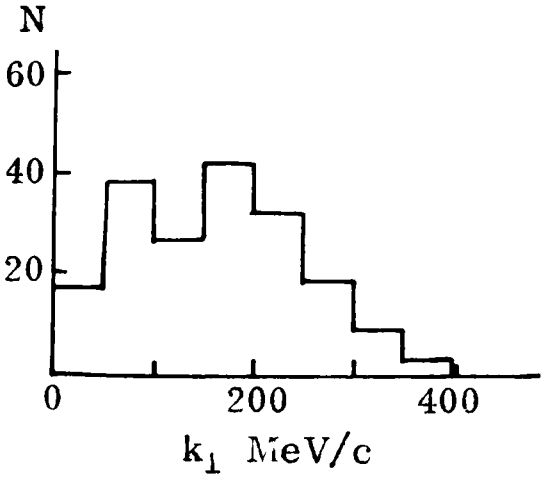

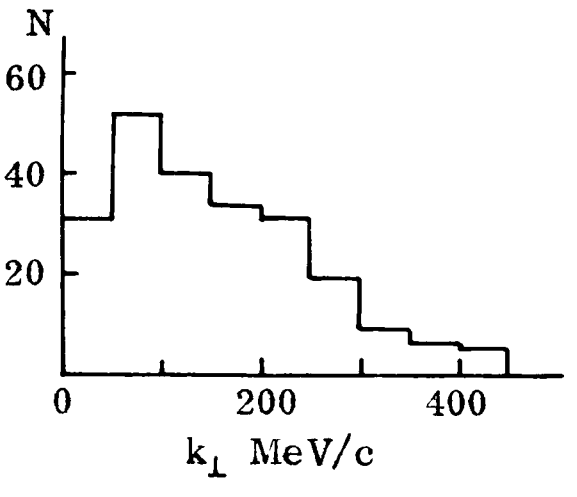

Fig. 8.1 Recoil nucleus momentum distributions.

115 MeV (the mean energy for the ground state events with $E_o > 100$ MeV) and is shown in figure 8.2.* The histogram shown with the curve is the experimental recoil nucleus momentum distribution, taken from figure 8.1. It is immediately evident that the compound nucleus reaction mechanism is not applicable for these events, because only a very small part of the available phase space is being occupied.

The quasi-elastic reaction hypothesis requires (to the extent that the Impulse Approximation holds (see section 1.4)) that for each reaction the momentum of the recoil nucleus be equal and opposite to that of the target nucleon at the time of the collision. The momentum distribution of the target nucleons depends upon the exact form of the potential well in which the nucleons are moving. For example, an infinite harmonic oscillator potential gives the following momentum distribution for $\ell=1$ nucleons:

$$\alpha(k) = k^2 e^{-k^2/a^2},$$

and HOFSTADTER's results (1963) for C^{12} suggest a value of $a = 125$ MeV/c.

It might be expected, therefore, that the recoil nucleus momentum distribution would be of this type if the quasi-elastic reaction hypothesis is correct. However, the situation is not quite as straightforward as this. Although, in each reaction the recoil nucleus momentum is equal and opposite to the struck

---

* The calculation of the phase space factor; of the recoil nucleus momentum distribution shown in figure 8.3; and of the nuclear radial wavefunction, was made by M.R. Bowman (1964), who has presented a detailed analysis of the momentum distribution for these events.

nucleon momentum, the probability of a collision with a nucleon of a given momentum depends not only upon the frequency with which this momentum occurs within the nucleus, but also upon the phase space available for the relevant final state and upon the cross-section for the nucleon-nucleon collision at the appropriate relative momentum. Thus, for example, the conservation laws forbid certain reactions; it can easily be shown that for an incident proton energy of 155 MeV, the maximum observable momentum for nucleons moving in directions at angles of 0, 45°, 90°, 135° and 180°, with the incident proton direction, are 180 MeV/c, 220 MeV/c, 450 MeV/c, 880 MeV/c and 1100 MeV/c respectively.

The factors mentioned above, however, can be allowed for and, assuming a nucleon momentum distribution of the type $\alpha(k)$, the expected recoil nucleus momentum distribution will be:

$$N(k) = \sigma(p,p)_k \; \alpha(k) \; \beta(k)$$

where:

$\sigma(p,p)_k$ is the elastic proton-proton cross-section at the relative momentum k (i.e. the Impulse Approximation holds), and

$\beta(k)$ is the phase space factor.

The results calculated for $E_o = 115$ MeV are shown in figure 8.3, together with the experimental results for the events with $E_o > 100$ MeV. There is, in contrast with the compound nucleus hypothesis, an excellent order of magnitude agreement between these two sets of results, and this points very definitely to the correctness of the quasi-elastic hypothesis. Although there are discrepancies

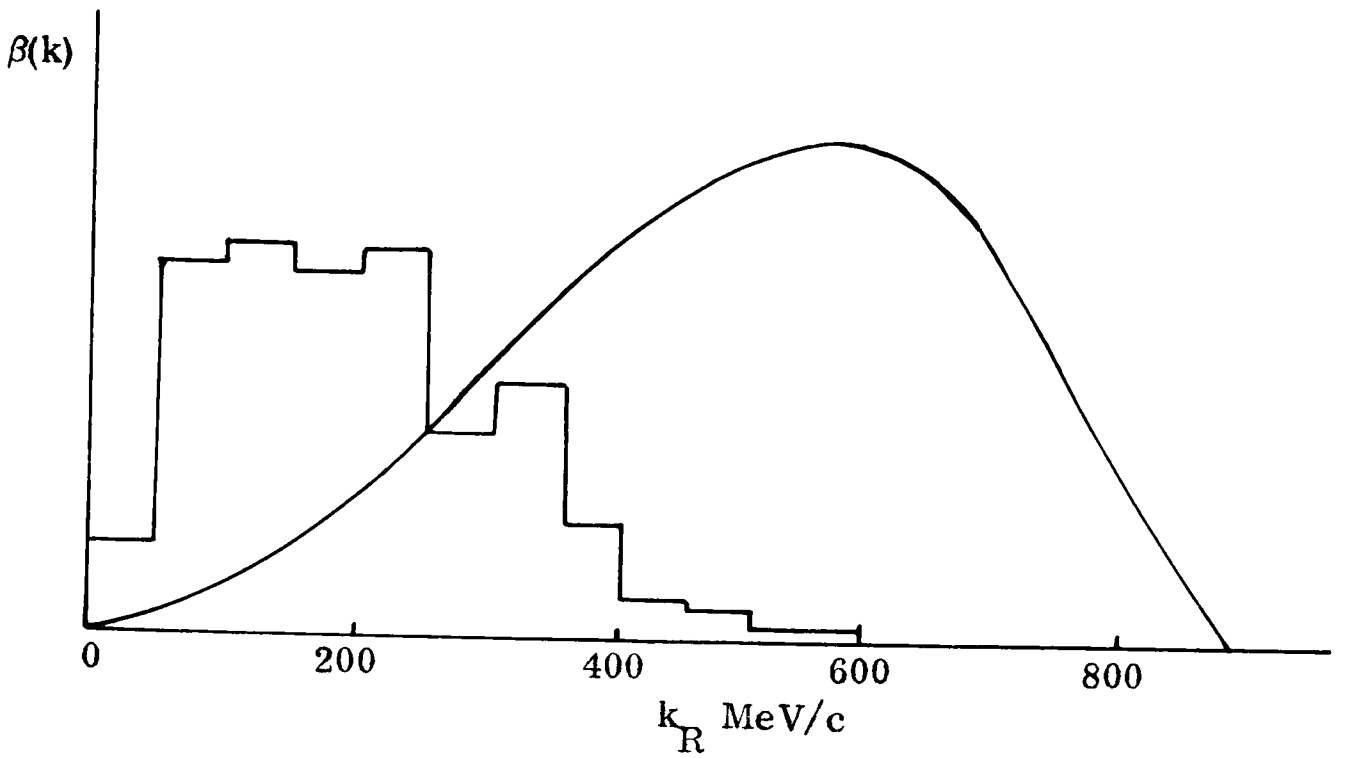

Fig. 8.2 Phase space factor (E_o=115 MeV).

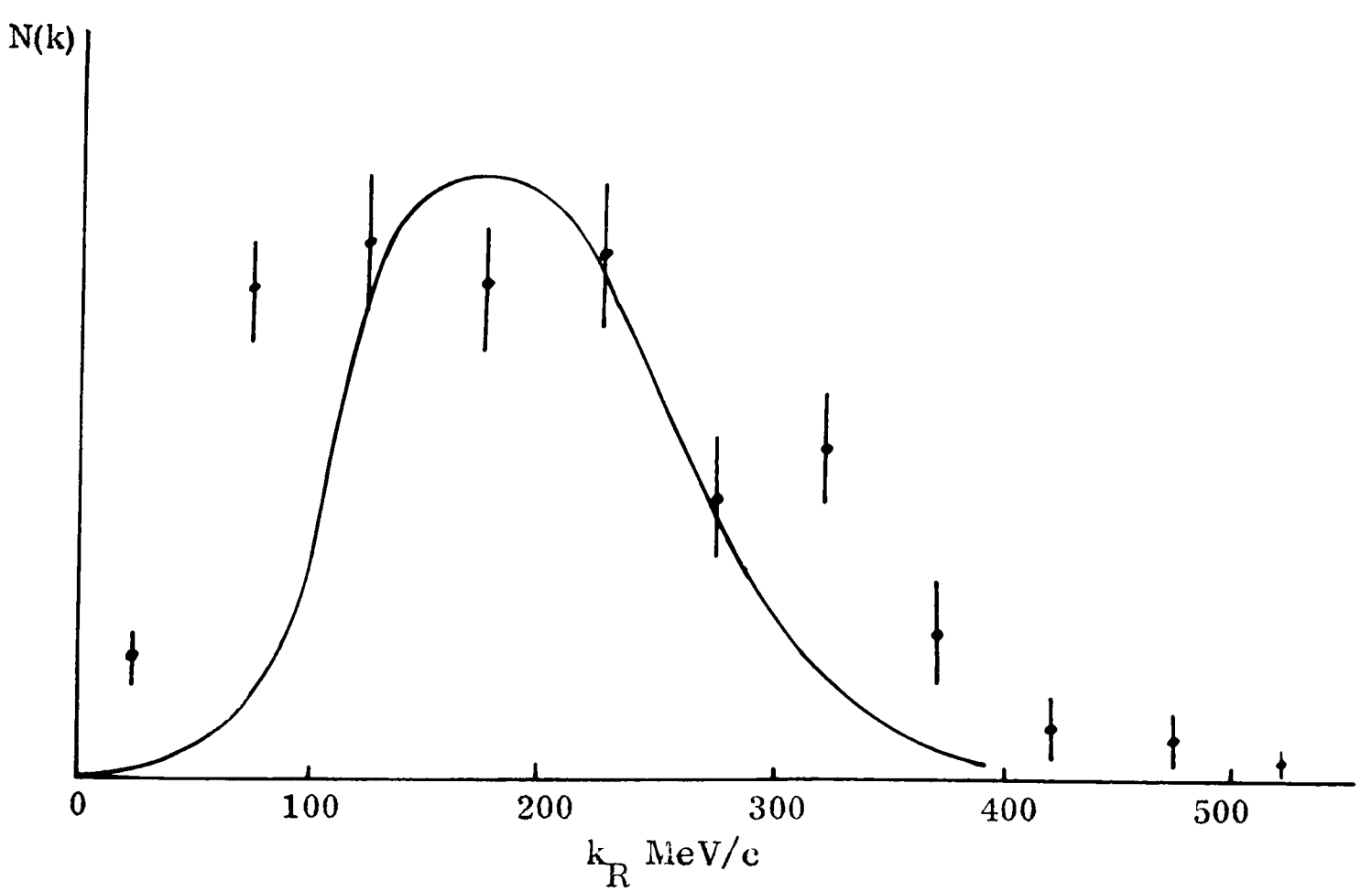

Fig. 8.3 The recoil nucleus momentum distribution and the momentum distribution calculated on the assumption of an oscillator potential.

between the experimental results and the theoretical results both at high momenta and at low momenta, this is perhaps not surprising in view of the idealized nuclear potential used in the calculation.

The tail of high momentum events is observed consistently in experiments of this sort and it can be attributed either to the effect of final state interactions, which make the momentum distribution "leak out" into the available phase space, or to the presence of nucleon correlation effects in the C^{12} and B^{11} ground states (although, in general, interactions involving the knock out of one of a correlated pair of nucleons might be expected to lead to B^{11} excited states).

If the high momentum tail is subtracted from the experimental results and the resulting distribution used for N(k), then by inverting the calculation process mentioned above, the nuclear radial wavefunction consistent with N(k) can be obtained. M.R. Bowman found that when this was done the wavefunction obtained was very similar to the infinite oscillator wavefunction up to about 4 fermis, but that it possessed a tail extending 3 fermis beyond the oscillator wavefunction cut-off radius (which is at approx 4.5 fermis). JOHANSSON & SAKAMOTO (1963) in an analysis of the (p, 2p) reaction in Li^6 and Li^7 found a similar high radius component of the wavefunction; they reconciled the change of the p-state radial wavefunction and the charge distribution of the whole nucleus (determined from electron scattering experiments) by reducing the radial extent of the s-shell wavefunction (they supposed that the s-shell protons moved in a square well potential). RILEY et al. (1960) proposed that the low momentum events might arise from surface localization of the reaction, but on this

assumption the agreement between the calculated and the experimental momentum distributions (figure 8.3) is improved at low momenta only at the expense of increasing the discrepancy at high momenta, with no improvement in the overall agreement.

8.3 A summary of the experimental results

The quasi-elastic nature of the reaction characterizes all the features of the experimental results; these results are summarized in figures 8.4 to 8.9 for the events with energy-losses between 12 MeV and 21 MeV, and some interpretive comments are given below.

Figures 8.4 and 8.5: Correlation between proton energies and angles.

For elastic proton-proton reactions, all the points would lie on the line $E_1/E_o = \cos^2\theta_1$. However, for quasi-elastic reactions the binding energy of the nucleons and the nucleon momentum distribution lead to the more complex relationship:

$$E_L = 2(\sqrt{E_o E_1}\cos\theta_1 + \sqrt{11E_o E_R}\cos\theta_R - \sqrt{11E_1 E_R}\cos\theta_{1R} - E_1 - 6E_R)$$

When $E_R/E_o \to 0$, this expression reduces to:

$$E_1 = E_o\cos^2\theta_1 - (E_L + E_L^2/4E_1)$$

The larger E_R/E_o becomes, the weaker becomes the correlation (assuming a given spread in E_R). This is well illustrated in figures 8.4 and 8.5, which show the distributions of points for two ranges of incident energies. The two curves show the correlation for the special cases:

$k_R = k_{//} = 92$ MeV/c (figure 8.4)

$k_R = k_{//} = 151$ MeV/c (figure 8.5)

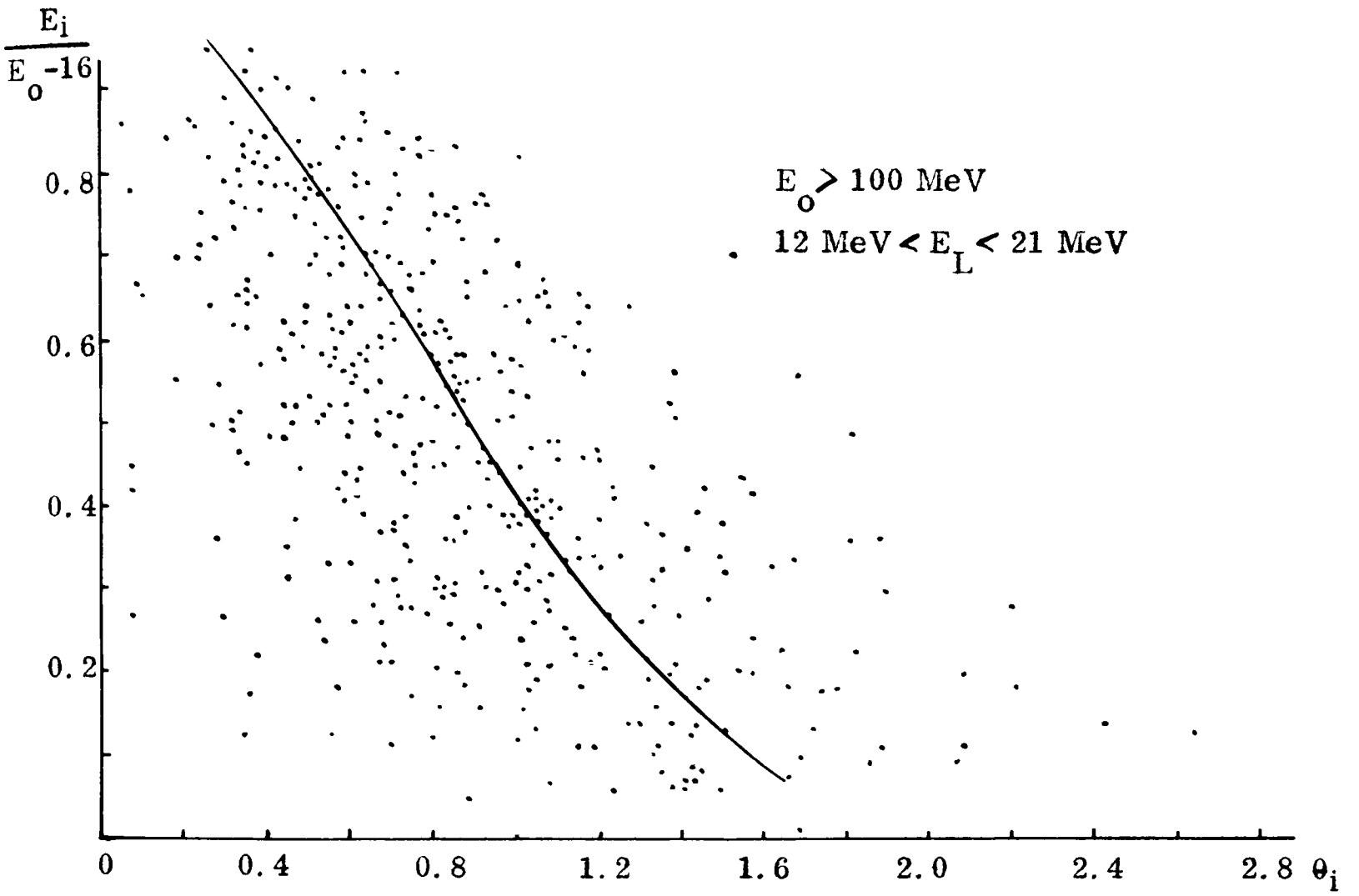

Fig. 8.4 Proton angle-energy correlations for p-shell events.

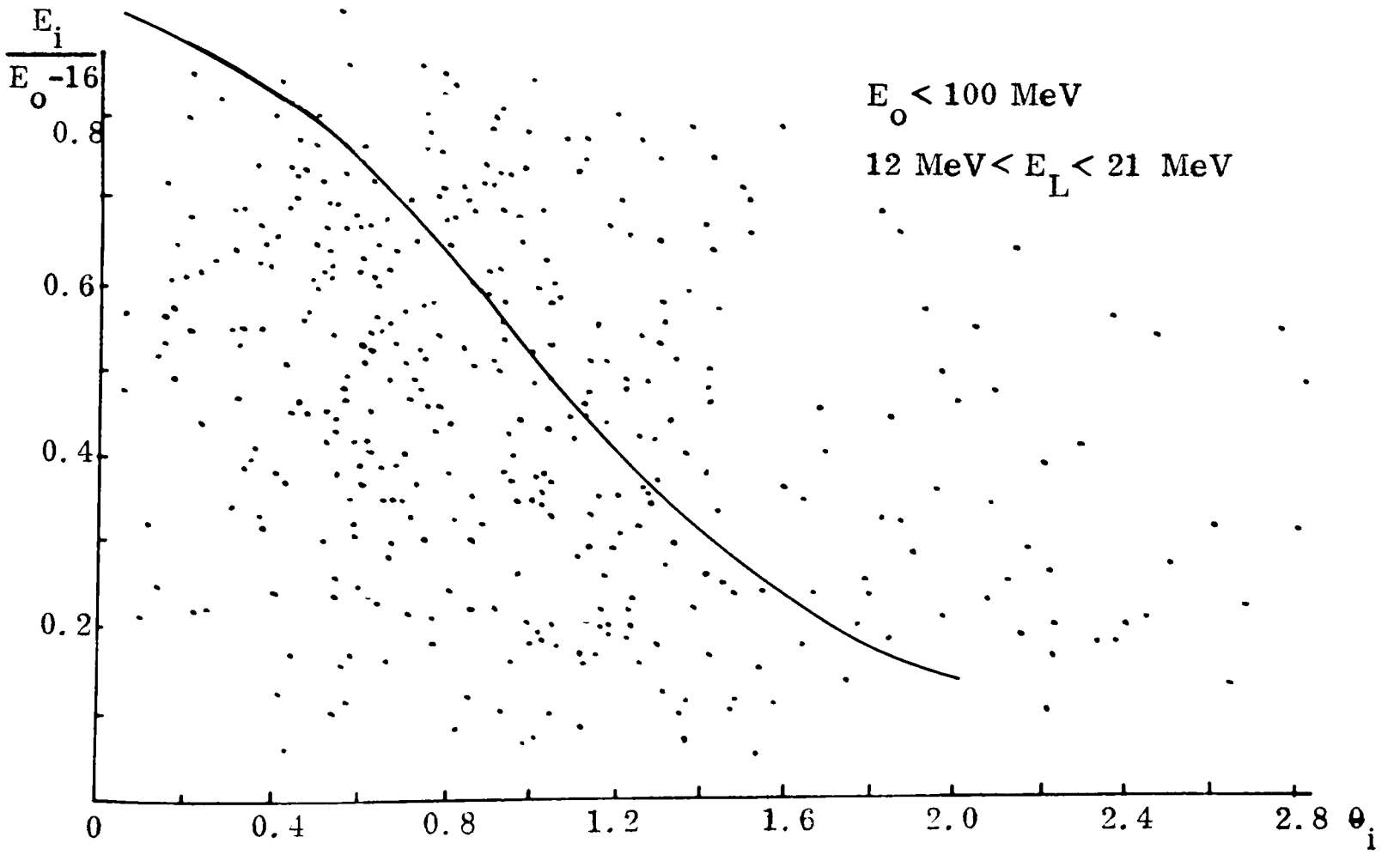

Fig. 8.5 Proton angle-energy correlations for p-shell events.

Figures 8.6 and 8.7: **Angle between the product protons**

This angle, which is always close to 90° for elastic proton-proton reactions (equal to 90° in the non-relativistic limit), depends markedly on the momentum of the target nucleon in the case of the quasi-elastic reaction:

$$\cos\phi_{12} = \frac{1.09k_{\perp}^2 + 1.09k_{//}^2 + 2mE_1 - 2k_0 k_{//}}{2k_1 k_2}$$

A marked correlation is seen in figure 8.6 between ϕ_{12} and $k_{//}$. The curve shows the special case: $k_{\perp} = 0$; $E_1 = E_2$; $E_0 = 115$ MeV.

Although the distributions of θ_{12}, shown in figure 8.7 for the two incident energy ranges, have mean values very close to 90°, it is evident from figure 8.6 that this is a somewhat fortuitous result caused by the balance, on average, of the reduction of θ_{12} due to the nucleon binding energy and the increase in θ_{12} due to the fact that the majority of collisions occur with nucleons moving towards the incident proton.

Figure 8.8: **Correlation between the angles of emergence of the product protons and the angle between them**

The crosses, which show the mean value of ϕ_{12} for each interval of θ_1, indicate a marked correlation effect; this correlation has been noted previously by GOODING & PUGH (1960), and by McKENZIE (1960) and ANDERSON (1960). It is directly attributable to the momentum distribution of the struck nucleons, and the latter authors showed that a classical calculation, using any reasonable nucleon momentum distribution, reproduced the correlation extremely well.

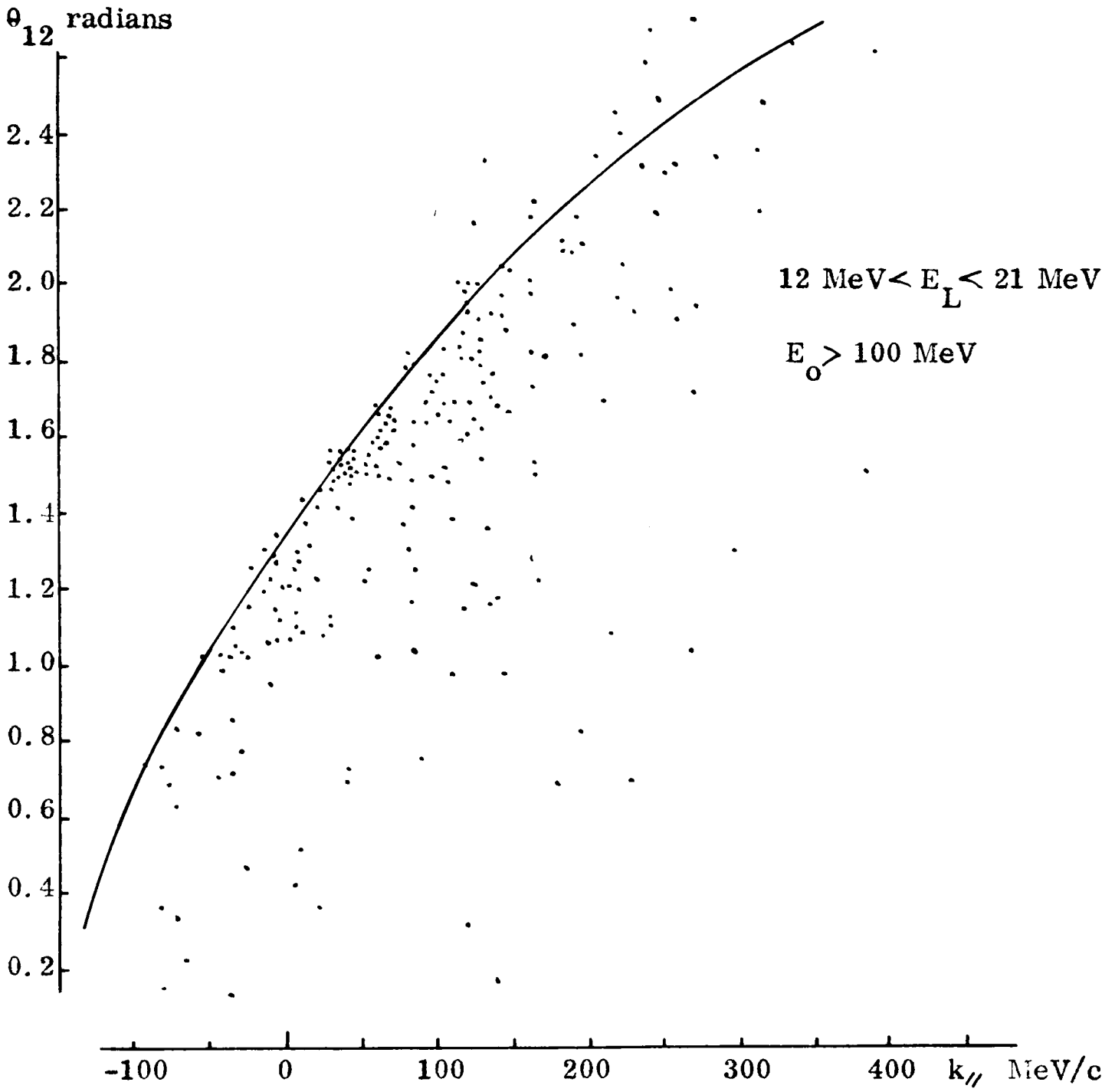

Fig. 8.6 Relationship between the angle between the product protons and the parallel component of the recoil nucleus momentum,

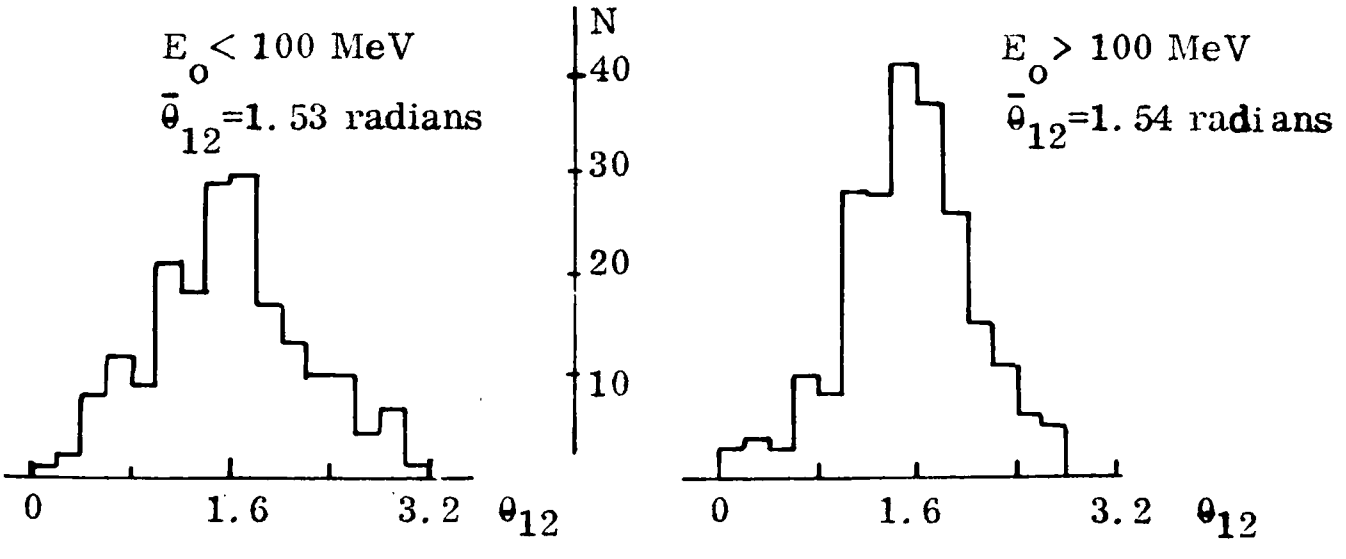

Fig. 8.7 Distributions of the angular correlation for p-shell events.

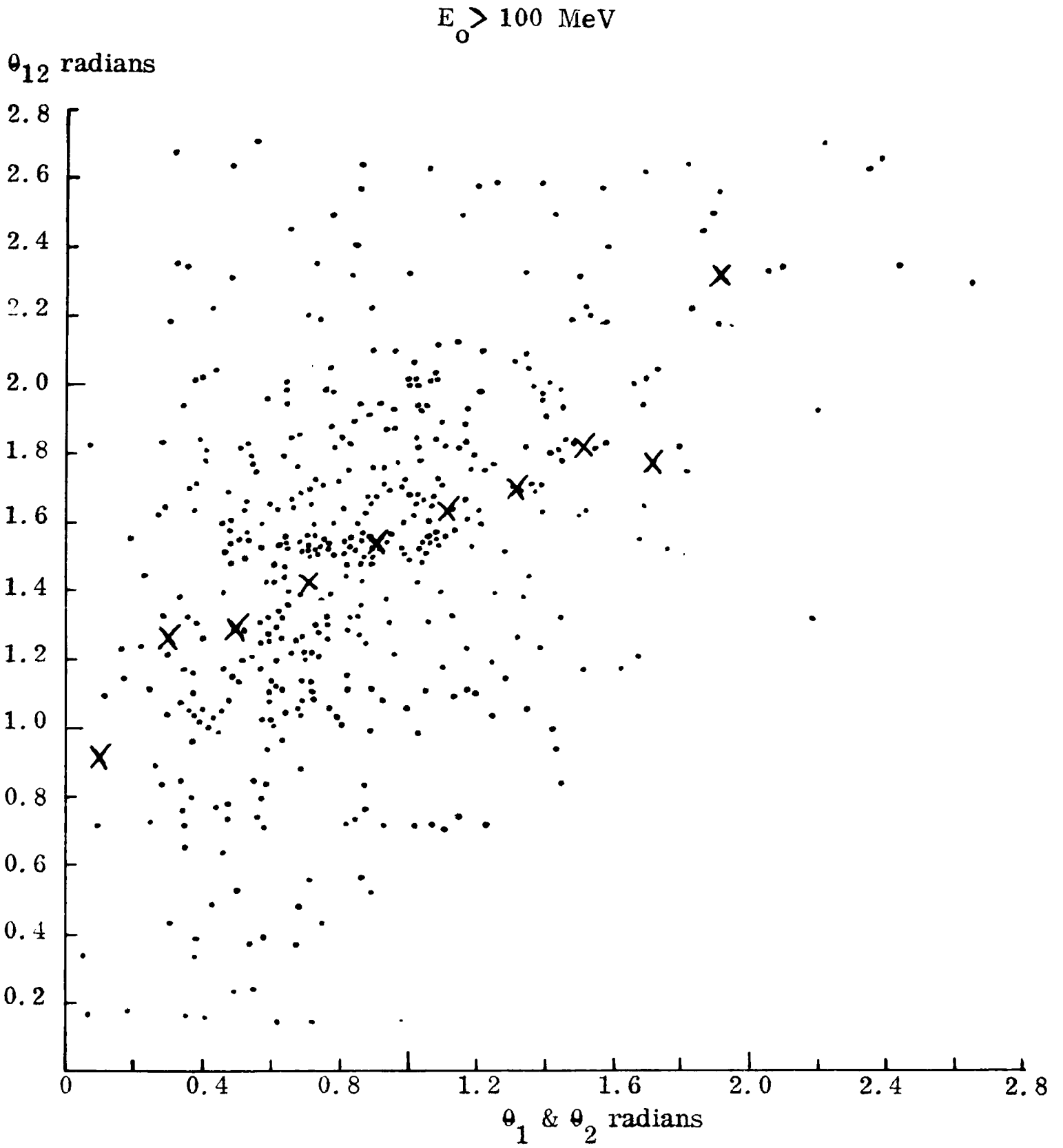

Fig. 8.8 Relationship between the angle of emergence of protons and the angle between the two protons, for p-shell events.

Figure 8.5: Coplanarity.

For elastic proton-proton reactions, the coplanarity is always zero. For the quasi-elastic reactions, the coplanarity is destroyed by the nucleon momentum distribution and the reactions will be less coplanar, on average, as the difference between k_o and k_R becomes smaller. The figure shows, as expected, that the reactions are less coplanar for the lower incident proton energies.

8.4 Events in the energy-loss region of 21 MeV to 30 MeV

Apart from a small contribution from background events, the only non-$C^{12}(p, 2p)B^{11*}$ reactions that can contribute events between 21 MeV and 30 MeV in the (p, 2p) energy-loss distribution are: (p, pd), (p, pα), and (p, 2pn).

From the observed number of background events appearing above the hydrogen peak in the (p, 2p) energy-loss distribution, the number of background events above the p-shell peak was estimated to be approximately three per MeV interval.

Heavy particle reactions were assumed to account for all those events that had energy-losses in the region of, or above, 7 MeV and 25 MeV when they were reconstructed on the reaction hypotheses (p, pd) and (p, pα) respectively. This gives an upper limit estimate, because (p, 2p) reactions producing very low energy protons also come into this category. A negligible number of the events below an energy-loss of 30 MeV come from the cascade (p, 2pn) reaction[≠]

≠ It is possible that there is a contribution from (p, 2p) reactions, where the residual B^{11} decays by neutron emission. For the present purpose such reactions are treated as (p, 2p) reactions.

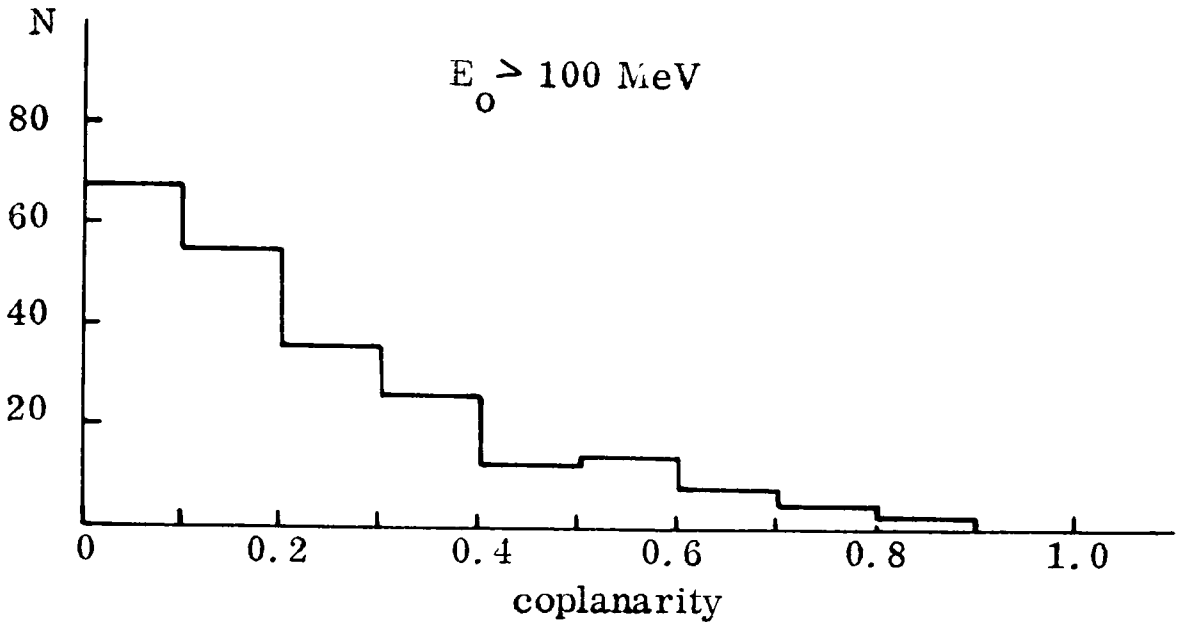

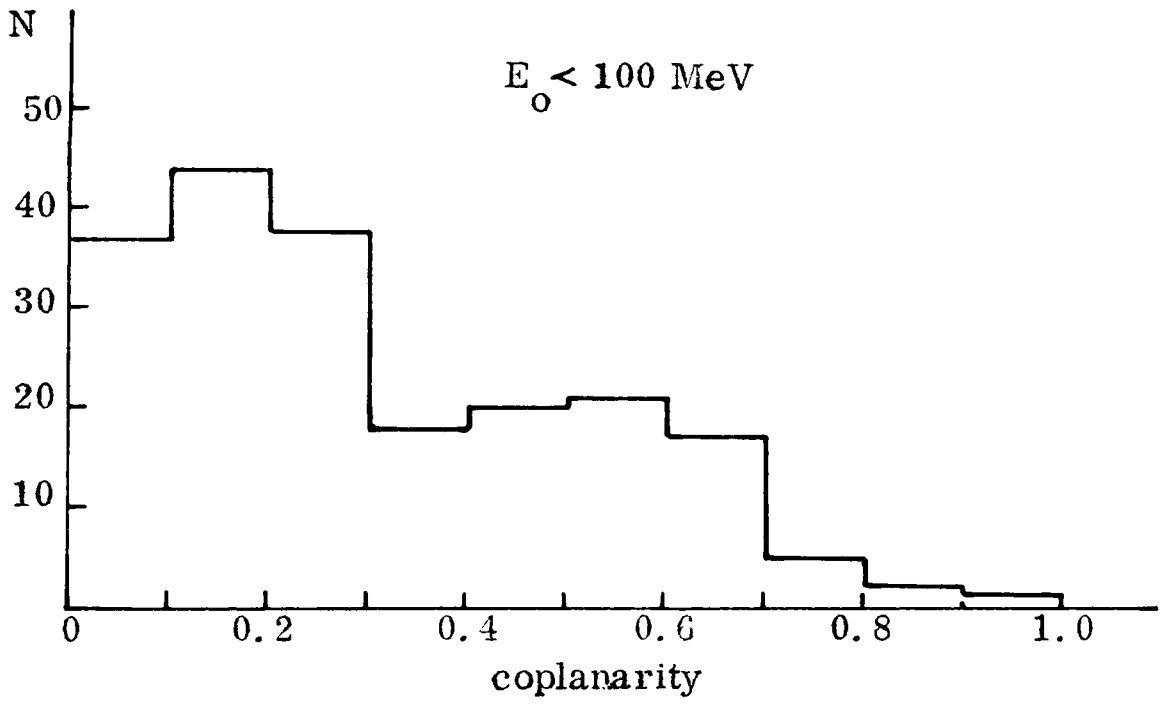

Fig. 8.9 Distribution of coplanarity for the p-shell events.

(see chapter 10, figure 33). Figure 8.10 shows the estimated number of background events and heavy particle events and figure 8.11 shows the relevant part of the (p,2p) energy-loss distribution after the events of figure 8.10 have been subtracted from it.

AUSTIN et al.(1962) have measured the cross-sections for the production of the low-lying excited states of B^{11} by the clean proton knock-out process; the details of the results have been given in section 1.4. Because the reaction mechanism leading to these states is the same as that for the production of the B^{11} ground state and since it has been shown in chapter 7 that the cross-section for the production of the ground state is approximately independent of the incident energy from 50 MeV to 130 MeV, it is assumed that the cross-sections quoted are also applicable throughout the energy range.

Using the figures tabulated in section 1.4, the numbers of events to be expected in figure 8.11 from the direct knock-out excited state reactions have been calculated. Figure 8.12 shows the resultant distribution when the events are smeared out to the measured resolution width of the ground state peak. These events were subtracted from the distribution of figure 8.11 and then the events in the ground state peak, constructed by reflecting the lower half of the peak about its median value, were also subtracted. The resulting distribution is shown in figure 8.13; evidently there is a large residue of events unaccounted for by the reactions already considered. The production cross-section is, on average, approximately half the cross-section for the production of the B^{11} g.s., but is much more dependent upon the incident energy. In the incident energy

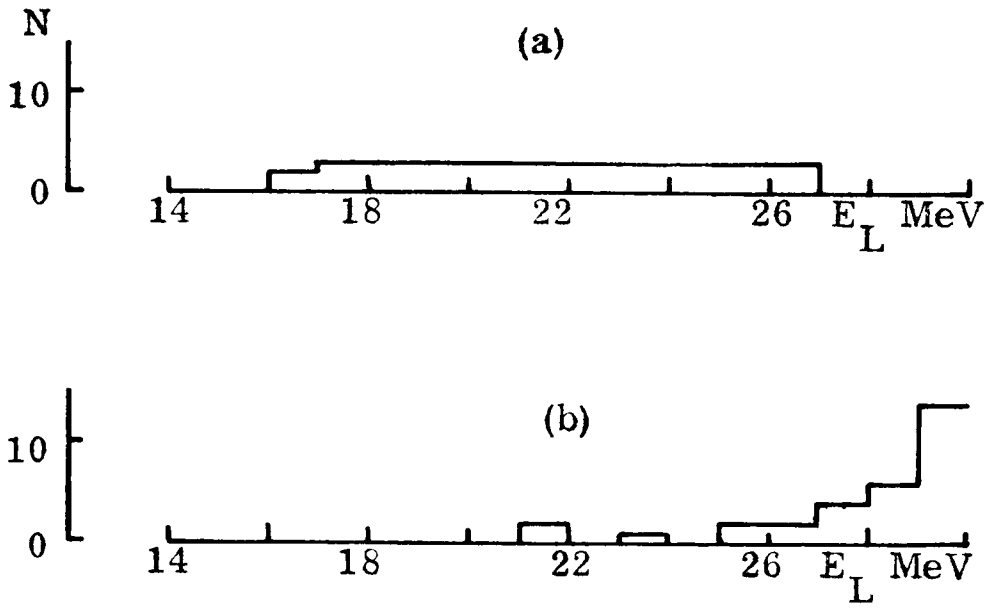

Fig. 8.10 (a) Number of background events.
(b) Number of heavy particle events.

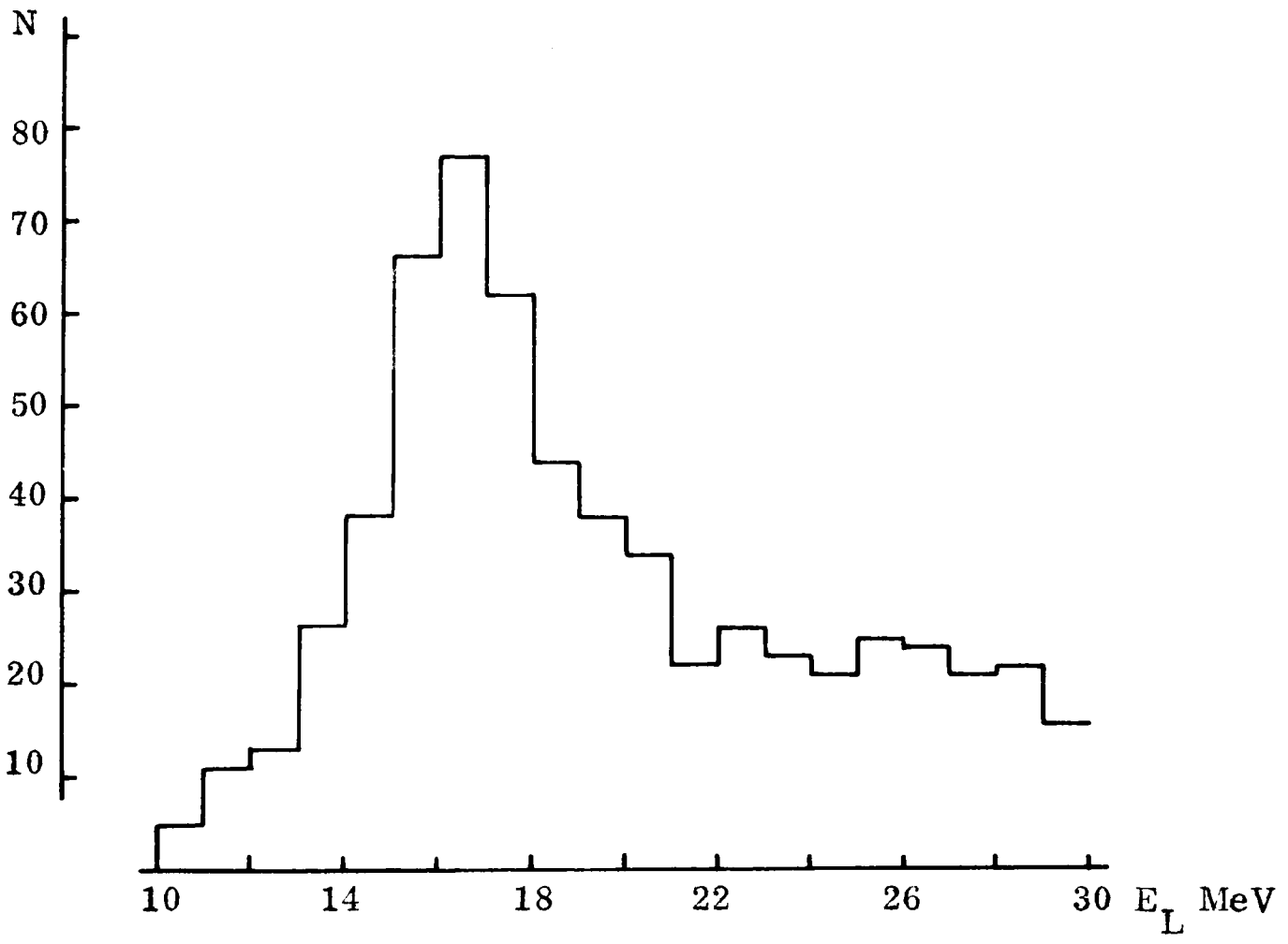

Fig. 8.11 The (p, 2p) energy-loss distribution after the subtraction of the events shown in figure 8.10.

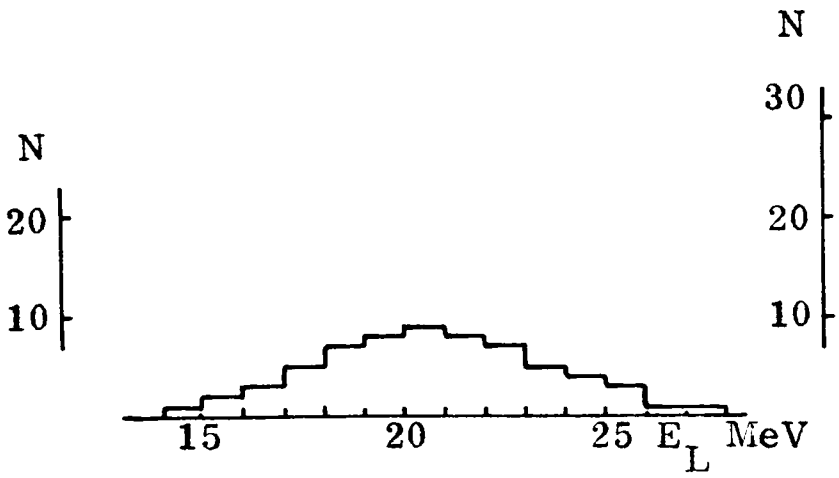

Fig. 8.12 Distribution of events expected from direct knock-out reactions; from the results of AUSTIN et al.

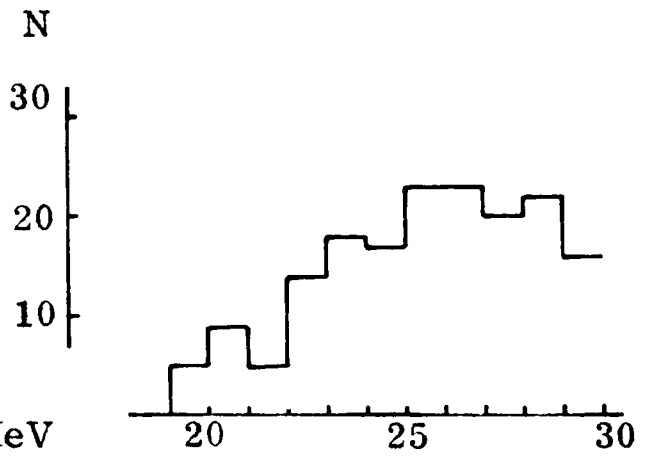

Fig. 8.13 The residue of excited state events.

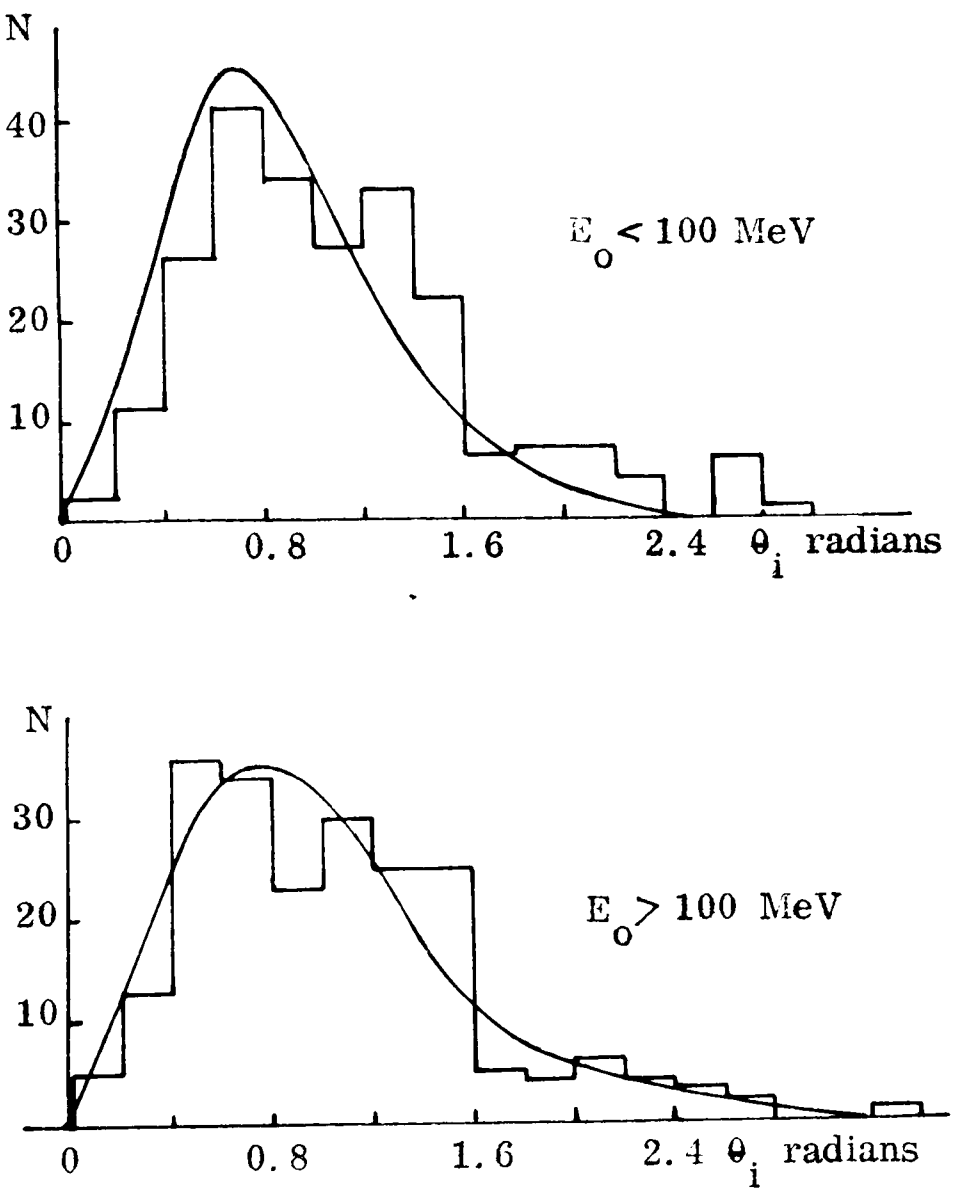

Fig. 8.14 Distributions of the product proton angles for the excited state events compared with those for the ground state events (curves).

region 50 MeV to 100 MeV the cross-section is $.5 \pm 1$ mb, and in the incident energy region 106 MeV to 130 MeV it is $5 \pm .05$ mb

To account for these events several possible reaction mechanisms, not already considered, can be envisaged; these are:

(i) A $C^{12}(p,p')C^{12*}$ reaction, leaving a highly excited state of C^{12} which subsequently evaporates a proton.

(ii) A (p, 2p) reaction with either an initial state interaction or a final state interaction.

(iii) A direct knock-out reaction involving a nuclear proton that is not in an independent particle state; such protons are usually associated with correlated nucleon pairs and have momenta larger than typical independent nucleon momenta.

The characteristics of events arising from such reaction mechanisms will differ from those arising from the quasi-elastic reaction mechanism that is responsible for the ground state events. An attempt is made to asses the differences between the experimental results for the ground state events and those for the excited state events, in terms of the relative importance of the three reaction mechanisms listed. The experimental statistics are not good and the differences in the two sets of results are not very great; consequently only a semi-qualitative approach is possible.

Comparison of the experimental results

Histograms were first plotted for the various kinematical distributions of all the events with energy-losses between 21 MeV and 3[illegible] MeV. To correct for

the presence of the clean knock-out events, estimated in figure 8.12, distributions of the appropriate magnitude and of exactly the same form as those obtained for the ground state events were subtracted from these histograms. The resulting histograms are shown in figures 8.14 to 8.16; the smooth curves indicate, for the sake of comparison, the suitably normalized distributions obtained for the ground state events.

The distributions for θ_{1}, θ_{12}, and coplanarity, are not significantly different for the two sets of events (figures 8.14, 8.15 and 8.16).

Figure 8.17, which shows the distribution of the events with incident energy reflects the result already noted: that the production cross-section for the excited state events decreases with increasing incident energy, whereas that for the ground state events is approximately independent of the incident energy.

In figure 8.18, the distribution of the product proton energies is shown for events with incident energies greater than 100 MeV; in (a), events consistent with the heavy particle reactions are included, and in (b) these events are excluded. In each case there are proportionately more low energy protons for the excited state events than for the ground state events.

The distributions of the recoil nucleus momentum and its components are shown, for two incident energy regions, in figure 8.19; the following table gives the mean values for k_R, $k_{//}$ and $k_{\perp}$ for the excited state events and for the ground state events.

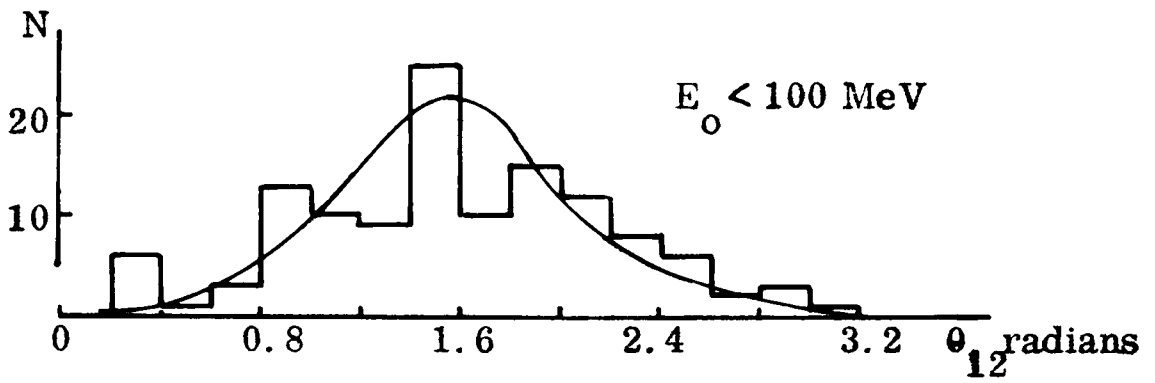

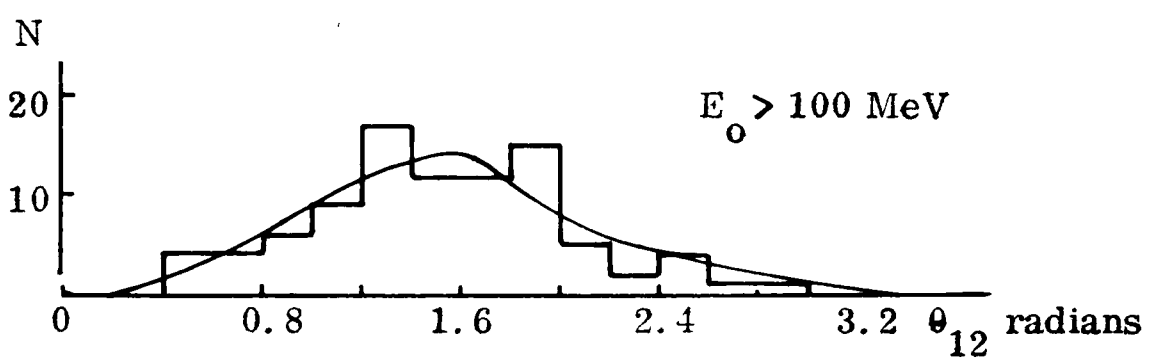

Fig. 8.15 Distributions of the angle between the two product protons for the excited state events compared with those for the ground state events(curves).

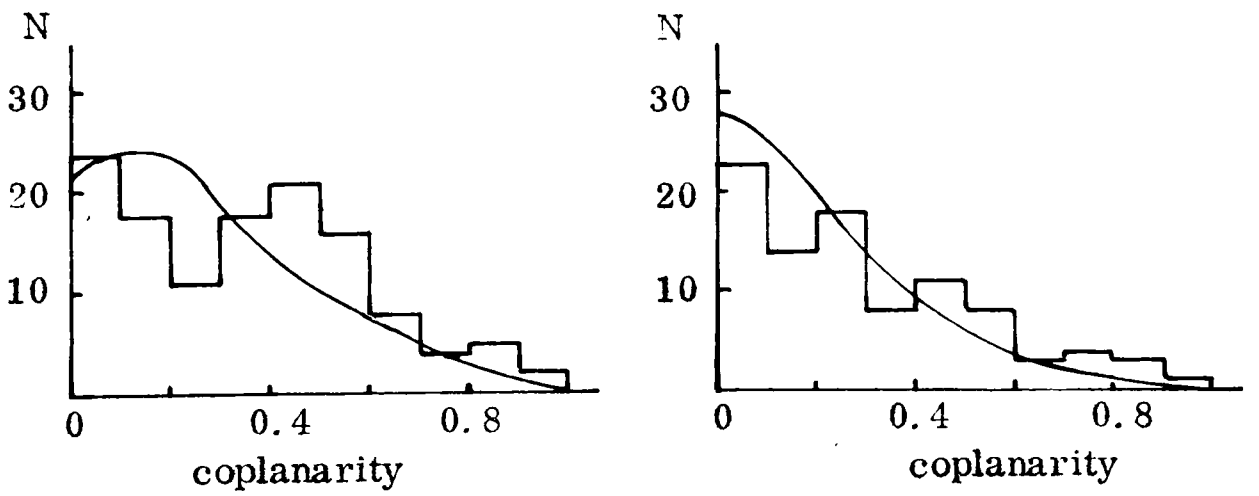

Fig. 8.16 Distributions of the coplanarity for the excited state events compared with those for the ground state events (curves).

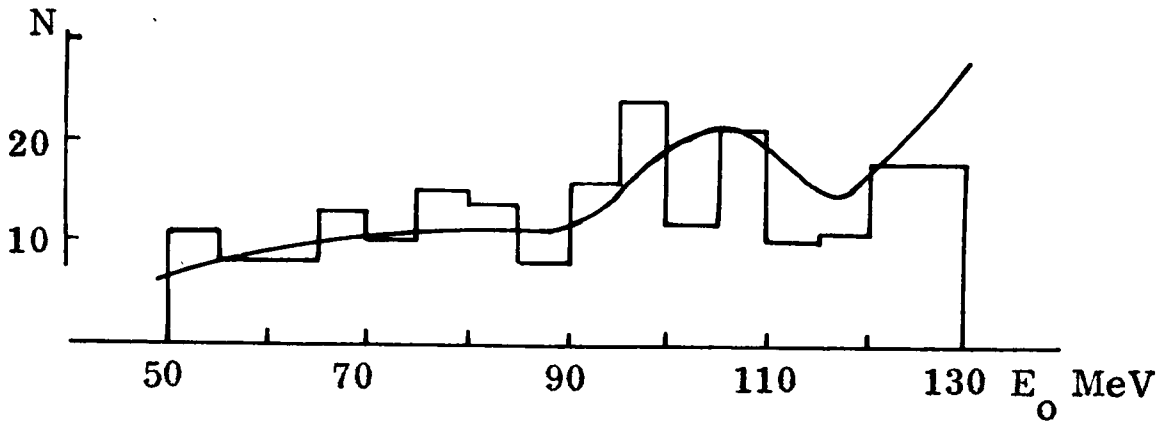

Fig. 8.17 Distribution with incident energy of the excited state events compared with that for the ground state events (curve).

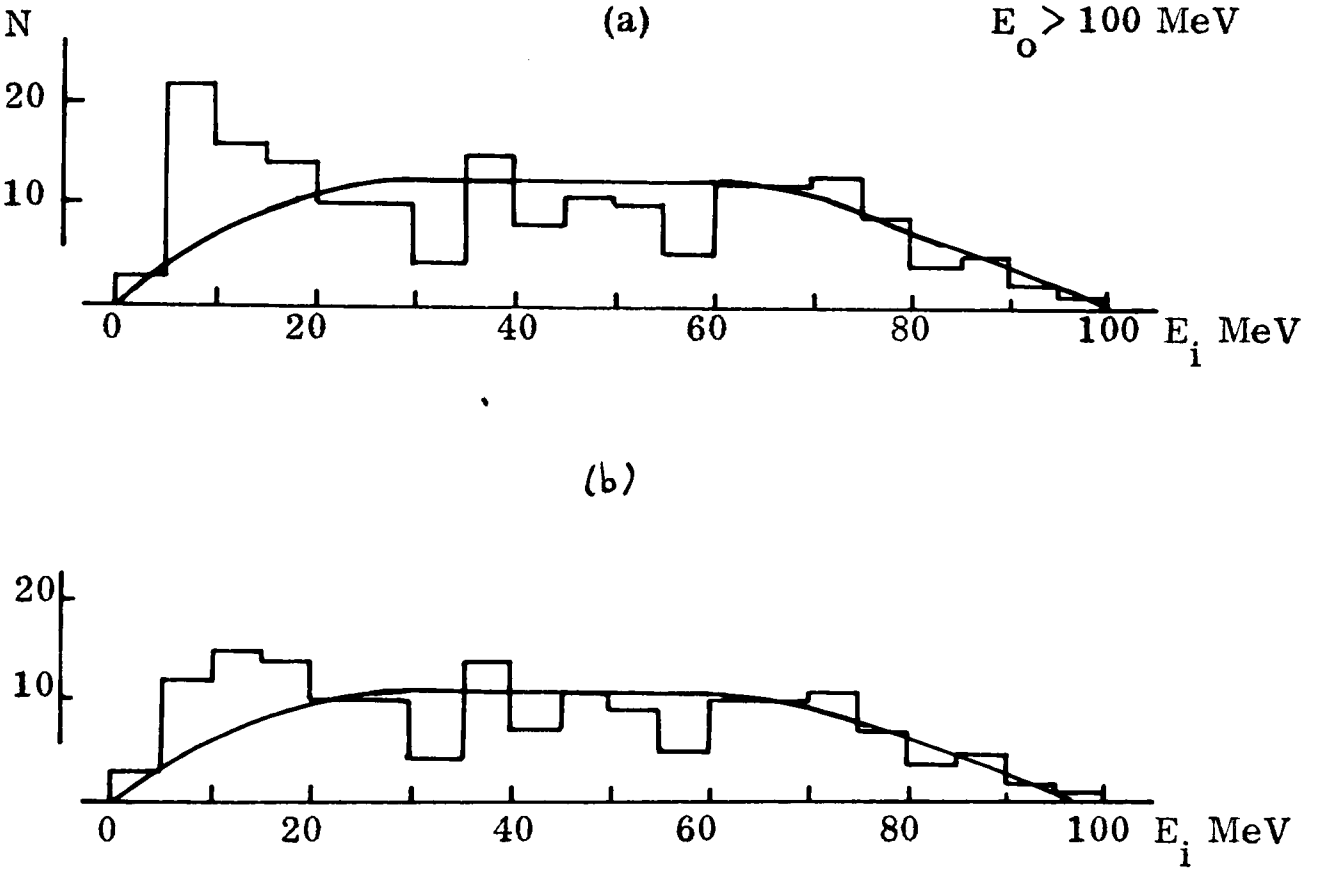

Fig. 8.18 Distributions of the product proton energies for the excited events compared with those for the ground state events (curves).

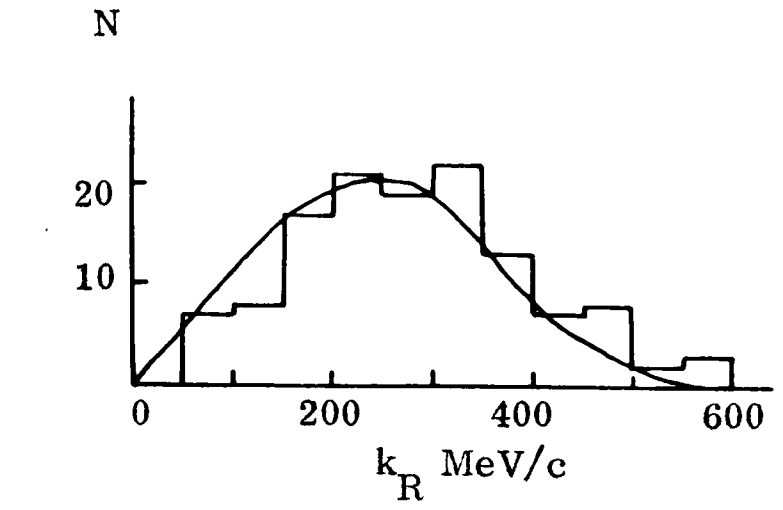

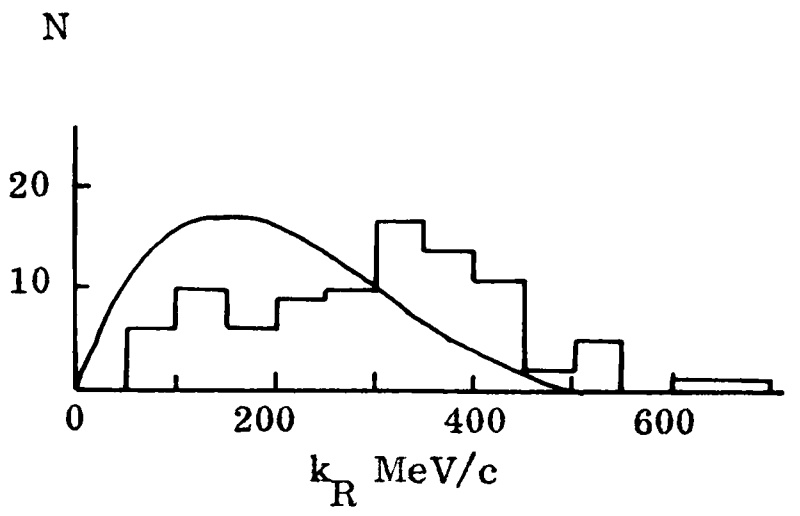

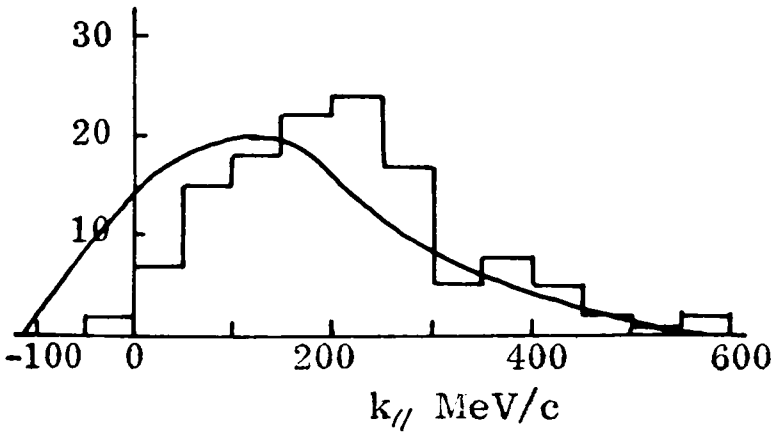

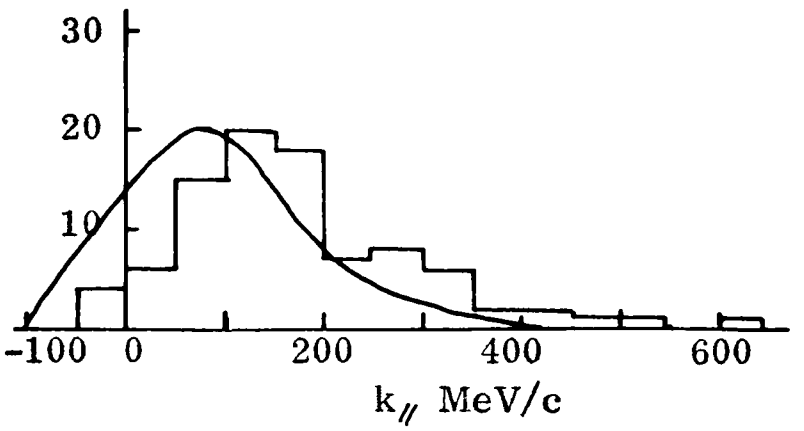

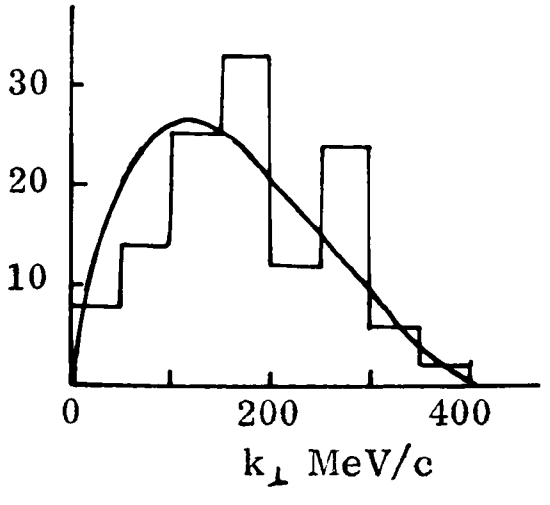

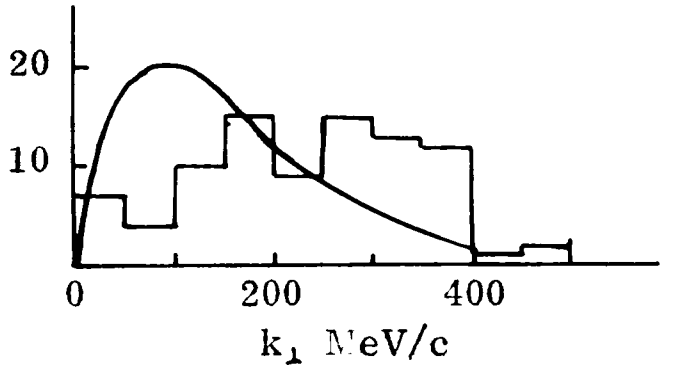

Fig. 8.19 The distributions of the recoil nucleus momentum and its components for the excited state events compared with those for the ground state events (curves).

	50 MeV < E_o < 100 MeV		100 MeV < E_o < 130 MeV	
	g. st. events	ex. st. events	g. st. events	ex. st. events
$\bar{k}_R$ MeV/c	247 ± 7	284 ± 10	196 ± 6	2.5 ±10
$\bar{k}_{//}$ MeV/c	151 ± 8	2?1 ± 10	92 ± 6	168 ± 8
$\bar{k}_{\perp}$ MeV/c	158 ± 7	178 ± 8	157 ± 6	234 ±15

the errors are the standard errors on the means

It was seen in section 8.2 that, because of kinematical limitations, the recoil nucleus momentum distribution is a distorted version of the nucleon momentum distribution and that the degree of distortion depends upon the relative momenta of the incident and target nucleons. For incident proton energies of 80 MeV and 115 MeV, the upper limits to the target nucleon momenta that can be observed in the parallel and perpendicular directions are approximately as follows:

	$k_{// max}$	$k_{// max}$
80 MeV	105 MeV/c	280 MeV/c
115 MeV	150 MeV/c	370 MeV/c

These phase space limits are shown in figure 8.2? in relation to the relevant components of the p-shell harmonic oscillator nucleon momentum distribution. It is evident that the phase space limitations have a marked distorting effect on $k_{//}$ because they forbid the observation of a large part of the total nucleon momentum distribution in the parallel direction; the effect is significantly different in the different incident energy regions. However, because

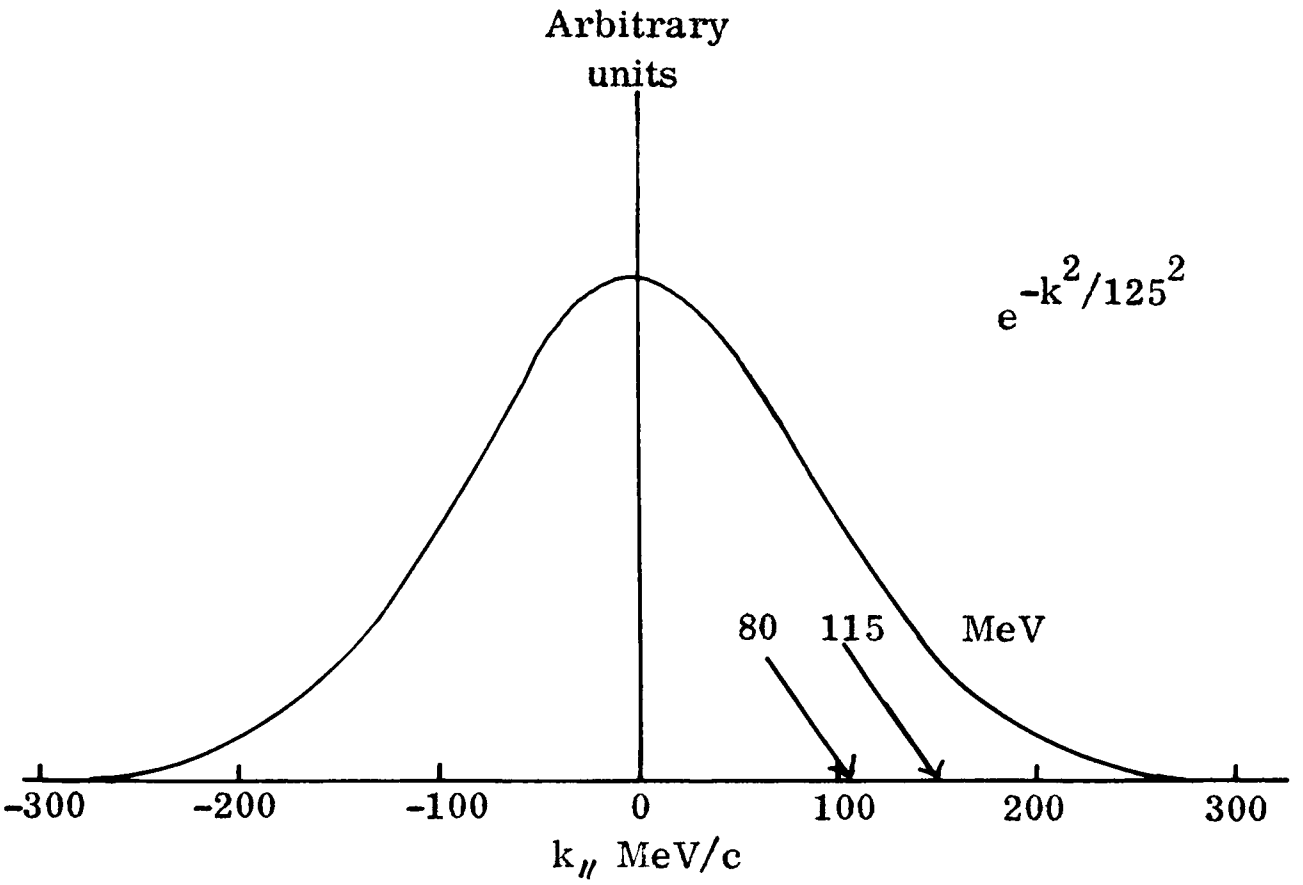

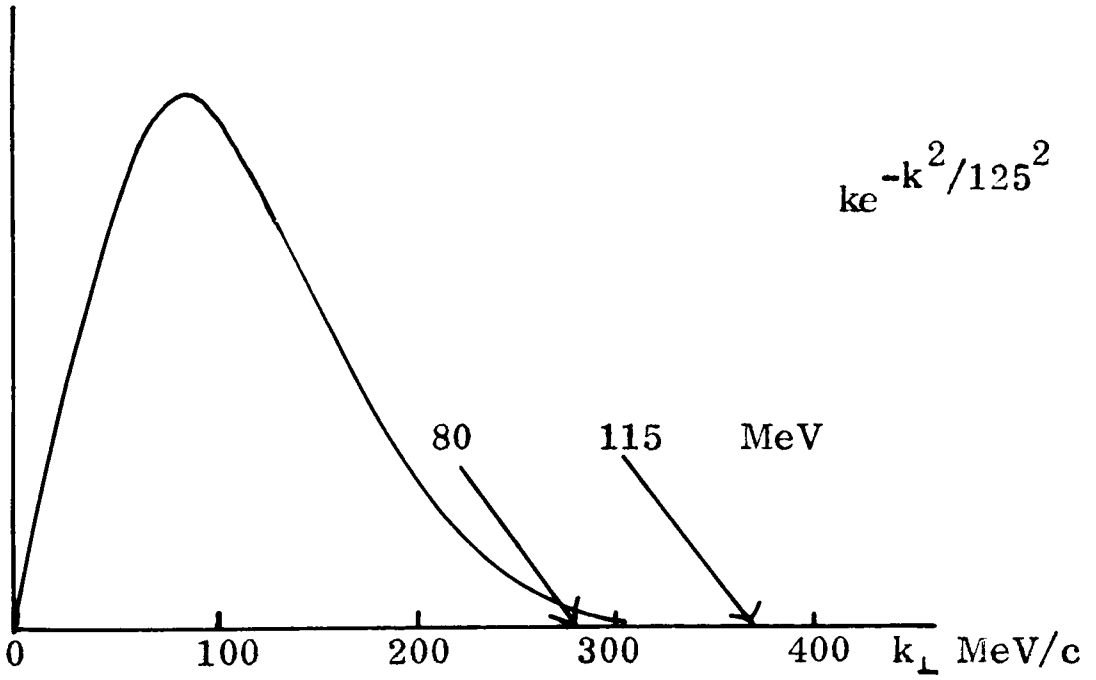

Fig. 8.20 The curves show the two components of an oscillator potential momentum distribution and the arrows show the upper limits of the available phase space for reactions initiated by 80 MeV protons and 115 MeV protons.

the phase space limitations on $k_\perp$ lie above the highest momenta that occur in the perpendicular nucleon momentum distribution, the distorting effects for $k_\perp$ are likely to be very much less than those for $k_{//}$. In fact, referring to the figures for the ground state events given in the table, it can be seen that there is no difference in $\bar{k}_\perp$ for the two regions of incident energy. It is concluded that phase space effects do not introduce significant energy-dependent effects for this component of the recoil nucleus momentum.

From the table it can be seen that $\bar{k}_\perp$ is significantly larger for the excited state events than it is for the ground state events and that the difference increases as the incident energy increases; the energy dependence is shown in more detail in figure 8.21, the results from the ground state events are shown for comparison in figure 8.22. It follows, therefore, that, quite apart from phase space effects, reactions leading to B^{11} excited states involve, on average, a larger transfer of momentum to the residual nucleus than reactions leading to the B^{11} g.s. In figure 8.23, the mean energy-loss for the events in the energy-loss range 21 MeV to 30 MeV is shown as a function of the incident energy. There is no systematic change in $\bar{E}_L$ with E_o, indicating that the $E_o, \bar{k}_\perp$ correlation of figure 8.21 does not reflect any change in the relative feeding of excited states as the incident energy changes.

In summary, the experimental results for the excited state events and for the ground state events are different in three ways:

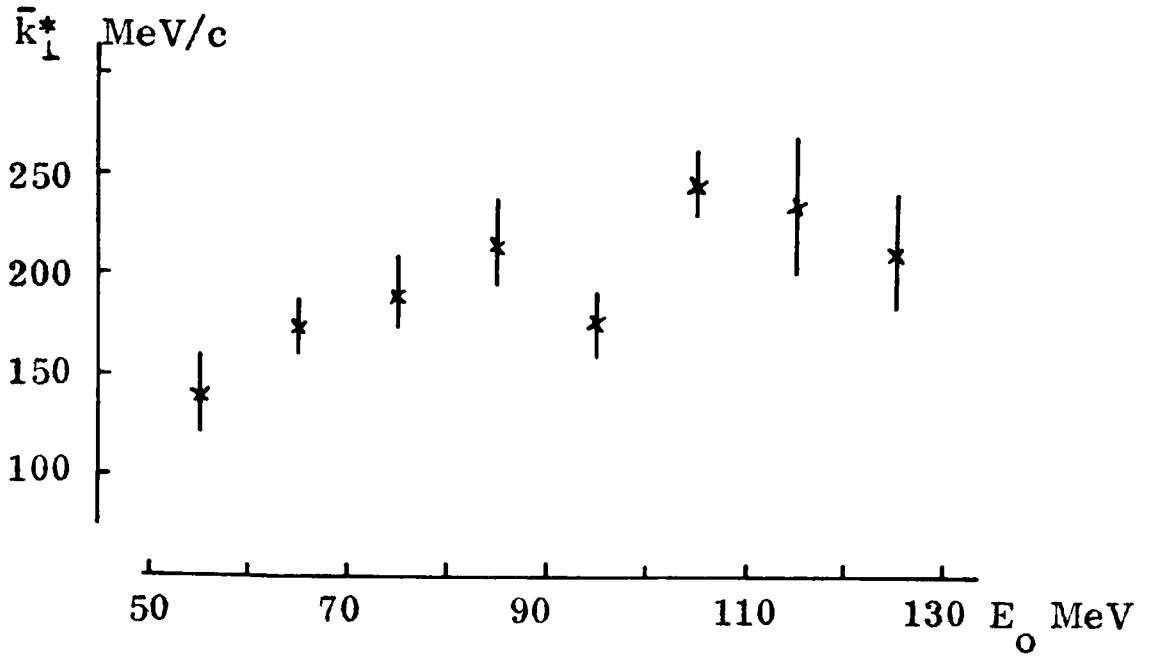

Fig. 8.21 Dependence of the perpendicular component of the recoil nucleus momentum on the incident proton energy for the excited state events.

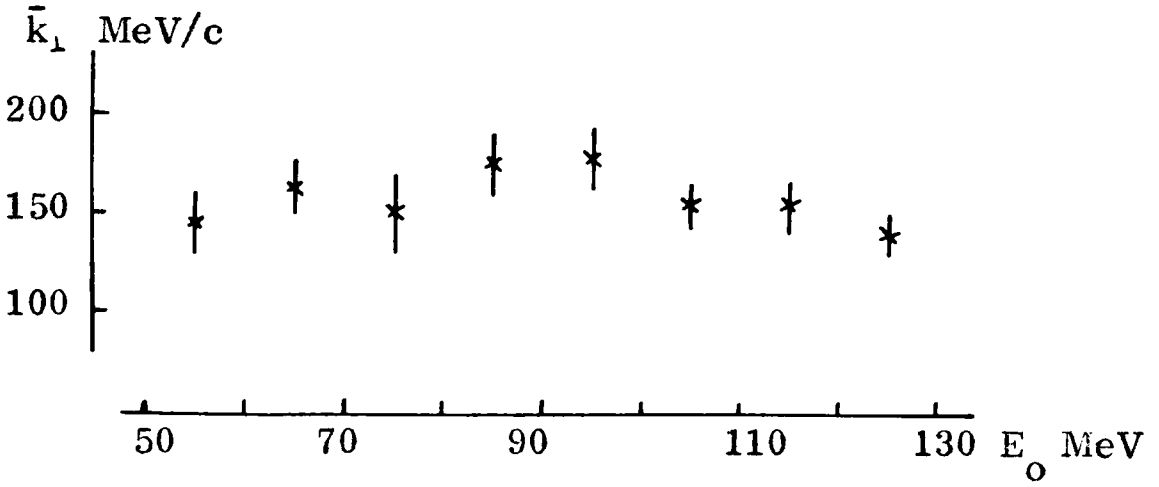

and Fig. 8.22, for the ground state events.

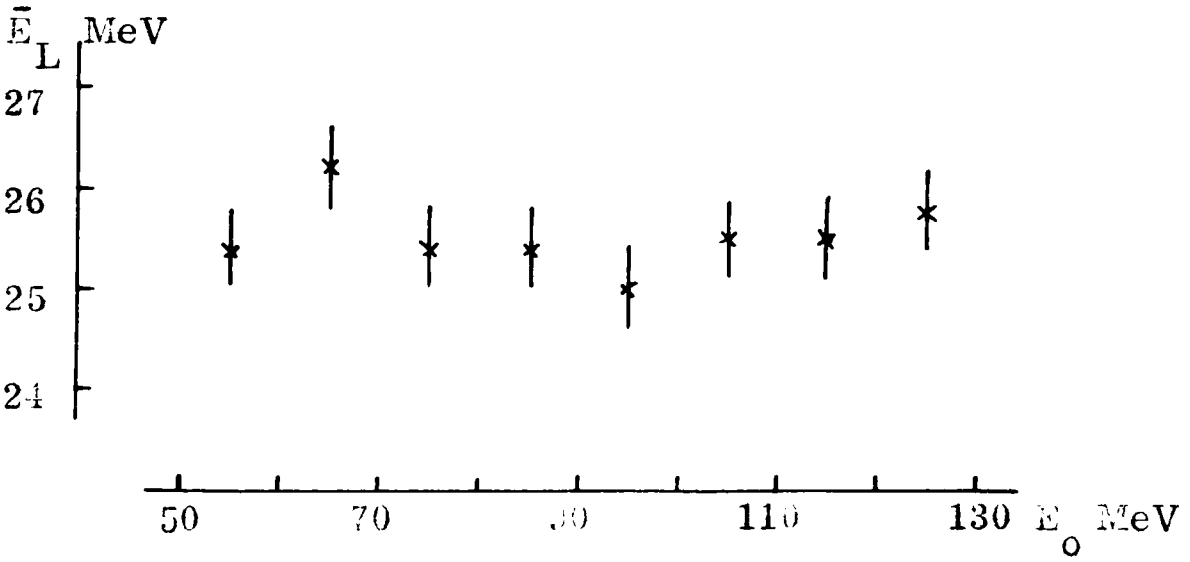

Fig. 8.23 Mean energy-loss for the excited state events as a function of the incident energy.

(a) in the spectrum of emitted protons,

(b) in the energy dependence of the production cross-section, and

(c) in the recoil nucleus momentum distribution.

The compatibility of these results with each of the three possible reaction mechanisms listed on page 110 is investigated below.

(i) $C^{12}(p,p')C^{12*}$; $C^{12*} \rightarrow B^{11} + p$

The energy distribution of evaporated protons from light nuclei is sharply peaked at low energies. Typically, the results of ZHDANOV & FEDOTOV (1960) show that for protons evaporated from C^{12} (and lighter cascade products) the energy distribution peaks in the region of 2 MeV and then falls off rapidly, reaching less than 10% of the peak probability at 10 MeV. Because of the very low detection efficiency for protons of energies below 10 MeV in the present experiment, only a very small proportion of events from the hypothesized mechanism would be seen.≠ However, it seems likely that the low energy protons observed for the excited state events in excess of those expected from the quasi-elastic reaction are due to this reaction.

If these low energy protons arise from evaporation, they must be isotropically distributed with respect to the centre of mass of the recoiling C^{12} nucleus. To test this, the component of the centre of mass proton momentum

---

≠ Only $C^{12}(p,p')C^{12*}$ reactions leading to C^{12}_{11} excited states above approx 28 MeV can contribute to the production of B^{11} excited states above 7 MeV: binding energy = 16 MeV; excitation energy ≥ 7 MeV; proton energy ≥ 5 MeV. (The giant dipole excitation in the region of 20 MeV cannot contribute.)

after components are subtracted to allow for the knock-out ($\gamma, 2p$) reaction which had been previously assumed to be thrown into the forward hemisphere,

in the direction of the incident proton was calculated for all protons of energy less than 2[illegible] MeV (including those for events that also fit a heavy particle reaction hypothesis).

$$k_{c.m.//} = k_1\cos\theta_1 - \frac{1}{12}(k_o - k_2\cos\theta_2)$$

subindex 1 refers to the low energy proton

The results for various proton energy ranges are shown in figure 8.24. The forward to backward ratios (F/B), ~~after isotropic components are subtracted to allow for the (p,p') components~~ (see opposite), are 11/11, 14/14, and 15/13, for protons of energies less than 10 MeV, 15 MeV, and 20 MeV respectively. Although the statistics are poor, the results definitely point to the isotropy of the low energy protons and, assuming that the same result applies for the events with $E_o < 100$ MeV, it is concluded that approximately 15% of the excited state events are consistent with the hypothesized reaction.

The momentum result is not significantly altered by the removal of the events with low proton energies.

(ii) Initial and final state interactions

Inelastic proton scattering reactions involving energy transfers to the nucleus of up to 14 MeV will give rise to excited state events in the region under examination. Since (p,p') reactions have cross-sections that increase with decreasing energy and since there are twice as many product protons as incident protons, final state interactions will be much more important than initial state interactions. SQUIRES (1959) has given evidence from neutron polarization experiments to support the existence of such final state interactions. The

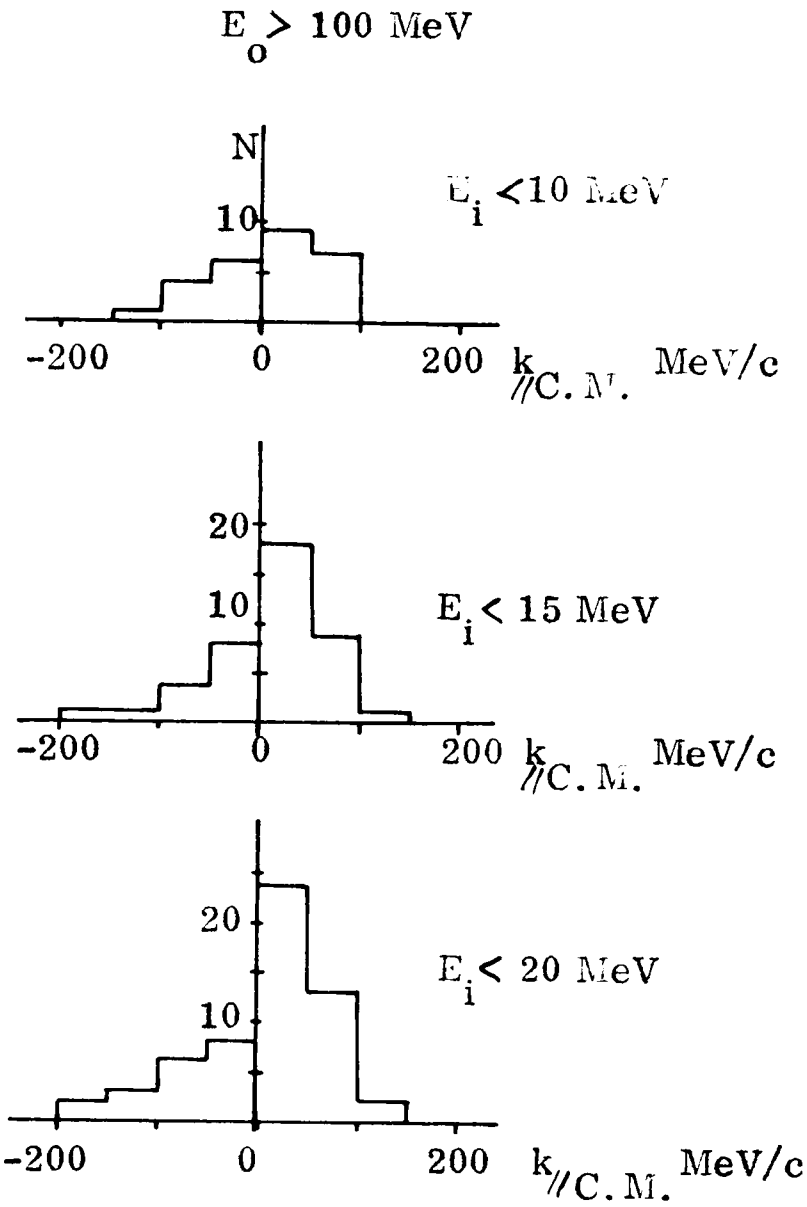

Fig. 8.24 The parallel component of the momentum of the lower energy proton in the centre of mass of the recoiling C^{12} nucleus.

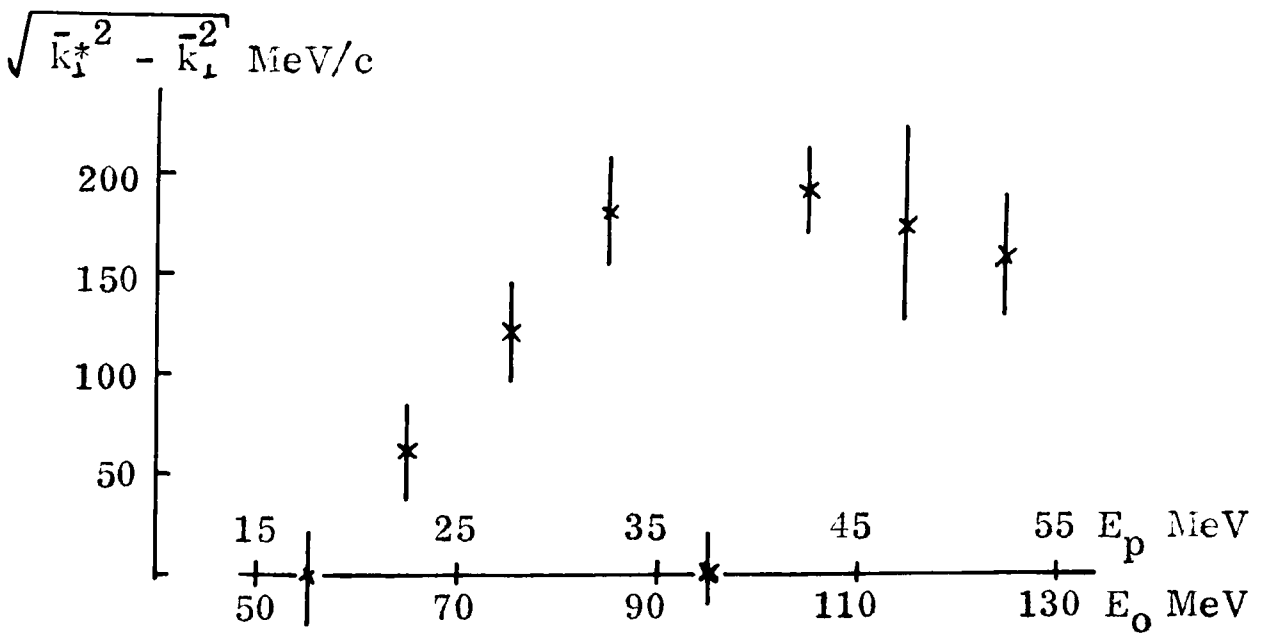

Fig. 8.25 The average additional perpendicular momentum transfer for the excited state events compared with the ground state events.

average energies of product protons from (p, 2p) reactions produced by 115 MeV and 80 MeV incident protons are approximately 47 MeV and 30 MeV respectively. Typically, DICKENS et al. (1963) report total (p, p') cross-sections at these energies[#] for the production of the states at 4.4 MeV, 7.7 MeV, 9.6 MeV, and 12.7 MeV in C^{12}, taken together, as approximately 25 mb and 31 mb. It is to be expected, therefore, that final state interactions that feed the low lying excited states of the residual B^{11} nucleus will be much more important for the events with $E_o < 100$ MeV than for those with $E_o > 100$ MeV. The measured production cross-sections for the excited state events are therefore in qualitative agreement with the final state interaction hypothesis.

With reference to the momentum distribution result, the second interaction will, on average, transfer additional momentum to the nucleus and the distribution will "leak out" into the available phase space. The final state interaction hypothesis therefore leads to the expectation of a recoil nucleus momentum distribution shifted to higher momenta than those of the distribution due to the clean knock-out (p, 2p) reactions. The shift should increase as the incident energy increases. The observed results (figures 8.19 and 8.21) are in qualitative agreement with the hypothesis.

Quantitatively, however, there is a difficulty. If the average additional momentum transfer in each incident energy region is taken to be $(\bar{k}_\perp^{*2} - \bar{k}_\perp^2)^{\frac{1}{2}}$, where $\bar{k}_\perp^*$ is the mean momentum transfer for the excited state events, then

---

[#] The result quoted for 47 MeV was obtained by extrapolating from 52 MeV.

taking the values from figures 8.21 and 8.22 it appears that the additional momentum transfer approaches zero at 50 MeV incident energy; i.e. at an average final state energy of 15 MeV (see figure 8.25). If this is the case (and points below 50 MeV would be necessary to verify the result with the present statistics), it is not easy to understand this result in terms of final state interactions.

(iii) Direct knock-out reactions involving correlated nucleons

It is more difficult to assess the results in terms of this mechanism because very little is known about nucleon correlations in nuclear matter; CLEGG (1963) and GOTTFRIED (1963) have pointed out some of the difficulties associated with gaining such information.

A brief discussion on the departure of nuclear ground states from pure shell model configurations has been given in section 1.4. GOSWAMI & PAL (1963) (referred to below as GP) have suggested that 35% of the C^{12} ground state intensity can be accounted for by 2 particle - 2 hole configurations other than the intermediate coupling configurations, and AUSTIN et al. (1962) proposed admixtures of the configurations $(1p)^7(1f2p)^1$ and $(1p)^6(1d2s)^2$ into the pure shell model configuration $(1p)^8$ as a possible explanation for the production of the low lying bound excited states of B^{11} observed by them (see section 1.4).

From the present experimental results:

$$\frac{\text{no. of excited state events with } E^* < 14 \text{ MeV}^{\#}}{\text{no. of ground state events}} \sim 0.5 \pm 0.1$$

---

excluding the events consistent with the mechanism $C^{12}(p,p')C^{12*}$; $C^{12*} \rightarrow B^{11} + p$.

From GP's result:

$$\frac{\text{intensity of admixed states}}{\text{intensity of pure shell model state}} \sim 2.55$$

Since, in the $p + C^{12}$ reaction, the admixed states can be responsible for higher excited states of B^{11} than those included above and also for two nucleon knock-out reactions etc., the experimental ratio of excited state events to ground state events is probably larger than can be explained by the GP admixture alone. This is not surprising in view of the fact that final state interactions must account for some events. Nevertheless, if the GP result is valid, it is evident that a large proportion of the excited state events could be produced by the direct reaction mechanism.

BRUECKNER et al (1956) laid emphasis upon the fact that the departure of the ground state from the $(1p)^8$ configuration introduced a high momentum component into the nucleon momentum distribution within the nucleus. It was pointed out by GOTTFRIED (see section 1.4) that in order to observe the high momenta experimentally, the incoming nucleon must have a suitably short wavelength and that the maximum observable momentum increases as the wavelength decreases.

If the de Broglie wavelength of the incident proton is $\lambda\!\!\!^{-}$, the interaction between the incident proton and the target proton is localized to the extent of this wavelength and it follows from the Uncertainty Principle that momenta up to a maximum of $\hbar/\lambda\!\!\!^{-}$ can be observed. Absolute values of the maximum momentum observable at a given energy cannot be obtained reliably in this way

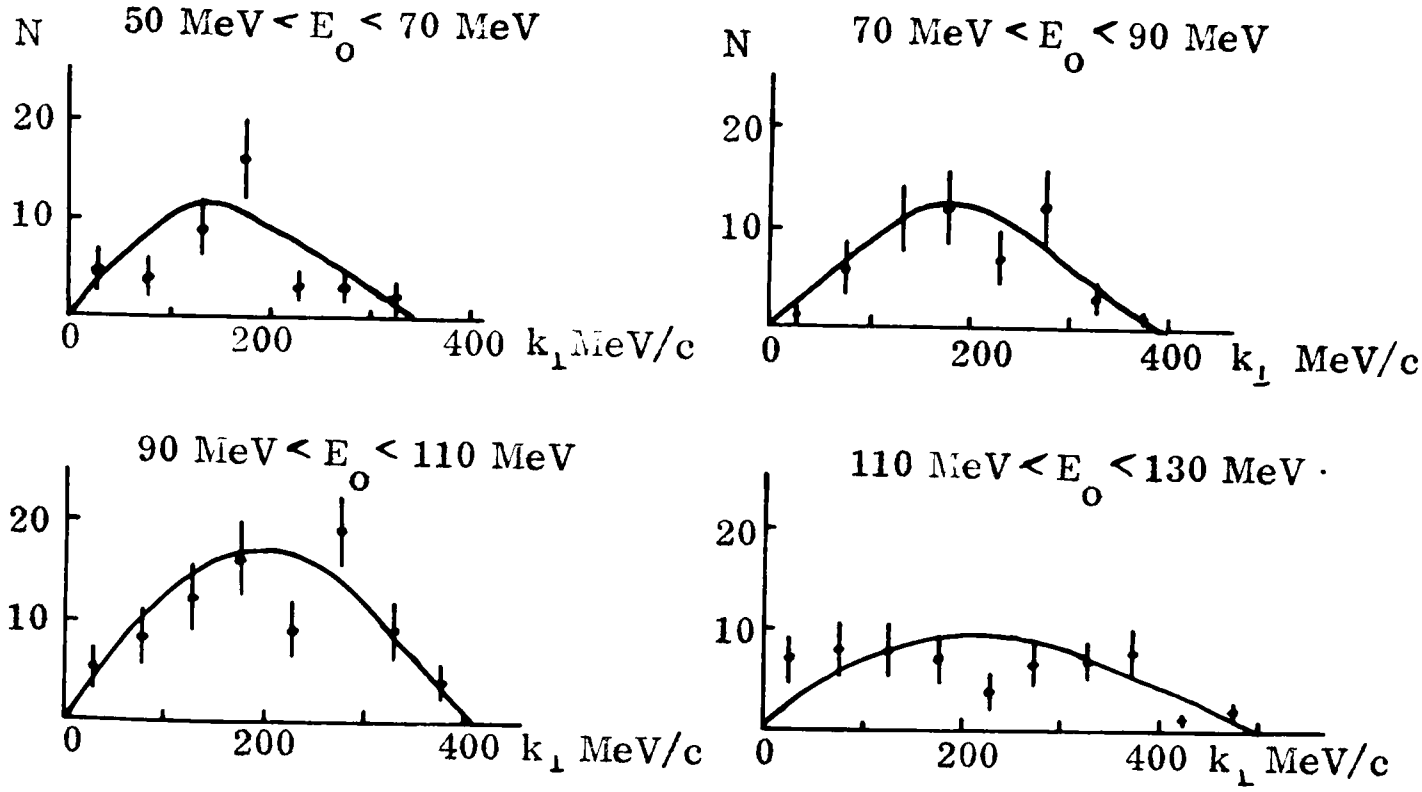

The curves show the fits to the points.

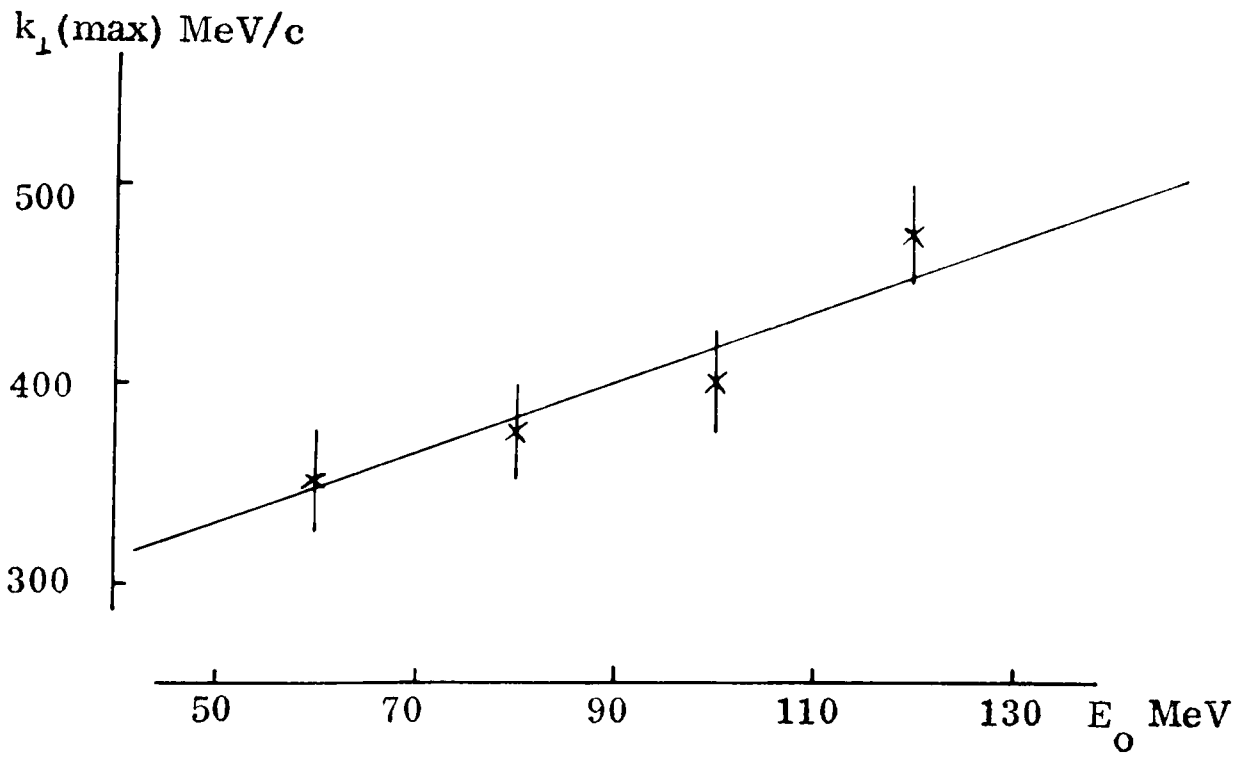

Fig. 8.26 Dependence of the maximum recoil nucleus momentum on the incident proton energy for the excited state events.

section; this could account for the experimental results. However, it could also be argued that since the mean recoil nucleus momentum is no different for the excited state events and the ground state events in the region of 50 MeV, then the operation of the Pauli principle will have the same effect for the excited state events and the ground state events at lower incident energies, but will have less effect at higher energies; this could lead to a cross-section increasing with incident energy in disagreement with the experimental results. Secondly, it might be argued that as the incident energy increases there is a greater tendency for both of the nucleons of the hypothesized correlated pair to be knocked out; this would suggest a reduction in the excited state cross-section as the incident energy increases, in agreement with the experimental result. On the other hand it is possible that a completely different part of the nuclear wavefunction is responsible for one nucleon knock-out and two nucleon knock-out.

In the present state of knowledge about these processes the necessary quantitative analysis is not possible and it must be concluded that the cross-section result yields no information on the validity of the hypothesized direct reaction mechanism.

8.5 Conclusion

Approximately 15% of the excited state events can be attributed to the inelastic proton scattering reaction. The remainder of the events have been shown to have properties consistent with two other reaction mechanisms and

it is not possible on the evidence available from the events analysed to determine their relative importance. However, the analysis of the 3-prong events throws some light onto the problem: the extent to which the 3-prong events can be explained by nucleon cascade reactions will reflect the importance of final state interactions and the extent to which they can be explained by the knock-out of correlated nucleon pairs will reflect the importance of the presence of nucleon correlations, with associated high momentum nucleons, within the nucleus. In chapter 10 it is shown that the 3-prong events are very well explained by nucleon cascade reactions but not by nucleon correlation reactions; it is therefore concluded that final state interactions are probably responsible for the majority of the excited state events.

CHAPTER 9

NUCLEON CASCADE MODEL

9.1 Introduction

Monte Carlo methods have been amongst the most useful tools in the analysis of reactions involving the knock-out of several nucleons from a nucleus. Some of the results from such calculations that are relevant to the present experiment have been presented in section 1.3.

However, none of the published results can be used to compare with the present experimental results, partly because they apply to nuclei of very different masses or they apply to incident nucleons of discrete and very different energies, but mainly because no distinction has been drawn between neutrons and protons; thus, for example, no (p,3p) energy-loss distributions are available.

It has been shown in section 6.4 that over 90% of the 3-prong events appear in the (p,3p) energy-loss distribution above the threshold energy for particle emission from Be^{10} - mostly well above this threshold energy. It is evident, therefore, that $C^{12}(p,3p)Be^{10}$ cannot be the correct, or at least the complete, description for the reaction. Reactions of the type $C^{12}(p,3pxn)Be^{1-x}$ (x=1,2,...) give a possible explanation for these events and, in order to assess the characteristics of the proton parts of such reactions, a cascade reaction mechanism model has been set up along the lines of the Monte Carlo methods. The purpose of the model is to calculate the (p,3p) energy-losses and the

distribution of proton energies arising from classical cascade reactions of the types (p, 3pxn) within the C^{12} nucleus.

The model is set out in detail in this chapter and the results from it are used in the next chapter.

9.2 The model

No attempt has been made to calculate the relative probabilities for the various reactions i.e. (p, 3pn), (p, 3p2n), (p, 3p3n) etc. Even in the most sophisticated Monte Carlo methods the calculation of cross-sections is particularly unsatisfactory. Each reaction is dealt with in turn and then, by comparing the calculated distributions with the experimental distributions, an upper limit can be assessed for the contribution from each reaction to the class of events under consideration.

For the purpose of this description, the reaction C^{12}(p, 3pn)Be^{9} will be taken as an example. In general, the reaction comprises a cascade part and an evaporation part. However, the simplifying assumption is made that the whole process can be described by a cascade model and it is set up in such a way as to make allowance for evaporation effects.

In the extreme classical limit, the cascade can be pictured as a series of nucleon-nucleon collisions with the nucleons having straight line trajectories between collisions and with all energy losses and transfers occurring at the collision apices. Several configuration modes for the cascade are possible for each reaction. For the (nucleon, 4 nucleon) reaction the following two modes are possible:

mode I

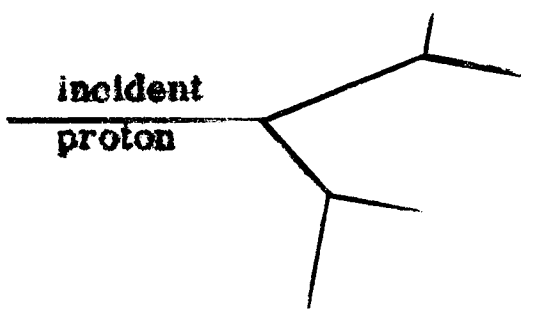

mode II

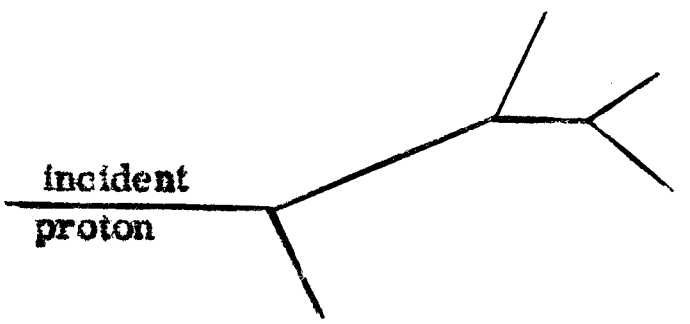

It is assumed that each collision has the properties of the free nucleon-nucleon interaction and therefore, that if an energy E is available for the two nucleons after collision, the probability p(e)de of either nucleon having an energy between e and e+de is constant in the range $0 \leq e \leq E$. The momentum of the struck nucleon is neglected when the energy sharing at each apex is considered, but an allowance is made in the energy balance for the recoiling nucleus momentum (it would not be possible to make this simplification for calculations involving angles). By choosing the total energy-loss in the cascade to be equal to the Q-value of the reaction plus the recoiling nucleus energy, the assumption is made that after all the particles have been emitted, the nucleus is left in its ground state.

A mode is chosen and the cascade is followed until the energy of each of the four product nucleons is obtained. The only restriction placed upon the energies of the nucleons participating in the cascade is that cascades producing protons of less than 5 MeV are disallowed since proton energies of less than 5 MeV are not observed in the experiment because of the limitations

of the apparatus. Although, in fact, low energy nucleons do not play an important part in the cascade phase of the reaction[≠], by including them and also by differentiating between neutrons and protons at energies below about 5 MeV, the model cascade qualitatively simulates the complete reaction (i.e. cascade + evaporation). It will be seen in figures 9.3 and 9.4 that the calculated proton spectra are, at the low energies, characteristic of evaporation spectra.

A mode II (p, 3pn) reaction will now be followed through step by step using the nomenclature of figure 9.1

At the first collision apex, the separation energy of the first target nucleon and an energy to allow for the recoiling nucleus are subtracted from the incident energy. The recoil nucleus energy is chosen randomly from the experimental recoil nucleus energy distribution which is shown in figure 9.2 (only a very small and insignificant bias is introduced by subtracting the total E_R at the first apex). $E_o - E_{s1} - E_R$ is, then, the energy available for the two nucleons leaving the apex and E_a is obtained by choosing a number at random from the range 0 to $E_o - E_{s1} - E_R$. E_a represents the first of the required

---

≠ As the energy of a cascade nucleon falls towards the energies of the nuclear nucleons, there is a rapidly increasing probability that it will be absorbed by the system to form a compound nucleus. Also, any low energy nucleons produced in the cascade cannot escape very easily through the nuclear surface; ELTON & GOMES (1957) have shown that total internal reflection severely restricts the escape of nucleons that have energies within 10 to 20 MeV of the average nuclear nucleon energy.

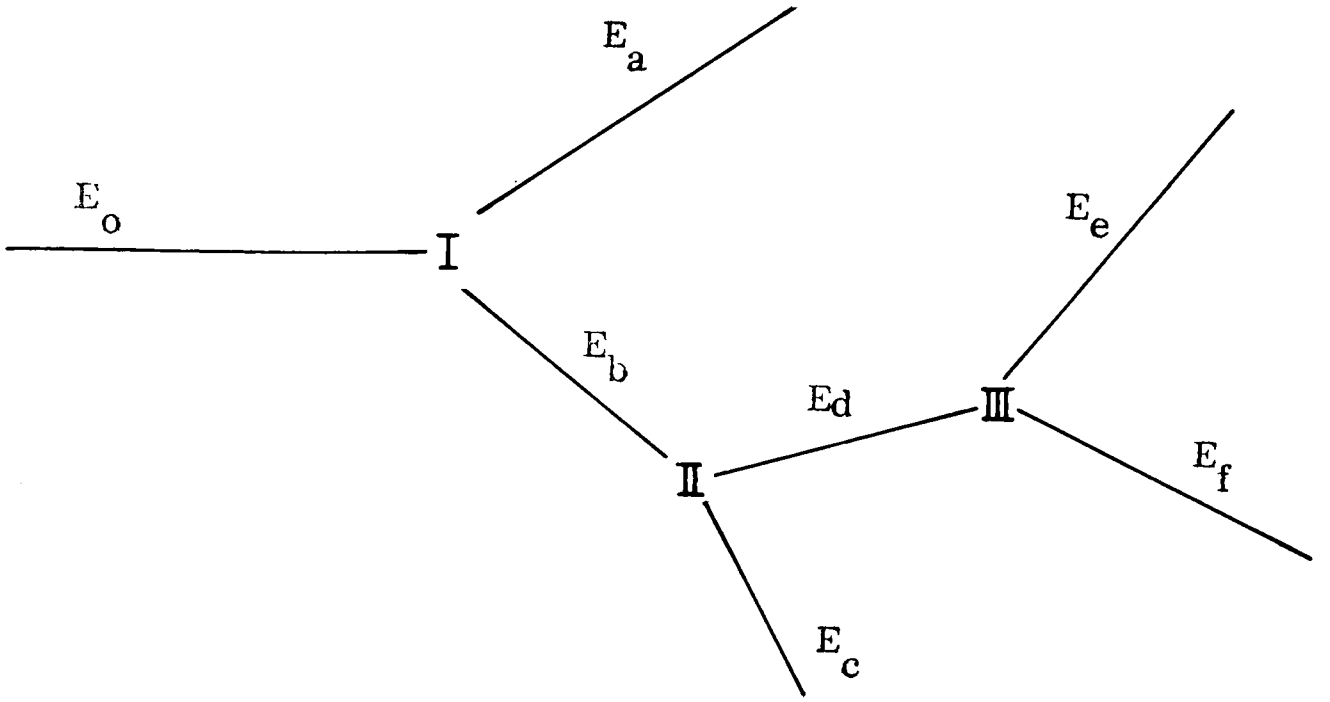

Energy available at apices:

I $E_o - E_{s1} - E_R$

II $E_b - E_{s2}$

III $E_d - E_{s3}$

$E_b = E_o - E_{s1} - E_R - E_a$

$E_d = E_b - E_{s2} - E_c$

E_o - incident energy

E_R - energy of recoil of the residual nucleus

E_{s1} - separation energy of 1st nucleon

E_{s2} - separation energy of 2nd nucleon

E_{s3} - separation energy of 3rd nucleon

Fig. 9.1 A (p,3pn) cascade.

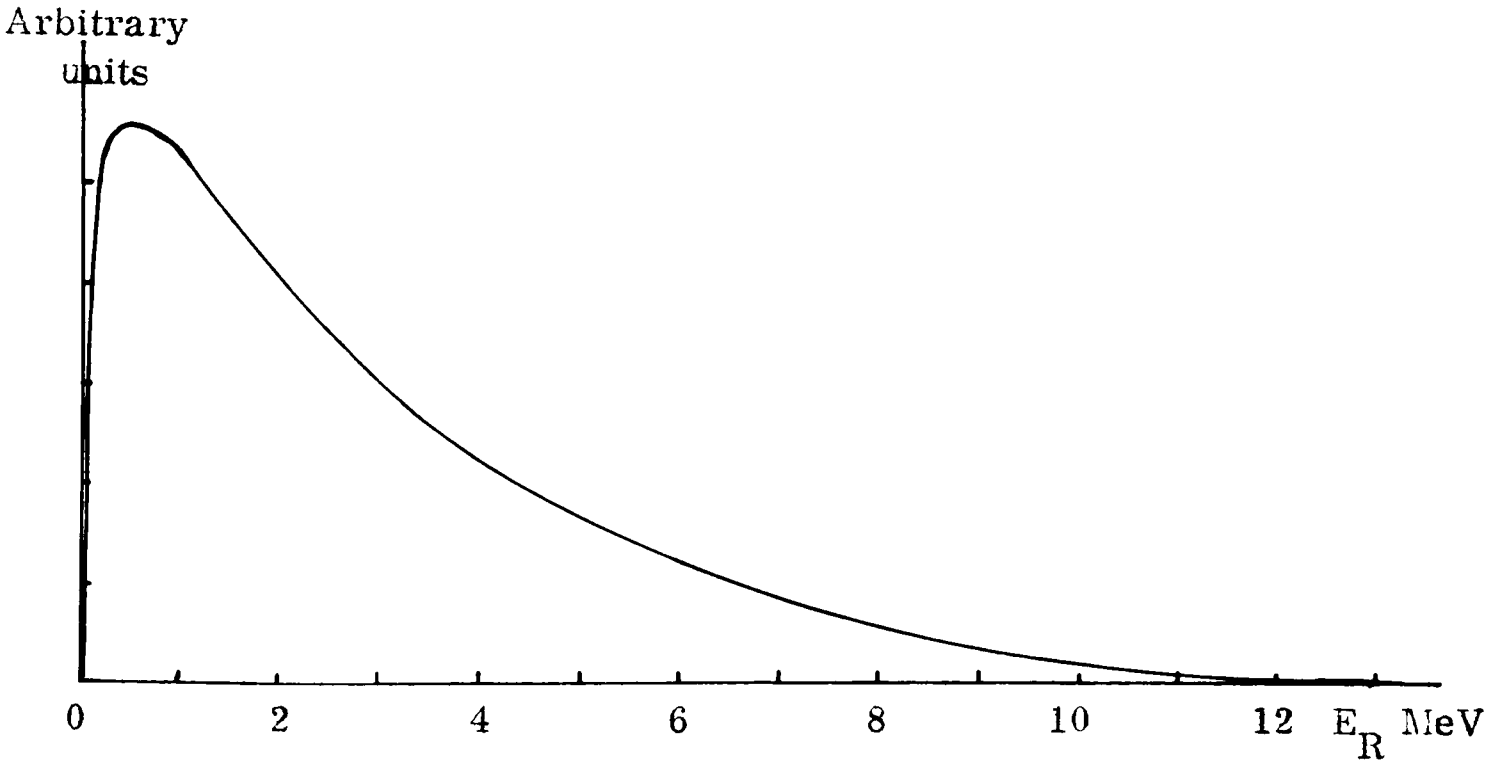

Fig. 9.2 Distribution of recoil nucleus energy.

nucleon energies because in the mode under discussion this nucleon escapes from the nucleus without further interaction.

E_b is now given by:

$$E_b = E_o - E_{s1} - E_R - E_a$$

and the energy available after the nucleon with this energy has collided is $E_b - E_{s2}$. If this is negative, the cascade is abandoned and a new one is started with the incident nucleon of energy E_o. If it is not negative, then the cascade is continued and E_c is chosen randomly from the range 0 to $E_b - E_{s2}$. E_c is the second of the required nuclear energies.

E_d is now given by:

$$E_d = E_b - E_{s2} - E_c$$

and the energy available after the third collision is $E_d - E_{s3}$. Again, if this is negative the cascade is abandoned and a new one is started with the incident nucleon. If it is not, the nucleon energy E_e is chosen randomly from the range 0 to $E_d - E_{s3}$ and the nucleon energy E_f is given by:

$$E_f = E_d - E_{s3} - E_e.$$

E_e and E_f are the two remaining required nucleon energies.

The energies of the four product nucleons are now known and it remains to associate one of these with the neutron; this is done by choosing one of them at random to be the neutron energy. The other three energies are inspected and if any one is below the chosen observational cut-off energy (approximately 8 MeV) then the event is once again abandoned and restarted with the incident nucleon. If all three proton energies are above the cut-off value, the event is finally accepted and noted.

To obtain distributions that can be compared with those obtained from the experiment a program was written for the "Mercury" computer to construct a large number of events by the procedure outlined above. Since the value of the incident energy has a direct effect on the results (e.g. the maximum (p, 3p) energy-loss possible is approx (E_o-15) MeV), the program was made to generate events from the same distribution of incident energies as was observed to give rise to those events in the (p, 3p) energy-loss distribution above the threshold energy for the reaction. After successfully following through a predetermined number of events (usually approximately twice the experimental statistics) and storing the results, histograms were printed for the following quantities in the incident energy regions $E_o > 100$ MeV and $E_o < 100$ MeV:

(i) the proton energies; E_{pi}

(ii) the (p, 3p) energy-loss; $E_o - \sum_{i=1}^{3} E_{pi} - E_R$

(iii) the ratio $\frac{E_{pMAX}}{\sum_i E_{pi}}$, and

(iv) the ratio $\frac{E_{pMIN}}{\sum_i E_{pi}}$

where E_{pMIN} is the lowest of the proton energies for the event, and E_{pMAX} is the highest.

Throughout the program, random numbers were generated from the standard "Autocode" random number routine.

9.3 Some sample results

In figure 9.3 the distributions of the above mentioned quantities, obtained

for the reaction $C^{12}(p,3pn)Be^{9}$, are shown for incident energy protons above 100 MeV. The following details apply to these results:

(i) Configuration mode I;

(ii) E_{s1} = 16 MeV, E_{s2} = 7 MeV, and E_{s3} = 11 MeV, giving, together, the $C^{12}(p,3pn)Be^{9}$ Q-value of 34 MeV;

(iii) a proton cut-off energy of 5 MeV; and

(iv) approximately 1000 events.

A series of calculations was made to assess the effect of changes in the details of the specification given above. In figure 9.4 the (p,3p) energy-loss distributions refer to the following specifications:

(a) (i) to (iv), as above;

(b) (i), (iii) and (iv) as above, and $E_{s1} = E_{s2} = E_{s3} = 11$ MeV;

(c) Configuration mode II, and (ii) to (iv) as above;

(d) a new series of random numbers, otherwise as for (a).

The results are not greatly different for all these variants of the initial specification. The calculated distributions for the other quantities listed in section 9.2 show the same small range of variation as the energy-loss results.

The method outlined in section 9.2 can quite easily be adapted for cascades of any number of neutrons and protons. For each reaction reconstructed in this way the distribution of incident energies used is that for the events above the appropriate threshold energy in the experimental energy-loss distribution. In figure 9.5 the results for the (p,3p) energy-loss distributions calculated for the reactions (p,3pn), (p,3p2n) and (p,3p3n) are shown for events of all incident

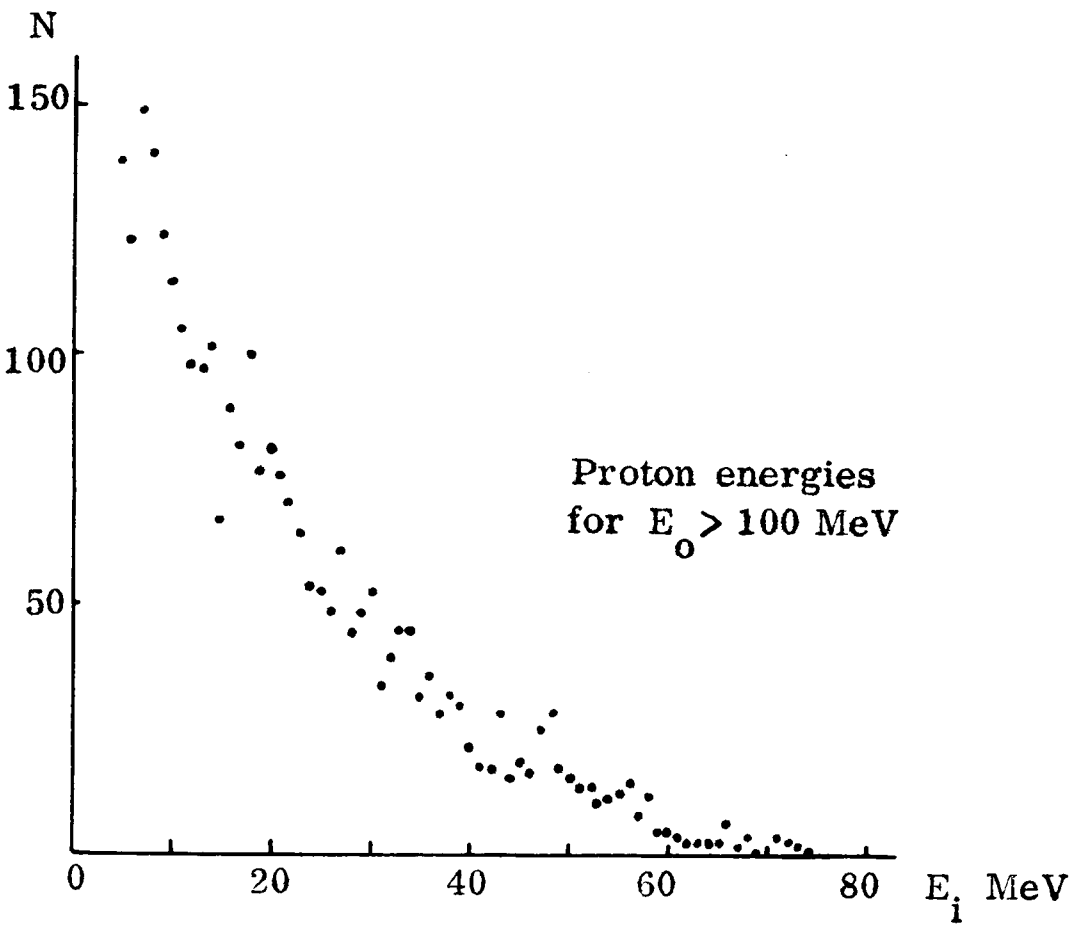

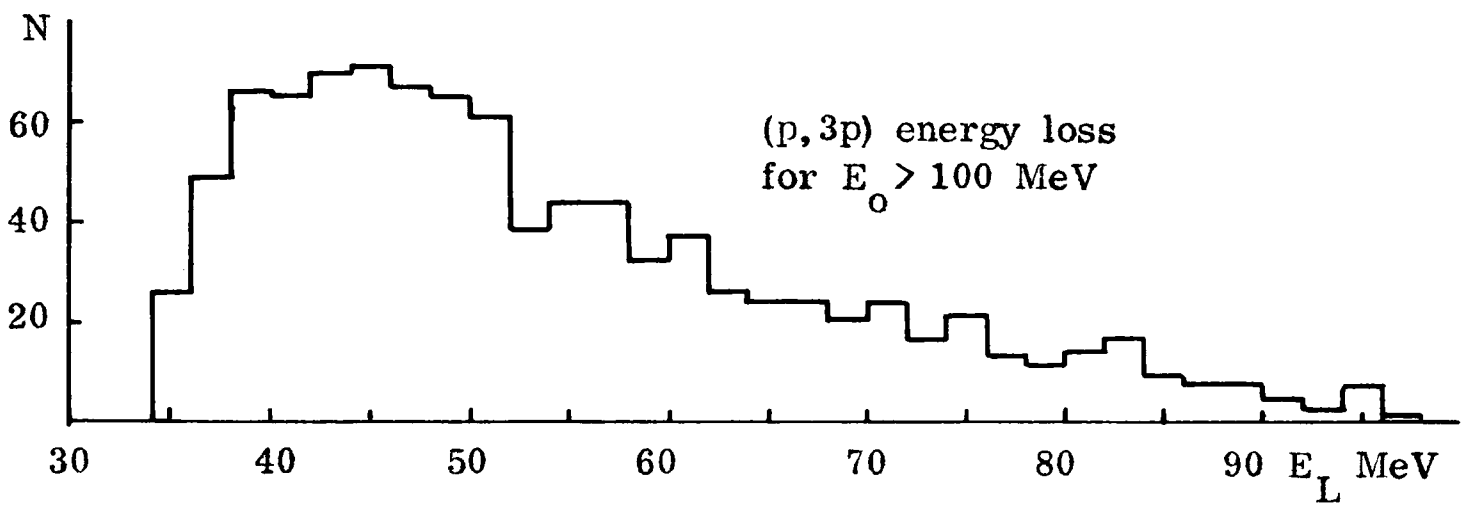

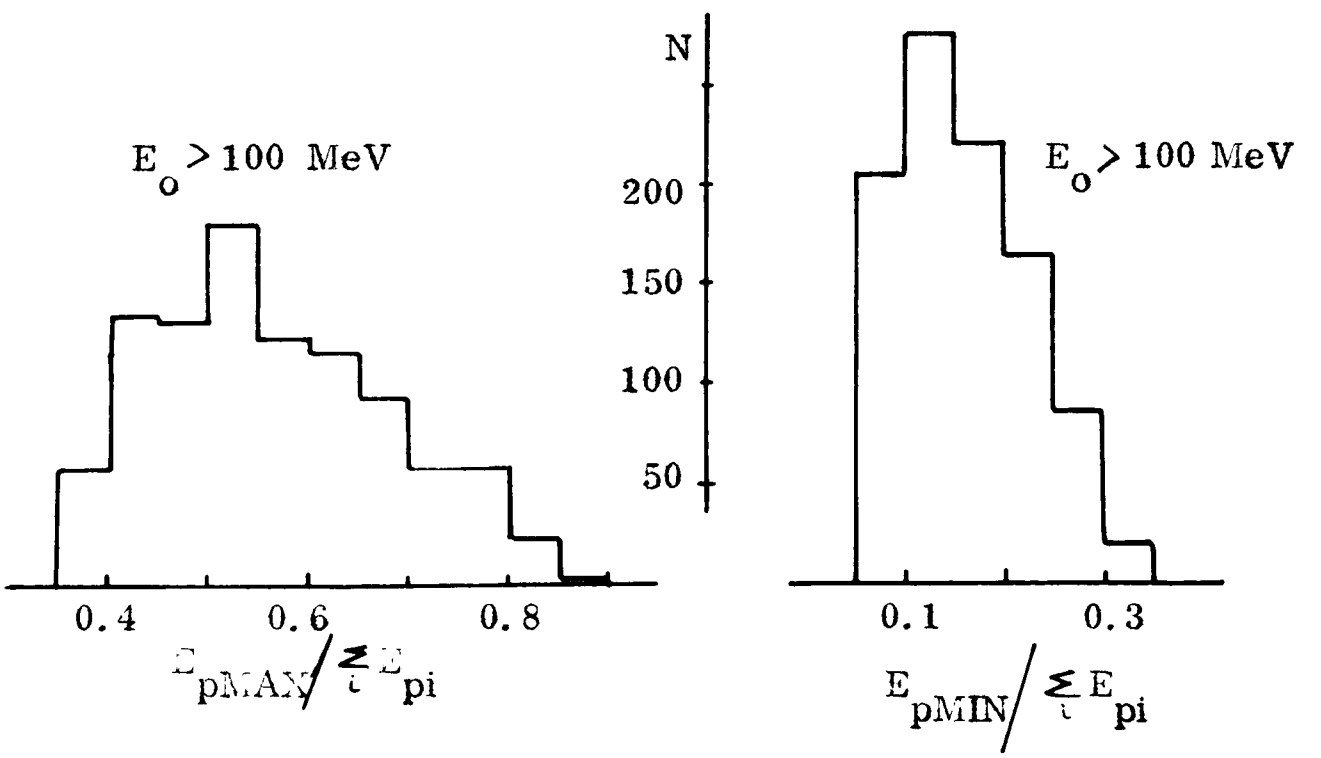

Fig. 9.3 Sample results for a (p, 3pn) cascade.

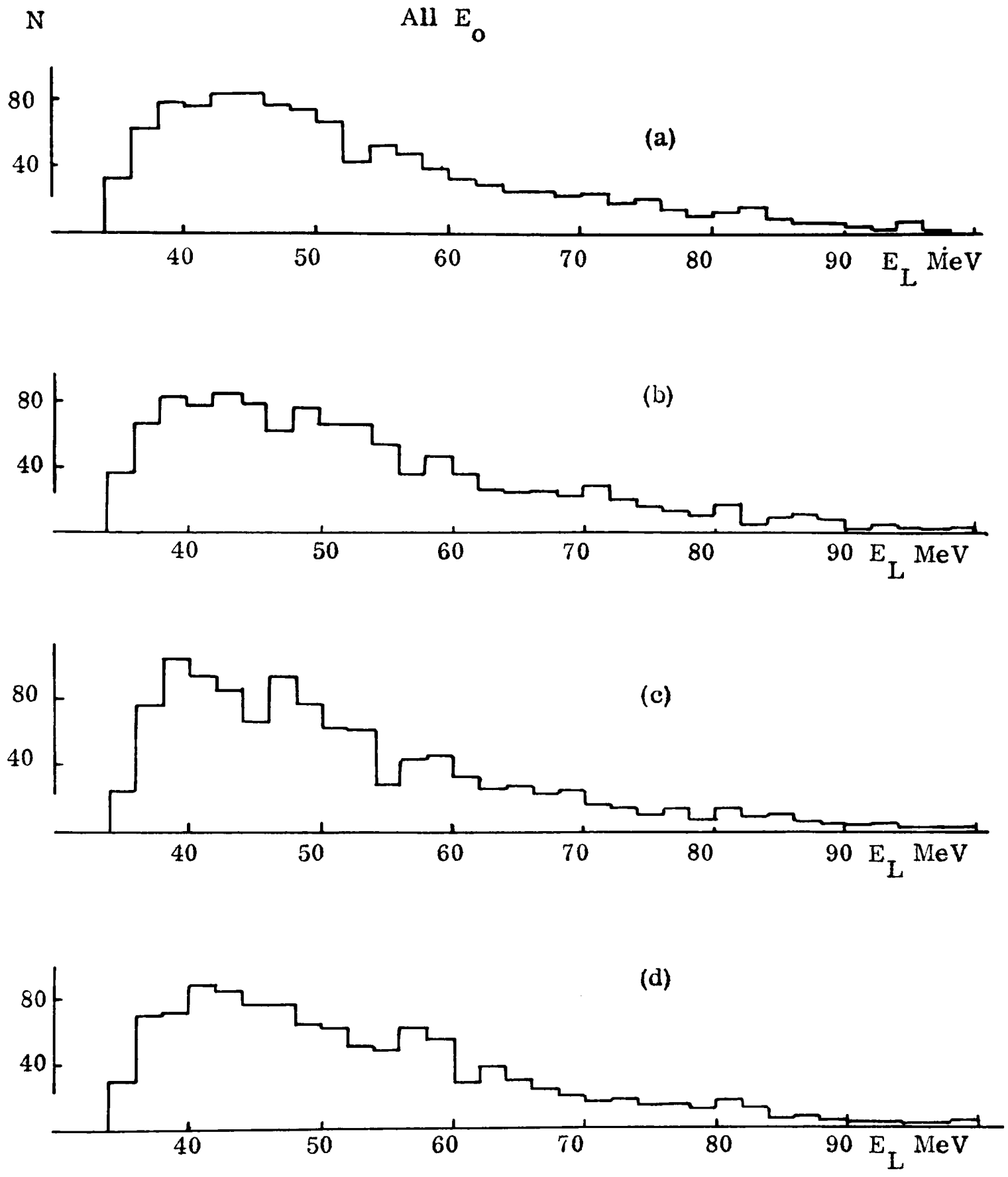

Fig. 9.4 (p,3p) energy-loss distributions for different model specifications for the (p,3pn) cascade.

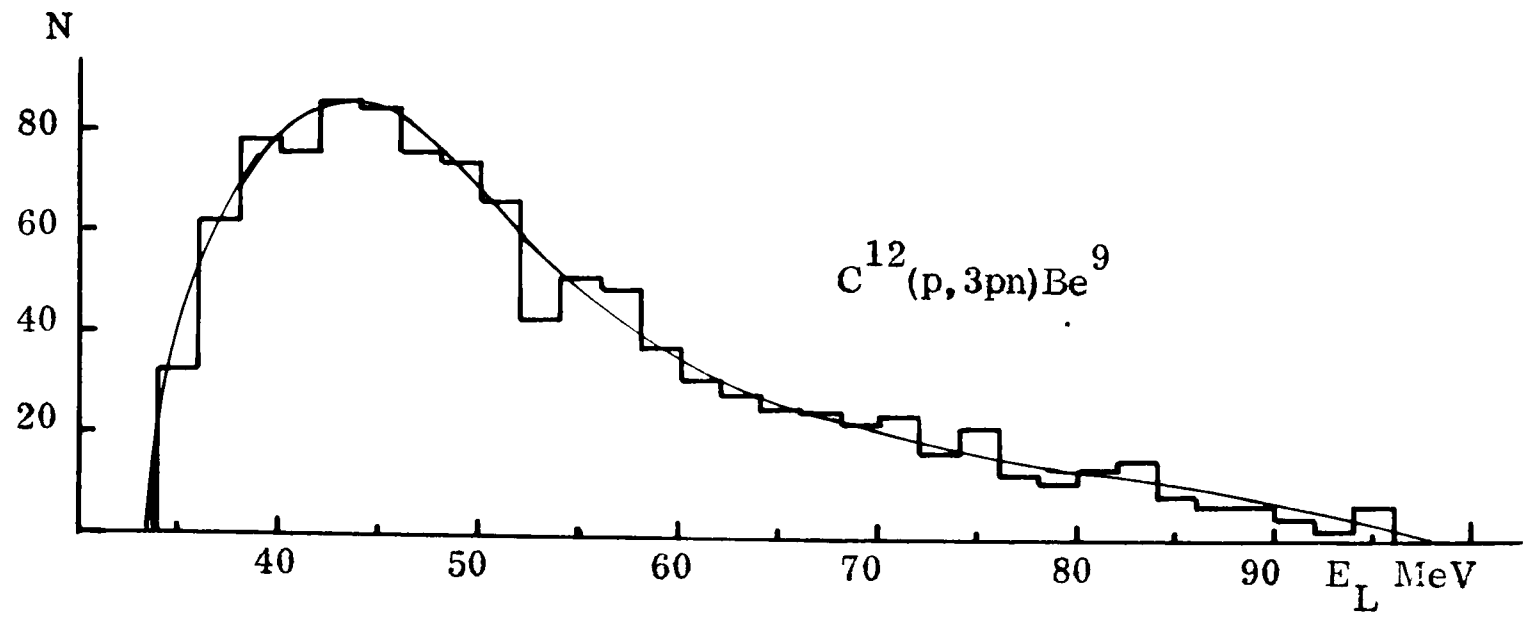

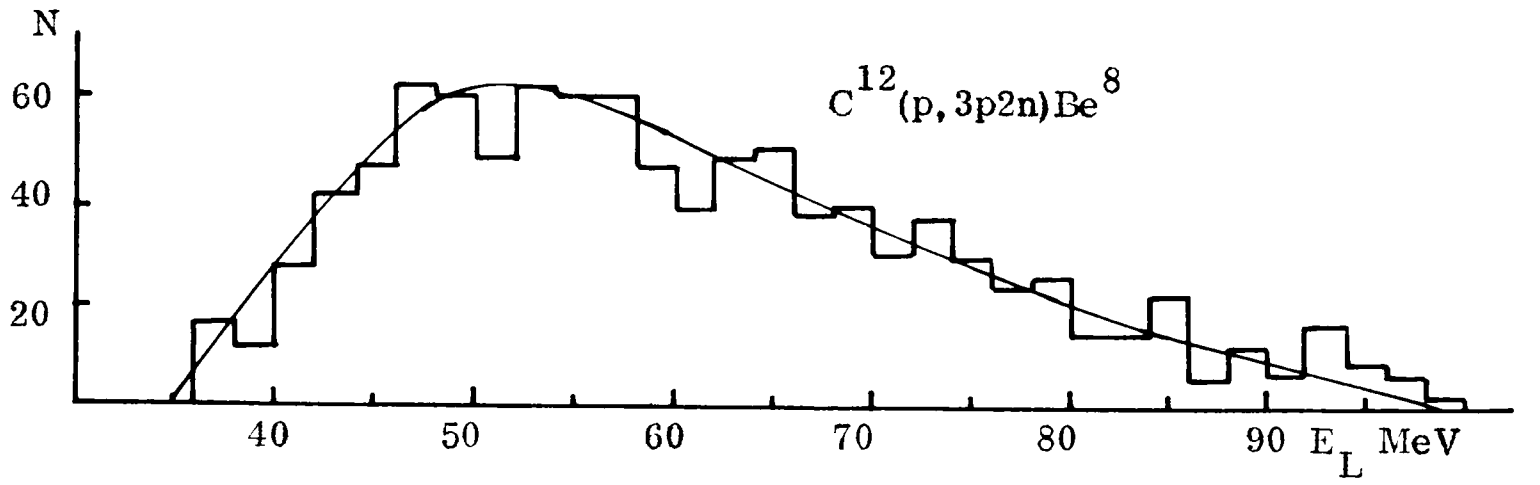

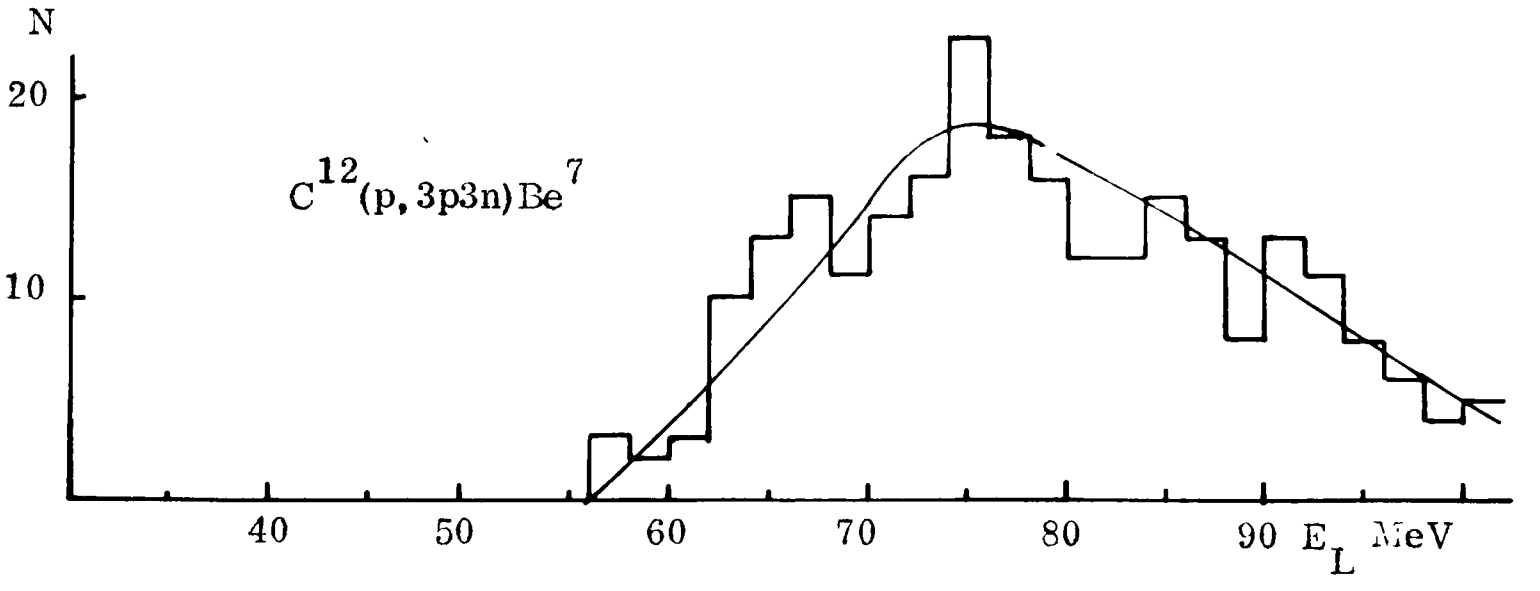

Fig. 9.5 (p, 3p) energy-loss distributions for different reactions.

energies. It is interesting to note that the results are quite different for the three reactions.

Therefore, whilst it must be emphasized that the treatment is based upon a simple model, the fact that the calculated results are sensitive to the type of reaction but insensitive to the details of the model means that they can be used usefully for a qualitative analysis of the experimental results.

CHAPTER 10

A STUDY OF THE 3-PRONG EVENTS AND SOME INFORMATION ON THE 4-PRONG EVENTS AND HIGH ENERGY-LOSS 2-PRONG EVENTS

10.1 Introduction

As pointed out in sections 6.4 and 9.1, the most noteworthy features of the results from the 3-prong events are the absence of any sharp peaks in the (p,3p) energy-loss distribution and the fairly uniform distribution of events with energy-loss from the minimum to the maximum possible values.

About 20% of the events have energy-losses of less than 40 MeV and so lie in the region of the distinct group of Be^{10} excited states known to exist within 12 MeV of the ground state. The probability that these events represent the reaction $C^{12}(p,3p)Be^{10*}$ is investigated in section 3.

For the events with higher energy-losses, two main types of explanation are possible. Firstly, that some of the observed tracks are caused by particles heavier than protons, and/or, that heavy particles are present but they have insufficient energy to be detected (α-particles in particular can be quite energetic without leaving visible tracks); these possibilities are investigated in section 4. Secondly, that energetic neutrons, which leave no tracks in the bubble chamber, are produced Two types of reaction mechanisms can be envisaged: one in which a nucleon cascade, of the type commonly used to explain reactions in much heavier nuclei, is set up, and the other, in which a correlated pair of nucleons is knocked out of the nucleus, leaving a highly excited residual

nucleus which decays by further particle emission. The first mechanism is examined in section 5 and the second in section 6.

When the clean knock-out (p, 2p) p-shell events are excluded from the (p, 2p) energy-loss distribution for the 2-prong events, the resultant distribution is similar in form to that of the (p, 3p) energy-loss distribution for the 3-prong events. The applicability of the conclusions concerning the 3-prong events to the results of the 2-prong events is considered in section 8.

Finally, in section 9, the results from the small number of 4-prong events observed are presented.

10.2 Some experimental results from the 3-prong events

Several aspects of the experimental results are presented in the subsequent sections of this chapter. Here, figures 10.1 to 10.6 are presented as a general introduction to the main features of the results. Figure 10.1 shows the correlation between the incident proton energies and the (p, 3p) energy-losses; it indicates the need for care in interpreting the data to account for the effects of the range of incident proton energies present. Figures 10.2 to 10.6 show that the events with different energy-losses do not have very different characteristics; this suggests that the same reaction mechanism, or at least very similar reaction mechanisms, account for all events. The small variations with energy-loss in the distribution of energy amongst the product particles (assumed to be protons), shown in figures 10.3 and 10.4, can be completely accounted for by the presence of the cut-off at approximately 5 MeV for the detection of protons.

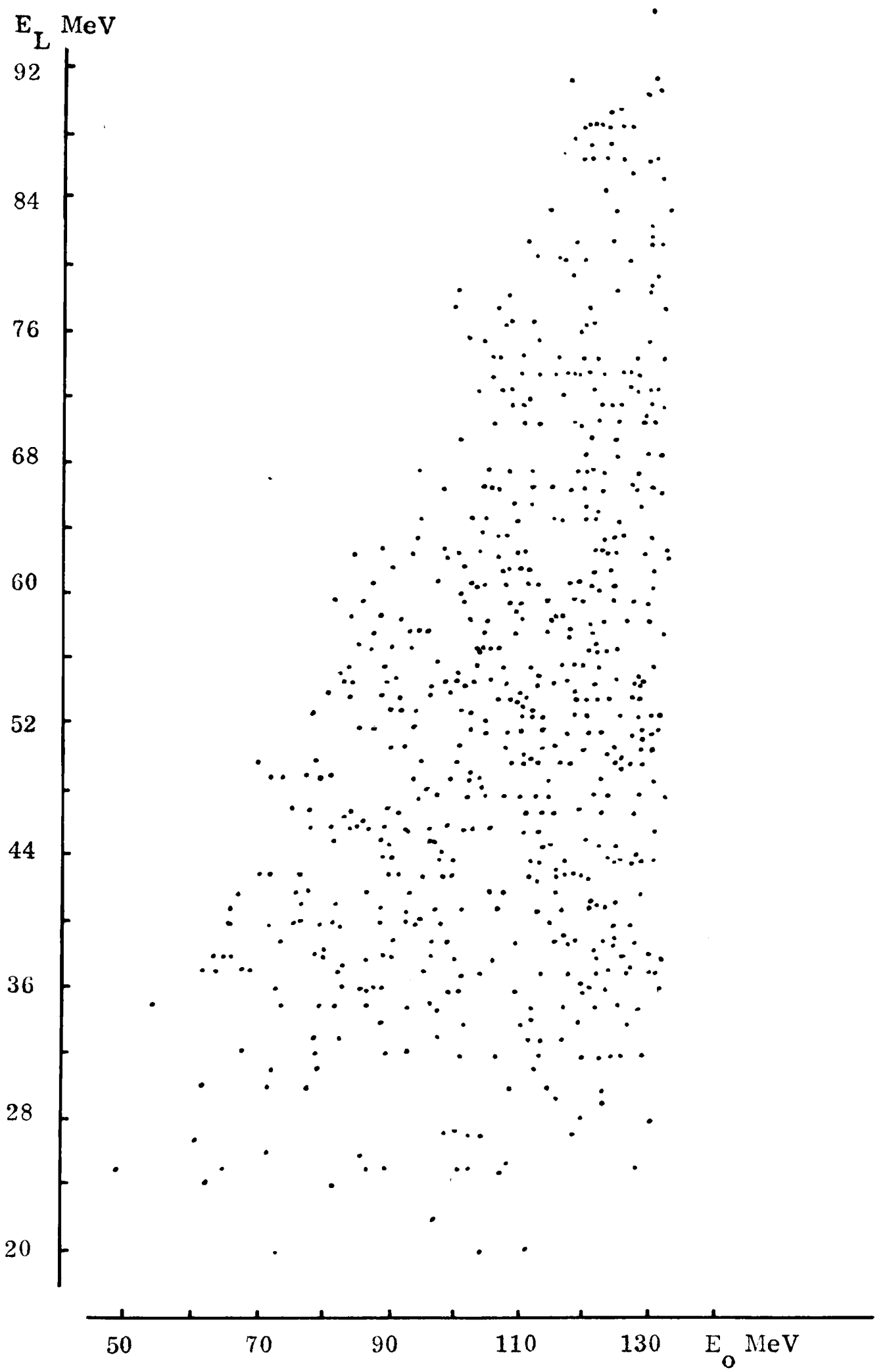

Fig. 10.1 Correlation between the incident proton energies and the (p, 3p) energy-losses.

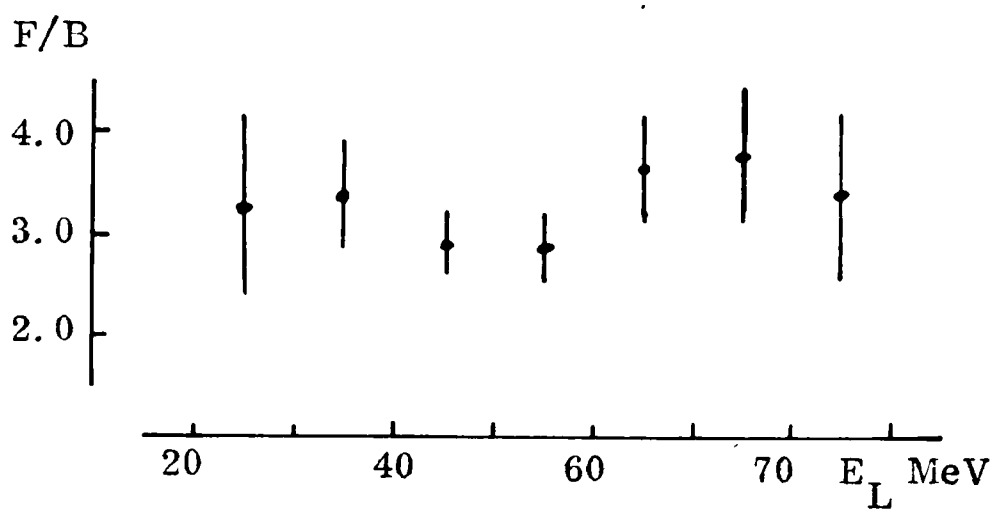

Fig. 10.2 Ratio of number of protons emitted in the forward hemisphere to the number emitted in the backward hemisphere.

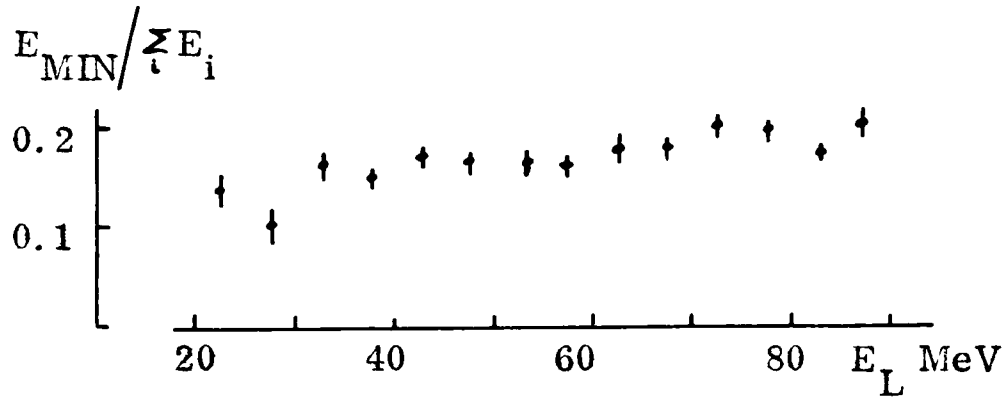

Fig. 10.3 Mean ratio of the minimum proton energy to the sum of the proton energies as a function of the incident proton energy.

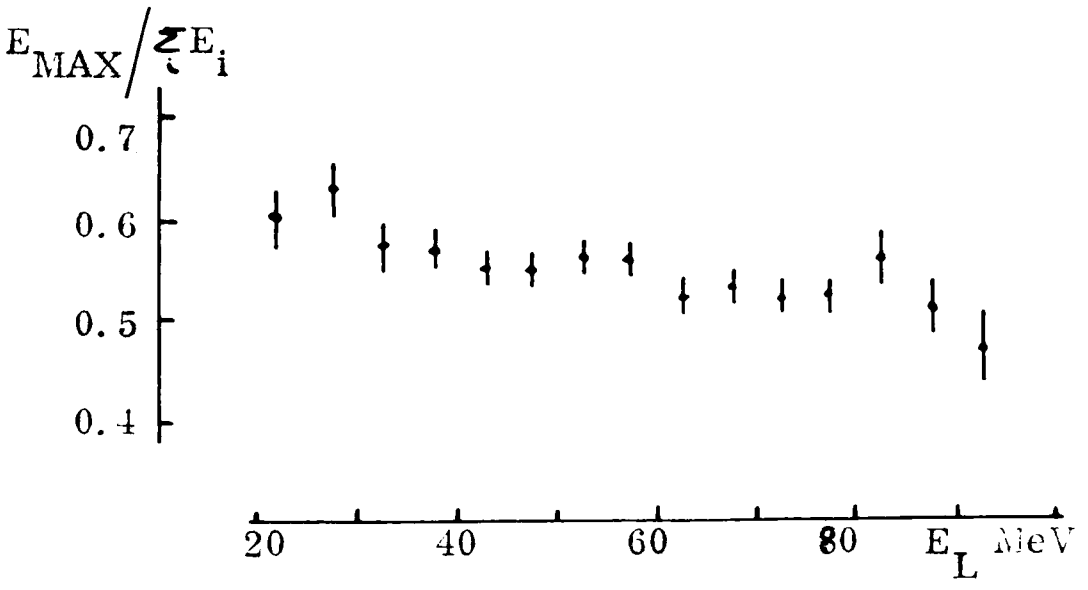

Fig. 10.4 Mean ratio of the maximum proton energy to the sum of the proton energies as a function of the incident proton energy.

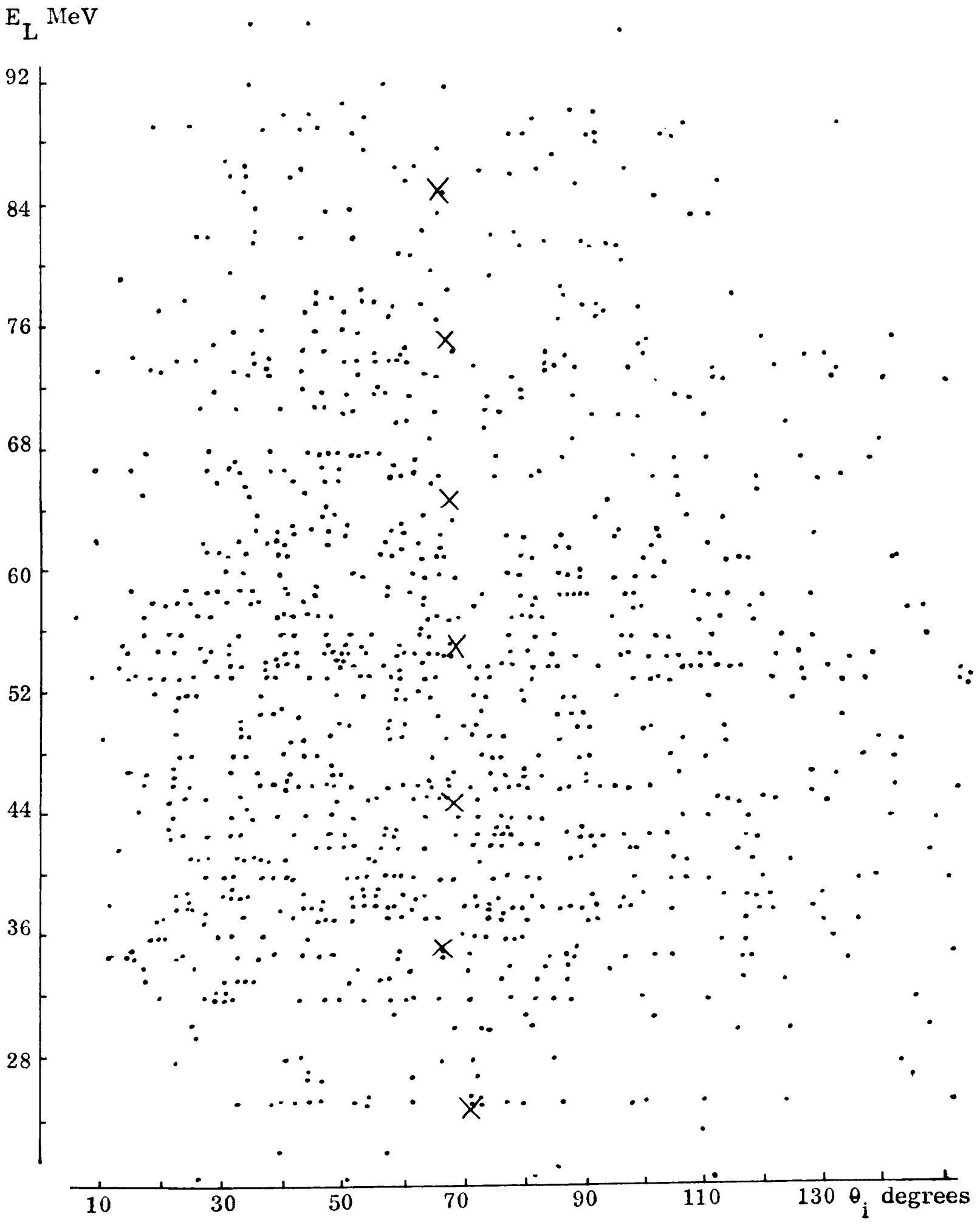

Fig. 10.5 Angles of the product protons for events of various (p, 3p) energy-losses.

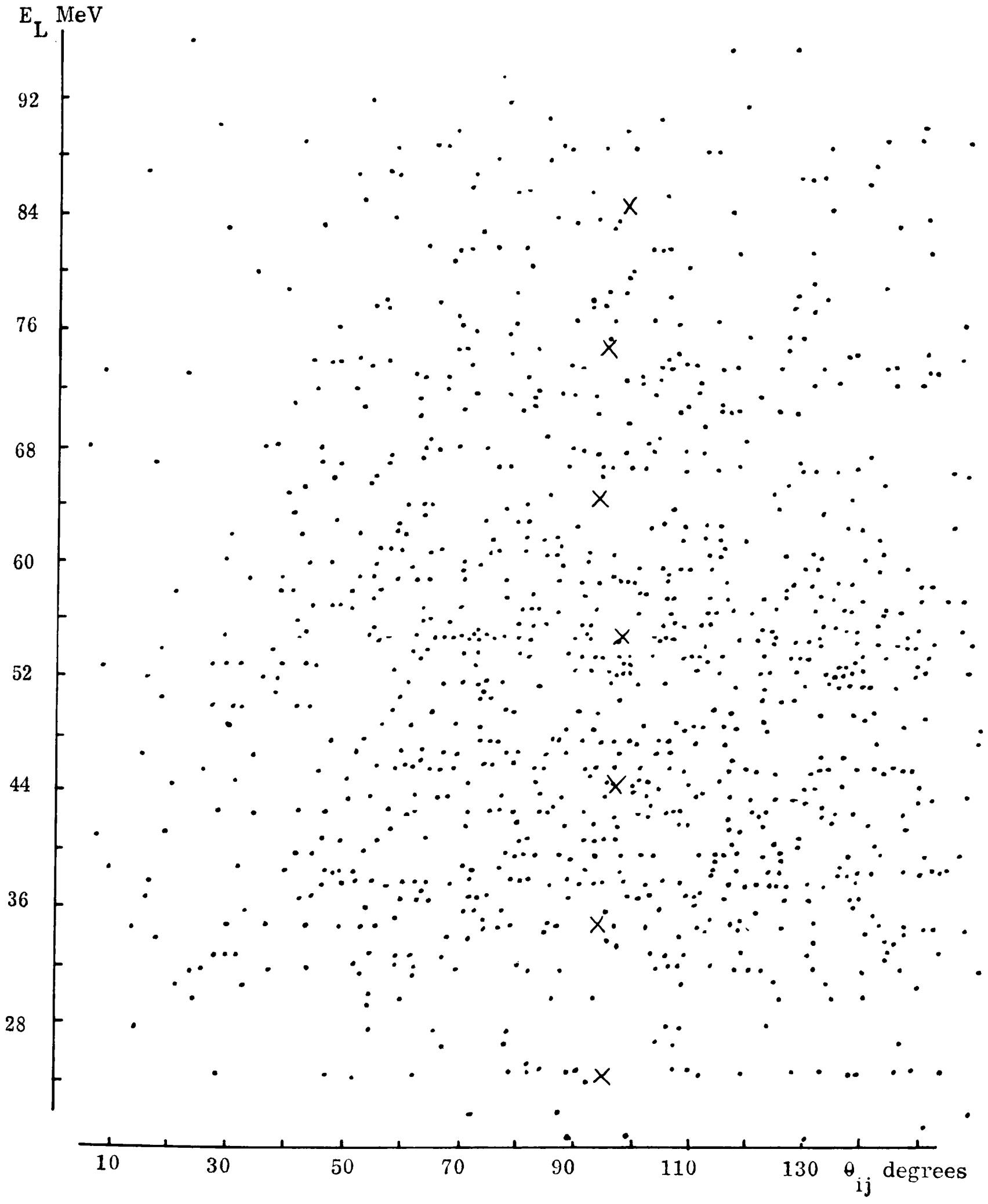

Fig. 10.6 Angles between the product protons for events of various (p, 3p) energy-losses.

In figures 10.5 and 10.6, the crosses show the mean angles for all events in each 10 MeV region of energy-loss.

It is not a practical proposition to present all aspects of the experimental results, but because there is very little experimental information available for these types of reaction in any published work, the basic information for each 3-prong event that was measured is recorded in appendix VIII; from this information each event can be reconstructed. It would be interesting to compare the predictions of a sophisticated Monte Carlo calculation with the detailed experimental results.

10.3 The reaction $C^{12}(p,3p)Be^{10}$ and the events with energy-losses below 40 MeV

Three possible reaction mechanisms can be envisaged for the (p, 3p) reaction; these are:

(i) an inelastic scatter of the incident proton, leaving the C^{12} nucleus with sufficient excitation energy for it to evaporate two protons,

(ii) a quasi-elastic (p, 2p) reaction, leaving the B^{11} nucleus with sufficient excitation energy for it to evaporate one proton, and

(iii) a cascade reaction involving only three protons.

The evidence for each of these mechanisms is examined below for the events below 40 MeV in the (p, 3p) energy-loss distribution. The possibility of events arising from the direct knock-out of a correlated pair of protons is considered separately in section 10.5.

(i) $\underline{C^{12}(p,p')C^{12*};\ C^{12*} \rightarrow Be^{10(*)} + 2p}$

For this reaction one of the protons will have an energy much greater than the other two. For example, for an incident proton with an energy of 100 MeV (which is approximately the mean incident energy for the events with energy-losses less than 40 MeV) there is approximately 60 MeV available for the kinetic energy of the three protons, after the binding energy and the energy of the recoiling nucleus have been allowed for. Assuming an upper limit of about 15 MeV for the sum of the energies of the two evaporated protons, a minimum ratio for $E_{MAX}/\Sigma E_i$ of 0.75 is obtained. The experimental value for this ratio for events with energy-losses below 40 MeV is 0.59 ± 0.02 (see figure 10.4). It is concluded from this evidence that the double evaporation reaction mechanism is not an important contributor to the low energy-loss events.

(ii) $\underline{C^{12}(p,2p)B^{11*};\ B^{11*} \rightarrow Be^{10(*)} + p}$

For this reaction the incident proton and the two protons from the initial stage of the reaction will be geometrically related to each other in a very similar way to the protons from a quasi-elastic (p,2p) reaction of the type discussed in chapter 8. Since the proton evaporated from the excited residual nucleus will, in almost all cases, have the lowest energy of the three protons, it is possible to pick out the direct knock-out part of the reaction.

In figure 10.7 the histogram shows the distribution of the angle between the two longer prongs for all the events with $E_L < 40$ MeV, and the curve, which is normalized to the number of events in the histogram, shows the results obtained for this distribution from the quasi-elastic events. The coplanarity

of the incident proton and the two longer prongs has been calculated for each event with $E_L < 40$ MeV and its distribution is shown in the histogram of figure 10.8; again the curve shows the result obtained from the quasi-elastic reaction.

In neither case does the curve give a good fit to the histogram and it is concluded that the single evaporation process is also unimportant.

(iii) $C^{12}(p, 3p)Be^{10(*)}$ by a proton cascade mechanism

This mechanism can be pictured as follows: the incident proton interacts quasi-elastically with one of the nuclear protons and one of the product protons then interacts quasi-elastically with a second nuclear proton.

It is difficult to establish criteria by which evidence for or against this mechanism can be judged. For example, it is not possible to pick out for each event which of the protons has undergone only one collision and which two come from the second collision. However, by using a model for the reaction it is possible to derive the spectrum of proton energies to be expected from a three proton cascade reaction. The model is the analytical equivalent of the statistical model outlined in chapter 9 for calculations on the more complex cascades involving neutrons; the approximations are the same.

The diagram below illustrates the (p, 3p) cascade:

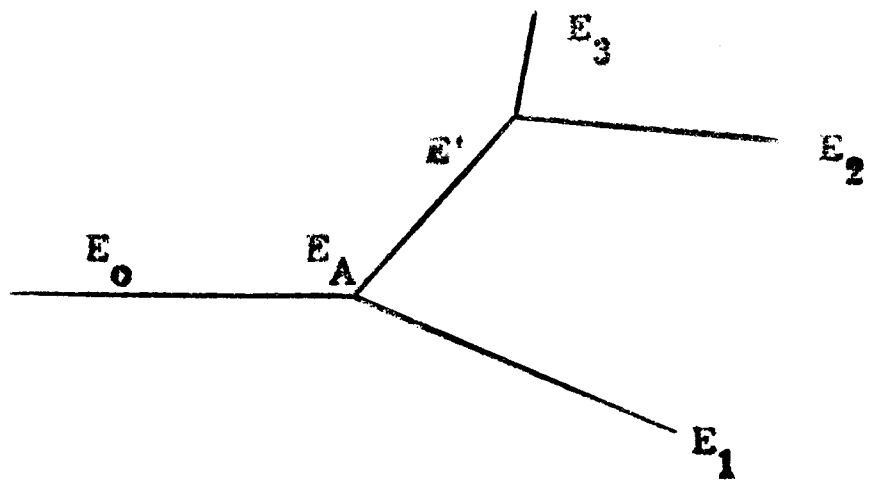

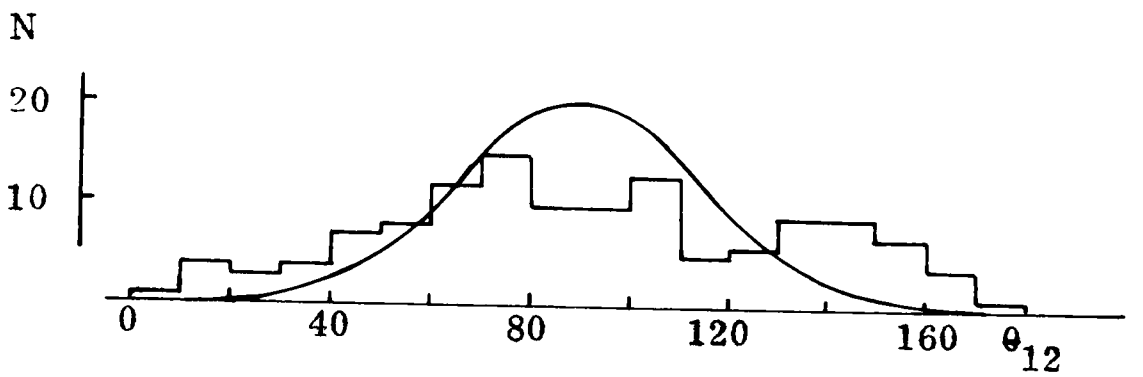

Fig. 10.7 The histogram shows the angles between the two longer prongs for events with $E_L < 40$ MeV and the curve is the distribution of the angles between the product protons for the quasi-elastic 2-prong events.

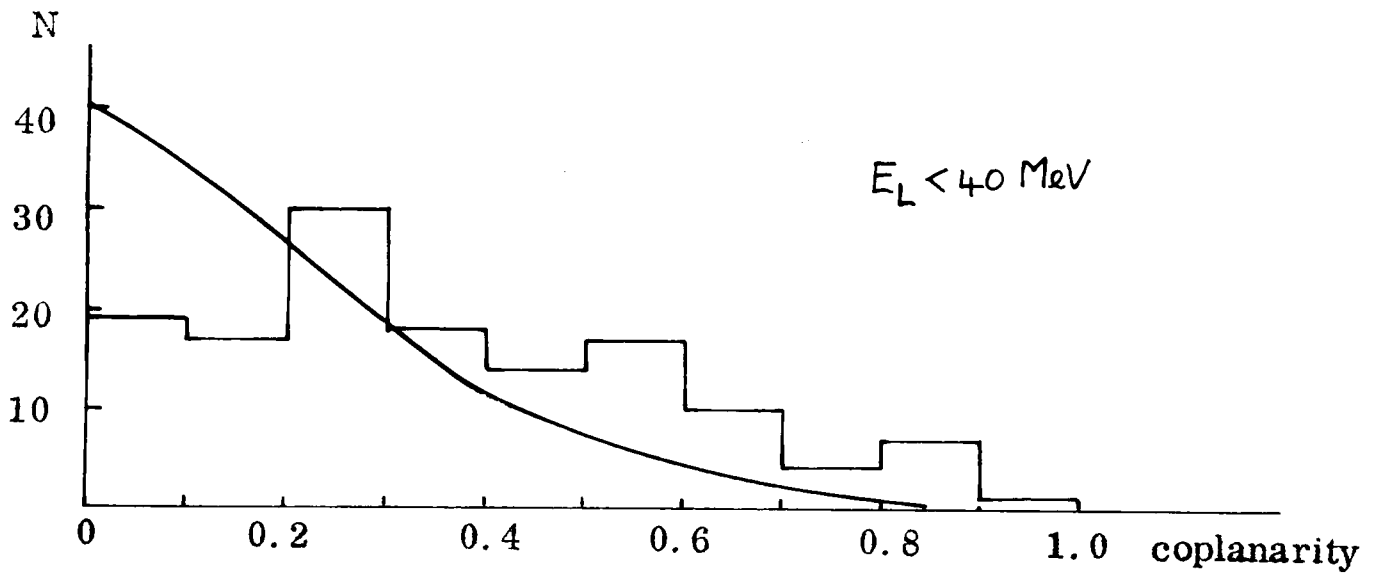

Fig. 10.8 The histogram shows the coplanarities calculated from the incident track and the two longer prongs for 3-prong events and the curve is the distribution of coplanarities for the quasi-elastic 2-prong events.

E_o is the incident energy,

$E_{1,2\ \&\ 3}$ are the final proton energies, and

E' is the energy of the intermediate proton.

If the total binding energy is E_L and the recoiling nucleus has an energy E_R, then there is an energy $E_o - E_L - E_R$, say E_A, available to be shared between the three protons that come from the nucleus. E_o is replaced by E_A [≠] and it is assumed that each collision has the properties of an elastic nucleon-nucleon collision; in particular it is assumed that either proton has a constant probability of taking any energy between zero and the total energy available at the interaction apex.

The probability of proton 1 having an energy between E and E + dE is dE/E_A, and the probability of proton 2 having an energy in the same range is the product of the probability that the intermediate proton has an energy E' greater than E and of the probability that proton 2 takes an energy between E and E + dE from the available energy E'; this is equal to:

$$\int_{E}^{E_A} \frac{dE'}{E_A} \cdot \frac{dE}{E'} = \frac{dE}{E_A} (\ln E_A - \ln E).$$

The same expression applies for proton 3.

Therefore, for the observation of a large number of events, the distribution of protons from the hypothesized reaction is:

$$P(E)dE = K\left[1 + 2(\ln E_A - \ln E)\right] ; \quad P=0, \ E>E_A$$

≠ The same result is obtained if the total energy-loss is shared between the collision apices.

The relevant experimental values for the events with an energy-loss (E_L) less than 40 MeV and incident energy (E_o) greater than 100 MeV are:

$$\bar{E}_L \sim 33 \text{ MeV}, \quad \bar{E}_o \sim 115 \text{ MeV}, \quad \bar{E}_R \sim 4 \text{ MeV},$$

and for those events with an incident less than 100 MeV:

$$\bar{E}_L \sim 34 \text{ MeV}, \quad \bar{E}_o \sim 82 \text{ MeV}, \quad \bar{E}_R \sim 5 \text{ MeV}.$$

In figures 10.9 and 10.10 the experimental distributions of the proton energies are shown for the two incident energy ranges; the full-line curves are normalized to the number of events in the experimental distributions above 8 MeV and they show P(E) calculated using the figures given above.

The experimental results and the model results are in good agreement for $E_o > 100$ MeV, but for $E_o < 100$ MeV the model result gives too small a component at the low energy end of the spectrum. However this discrepancy for low incident energies can be accounted for by the fact that, in the analytical model, no allowance is made for the non-detection of those 3-prong events with one proton of energy less than 4 to 5 MeV. The broken-line curve in figure 10.10 shows the proton spectrum obtained by using the statistical model of chapter 9 for the (p, 3p) reaction, and the agreement is good; in this model the distortion on the spectrum due to loss of the events with low energy protons is automatically accounted for. For $E_o > 100$ MeV the distorting effect is much less severe and, in fact, the statistical model calculation produces a spectrum indistinguishable from the analytical model spectrum.

The agreement between the experimental proton spectra and the model spectra lead to the conclusion that the events with (p, 3p) energy-losses below 40 MeV are consistent with the simple 3-proton cascade reaction mechanism.

The points show the experimental proton energy distributions and the full line curves are the analytically predicted distributions. The broken line curve of Fig. 10.10 shows the statistical model result.

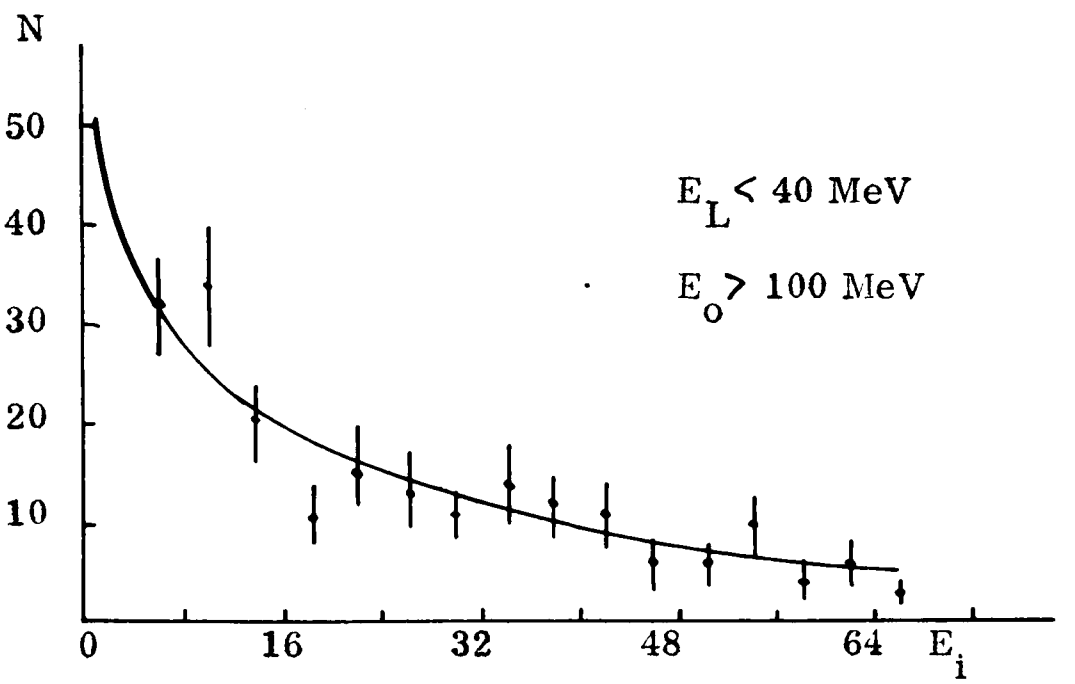

Fig. 10.9

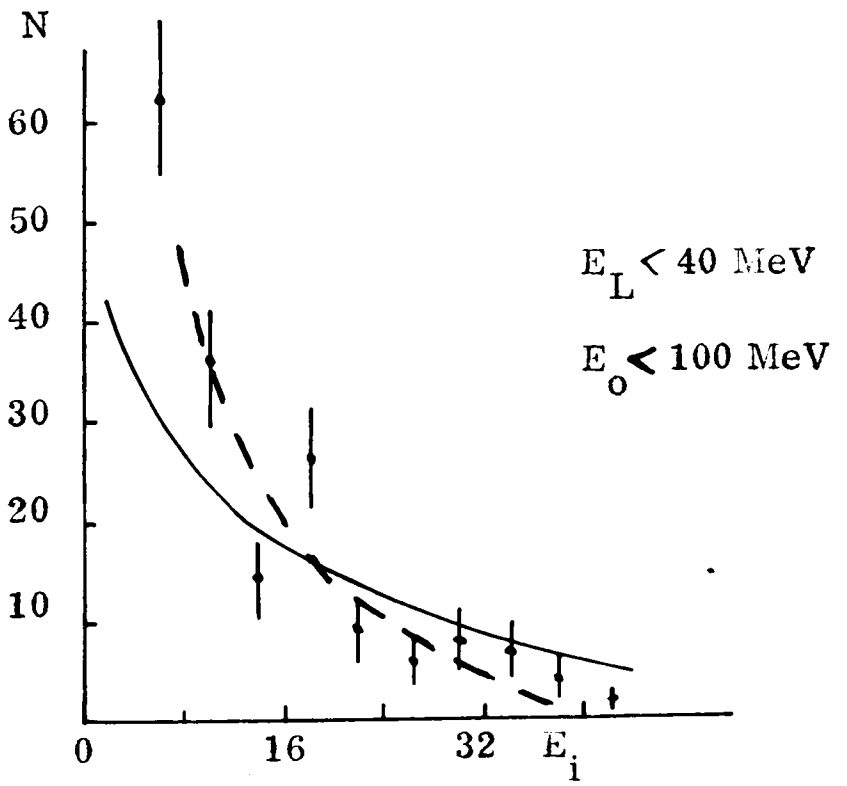

Fig. 10.10

10.4 Reactions involving heavy particles

Heavy particles have been observed amongst the particles emitted from light nuclei when they are bombarded with high energy protons and they have been attributed to:

(a) the direct knock-out of preformed clusters in the nucleus,
e.g. the quasi-elastic $C^{12}(p,p\alpha)Be^{8}$ reactions at 150 MeV reported by JAMES & PUGH (1963); α, d and t knock-out from the light emulsion nuclei at 340 MeV reported by ZAMMAN, CÜER, COMBE et al. (1954, 1955, 1956, 1958) and at 660 MeV by OSTROUMOV & FILOV (1960), α-particles being the most frequently observed particles;

(b) evaporation of preformed clusters from excited residual nuclei,
e.g. ZHDANOV & FEDOTOV (1960) and PERFILOV & SEREBRENNIKOV (1961) found a large ratio of α-particles to protons amongst the evaporation products from residual light emulsion nuclei;

(c) pick-up reactions by nucleons as they move through the nucleus,
e.g. RADVANYI & GÉNIN (1960) attributed the deuterons and tritons observed by them in $p + C^{12}$ reactions at 150 MeV to pick-up reactions.

There are several theoretical papers which show that the clustering of nucleons within the nucleus is not inconsistent with an independent particle model for the nucleus and that the quasi-α cluster is particularly favoured (e.g. BAZ (1956), BLOKHINTSEV (1958), SHELINE & WILDERMUTH (1960) and BUNAKOV (1963), but the theoretical understanding of the production of heavy particles in nucleon-nucleus interactions is not yet very well developed.

It seems possible, therefore, that heavy particle reactions could account for some of the 3-prong events. The large (p,3p) energy-losses could be accounted for in two ways. Firstly, if the particles have sufficient energy to leave observable tracks in the bubble chamber, their calculated energies (assuming them to be protons) will be below their true energies; for example, a 40 MeV α-particle would appear to be a 10 MeV proton. Secondly, if they have insufficient energy to be detected then they are obviously omitted from the energy balance for the reaction; up to 16 MeV can be accounted for in this way by one α-particle. Evidence for these two sources of energy-loss will be considered separately.

(i) Observed heavy particles If the three prongs of each event represent the sole reaction products, apart from the recoiling nucleus, it is possible to calculate the energy-loss for any reaction of the type C^{12}(p, pAB) or C^{12}(p, 2pA), where A and B represent particles such as d, t, He^3 and α. The energy-loss calculated with a correct reaction hypothesis for an event will be equal to, or just above, the threshold energy for that reaction. Peaks at these energies in the energy-loss distributions would therefore point to the presence of heavy particle reactions.

For a given reaction, three possible energy-losses can be calculated, due to the different ways in which the hypothesized product particles can be assigned to the three prongs. In figures 10.11 to 10.18, the distributions of energy-loss calculated for various hypotheses (including the three possibilities for each event) are shown with the appropriate threshold energies. Only for the reactions

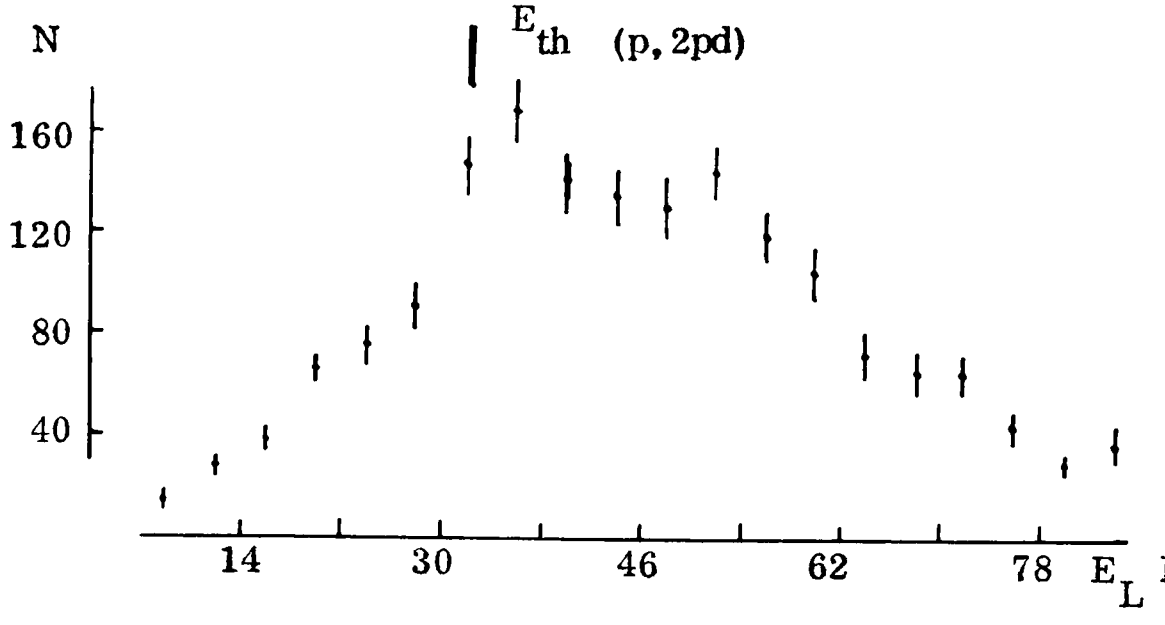

Fig. 10.11

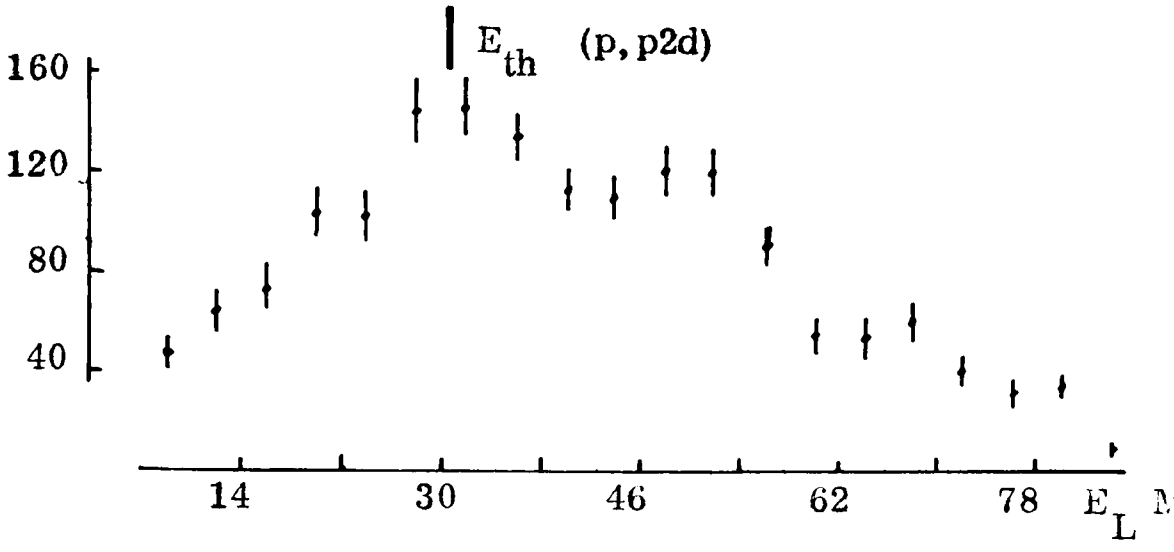

Fig. 10.12

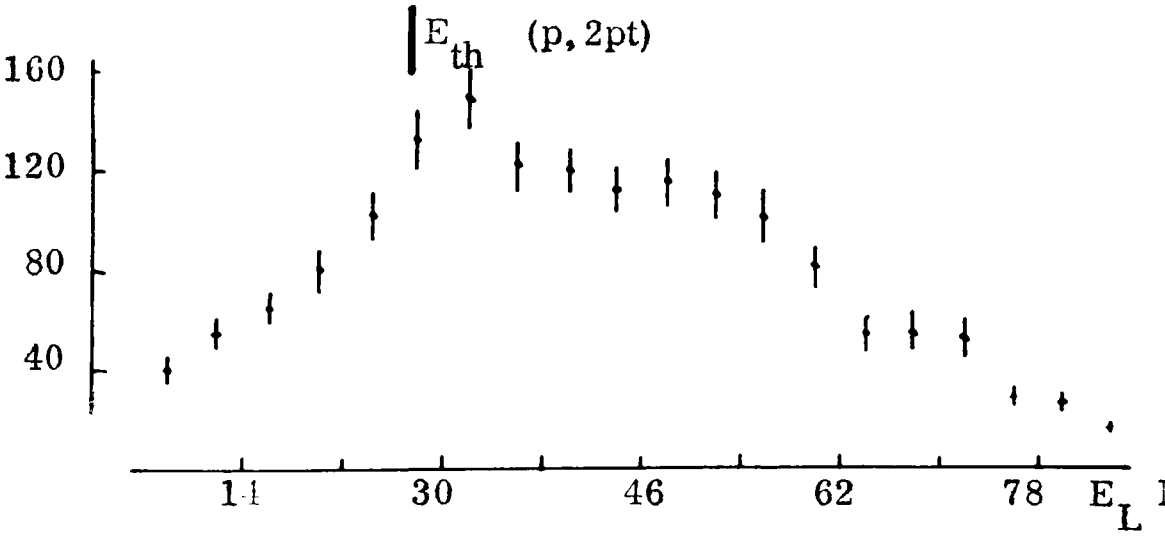

Fig. 10.13

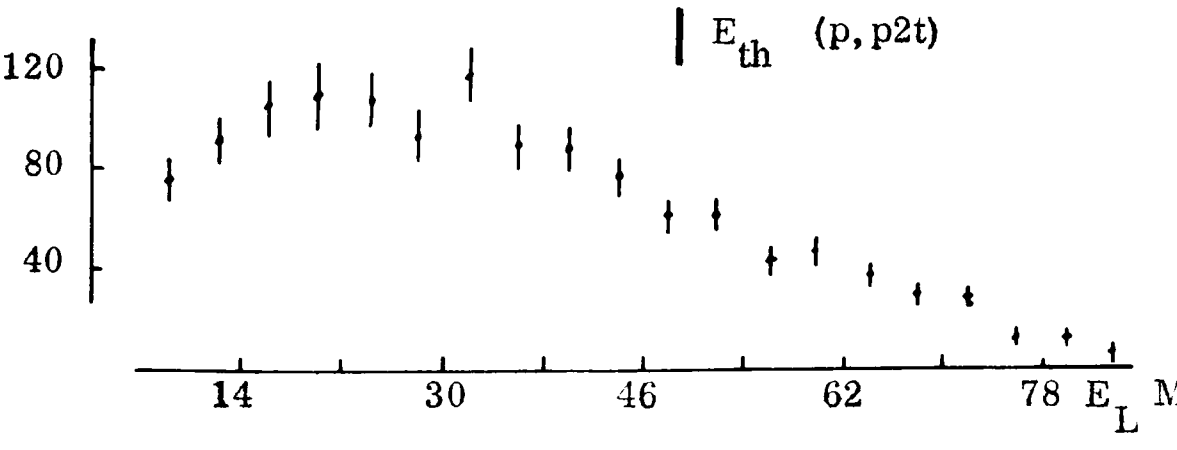

Fig. 10.14

Energy-loss distributions obtained for various reaction hypotheses.

Energy-loss distributions obtained for various reaction hypotheses.

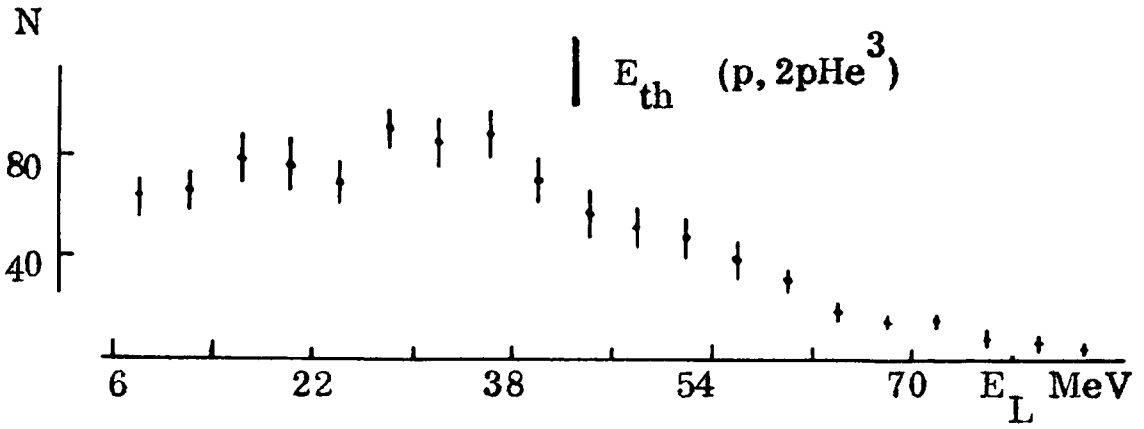

Fig. 10.15

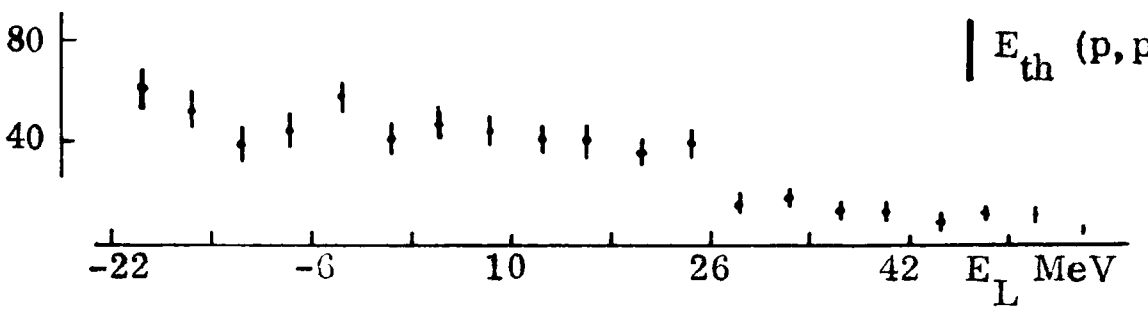

Fig. 10.16

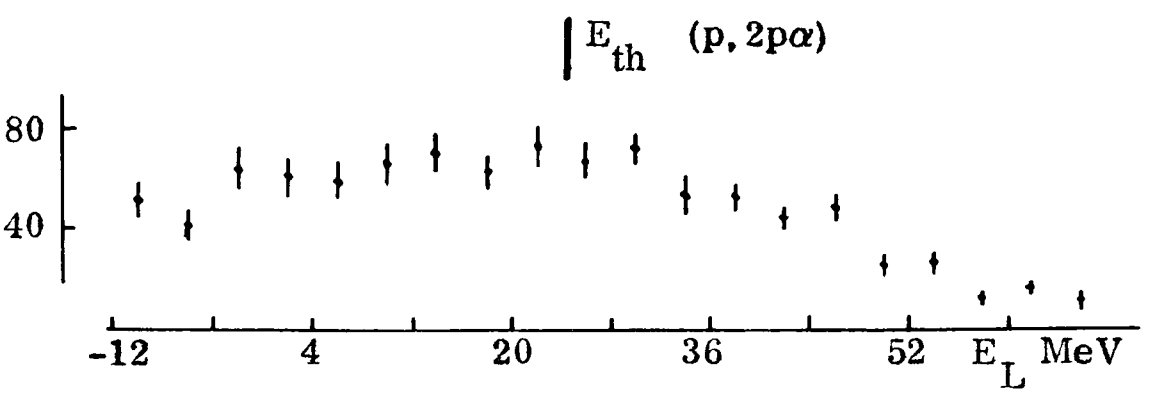

Fig. 10.17

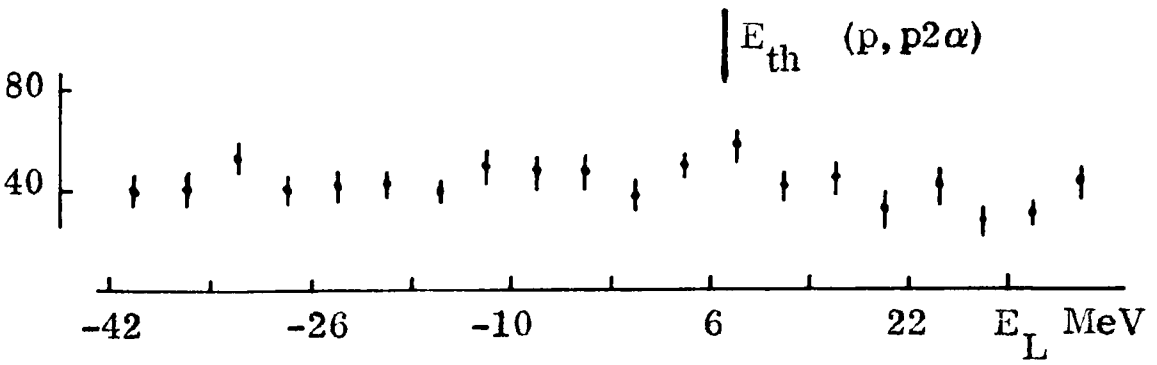

Fig. 10.18

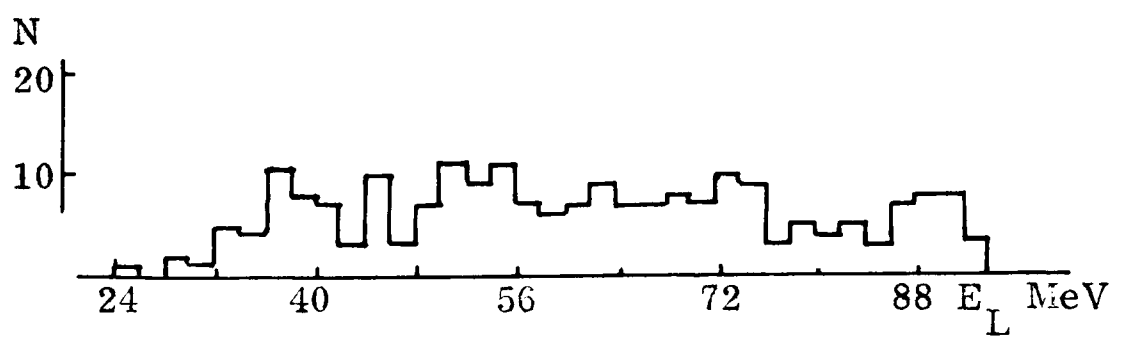

Fig. 10.19 (p, 3p) energy-loss distribution for events with incident energies greater than 120 MeV.

$C^{12}(p, 2pd)Be^{6}$, $C^{12}(p, 2pt)Be^{6}$, and $C^{12}(p, p2d)Be^{6}$ is there any indication of peaking at the threshold energies, and furthermore it is found that, broadly speaking, the same body of events is responsible for each of the peaks.

It is estimated from the distributions that up to 10% of the total number of 3-prong events can be attributed to reactions involving heavy particles.

(ii) Unobserved heavy particles Only an indirect assessment can be made of the importance of these reactions. It has been noted that results from emulsion experiments, in which heavy particles can be detected to energies below 1 MeV, show that, of the heavy particles emitted from light nuclei, α-particles predominate. Two assumptions will be made: firstly that the observed particles are protons, and secondly that any unobserved heavy particles are α-particles. The break up of the C^{12} nucleus must therefore be as follows:

$$C^{12} \rightarrow 2p + \alpha + \alpha + 2n,$$

because once one α-particle is emitted with 3 protons, the residual He^{6} is unstable against the decay: $He^{6} \rightarrow \alpha + 2n$.

ZHDANOV & FEDOTOV (1960) showed that, for the reaction $p + C^{12}$ at 660 MeV, the ratio of the number of α-particles knocked out of the nucleus to the number of protons knocked out is 0.2, and a similar result was reported by PERFILOV & SEREBRENNIKOV (1961) for the nuclei C, N, O taken together. If this result is assumed to apply at energies in the region of 100 MeV[≠], the

---

≠ This is not an unreasonable assumption since Ostroumov & Filov have shown that the cross-section for the knock-out of high energy α-particles from the light emulsion nuclei is constant for incident energies between 100 MeV and 700 MeV.

hypothesized C^{12} break up will, in four cases out of ten, involve one knocked-out α-particle. The energies of the various particles can be estimated as:

knocked-out α	$\lesssim$	16 MeV
evaporated α	$\lesssim$	6 MeV#
two evaporated neutrons	$\lesssim$	8 MeV

and the total binding energy is 36 MeV.

When a knock-out α-particle is involved, the maximum energy unaccounted for will therefore be 60 MeV, and when both α-particles are evaporated the maximum unobserved energy will be 56 MeV. If the hypothesized process is important, it is to be expected that the (p, 3p) energy-loss distribution will have a structure reflecting the presence of the above two components.

In figure 10.1⅝, the (p, 3p) energy-loss distribution is shown for events with $E_o > 12$⅝ MeV (to eliminate most of the effect on the distribution of the spread of incident energies (see figure 10.1)). The distribution shows no marked structure and in particular shows no discontinuities in the region of 56 MeV and 66 MeV. Furthermore, it was shown in section 10.2 that all the other characteristics of the 3-prong events are quite independent of energy-loss right up to the maximum energy-losses observed (~ 85 MeV).

The evidence for the presence of energetic heavy particles shows that an upper limit of 10% of the 3-prong events could be explained by reactions

---

Perfilov & Serebrennikov showed that, for the decay of residual light nuclei, the ratio of α-particles to protons is approximately 1.7 and that the energy spectrum of the α-particles is peaked at 3 MeV and falls off rapidly above this energy.

involving heavy particles. The indirect evidence for the presence of low energy heavy particles lends no support at all to their importance. Therefore, subject to the limitations of the analysis, it is concluded that the presence of heavy particle reaction products cannot account for the main body of the 3-prong events.

10.5 The nucleon cascade and evaporation mechanism

Traditionally, this mechanism has been used to interpret nucleon-nucleus interactions for heavy nuclei and for high energy incident nucleons, but the work of ZHDANOV & FEDOTOV (1960, 1962, 1964), ABATE (1961), and BERTINI (1963, 1964) has shown that it is also applicable for nuclei as light as carbon and for energies as low as 50 MeV; some of their results were reported in section 1.3.

If the reactions $C^{12}(p,3pxn)Be^{10-x}$, x=1,2,..., are important contributors to the 3-prong events it is easily seen that they can produce very low and very high (p,3p) energy-losses. Low energy-losses would result from interactions in which the neutrons take away a small proportion of the available energy- as they would, for example, if they were produced in the evaporation phase of the reaction - and high energy-losses would result, for example, from reactions in which high energy neutrons produced in the first stages of the cascade reaction escaped from the nucleus without further interaction. To assess the relative importance of these various possibilities, the model, described in detail in the preceding chapter, was set up. As pointed out in that chapter,

each reaction of the type (p, 3pxn) is assumed, in turn, to account for all of the observed events and, by comparing the results from each calculation with the experimental results, an assessment of their relative importances can be made.

The results predicted by the model for the (p, 3p) energy-losses, the proton energy spectra, and the energy sharing between product protons for the reactions C^{12}(p, 3pn)Be^{9} and C^{12}(p, 3p2n)Be^{8} are presented in figures 10.20 to 10.28. One energy-loss distribution is also shown for the reaction C^{12}(p, 3p3n)Be^{7}. The model results have been smoothed out to curves and the experimental distributions are shown by the points. The first observation is that the model predictions do indeed produce distributions very similar to the experimental distributions.

An examination of figure 10.20 shows that the contribution to the events from the C^{12}(p, 3p3n)Be^{7} reaction, with its high threshold energy, is likely to be minimal. Firstly because it can contribute events only in the tail of the energy-loss distribution, and secondly because if it were important in this region, the contribution from the reactions (p, 3pn) and (p, 3p2n) would have to be very small to retain a good fit for the high energy-loss end of the distribution; this would leave a large proportion of the main body of the events, at lower energy-losses, unexplained. The unimportance of the (p, 3p3n) reaction can easily be explained by the fact that this reaction would require the breaking up of two α subgroups in the nucleus compared with the breaking up of only one for the (p, 3pn) and (p, 3p2n) reactions.

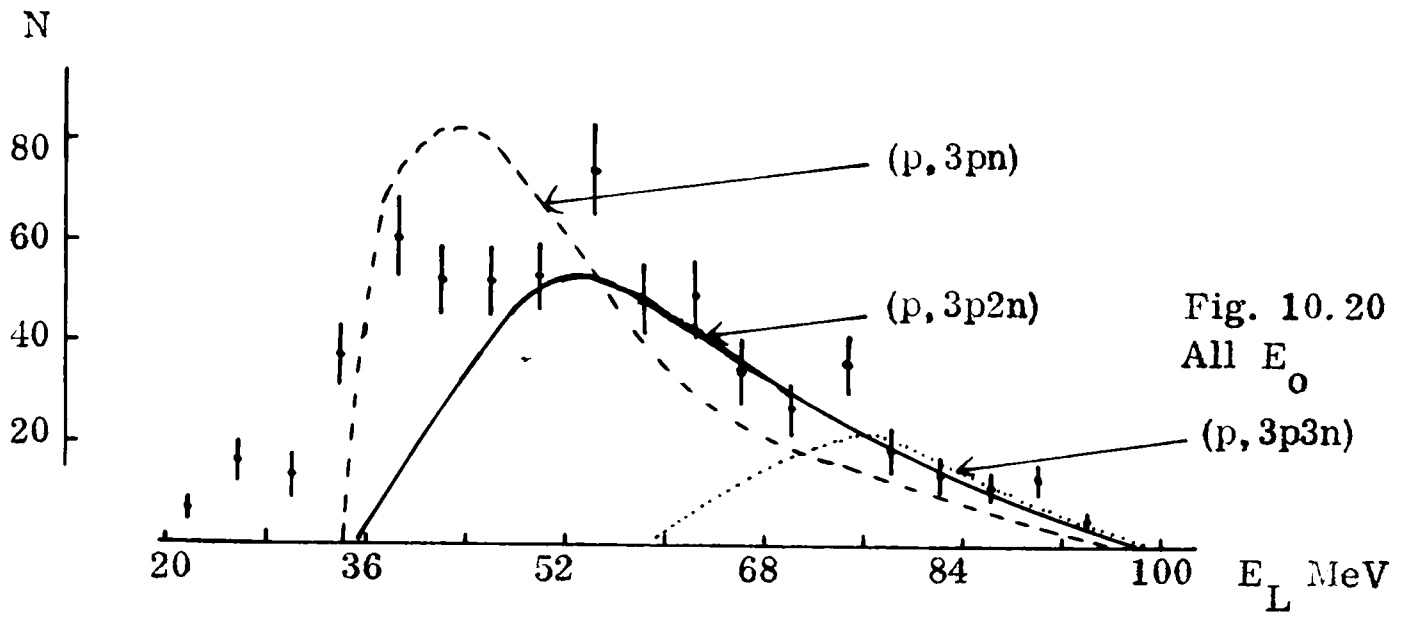

Fig. 10.20
All E_o

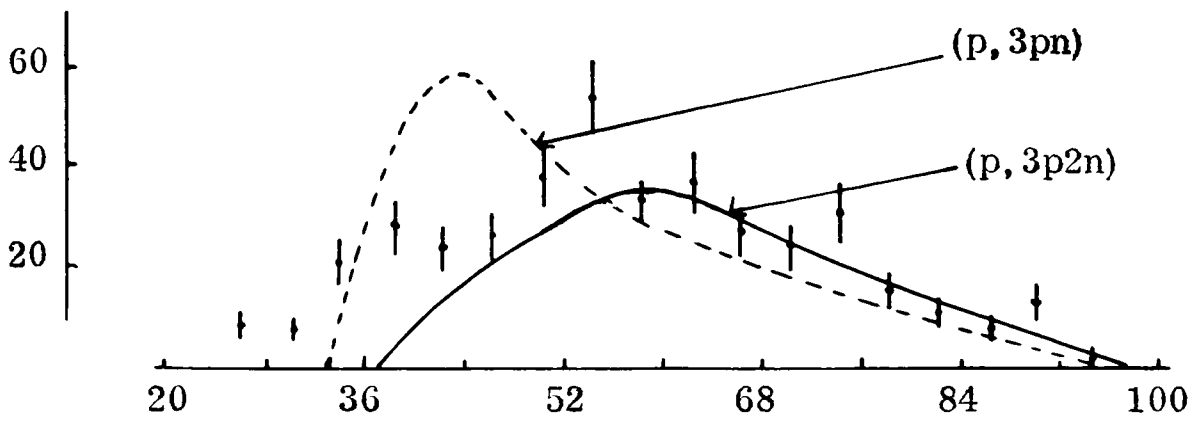

Fig. 10.21
$E_o > 100$ MeV

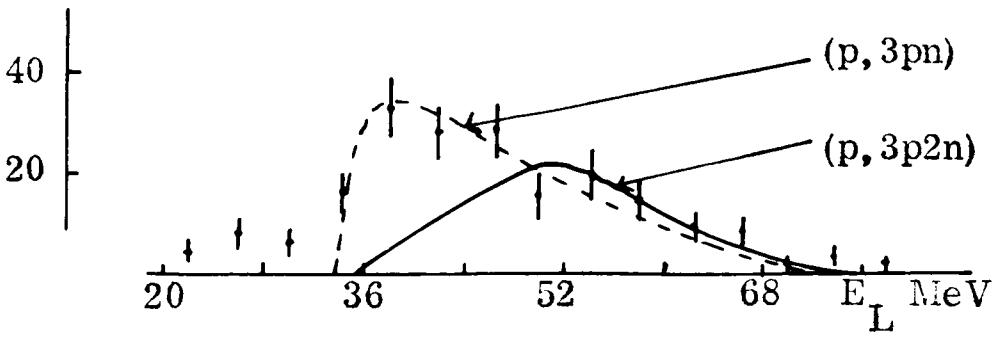

Fig. 10.22
$E_o < 100$ MeV

The points show the experimental (p, 3p) energy-loss distributions and the curves show the distributions predicted by the cascade model for various reactions.

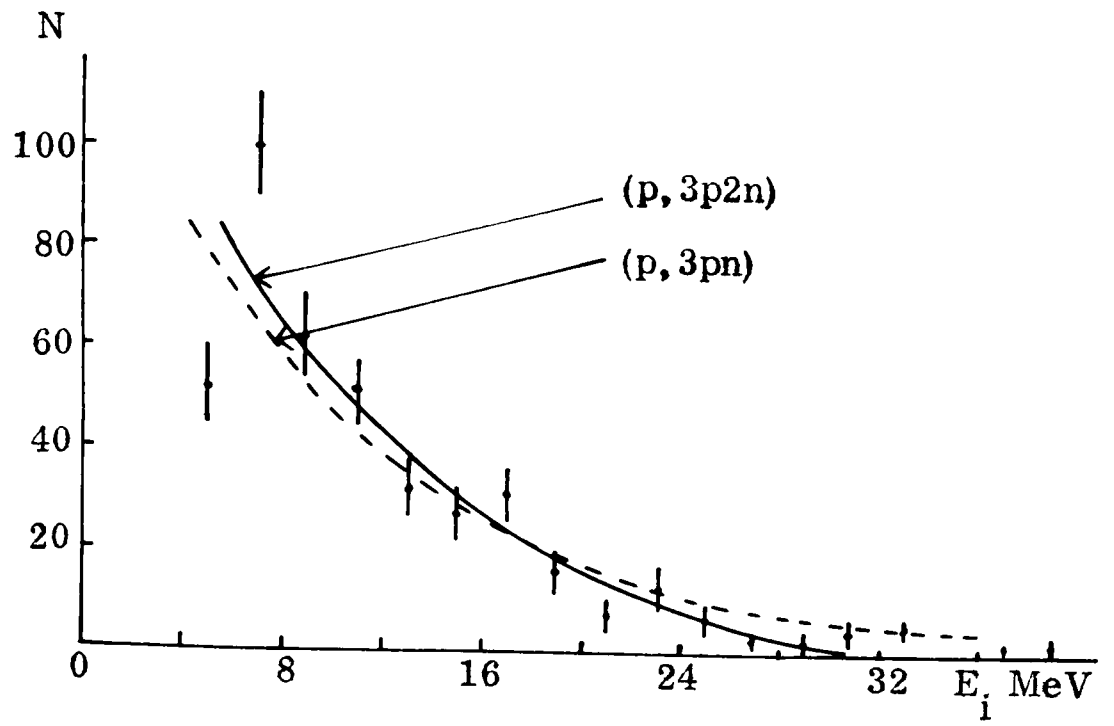

Fig. 10.24
$E_o < 100$ MeV
$E_L > 36$ MeV

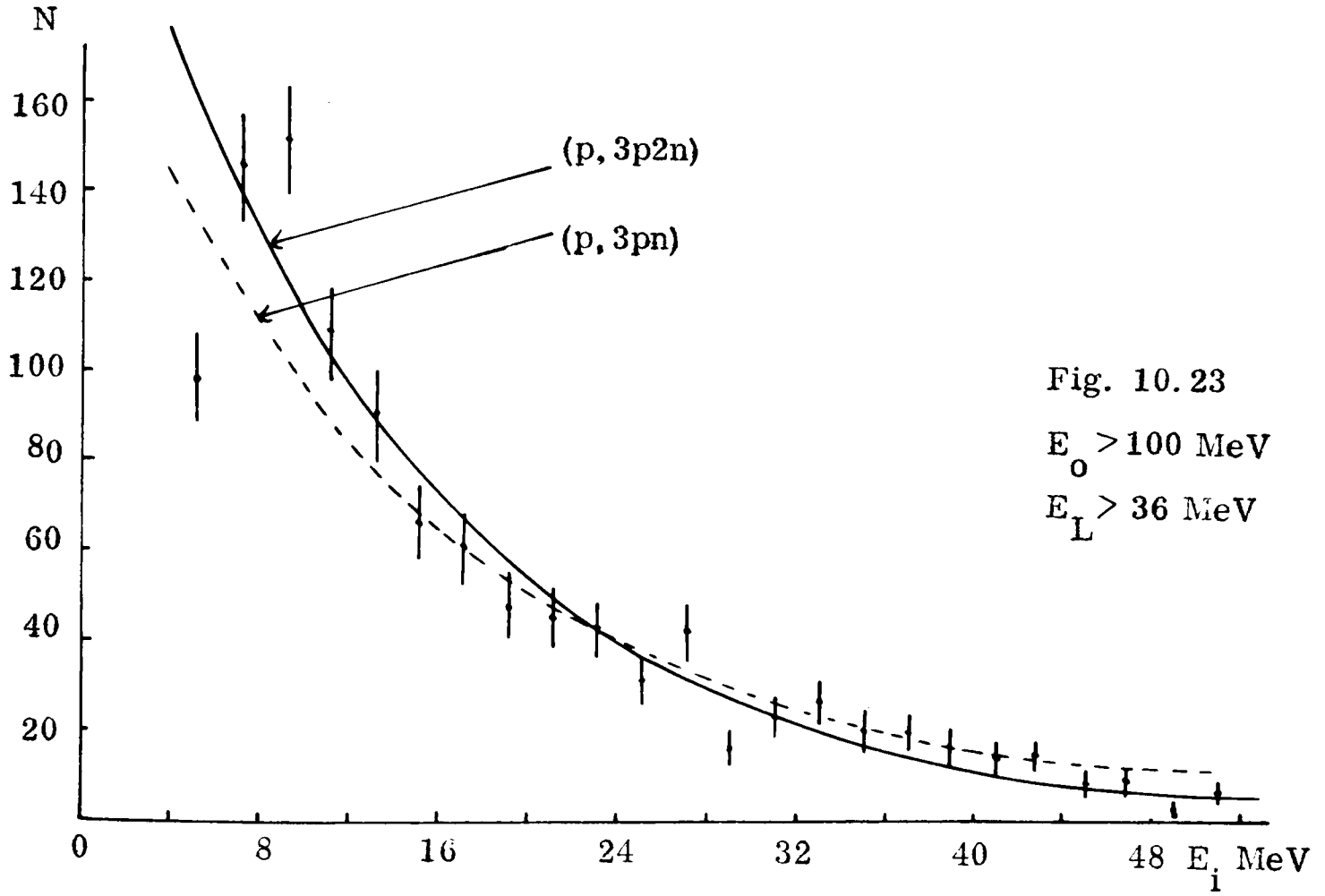

Fig. 10.23
$E_o > 100$ MeV
$E_L > 36$ MeV

The points show the experimental proton energy distributions and the curves show the distributions predicted by the cascade model for various reactions.

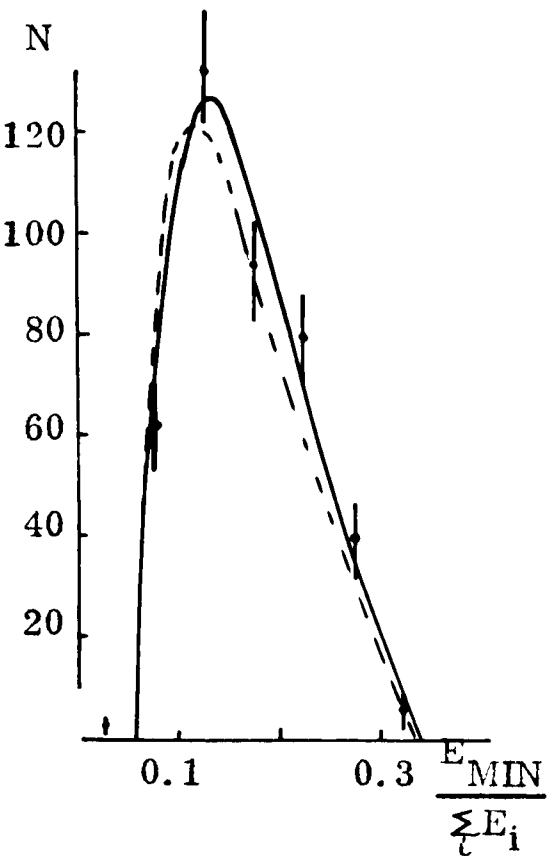

Fig. 10.25

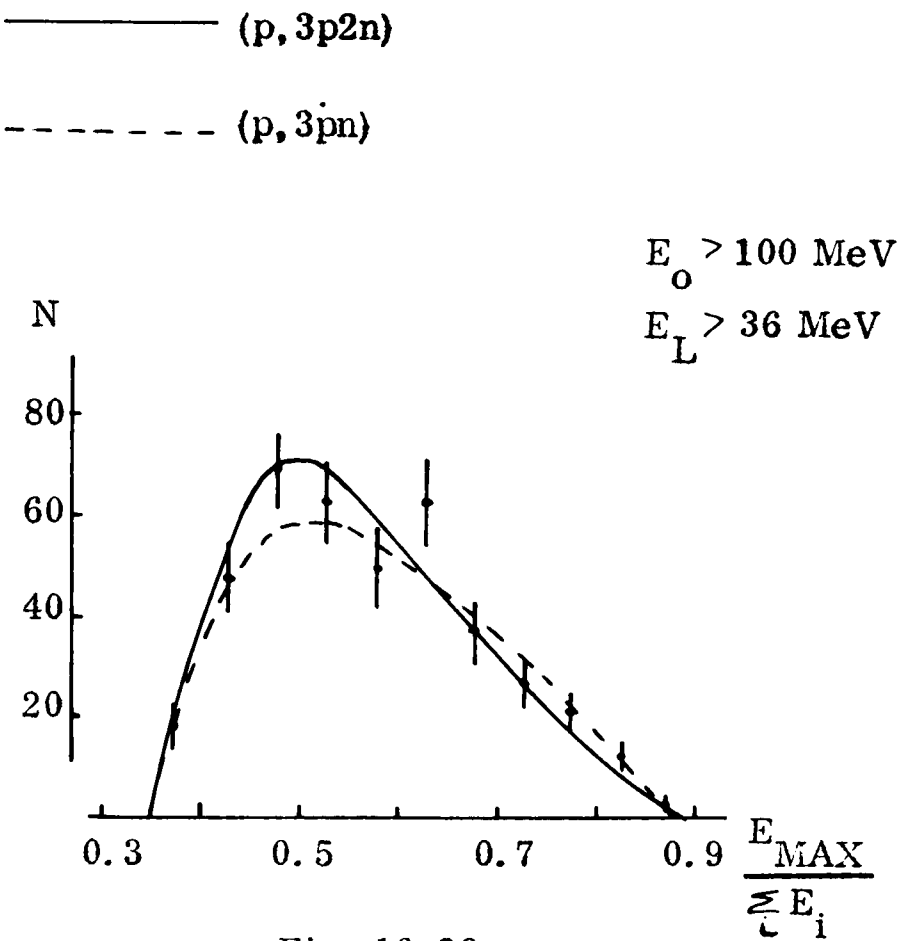

Fig. 10.26

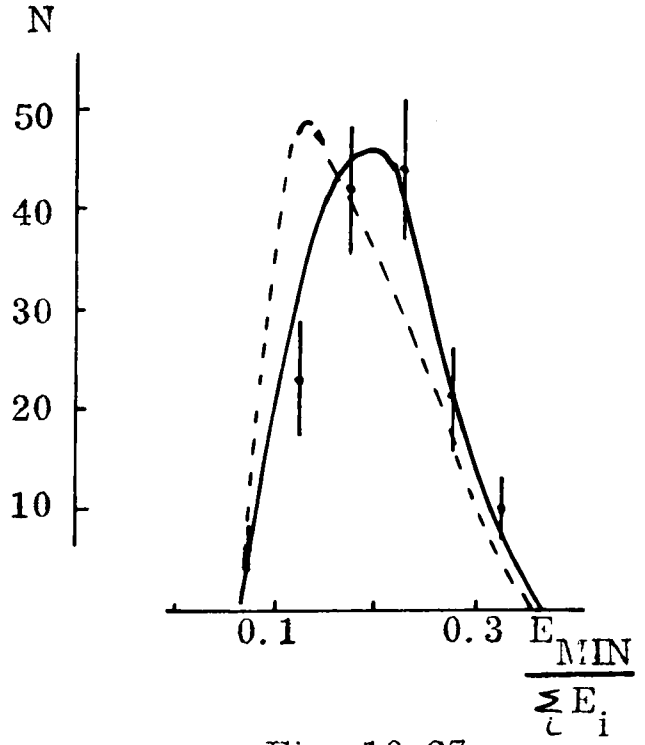

Fig. 10.27

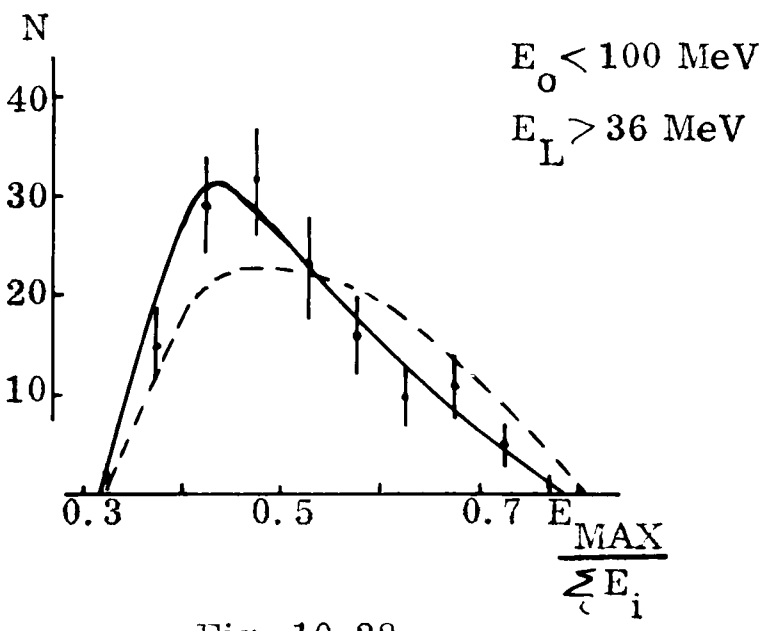

Fig. 10.28

Characteristics of the energy-sharing between the three product protons. The points show the experimental results and the curves show the results predicted by the cascade model for various reactions.

No such clear-cut observations can be made concerning the relative importances of the (p, 3pn) and (p, 3p2n) reactions. The table below summarizes the goodness of fit between the model predictions and the experimental results shown by figures 10.20 to 10.23.

Type of result \ Incident energy	$E_o > 100$ MeV	$E_o < 100$ MeV
(p, 3p) energy-loss	(p, 3p2n) better	both fit over different ranges
proton energy spectrum	(p, 3p2n) better	(p, 3p2n) marginally better
energy ratios	both fit equally well	(p, 3p2n) better

The experimental proton energy spectra seem to have more low energy protons than is predicted by the model for either reaction. This could well be due to the very phenomenological manner in which evaporation has been included in the model, because the proton contribution from evaporation begins to be important at the lowest proton energies observed in the experiment.

The general conclusion to emerge from the table is that the model predictions for the (p, 3p2n) reaction give a better fit to the experimental distributions than the (p, 3pn) predictions do. Let us examine further the energy-loss distributions to see to what extent the dominance of the (p, 3p2n) reaction can be substantiated

Firstly, what are the implications of hypothesizing that there is no contribution at all from the (p, 3pn) reaction? In figure 10.25 the histograms show the differences between the predicted (p, 3p2n) energy-loss distributions

and the experimental energy-loss distributions; also shown are the energy levels corresponding to the production of the known low-lying excited states of Be^{10}. It can be seen that the (p, 3p2n) reaction can account for all of the events with $E_o > 100$ MeV and $E_L > 56$ MeV, and for all those with $E_o < 100$ MeV and $E_L > 48$ MeV. The remaining events all occur in the region of energy-loss corresponding to the low-lying excited states of Be^{10} and so they could be attributed to the (p, 3p) reaction; it has already been shown (section 10.3) that these events have proton spectra consistent with a (p, 3p) cascade reaction mechanism. It seems quite possible, therefore, that the (p, 3pn) reaction is unimportant and that all of the observed events are produced by the two reactions: $C^{12}(p, 3p2n)Be^{8}$ and $C^{12}(p, 3p)Be^{10}$.

Having established that the possible minimum contribution from the (p, 3pn) reaction is zero, it will now be interesting to see whether an upper limit can be set to the (p, 3pn) contribution. In the first place it can be seen from figures 10.21 and 10.22 that there is a small residue of low energy-loss events that cannot possibly be accounted for by the (p, 3pn) reaction because they are below the threshold energy for the reaction; these must be attributed to the (p, 3p) reaction. Apart from these, however, many of the events shown in figure 10.20 can be accounted for if contributions to the events from the (p, 3pn) reaction are hypothesized. For incident energies below 100 MeV, it can be seen from figure 10.22 that the contribution from the (p, 3pn) reaction could be almost as high as 100% without producing significant discrepancies between the predicted and the experimental distributions, but the energy sharing results

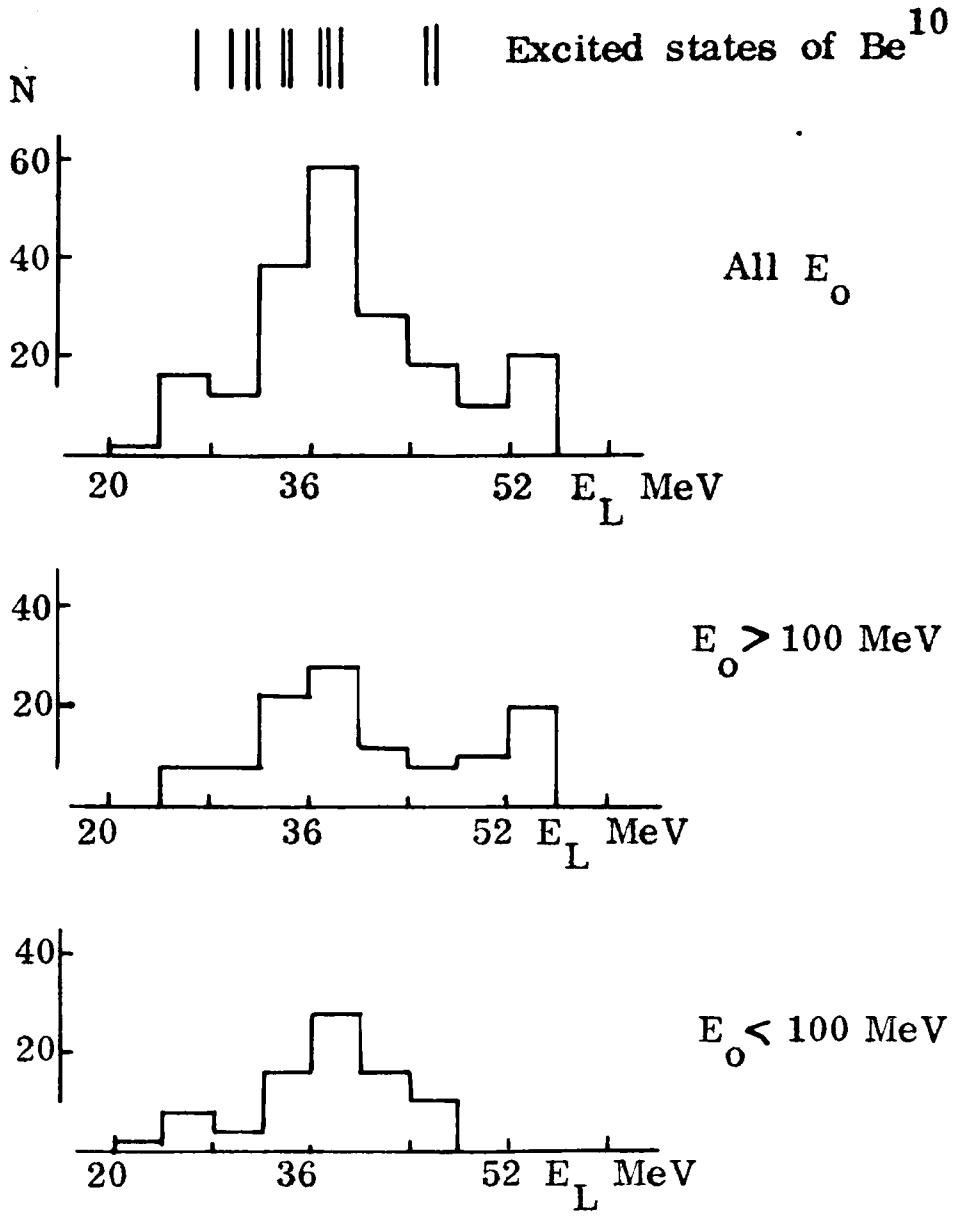

Fig. 10.29 The difference between the experimental energy-loss distributions and the predicted (p, 3p2n) (p, 3p) energy-loss distributions.

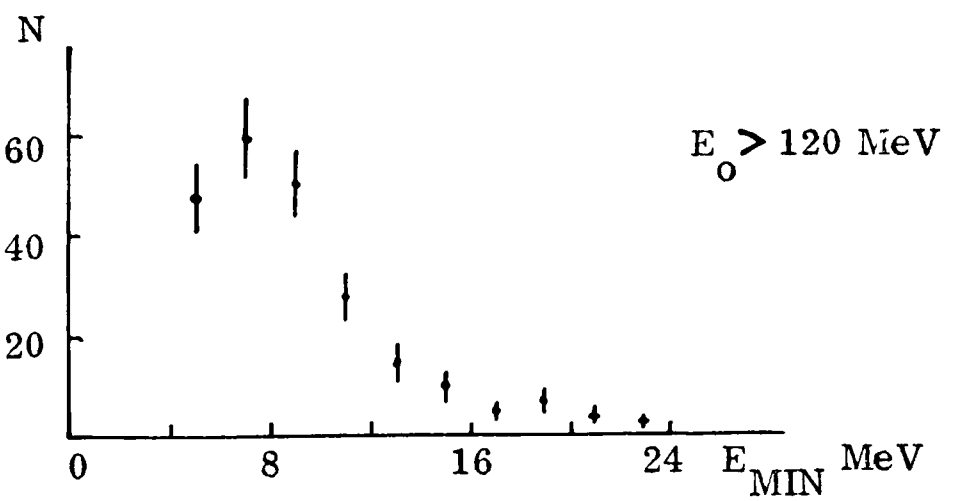

Fig. 10.30 Distribution of the lowest energy proton for the high incident energy 3-prong events.

of figures 10.27 and 10.28 would be in disagreement with the experimental results if very large contributions were hypothesized. On the other hand, for incident energies above 100 MeV large contributions from the (p,3pn) reaction would produce a distribution with more events in the energy-loss region of 36 MeV to 46 MeV than are observed experimentally. In figure 10.31 the experimental distribution is shown along with the distributions predicted for various combinations of contributions from the (p,3pn) and (p,3p2n) reactions. Certainly, (p,3pn) contributions of 50% and above imply an excess of events in the 36 MeV - 46 MeV region but a contribution of up to approximately 40% would give a distribution consistent with the experimental one. It must be borne in mind, though, that the lower the hypothesized contribution from the (p,3pn) reaction, the better will be the agreement between the experimental and the theoretical distributions for the other results summarized in the table.

To summarize: all the events can be accounted for by the two reactions $C^{12}(p,3p)Be^{10}$ and $C^{12}(p,3p2n)Be^{8}$ (30% and 70% respectively), but up to 40% of the events could be due to the reaction $C^{12}(p,3pn)Be^{9}$, although the evidence points to the fact that the contribution from this reaction is probably well below 40%.

10.6 Knock-out of correlated pairs of protons

It would be extremely interesting if a body of events attributable to the direct knock-out of a correlated pair of protons could be recognized, because very little is known about such correlations. Although the 3-prong events

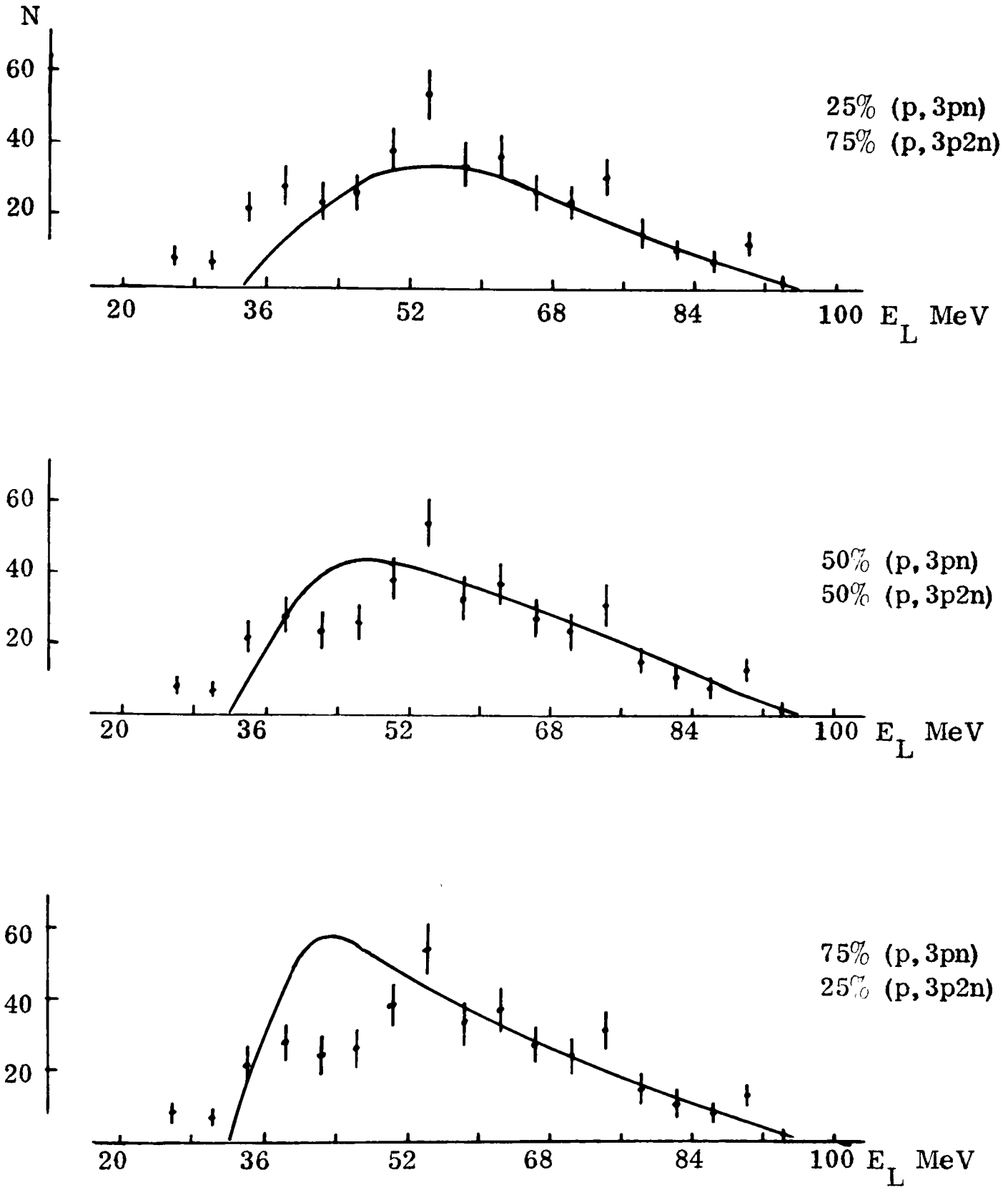

Fig. 10.31 The experimental energy-loss distribution compared with the results predicted by the cascade model for various combinations of the reactions (p, 3pn) and (p, 3p2n) (curves).

have been shown to be consistent with nucleon cascade reactions, the evidence is not conclusive and the possibility that the three protons emerging from the nucleus arise from a proton-diproton collision within the nucleus remains open.

If such reactions were present, the spectrum of excited states produced in the residual Be^{10} nucleus would reflect the parentage coefficients for the expansion of the C^{12} ground state in terms of two protons and Be^{10}. Since the evidence from the results, presented in section 10.2, shows that the event characteristics are no different, on average, throughout the energy-loss range, it is presumed that if the proton-diproton mechanism is important it contributes events at all energy-losses, and it was seen in figure 10.15 that, for a given incident energy, events are distributed uniformly with energy-loss up to the maximum possible level. This implies that the sums of the parentage coefficients for equal intervals of Be^{10} excitation energies are constant at least up to the maximum excitation energies observable. However, BALASHOV & BOYARKINA (1964) showed that the expansion of the C^{12} wavefunction in terms of a proton-neutron pair and B^{10} involved finite parentage coefficients for only the very low-lying excited states in the residual C^{10} nucleus and it seems likely that the result would not be greatly different if the expansion were for a proton-proton pair and Be^{10}. This evidence suggests that the clean knock-out proton-diproton reaction mechanism is not an important contributor to the observed 3-prong events.

In figure 10.30 the spectrum of the lowest energy protons from each event is shown for all events with $E_o > 120$ MeV; bearing in mind the loss of

low energy protons, the spectrum is characteristic of an evaporation spectrum (see, for example, ZHDANOV & FEDOTOV (1960)). This further suggests that diproton direct knock-out is not important because in such a reaction there are no evaporated protons.

Finally, there is the question of how the missing energy is accounted for. If the measured energy-loss represents the excitation energy of the Be^{10} nucleus before it breaks up, as it would for a clean diproton knock-out reaction, then as the incident energy increases and the highest energy-losses increase, so the Be^{10} break-up products ($2\alpha + 2n$) take away, on average, more energy. For $E_o = 120$ MeV and $E_L = 80$ MeV, the four particles must take away approximately 50 MeV. As the incident energy increases, this value will be at least as large as that, but if the present results are extrapolated they suggest that higher incident energies would give rise to higher (p, 3p) energy-losses and consequently that even more energy must be accounted for by the α-particles and neutrons. However, ZHDANOV & FEDOTOV (1960) showed that, even at an incident energy of 660 MeV, the energy spectrum of the α-particles is peaked at 4 MeV and drops exponentially to 10% of the peak value at 20 MeV.[≠] This is a typical evaporation spectrum and it certainly suggests that the average α-particle energy does not increase as the incident energy increases. To account for the high energy-losses, therefore, neutron energies above these encountered in evaporation spectra are required. The presence of high energy neutrons but

---

≠ Over half of the α-particles they observed came from the reactions involving the knock-out of two protons from C^{12}.

not high energy α-particles cannot easily be accounted for by a model involving the spontaneous break up of highly excited Be^{10} nuclei.

Only an indirect approach to the problem has been possible, but from the separate bits of evidence, which all show that a proton-diproton reaction mechanism could not easily account for the results obtained from the 3-prong events, it is concluded that the mechanism is not responsible for a significant proportion of the observed events.

The analysis does not rule out the possibility of a proton-diproton interaction followed by final state interactions, which have the effect of establishing a nucleon cascade; nor does it rule out the possibility of a proton-quasi deuteron interaction, because in the case a large amount of energy could be carried away by a neutron. But these possibilities are not susceptible to analysis.

There are no difficulties of the type discussed in this section if nucleon cascade and evaporation reactions are admitted.

10.7 Summary and conclusions concerning the 3-prong events

Several possible reaction mechanisms for the production of the observed 3-prong events have been investigated.

Nucleon cascade and evaporation mechanisms leading to reactions of the type $C^{12}(p, 3pxn)Be^{10-x}$, when interpreted with a relatively elementary model, accurately predict the various experimental energy distributions for all of the 3-prong events. The evidence suggests that the (p, 3p2n) reaction is the dominant one but at least some contribution, at low energy-losses, must come

from the (p, 3p) reaction. Although no contribution from the (p, 3pn) reaction is needed to explain the experimental results, a contribution of up to 40% can be admitted before the agreement with these results is violated; however, the lower the hypothesized proportion, the better is the agreement.

Apart from the nucleon cascade reactions, the analysis shows that up to 10% of the events could be due to one, or to a mixture, of the reactions $C^{12}(p, 2pd)Be^{9}$, $C^{12}(p, 2pt)Be^{8}$, and $C^{12}(p, p2d)Be^{8}$. No evidence was found for reactions involving the clean knock-out of a correlated pair of protons. However more complex reactions cannot be ruled out because it is not possible to test for their presence; this category includes, for example: a cascade reaction involving correlated pair interactions; and participation of heavy particles in a cascade. Nevertheless, the excellent agreement between the experimental results and the results predicted for the nucleon cascade reactions does stand out as the most striking feature of the analysis.

At first sight, the conclusion that the reaction $C^{12}(p, 3p2n)Be^{8}$ is the most important single contributor to the 3-prong events, seems contrary to the predictions of the detailed Monte Carlo calculations performed by other authors. For example, the results of Bertini reported in section 1.3, predict that $\sigma(p, 3p) > \sigma(p, 3pn) > \sigma(p, 3p2n)$; the results of ABATE et al. (1961) and GRADSTEJN (1962) also show the same feature. If the cross-section of 2.6 ± 0.5 mb, calculated in section 7.6 for the events with energy-losses less than 40 MeV and incident energies greater than 100 MeV is very approximately corrected for the loss of low energy protons, by assuming that the number of

protons missing from the spectrum of figure 10.9 is equal to the number of missing events, a value of 4.4 ± 1 mb is obtained; this applies to the mean incident energy of 117 MeV. An interpolation of Bertini's results gives a cross-section of 5.1 mb for the (p, 3p) reaction at this energy which is in agreement with the experimental result. The Monte Carlo results for the (p, 3pn) cross-section - largest in Bertini's results where it is approximately equal to the (p, 3p) cross-section - implies a contribution of 10% from this reaction in the present instance and this is well within the possible upper limit of 40% suggested in section 10.5. This leaves a very large contribution from the (p, 3p2n) reaction which cannot be accounted for by the Monte Carlo cascade model predictions.

There are two possible explanations.

Firstly, if α substructures in C^{12} play an important part in the proton-nucleus reaction then it seems likely that the interaction of the incident proton with a nucleon when it is participating in a sub-α correlation (not necessarily a spatial correlation - see BAZ (1956)) could result in the ejection of all four of the correlated nucleons. Since this nuclear structure effect has not been allowed for in any of the Monte Carlo calculations this could account for the fact that the predicted cross-section is very much smaller than the experimentally deduced cross-section for the reaction $C^{12}(p, 3p2n)Be^{8}$.

Secondly, since the cascade calculations make no allowance for evaporation from the nuclei remaining after the cascade stage of the reaction, it is possible that the evaporation part of the reaction greatly reinforces the (p, 3p2n) reaction

but not the other reactions. It can be seen from the results of Metropolis (see section 1.3) that, for medium weight nuclei at least, (nucleon, x nucleon) cascade reactions leave the residual nuclei with considerable amounts of excitation energy which will be dissipated by particle evaporation. ZHDANOV & FEDOTOV (1964) investigated this possibility for their experimental conditions of 660 MeV protons on C^{12}, because their experimental results also indicated a predominance of the reaction (p, 3p2n).$^{\neq}$ As reported in section 1.3, they did in fact find that a very strong reinforcement of the cross-section for the production of the final nucleus Be^{8} (or two low energy α-particles) was predicted if a conventional nucleon cascade calculation was followed by a decay mode calculation. They showed that the effect was due to the stability of the α grouping within the nucleus which makes Be^{8} (or 2α) a highly favoured final product.

Therefore both explanations depend upon α-particle substructure. It is interesting to recall (see section 1.3) that the Monte Carlo calculations of other authors gave better agreement with experimental results if the presence of α-particles in C^{12} was admitted, although in these calculations the α-particles were treated as subparticles which do not break up.

On the basis of the evidence presented, it is concluded that α-particle substructures play an important rôle in determining the course of nucleon interactions with the C^{12} nucleus and that the 3-prong events arise from reactions of the type $C^{12}(p, 3pxn)Be^{10-x}$; with $x=2$ predominating.

$\neq$ 60% of all the non-mesonic reactions with three or more charged products (excluding the residual nucleus) were attributed to the (p, 3p2n) reaction.

10.8 The 2-prong events and neutron producing reactions

The 2-prong events that have (p, 2p) energy-losses in the region of 16 MeV have been explained by the quasi-elastic (p, 2p) reaction, but the majority of the events have energy-losses well above that corresponding to the most simple knock-out reaction. There is no evidence for a dominant contribution to the events from the heavy particle reactions (p, pd), (p, pt), (p, pHe^3) and (p, pα), as can be seen from the energy-loss distributions obtained by constructing the events according to these hypotheses - shown in figure 10.32. Following the conclusions drawn from the 3-prong events, it was interesting to investigate to what extent the high energy-loss 2-prong events could be attributed to reactions of the type $C^{12}(p, 2pxn)B^{11-x}$; to do this the reaction model described in chapter 9 was modified to calculate the various energy-loss distributions. The results are shown in figure 10.33 together with the experimental distributions≠.

It can be seen from figure 10.33athat the reaction $C^{12}(p, 2p3n)B^8$ is of no importance for explaining the experimental results.

≠ Because the 2-prong events were not measured with a microscope, as were the 3-prong events, a large number of events with one or two very short prongs were not measured (see appendix VII). This means that there are events missing from the high energy-loss end of the energy-loss distributions and consequently it is not possible to make a very accurate normalization of the distributions predicted by the model to the experimental distributions. The normalizations shown in figure 10.33 are, therefore, somewhat arbitrary.

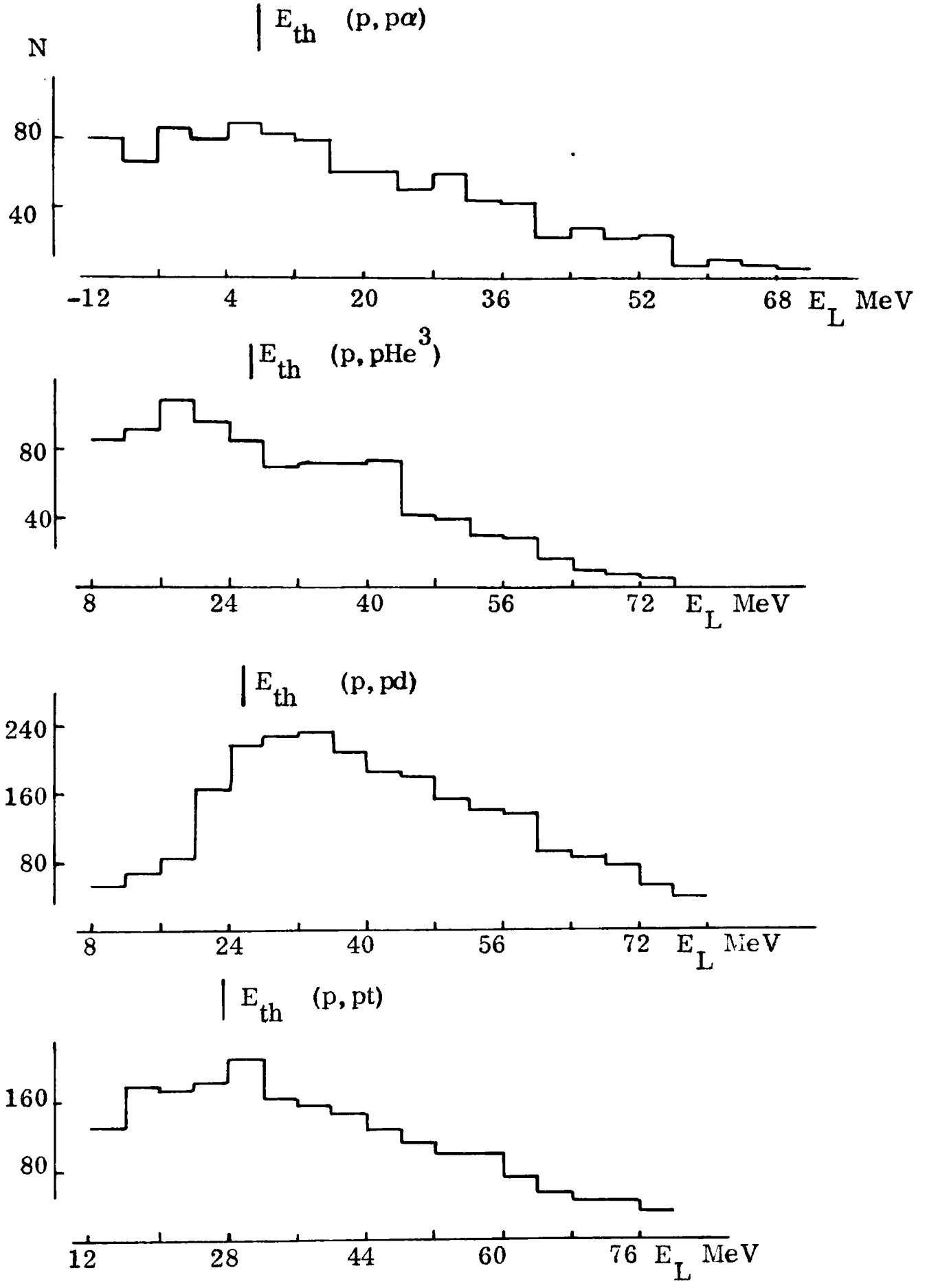

Fig. 10.32 Energy-loss distributions for 2-prong events according to several different reaction hypotheses.

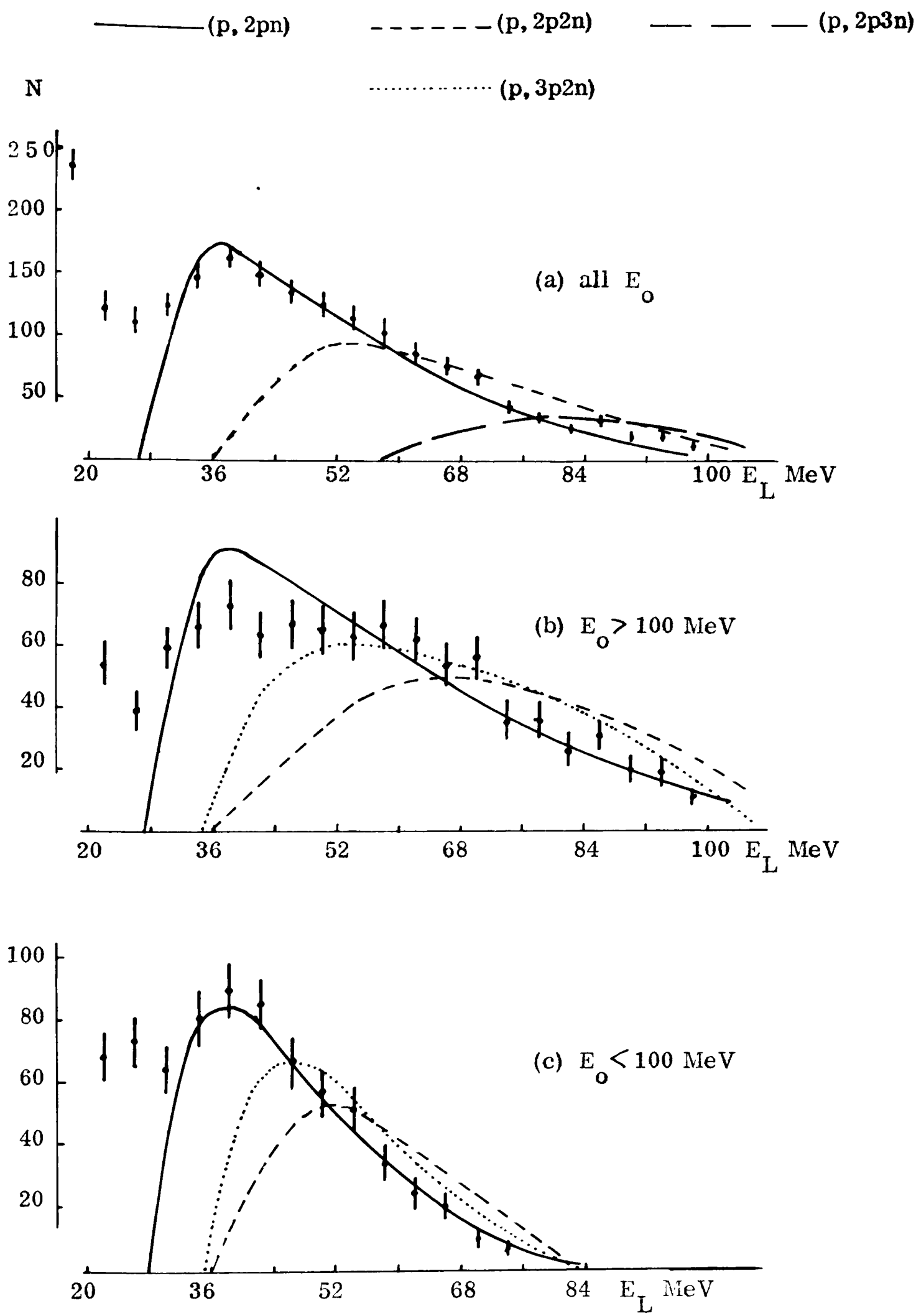

Fig. 10.33 Experimental energy-loss distributions and the cascade model results for various reactions.

If, as deduced from the 3-prong events, the α-particle substructure of C^{12} is important, and the (p, 3p2n) reaction has a very high cross-section, a large number of 2-prong events will be produced by (p, 3p2n) reactions in which one proton has insufficient energy to be detected. As well as the cascade model calculations for the (p, 2pxn) reactions, therefore, (p, 3p2n) reactions with one proton of energy below 5 MeV have also been simulated and the resulting predicted (p, 2p) energy-loss distributions are also shown in figure 10.33.

Several points emerge from an examination of figure 10.33. Firstly, the (p, 2pn) reaction alone could be responsible for all of the events observed at the lower incident proton energies and for a large proportion of the events at the higher incident energies. Secondly, either the reaction C^{12}(p, 3p2n)Be^{8} or the reaction C^{12}(p, 2p2n)B^{9} can account for all of the high energy-loss events (above $E_L \sim 50$ MeV for the (p, 3p2n) reaction and above $E_L \sim 60$ MeV for the (p, 2p2n) reaction) for both incident energy regions. Taking the curve normalizations given in figure 10.33 for these two reactions in turn, the residues of events that they leave unaccounted for are obtained by subtracting the curves from the experimental distributions; these are shown in figures 10.34 to 10.37. In the case of the reactions C^{12}(p, 3p2n)Be^{8}, the residual events for both incident energy regions all lie in the region of energy-loss expected for the quasi-elastic (p, 2p) reaction involving the knock-out of an s-shell proton (E_L = 34 MeV, $\Delta E_L = \pm 5$ MeV (TYREN et al. 1965)). In the case of the (p, 2p2n) reaction at the higher incident energies, there are residual events

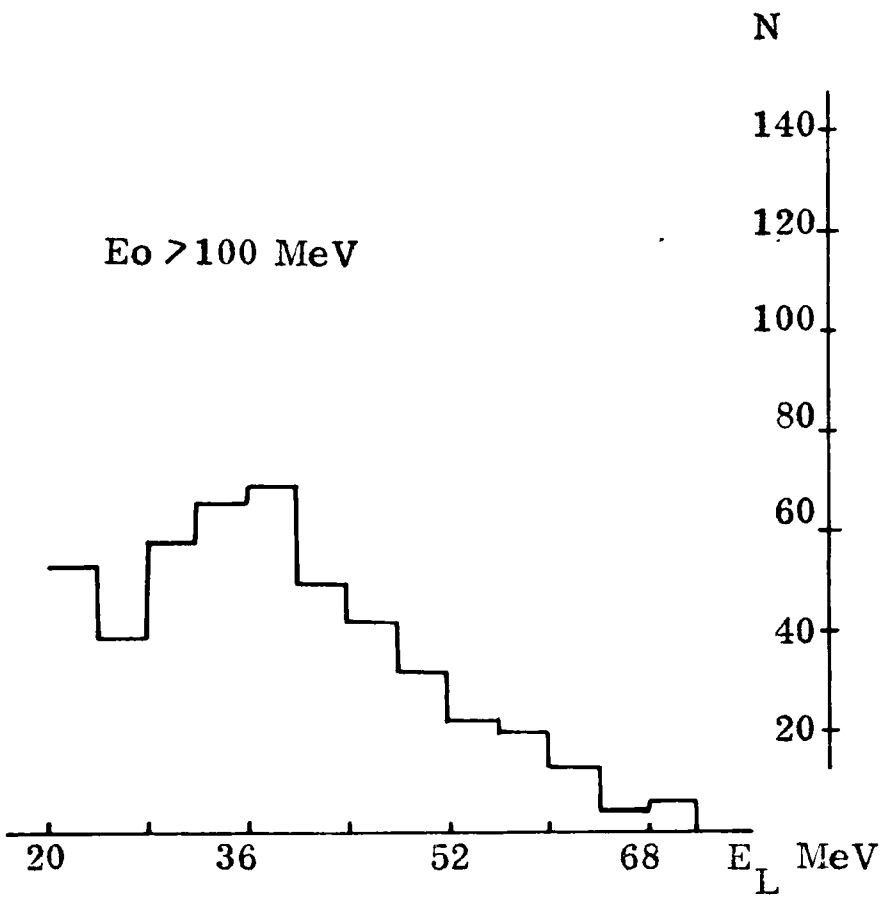

Fig. 10.34 Residual (p, 2p) energy-loss distribution after the subtraction of the (p, 2p2n) curve.

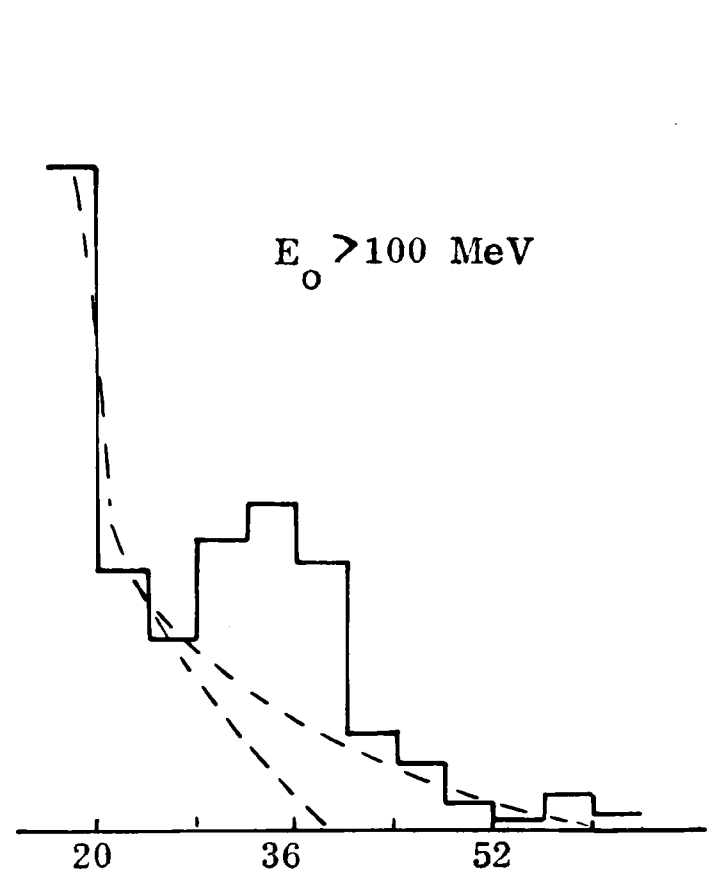

Fig. 10.35 Residual (p, 2p) energy-loss distribution after the subtraction of the (p, 3p2n) curve.

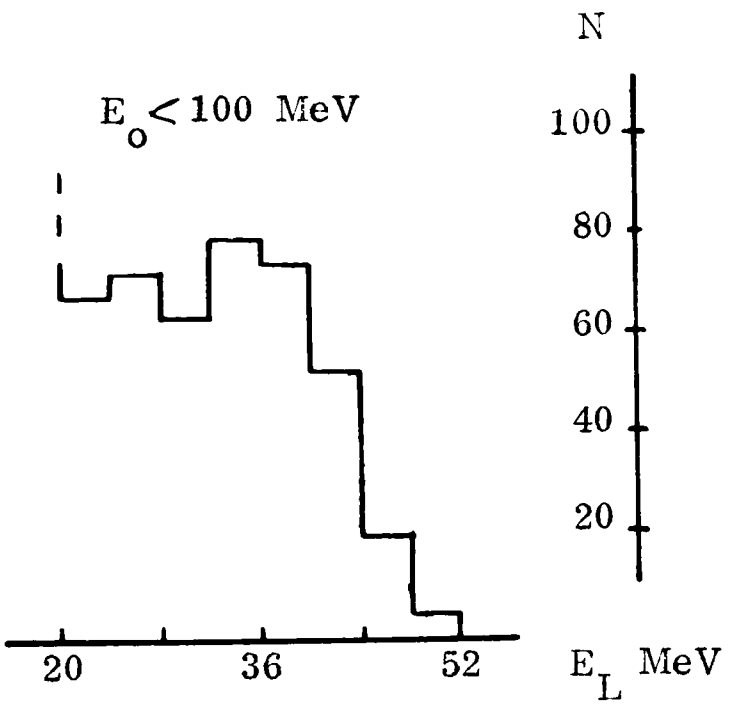

Fig. 10.36 Residual (p, 2p) energy-loss distribution after the subtraction of the (p, 2p2n) curve.

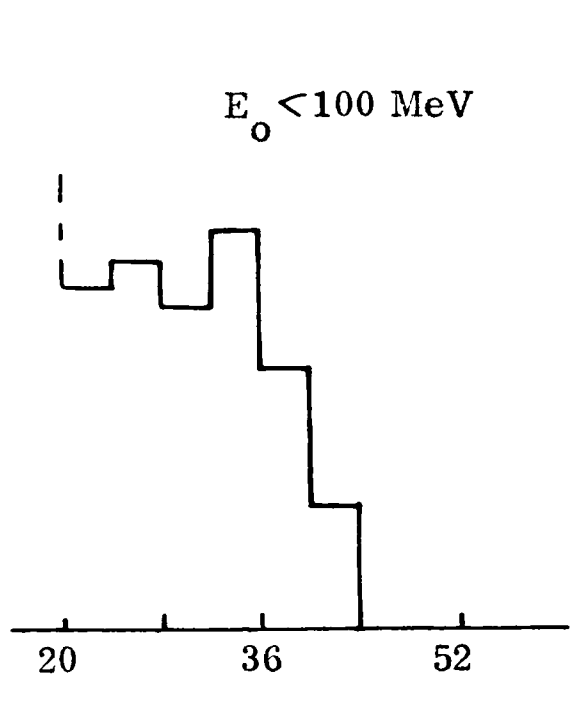

Fig. 10.37. Residual (p, 2p) energy-loss distribution after the subtraction of the (p, 3p2n) curve.

in the region of the quasi-elastic s-shell binding energy and also some above the range of energy-losses covered by the quasi-elastic reaction.

Unfortunately, a very wide range of suitably normalized combinations of contributions from the reactions $C^{12}(p, 2p)_g B^{11}$, $C^{12}(p, 3p2n)Be^{8}$, $C^{12}(p, 2pn)B^{10}$, and $C^{12}(p, 2p2n)B^{9}$ will give (p, 2p) energy-loss distributions that fit the experimentally observed distribution so that, whilst it is established that the experimental results for the high (p, 2p) energy-loss events are consistent with the results to be expected from nucleon cascade reactions, it is not possible to determine the relative importances of the various reactions. However, the following points can be made.

Firstly, one way of fitting the experimental results is by a combination of the two reactions $C^{12}(p, 2p)_g B^{11}$ and $C^{12}(p, 3p2n)Be^{8}$ (one proton energy < 5 MeV). Taking the extreme case of no contributions from the (p, 2pn) and (p, 2p2n) reactions, and accepting the normalization of the predicted (p, 3p2n) energy-loss curve shown in figure 10.33b for the events with $E_o > 100$ MeV, the residue of events, shown in figure 10.35, represents the quasi-elastic $(p, 2p)_g$ reaction and the background of unclean knock-out (p, 2p) reactions only. An order of magnitude determination of the quasi-elastic $(p, 2p)_g$ reaction in the energy range 100 MeV to 130 MeV can be made from these events. The dotted curves show two alternative estimates for the background events and on subtracting these from the histogram, the two estimates obtained for the number of s-shell events are 100 and 160. Taking the average of these and assuming that the events are subject to exactly the same corrections as the p-shell events (see section 7.4),

the estimated s-shell cross-section for 100 MeV$< E_o <$ 130 MeV is ~ 8 mb; this is approximately half of the cross-section calculated for the quasi-elastic knock-out of p-shell protons. Since there are half as many s-shell protons in C^{12} as p-shell protons, this value is probably$^{\neq}$ of the correct order of magnitude for the cross-section. This result shows that it is not unreasonable to hypothesize that the reaction $C^{12}(p, 3p2n)Be^{8}$ is the dominant contributor to the high energy-loss 2-prong events and it is therefore concluded that the results from the 2-prong events are consistent with the conclusions reached in the previous section, i.e. that the α-particle substructure in C^{12} plays an important part in determining the course of the nucleon-nucleus reaction.

Secondly, admitting the fallibility of the above deductions and looking at the results in another way, the fact that the (p, 2pn) reaction gives rise to an energy-loss distribution with a pronounced peak in the same region as the energy-loss for quasi-elastic $(p, 2p)_s$ reactions shows that it is not necessarily correct to attribute the experimentally observed peak to the quasi-elastic reaction, as has been the custom of previous authors.

10.9 The 4-prong events

Sixty-one 4-prong events were measured. The experimental information on the distribution of these events with incident energy and (p, 4p) energy-loss is shown in figure 10.38. In figure 10.39 the spectrum of the energies of the prongs, treated as protons, is given.

$^{\neq}$ See the comments in the footnote on page 83

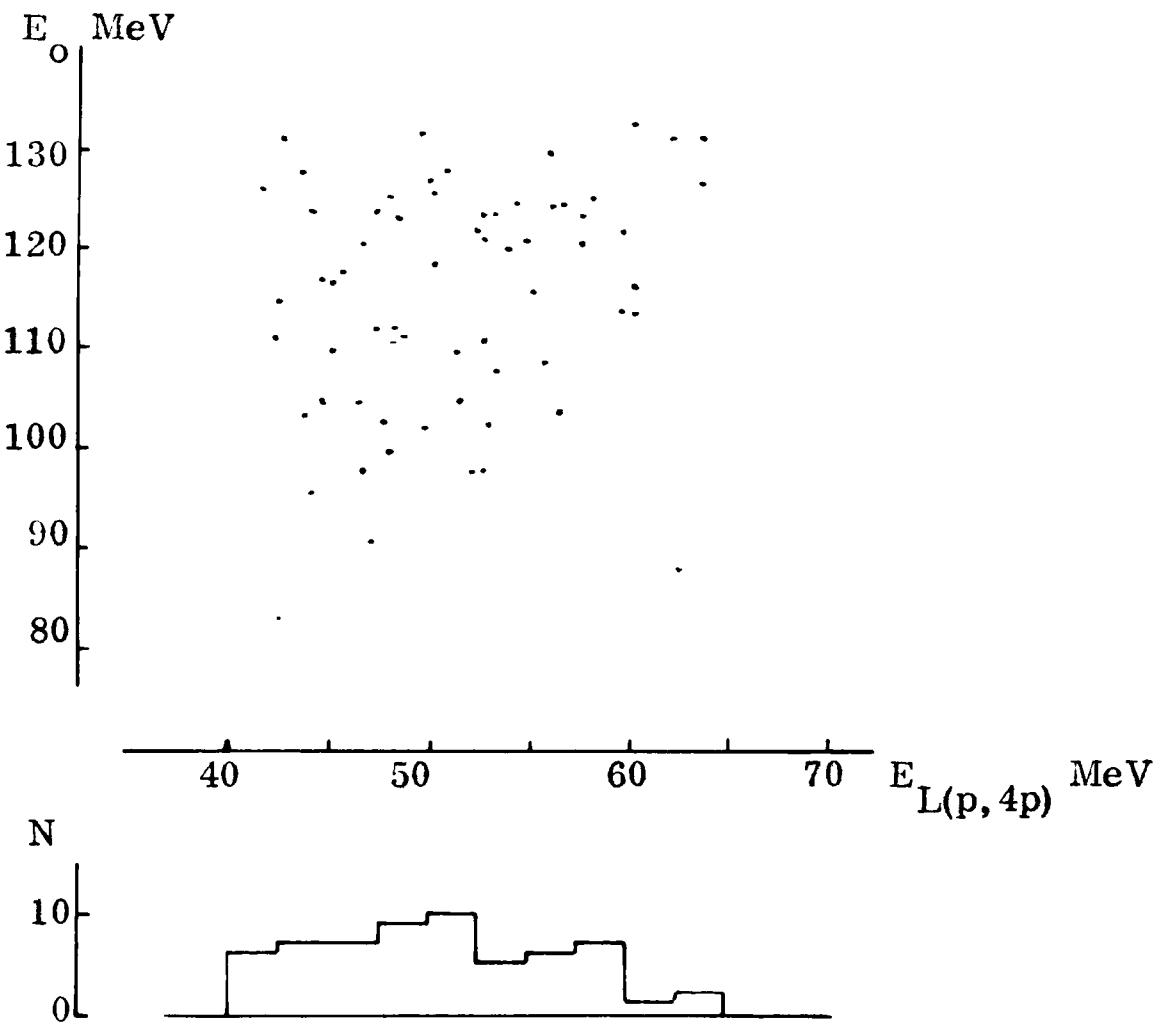

Fig. 10.38 Distribution of the 4-prong events with incident energy and with (p, 4p) energy-loss.

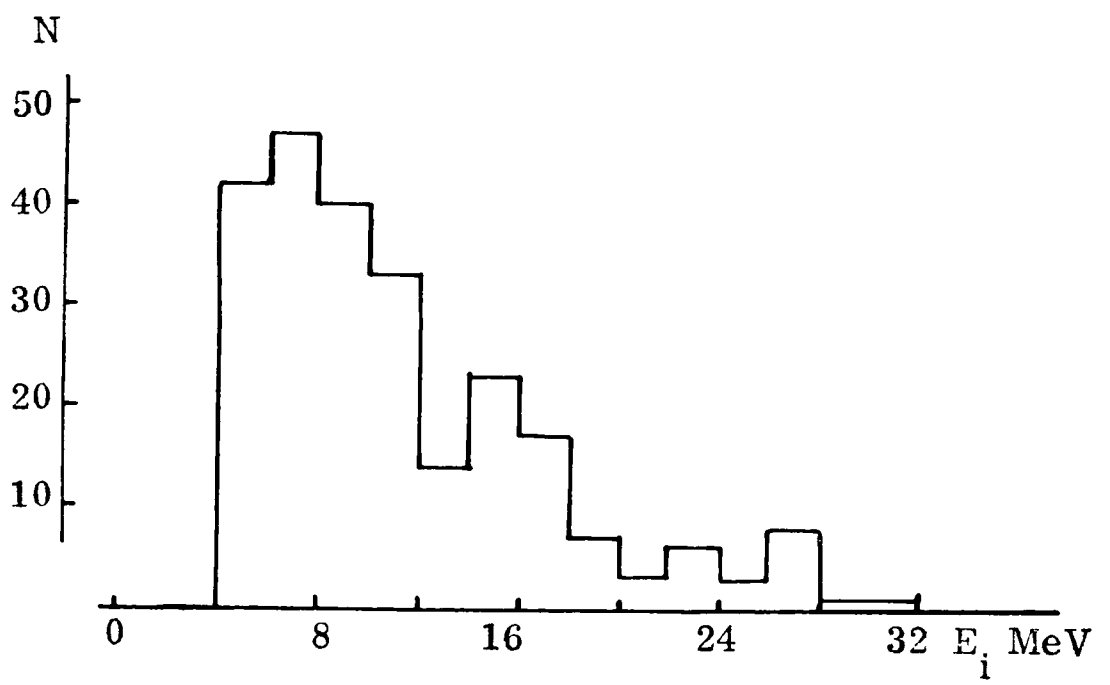

Fig. 10.39 Distribution of proton energies for the 4-prong events.

The presence of the reaction $p + C^{12} \rightarrow p + 3\alpha$ was tested for, but in the energy-loss distribution obtained when the events were reconstructed according to this hypothesis there was no evidence of a peak at zero; this reaction is, therefore, not being observed.

The (p, 4p) energy-loss distribution is of the same nature as the 3-prong (p, 3p) energy-loss distribution and the 2-prong (p, 2p) energy-loss distribution above the p-shell peak. It seems likely, therefore, that the 4-prong events are also caused by reactions of the type $C^{12}(p, 4p\alpha n)Li^{5-x}$.

CHAPTER 11

CONCLUDING REMARKS

The work reported has provided the author with interesting and valuable experience in the fields of experimental techniques, data processing, computer programming and manipulation, and the interpretation of experimental results in terms of the physics of the nucleus.

The quasi-elastic nature of the $C^{12}(p, 2p)$ reaction leaving the residual B^{11} nucleus in its ground state, previously established by other experimenters, has been confirmed, and the energy dependence of the cross-section between 50 MeV and 139 MeV has been seen to be consistent with the effect of the Pauli principle, operating within the nucleus, on the free proton-proton cross-section. For the higher incident energies the measured cross-section is in agreement with the results of other experimenters.

It has not been possible to study the quasi-elastic reaction involving s-shell protons nor to measure its cross-section, because events from this reaction were not separable from the events from other reactions.

Multiple scattering of nucleons within the C^{12} nucleus, leading to the establishment of intranuclear nucleon cascades has been shown to be extremely important; nucleon cascades and evaporation reactions can account for the majority of the 2-prong events and for all the 3-prong events and 4-prong events, the production of the low excited states of B^{11} has also been seen to be consistent with multiple scattering of the protons produced in the quasi-elastic reaction.

It seems surprising that nucleon cascade and evaporation reactions are so important in a nucleus of only twelve nucleons. A possible explanation for this, deduced from the observation that the experimental evidence points to a very large cross-section for the reaction $C^{12}(p, 3p2n)Be^{8}$ is that α-particle substructure effects in the nucleus are frequently responsible for the ejection of four nucleons from the nucleus when it is disturbed by the incidence of a high energy nucleon.

By setting up a proton beam with very little energy spread in it, the propane bubble chamber has been used at the limit of its resolution (determined by straggling). The main disadvantages of the apparatus have proved to be its inability (a) to differentiate between protons and other charged particles, (b) to detect protons with energies below 5 to 10 MeV, and (c), in common with most other detectors, to detect neutrons. The first two disadvantages could be alleviated by using for the study a diamond loaded emulsion or a cloud chamber; both of these methods have their own disadvantages but the former has been used successfully by Zhdanov & Fedotov for 660 MeV protons.

Perhaps the most useful next step would be to compare the experimental results with predictions of sophisticated Monte Carlo calculations, it would be particularly interesting if the effects of α-particle substructures in the nucleus could be simulated in such calculations.

Appendices

Appendix I

Technical Notes

1. The chamber body was machined from a solid dural block $15\frac{1}{2}$" x $18\frac{1}{2}$" x $12\frac{1}{2}$". Supplied and heat treated by "Northern Aluminium Co. Ltd."
2. "Heavell" Compressor able to supply ½ litre of air/sec at 55 atmos.
3. 'Foxboro' Needle Valve
4. "Foxboro" M/40 Stabilog Pressure Controller
5. "Barksdale" Crescent Series Valve. Model A1038
6. Supplied by 'Marston Excellsior Ltd." (I.C.I.) MM341
7. "G.E.C." FT 230
8. "Dallmeyer" Series F/6.5. Wide angle, astigmatic and coated. Focal length 2 3/8".
9. "Ilford" 35 mm perforated Pan F film
10. "Ericson" GR 10G
11. 99% pure propane from "Calor Gas".

Appendix II

Choice of Aperure for the Camera Lenses

The diagram shows the image space of a camera lens. It is assumed that the bubbles in the chamber act as point sources and for simplicity, only points on the principal axis of the lens are considered.

I_1 is the image point for a point in the centre of the chamber

I_2 is the image point for a point on the bubble chamber window

M is the plane of the film

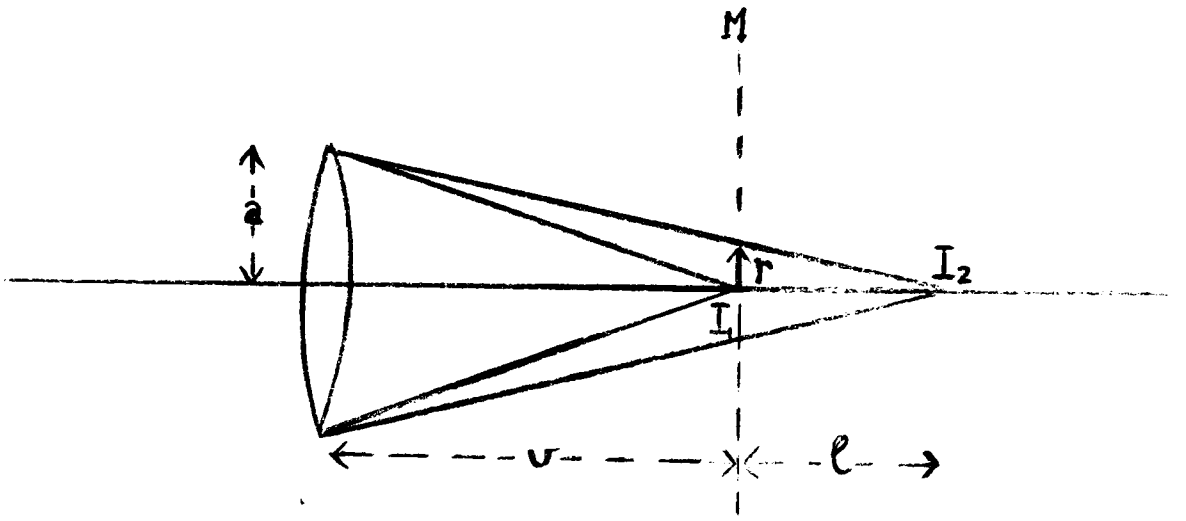

The radius (r) at M of the light cone of I_2 is given by

$$\frac{a}{v+\ell} = \frac{r}{\ell}$$

and since $\ell \ll v$

$$r = \frac{\ell a}{v} \qquad (1)$$

Thus, to reduce the loss of resolution due to this geometrical effect, the aperture radius a should be as small as possible. However, as a is reduced, diffraction effects become important.

Using the Rayleigh criterion, the diffraction radius for the image I_1 can be written as

$$r' = \frac{1.22\lambda v}{a} \tag{2}$$

The optimum resolution over the whole chamber will be achieved when $r \sim r'$; that is when

$$\frac{1.22\lambda v}{a} = \frac{fa}{v} \tag{3}$$

if D is the depth of field in the object space and m is the demagnification from the bubble chamber to the film

$$f = \frac{D}{2m^2} \tag{4}$$

and equation (3) gives

$$a = v\sqrt{\frac{2.44\lambda m^2}{D}} \tag{5}$$

Since $u \sim 13f$, $v \sim f$, the focal length of the lens.

Therefore the stop number (F) of the lens is given by

$$F = \frac{f}{2a} = \frac{1}{2m}\sqrt{\frac{D}{2.44\lambda}} \tag{6}$$

Using the relevant values

$m = 14$

$\bar{\lambda} = 5 \times 10^{-5}$ cms

$D = 30$ cms

$$\underline{F = 19}$$

The number of bubbles (n) resolved per centimetre in the object space $(= \frac{1}{2mr})$ is given from equations (1) and (4)

$$n = \frac{2mF}{D}$$

$$\underline{n \sim 18 \text{ bubbles/cm}}$$

From microscope observations on the film it is found that at P19 20 to 25 bubbles/cm are resolved - in good agreement with the result from the approximate treatment given above. A more detailed treatment is not justified because of the somewhat arbitrary nature of the Rayleigh criterion.

Appendix III

The magnification of an energy spread in a proton beam as it is degraded in energy

In the diagram

R is the residual range in propane of a proton of energy E

dE is the initial RMS energy spread in the beam

R+dR is the residual range of a proton of energy E + dE

and E_o is the energy of the protons at the plane A

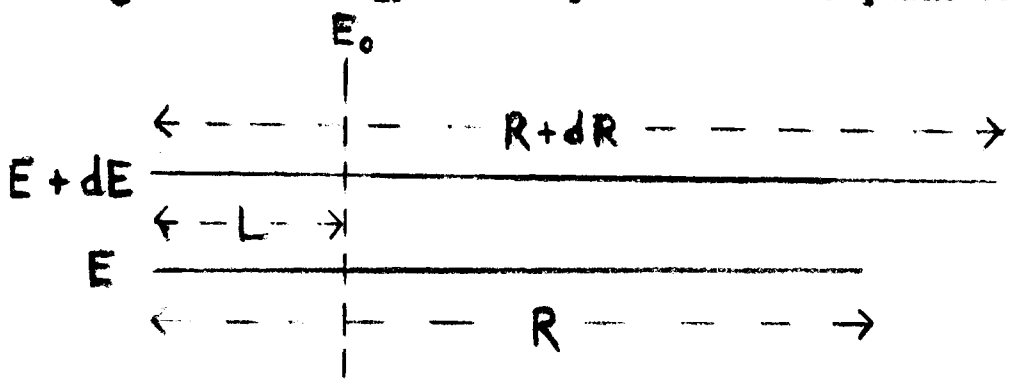

It is required to find the energy spread at the plane A when energies are measured by the method of residual ranges.

A range-energy relationship of the form $E = AR^B$ is assumed; this introduces an error of less than 1%.

Using this, the difference in ranges of the two protons is

$$dR = \frac{dE}{ABR^{B-1}} \qquad (1)$$

The energy difference (dE_{o1}) at plane A, measured by the method of residual ranges is

$$dE_{o1} = A(R+dR-L)^B - A(R-L)^B \qquad (2)$$

For $\frac{dR}{R-L} \ll 1$ which applies for all but the last centimetre or so of the path in propane

$$dE_{ol} = \frac{ABdR}{(R-L)^{1-B}} \tag{3}$$

The expression can be presented more concisely if the approximation $B = 0.5$ is made ($B \sim 0.54$). Using this approximation and substituting for dR

$$dE_{ol} = \frac{EdE}{A\sqrt{R-L}} \tag{4}$$

Appendix IV

The energy spread in a proton beam as it is degraded in energy due to the statistical nature of the slowing down process

STERNHEIMER (1960) has calculated the RMS percentage straggle in the range of a stopped proton beam (the straggle coefficient) for a series of elements and incident energies.

Consider the energy uncertainty due to this effect at a depth of penetration L where the average beam energy is E_o

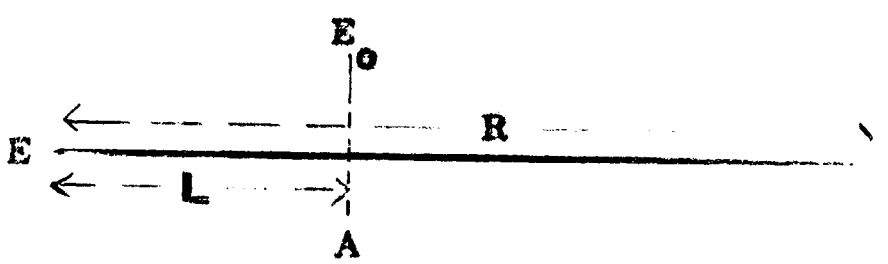

For protons of a given energy E_o at the depth L, the straggle in the range produced by stopping them is

$$k_o (R-L)$$

where k_o is the straggle coefficient for protons of energy E_o.

The total range straggle produced by stopping the incident protons is

$$kR$$

where k is the straggle coefficient for protons of energy E. The range straggle produced up to the plane A can therefore be expressed as

$$dL = \sqrt{k^2R^2 - k_o^2 (R-L)^2} \qquad (1)$$

The equivalent RMS spread in energies at A is obtained from the range-energy relationship

$$E_o = A(R-L)^B$$

hence $$\left| dE_{o2} \right| = AB(R-L)^{B-1} dL \tag{2}$$

and substituting for dL

$$dE_{o2} = AB(R-L)^{B-1} \sqrt{k^2 R - k_o^2 (R-L)^2} \tag{3}$$

Making the approximation B = 0.5, as in the previous appendix, and assuming that $k = k_o$ = constant (true to within $\pm$ 5%) equation (3) can be written as

$$dE_{o2} = \frac{kA}{2} \sqrt{\frac{2RL - L^2}{R-L}} \tag{4}$$

Appendix V

A. Scanning Procedure

Use, on view 1, the template provided.
CD defines the beam entry window;
AB defines the edge of the illuminated region; tracks should be visible from here on.

The chamber is divided into ten regions, labelled 1 to 10 on the template.

1. Selection of a frame

Firstly, decide whether or not the frame is to be "accepted". To do this, ask the following question: Can I see, quite clearly, everything that happens on this frame? If the answer to this question is 'no', the frame is to be rejected and noted on a separate scanning sheet.

2. Selection of an event

Having accepted a frame, scan it for 2-prong, 3-prong and 4-prong events.

If an event is seen:

(a) Check on view 1 that the incident proton has entered through the beam window; the track, when projected backwards, should intersect the line CD. If it does not, ignore the event.

(b) Check on view 1 that the angle made by the incident track with the reference line is less than 3^{o} (the incident track is to be considered only over the first 2" or so). If the angle is larger than 3^{o}, ignore the event.

(c) Check ON ALL VIEWS that there is no scatter on the incident track. The diagram below shows such a scatter and indicates that unless care is taken the scatter may be overlooked.

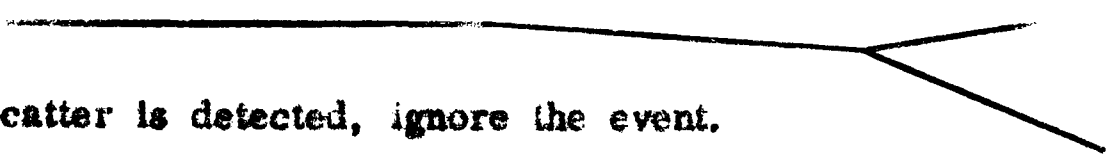

If a scatter is detected, ignore the event.

3. Recording of an event

Fill in the first four columns on the scanning sheet.

Some events are very clearly 2-, 3-, or 4-prong events, but sometimes events may be wrongly classed if care is not taken.

(a) Apparent 0-prong events may have very short stubs,

e.g.

For such events, write "stub(s)" in the comment column of the scanning sheet. Record any uncertainty about the number of prongs.

(b) Apparent 1-prong events often have a short second prong,

e.g.

Record, where necessary, as above.

(c) If a 2-prong event with two short prongs is seen, look very carefully for the presence of a third prong, especially if the event occurs in the first half of the chamber. This is important as nearly all 3-prong events are of this type,

e.g.

Generally, for deciding on the number of prongs, all three views should be looked at.

4. Comments

Under the scanning sheet column headed "Comments", record, when relevant, the following features:

(a) Short stubs.

(b) An event that is visible on one or two views only.

(c) A scatter or event on one of the prongs of an event,

e.g. •

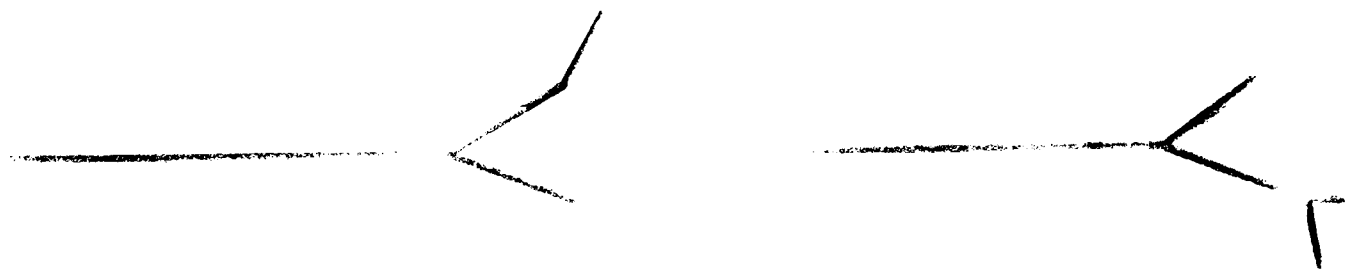

(d) Anything that appears unusual.

5. Beam Tracks

On every tenth frame count the number of "acceptable" beam tracks (see sections 2a and 2b) and record with the frame number.

6. Stopping Tracks

At the end of most of the rolls of film there are about 50 frames with tracks stopping at the end of the chamber, followed by some frames with tracks stopping halfway across the chamber.

Do not scan these frames for events but merely record the frame numbers.

B. Measuring Procedure for 2-prong Events

Set up the film on the measuring machine so that the tracks enter at the end close to you, and the frame number is on your right. The relevant views can be recognized by the fiducial positions: the position where the "George" and "Andrew" crosses are close together indicates the view number.

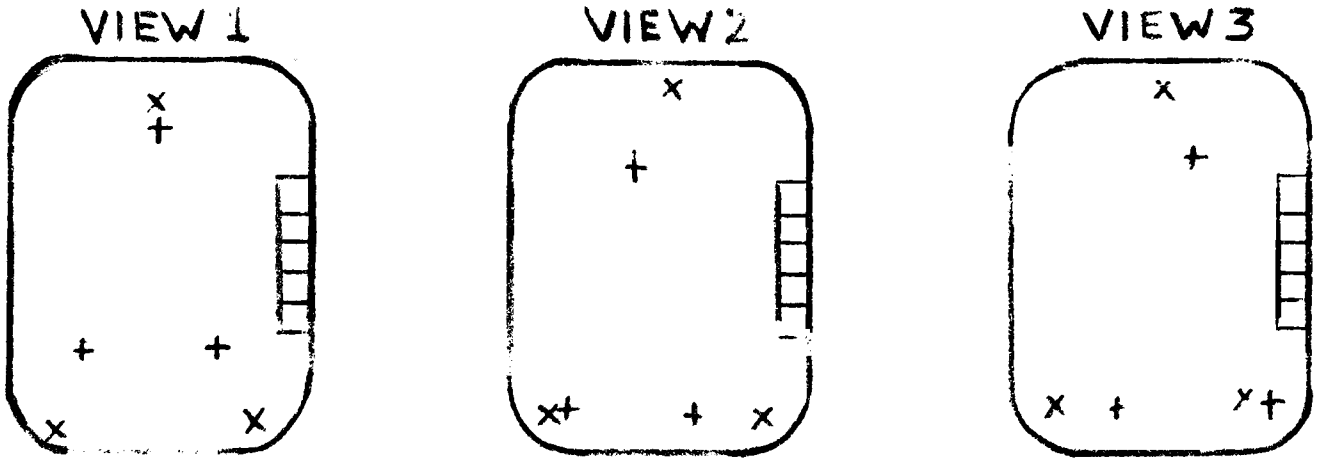

Firstly, look at the three views and decide upon which two the event concerned can most easily be measured; the appropriate view numbers will be included in the event identification number (I.D.)

Decide what type-number to associate with the event; the type-number determines the measuring procedure which has to be used. If the event has two long prongs (longer than about 1½ cms on the screen), it is a type 3 event; one long prong and one short prong characterize a type 2 event and two short prongs a type 1 event.

The following I.D. must be typed out immediately before each event measured:

Characters typed	Significance
→→	Event commences
5 digits	Frame number
1 digit	Event number. Events on each frame are numbered from the beam entry end of the chamber.
2 digits	View numbers used; in increasing order
1 digit	Event type-number

Then * For an event without complications
or ≠ If there is any uncertainty (e.g. about position of end point or presence of a scatter etc.)
or > If there is a very short stub

Then, taking the prongs clockwise, or in the case of a type 2 event, taking the shorter prong first, punch:

F.S. If neither prong scatters
or 1 If the first prong scatters
or 2 If the second prong scatters
or 3 If both prongs scatter

For a prong that has a scatter, take the scattering point as the end of the track.

For frames with more than one event, a new I.D. must be punched before each event.

Measurement

Choose the lower number view of the two selected and measure as indicated below:

(a) Zero the machine on the central fiducial mark - the fiducials to be used are the "Andrew" crosses. Punch out this co-ordinate and then proceed to measure fiducials 2 and 3 in order.

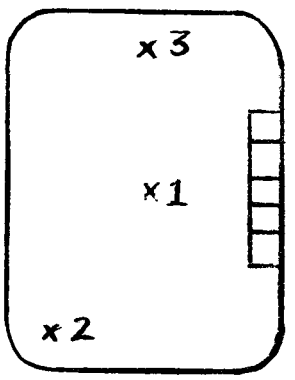

(b) Set the machine on the incident track close to the beginning of the track and punch out the co-ordinate. Repeat for a second point halfway along the track, and also for the apex.

Then,

For a type 1 event:

Measure the two end points, taking them in the order of a clockwise movement. Take great care to get an accurate setting.

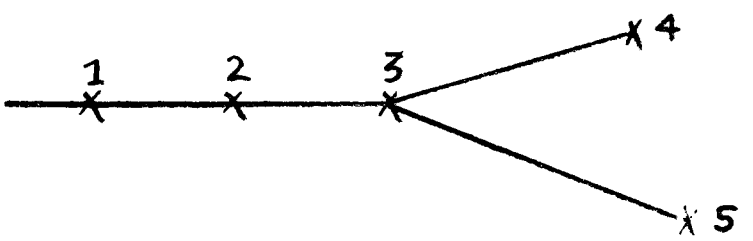

For a type 2 event:

Measure the end point of the **short** track first, then measure a point about 1" from the apex on the long track, and finally, measure the end point of the long track.

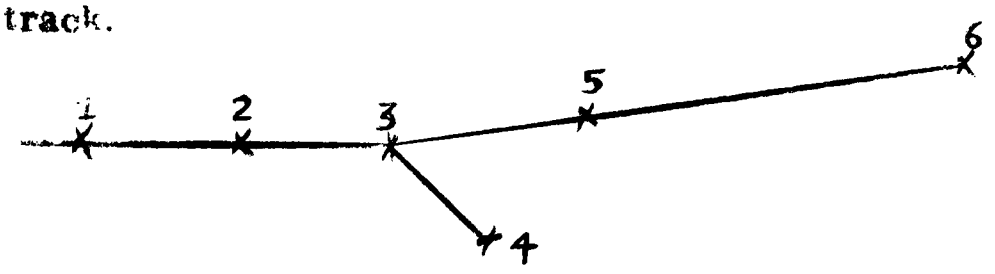

For a type 3 event:

Measure the prongs in a clockwise direction

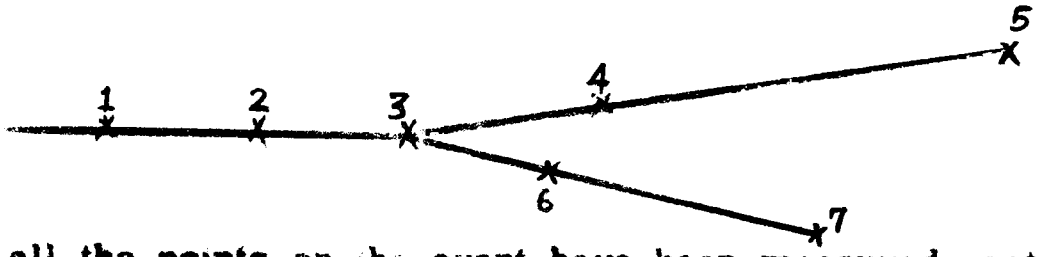

When all the points on the event have been measured, set the machine on fiducial 3 again and punch out.

Now return to the centre fiducial and check that the counters return to zero (within 3 to 5 counts on each axis). DO NOT punch out this point.

The measurement on the first view is now complete.

Switch to the second view and repeat the measuring procedure given above. When the second view has been finished (with the zero check), type out the symbol + on the data tape and run out some blank tape.

Cancellation Symbols

The following cancellation symbols are available for error removal:

(a) If an incorrect point is measured, type out the characters LS and * on the tape immediately after the erroneous measurement and remeasure the point.

(b) If several consecutive points are to be cancelled, type LS followed by the same number of *s as there are points to be cancelled.

(c) If a complete view is incorrect, then, AT THE END OF THE VIEW, type a comma.

(d) If after completing the measurement of an event it is to be cancelled, type a full stop and start again WITH A NEW I.D.

Cancellation symbols have no effect after the symbol + has been typed. In the case of discovering some error after typing +, either remove the event from the tape or cover the + and type the relevant cancellation symbol.

Before removing a data tape from the tape punching machine, terminate it with ten line-feeds.

Appendix VI

The reconstruction of corresponding points and incident track angles

The points measured on the measuring machine or on the microscope are in an arbitrarily oriented cartesian co-ordinate system (the machine system).

Camera positions and the various bubble chamber parameters are best expressed in a co-ordinate system linked to the fiducials etched on to the front face of the front window of the bubble chamber (the fiducial system).

For reconstruction, the most suitable co-ordinate system is linked to the line joining the intersections of the principal axes of the two views with the front of the chamber window (the camera system - see figure VI-1).

It is assumed in this appendix, as in chapter 5, that all co-ordinates are expressed in the camera system. The various transformations before and after the reconstruction of the event are performed in the analysis computer-program.

Consider the point P in the bubble chamber. Assuming no distortions in the camera lenses, it can be seen from figure VI-1 that similar triangles in the bubble chamber and on the left-hand view give

$$\frac{-Y}{X+l/2} = -\frac{y'}{x'} \qquad (1)$$

and

$$\frac{-Y}{y'} = \frac{r'}{\rho'} \qquad (2)$$

For the right-hand view

$$\frac{-Y}{l/2-X} = \frac{y''}{x''} \qquad (3)$$

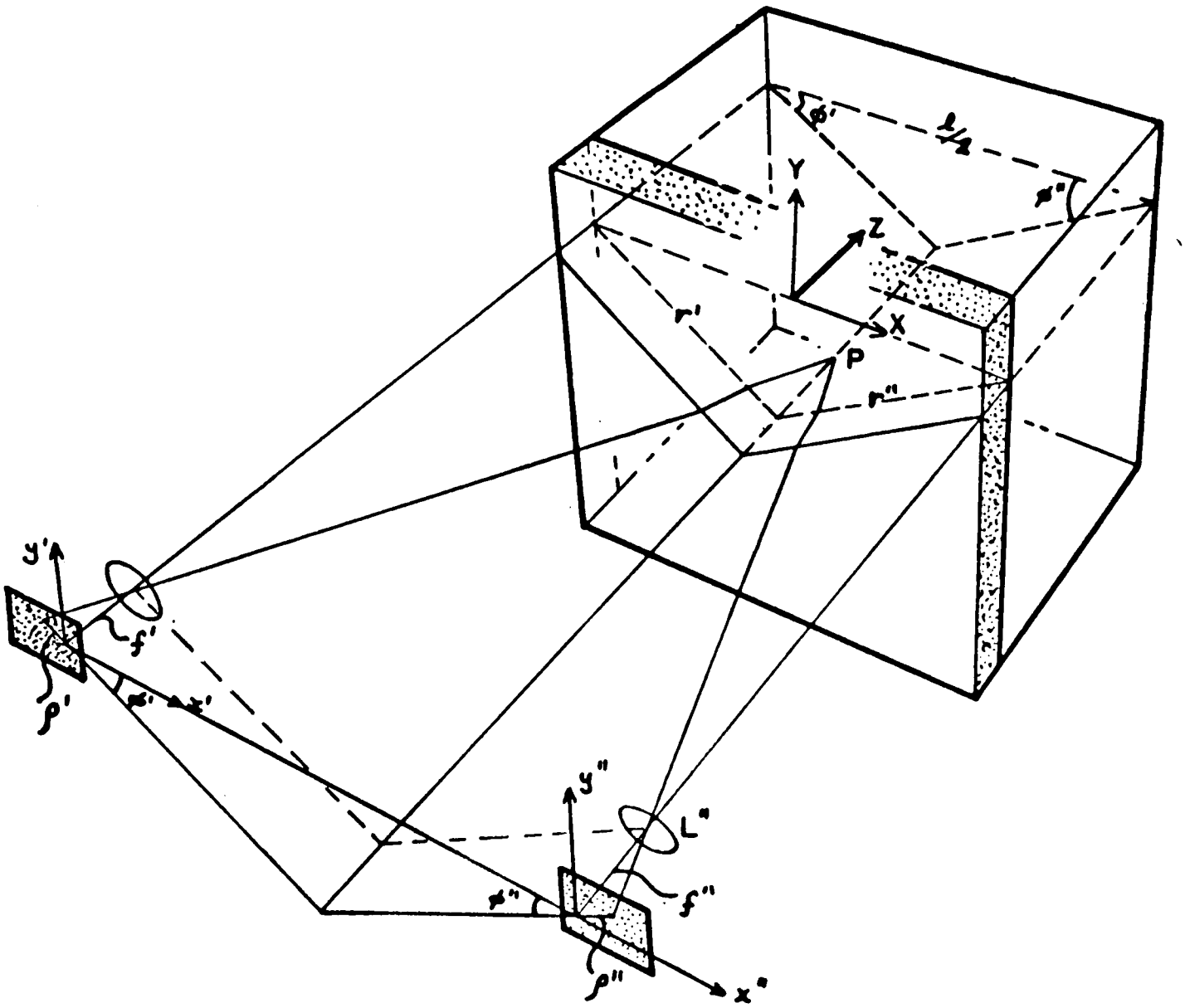

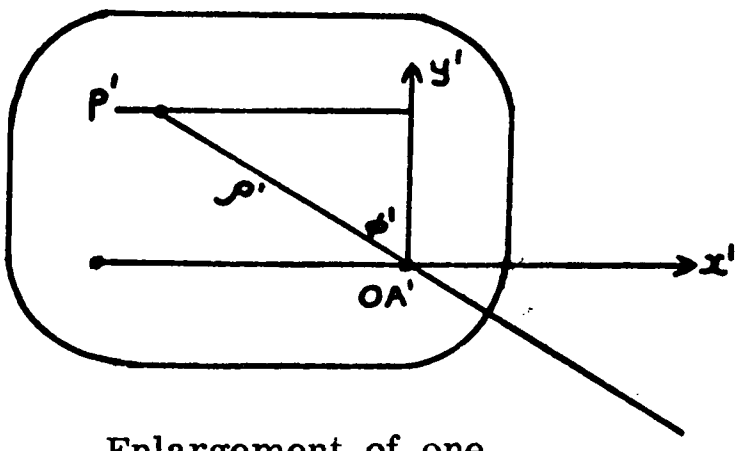

Enlargement of one of the image planes

FIG. VI-1 BUBBLE CHAMBER OPTICS

From (1) and (3)

$$\frac{\ell/2 - X}{X + \ell/2} = \frac{-y'x''}{y'x'}$$

$$X = \frac{\ell/2(y'x''+y'x')}{(y''x'-y'x'')} \quad (4)$$

$$Y = \frac{\ell\, y'y''}{(y'x'-y'x'')} \quad (5)$$

From figure VI-2

$$r' = \frac{\rho'}{f} d' + \delta \tan b + Z \tan a \quad (6)$$

and, $\tan c = \frac{\rho'}{f}$; $\frac{\sin c}{\sin b} = n^*$; $\frac{\sin c}{\sin a} = n$ (7)

therefore

$$\sin c = \frac{\rho'}{\sqrt{\rho'^2 + f^2}}$$

$$\tan b = \frac{\rho'}{\sqrt{n^{*2}f^2 + \rho'^2(n^{*2}-1)}}$$

$$\tan a = \frac{\rho'}{\sqrt{n^2 f^2 + \rho'^2(n^2-1)}}$$

Therefore, from equation (6)

$$\frac{r'}{\rho'} = \frac{d}{f} + \delta\left[n^{*2}f^2 + \rho'^2(n^{*2}-1)\right]^{-\frac{1}{2}} + Z\left[n^2 f^2 + \rho'^2(n^2-1)\right]^{-\frac{1}{2}} \quad (8)$$

From (2) and (5)

$$\frac{fy''}{y'x''-y''x'} = \frac{r'}{\rho'} \quad (9)$$

Therefore, using $\rho'^2 = (x'^2+y'^2)$ in (8) and (9)

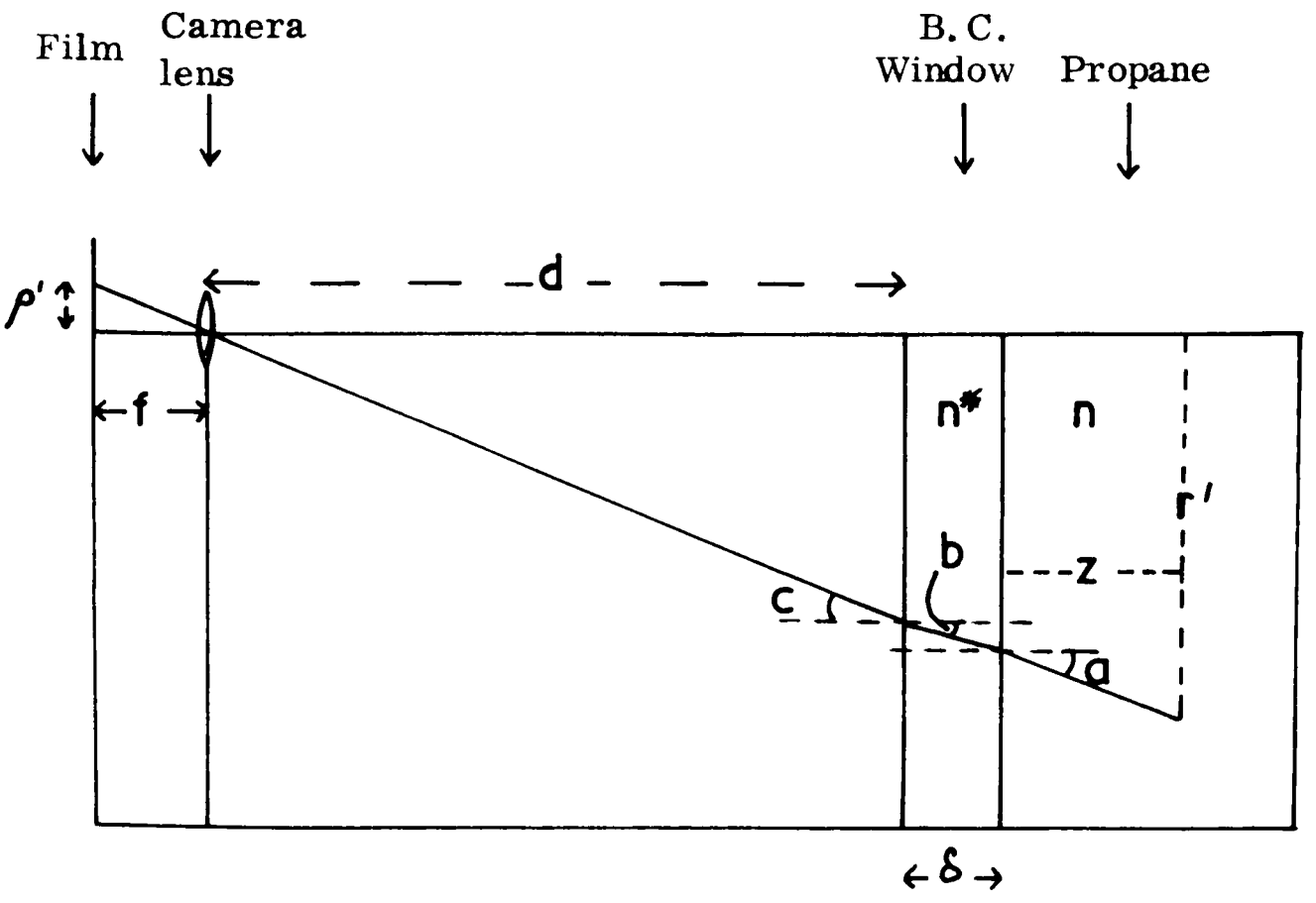

Fig. VI-2. Object to image ray in the normal plane.

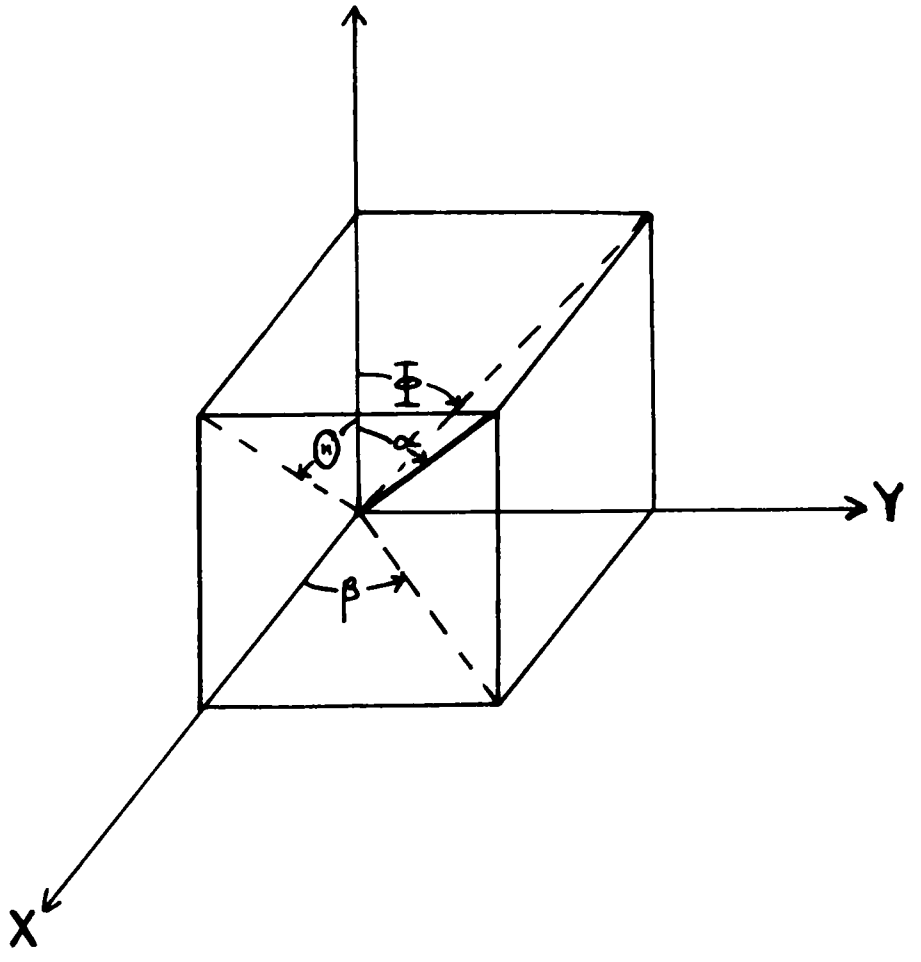

Fig. VI-3 Relationship between the various angles.

$$Z = \left[\frac{fy''}{(y'x''-y''x')} - \frac{d}{f} - \left\{n^{*2}f^2 + (x'^2+y'^2)(n^{*2}-1)\right\}^{-\frac{1}{2}}\right] \times$$

$$\left[n^2f^2 + (x'^2+y'^2)(n^2-1)\right]^{\frac{1}{2}} \qquad (10)$$

Equations (4), (5) and (10) give the exact first order reconstruction relationships.

The angles α and β and the co-ordinates of the apex of the event are used to define the incident track of an event. The auxiliary angles Θ and Φ are calculated first. The relationship between these angles is shown in figure VI-3.

Approximate forms of equations (4), (5) and (10) are used; these are derived by assuming that, for the small angles a, b and c

$$\tan(a; b; c) = \sin(a; b; c)$$

Using equations (6) and (7) and substituting for the tangents

$$r' = \rho'\frac{d}{f} + \rho'\frac{\delta}{fn^*} + \rho'\frac{Z}{fn}$$

Similarly $$r'' = \rho''\frac{d}{f} + \rho''\frac{\delta}{fn^*} + \rho''\frac{Z}{fn}$$

Therefore $$\frac{r'}{r''} = \frac{\rho'}{\rho''} \qquad (11)$$

and it can be seen from figure VI-1 that

$$\frac{y'}{y''} = \frac{\rho'\sin\phi'}{\rho''\sin\phi''} \qquad (12)$$

It follows from (11), (12) and the sine rule that $y' = y''$. From (2), (5) and (6)

$$\frac{fy''}{y'x'-y'x''} = \frac{d}{f} + \frac{Z}{fn} + \frac{\delta}{fn^*}$$

Inserting $y' = y''$

$$Z = n\left(\frac{\ell f}{x''-x'} - d - \frac{\delta}{n^*}\right) \tag{13}$$

and from (4) and (5)

$$X = \frac{\ell/2\,(x''+x')}{x'-x''} \tag{14}$$

$$Y = \frac{\ell y'}{x'-x''} \tag{15}$$

The errors arising from the approximation are about 1% in Z and about 0.2% in X and Y.

From equations (13) to (15)

$$y' = \frac{-nfY}{Z + nd + n\delta/n^*} \tag{16}$$

$$x' = \frac{-nf(X + \ell/2)}{Z + nd + n\delta/n^*} \tag{17}$$

Differentiating (16) and (17) and dividing

$$\frac{dy'}{dx'} = \tan \Phi' = \frac{Y - (Z + nd + n\delta/n^*) \tan \Theta}{X + \ell/2 - (Z + nd + n\delta/n^*) \tan \Phi} \tag{18}$$

where $\tan \Theta$ and $\tan \Phi$ have been substituted for $\frac{dX}{dZ}$ and $\frac{dY}{dZ}$ respectively

XYZ is a point on the incident track;

similarly

$$\tan \Phi'' = \frac{Y - (Z + nd + n\delta/n^*) \tan \Theta}{X - \ell/2 - (Z + nd + n\delta/n^*) \tan \Phi} \tag{19}$$

Solving (18) and (19)

$$\tan \Phi = \frac{(X-\ell/2) \tan \Phi'' - (X+\ell/2) \tan \Phi'}{(Z + nd + n\delta/n^*)(\tan \Phi'' - \tan \Phi')}$$

$$\tan \Theta = \frac{Y}{(Z + nd + n\delta/n^*)} - \frac{\ell \tan\Phi' \tan\Phi''}{(Z + nd + n\delta/n^*)(\tan\Phi''-\tan\Phi')}$$

From figure VI-3 it can be seen that, finally,

$$\beta = \tan^{-1} (\tan \Phi / \tan \theta)$$

and $$\alpha = \tan^{-1} (\tan \Phi / \sin \beta).$$

Appendix VII

A break-down of the 2-prong events

Figure VII-1 gives a detailed break-down of the events, listed at the scanning stage, into the various categories established during the measuring stage of the analysis. The following explanatory notes refer to the superscripts in the table.

(1) On average, an event had to be measured twice before its geometrical reconstruction passed the acceptance tolerances set in the program. To minimize measuring effort, those events that failed to pass the tolerances but were unquestionably hydrogen events were not remeasured. The establishment, in this way, of a set of events of inferior accuracy was permissible because accurate data was not required for all the hydrogen events.

(2) Events that fell outside the acceptance limits set on the beam angle and the Z co-ordinate of the event apex.

(3) The events with an energy-loss, $E_L = 0 \pm 5$ MeV, were classed as hydrogen events.

(4) Because events with a scatter on one or both prongs are not completely determined by measurement, their identity could not be determined by the energy-loss criterion. However, the hydrogen events could be recognized by a combination of their kinematical properties, and the incident energy distributions of the separated hydrogen and carbon components of the scatter events are shown in figure VII-II. A method of assessing the p-shell component of the carbon events follows from the following reasoning: the probability of a

scatter on a prong is a function of its energy, and the distribution of prong energies for p-shell events (E_L = 16 MeV) at an incident energy of E_o is very similar to that for hydrogen events at an incident energy of (E_o-16) MeV. Therefore, if:

N'_p = no. of p-shell events in the incident energy interval $E_o \pm dE$ with a scatter

N_p = no. of p-shell events without a scatter in the same energy interval,

N'_H = no. of hydrogen events in the incident energy interval (E_o-16) $\pm$ dE with a scatter, and

N_H = no. of hydrogen events without a scatter in the same energy interval

$$N'_p(E_o) = \frac{N'_H(E_o\text{-}16)}{N_H(E_o\text{-}16)} \cdot N_p(E_o).$$

The ratio $\frac{N'_H}{N_H}$ and the derived scattering component for p-shell events are shown in figure VII-11.

(5) For example: events with scatters on the incident track; events with a third, very short, prong; misleading scratch marks on the film.

(6) About 50% of these had one prong too short to be measured, 20% had both prongs too short, and 30% had end points or apices hidden by scratches, spurious tracks, distortions, etc. The first two sets will be accounted for by the short prong correction factor and are excluded from the analysis; the third set was approximately categorised by making ruler measurements on the projected images.

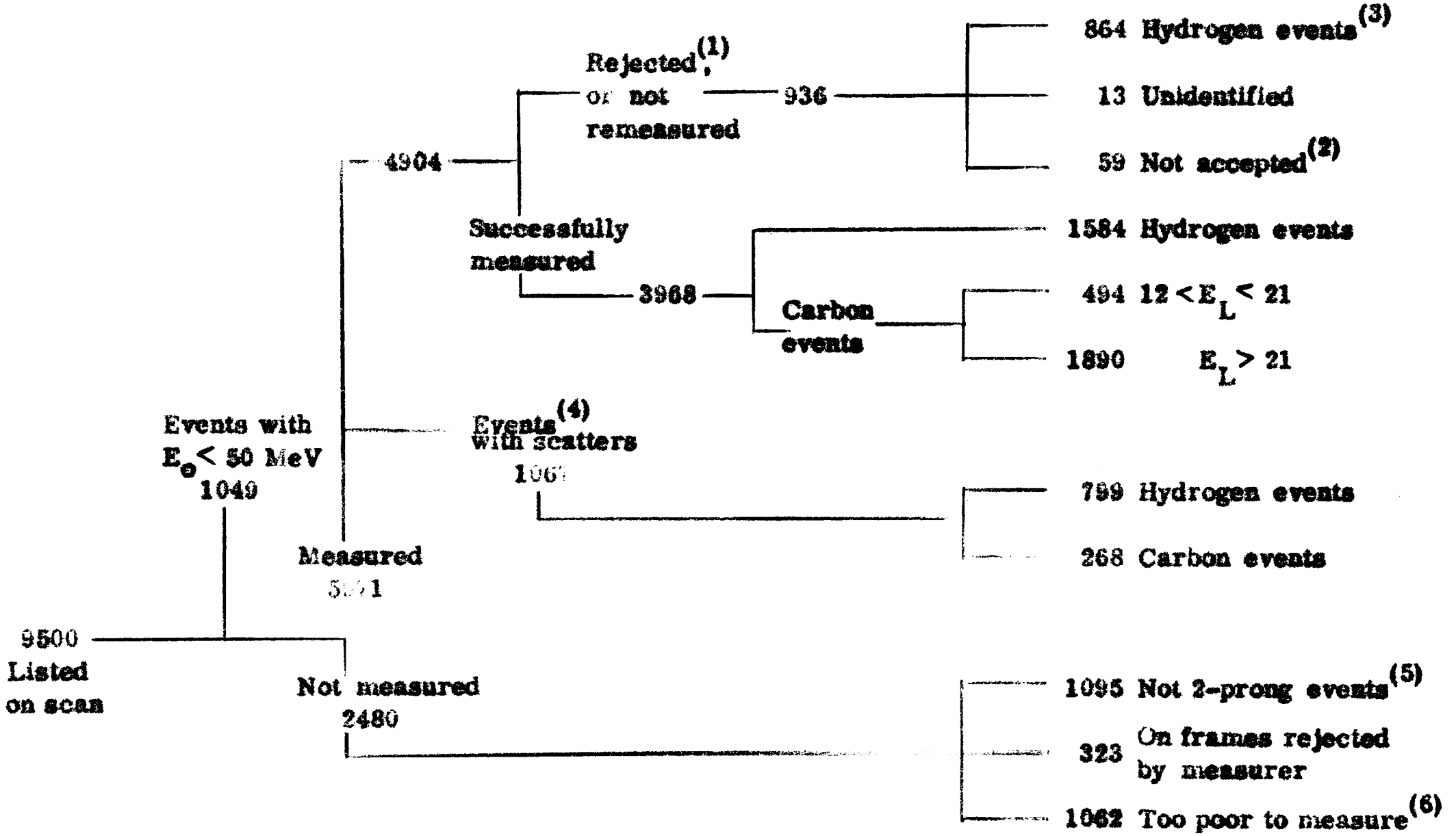

Figure VII-1. Summary of the measuring stage of the analysis.

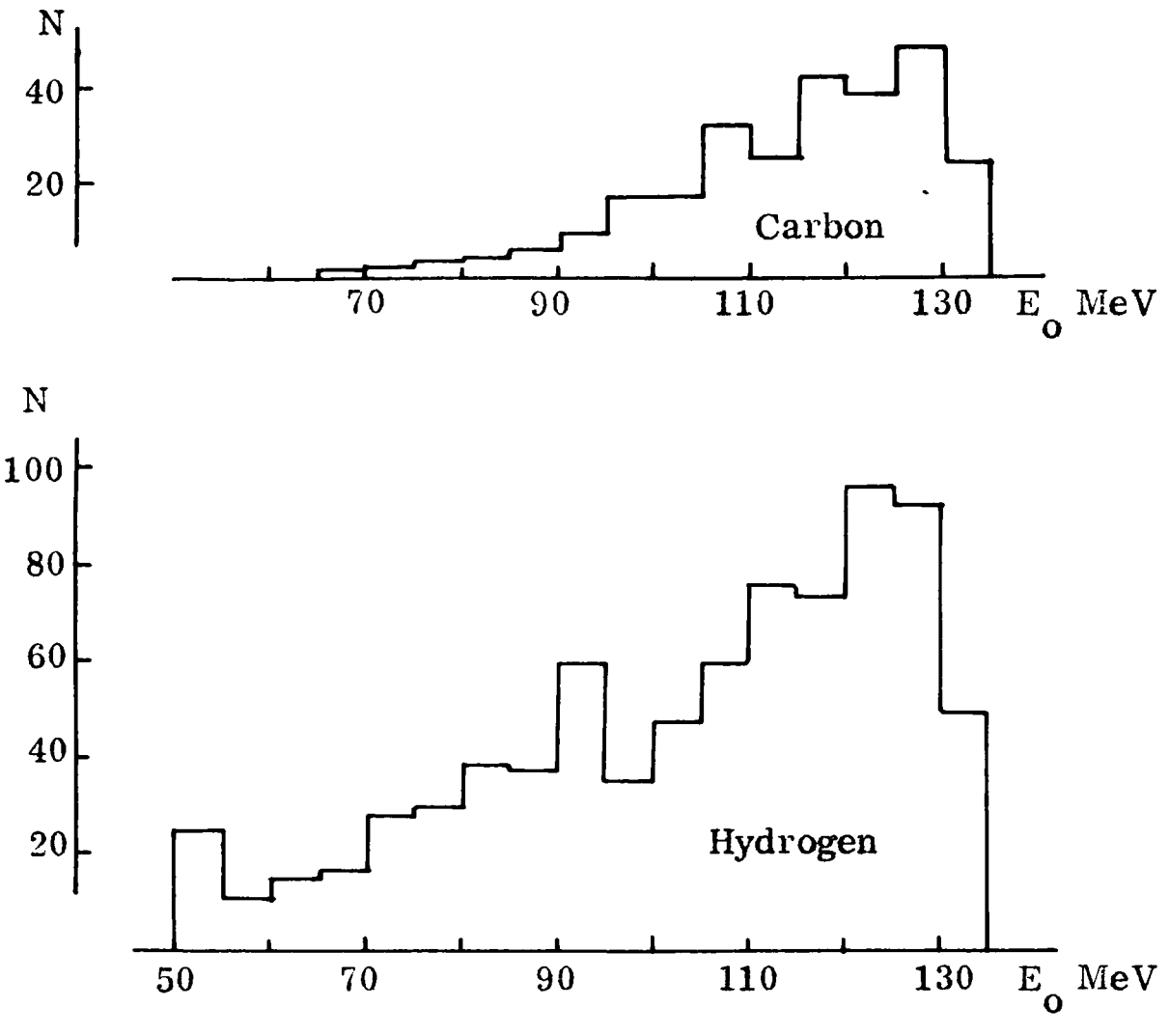

Function used to determine p-shell component

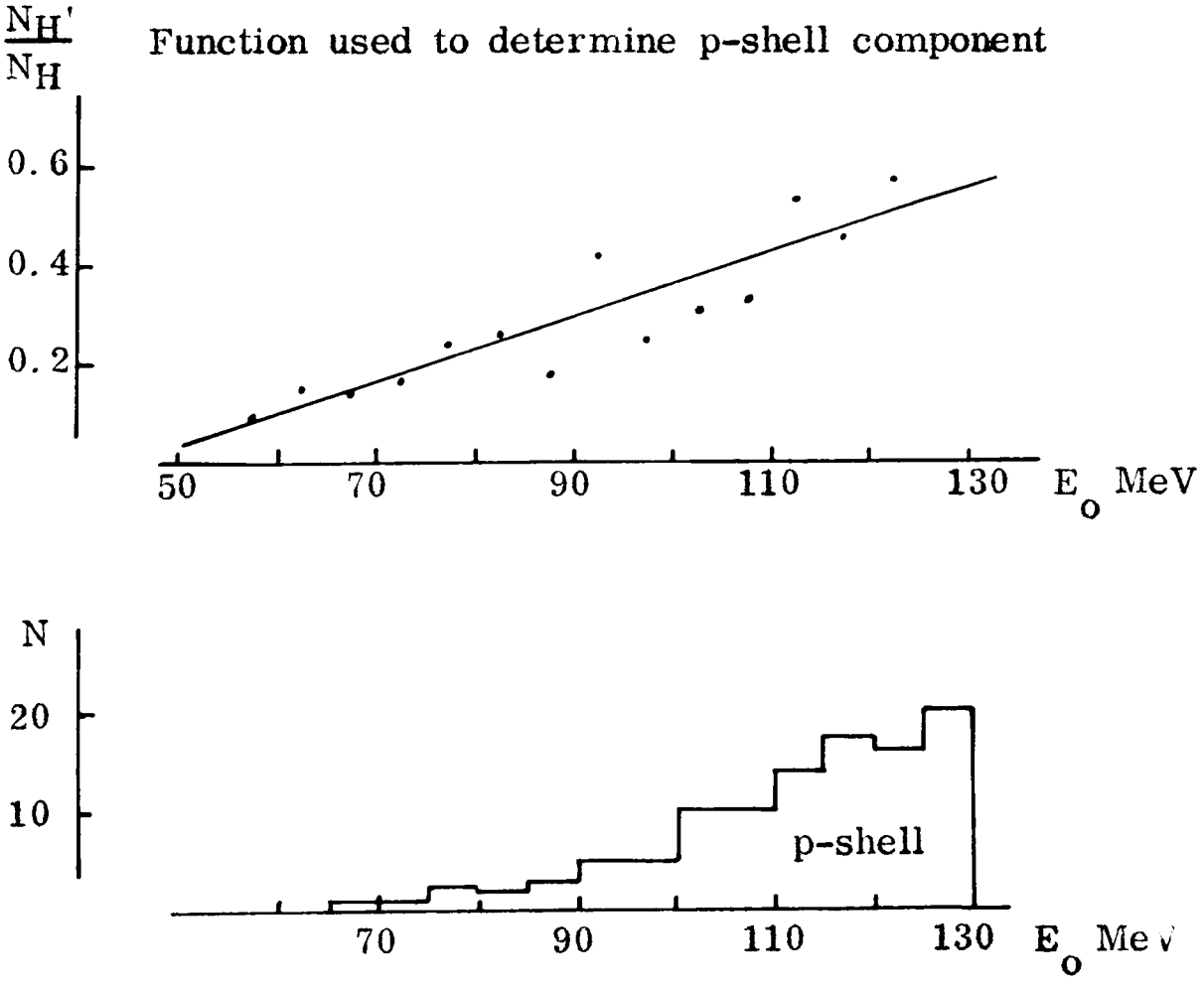

Fig. VII-II. Breakdown of the events with scatters.

P 180 (missing)

Appendix VIII

Basic data for the measured 3-prong events

The quantities given in the table are :

E_0 - the energy of the incident proton (MeV)

E_1, E_2, E_3 - the energies of the product particles (MeV), assumed to be protons, and calculated from the range-energy relationship given on page 69

$\theta_1, \theta_2, \theta_3$ - the angles that the product particles make with the direction of the incident proton (degrees)

$\theta_{12}, \theta_{13}, \theta_{23}$ - the angles between pairs of product particles (degrees)

From this data the components of the momentum for each proton can be obtained.

Choosing cartesian axes such that the z-axis lies along the beam direction, and the x axis lies along one of the product proton directions, the component momenta can be derived from the equations :

$$\underline{k}_i \cdot \underline{k}_j = k_{ix}k_{jx} + k_{iy}k_{jy} + k_{iz}k_{jz} = k_i k_j \cos\theta_{ij}$$

$i = 1, 2, 3 \qquad i \neq j$

E_o	E_1	E_2	E_3	θ_1	θ_2	θ_3	θ_{12}	θ_{13}	θ_{23}
120	8	14	33	36	110	106	104	136	110
73	15	6	11	52	32	143	74	133	114
129	6	55	8	53	36	120	77	151	96
131	23	5	8	61	36	116	95	172	84
99	5	9	30	65	67	91	73	111	43
97	9	18	24	90	60	53	96	63	106
131	8	11	41	132	50	69	106	114	119
131	20	51	11	88	24	60	89	147	61
111	8	10	20	71	82	92	107	112	17
87	15	8	22	67	35	101	102	74	117
90	15	20	9	107	47	97	125	61	143
108	7	26	9	78	57	75	86	99	116
102	17	5	26	105	24	62	104	150	61
98	5	39	18	107	56	36	86	95	88
123	37	27	7	25	24	111	16	130	135
109	7	9	22	66	57	87	115	143	30
88	10	5	12	65	43	83	47	121	113
104	5	21	10	63	77	128	85	133	90
109	15	7	9	43	20	131	63	155	114
124	18	9	12	42	35	90	69	130	70
122	7	8	42	110	38	26	81	112	42
84	12	5	7	23	42	147	63	158	106
129	14	27	32	66	42	14	67	74	55
64	8	8	5	112	31	82	102	131	71
112	21	15	30	88	38	116	53	148	153
108	10	10	5	85	19	92	96	157	89
82	22	16	6	70	15	125	85	119	117
112	13	12	51	76	56	57	31	131	106
97	33	28	12	57	39	103	87	159	72
102	11	15	29	97	48	25	98	117	59
87	13	15	10	45	75	115	117	148	45
118	11	23	10	116	100	40	96	87	132
131	54	8	14	76	51	110	77	170	111
97	33	16	6	76	31	76	98	148	51
118	6	37	5	51	65	101	29	114	101
90	4	35	17	41	54	123	62	146	90
125	6	6	56	97	59	31	70	125	80
113	49	7	5	33	33	90	42	117	76
116	4	54	5	74	29	98	98	173	75
128	66	16	4	51	30	117	72	136	114
131	15	67	5	143	71	66	105	108	124
94	22	17	5	91	51	50	57	118	70
98	9	16	9	56	30	57	65	113	56
108	4	15	29	123	32	63	124	139	83
113	10	17	5	99	50	96	52	125	109
106	14	6	10	65	51	73	116	93	70
93	8	40	11	61	27	77	43	121	104
128	6	4	31	63	37	113	67	111	135
126	8	15	49	154	18	14	140	159	27
127	5	39	4	80	15	104	69	146	113
116	9	17	11	28	23	87	38	83	67
105	8	11	24	66	56	73	68	139	83
97	5	33	9	76	50	108	112	118	113
107	7	13	6	61	12	62	62	84	67
119	9	44	6	98	57	76	94	99	126
128	22	10	45	86	34	13	58	91	39
125	34	7	9	51	59	75	90	120	80
125	16	11	48	60	61	78	92	108	83
103	5	33	13	65	52	93	104	80	93

E_o	E_1	E_2	E_3	θ_1	θ_2	θ_3	θ_{12}	θ_{13}	θ_{23}
121	34	10	11	43	20	61	49	103	63
115	10	31	26	83	15	79	90	141	66
107	19	13	10	61	47	39	69	97	50
62	8	6	6	86	54	89	58	156	128
86	19	10	5	93	54	59	79	124	106
80	12	6	7	85	37	94	58	164	121
119	9	17	17	84	64	37	42	120	90
101	7	6	8	124	47	82	94	131	87
86	7	9	16	72	107	133	122	82	70
95	12	6	4	106	35	76	89	126	80
130	27	15	13	64	43	34	92	86	54
84	8	19	5	95	60	96	114	116	99
130	7	6	31	66	43	83	39	122	97
94	17	16	10	117	9	35	120	141	29
97	17	4	33	74	24	87	81	139	85
103	19	21	9	22	69	113	61	123	147
120	28	10	46	78	37	44	54	122	77
95	17	6	5	154	31	101	138	99	97
83	16	13	9	98	58	41	80	137	78
86	8	3	10	85	5	113	82	147	114
123	6	13	13	101	33	66	133	116	52
96	9	7	23	57	57	101	94	91	139
109	9	4	27	58	60	157	77	140	122
54	6	6	6	59	11	101	55	126	102
89	8	30	8	74	31	30	45	90	53
94	8	17	6	79	72	107	36	105	74
120	5	74	5	87	30	84	61	132	108
112	6	30	11	102	39	97	112	135	63
111	9	26	21	126	22	38	137	151	29
105	11	14	7	114	79	86	96	131	52
131	12	14	31	37	52	18	61	54	59
108	10	33	8	65	39	133	74	123	112
101	14	8	38	79	29	77	59	142	95
90	6	10	15	106	40	59	98	147	69
119	25	6	8	60	45	92	48	145	110
120	8	8	32	76	46	39	115	108	40
123	5	40	18	61	34	45	88	99	33
119	24	5	24	37	74	153	109	152	88
91	7	8	16	72	85	87	127	127	38
118	24	17	24	19	23	73	38	70	84
119	30	23	9	66	27	81	93	129	62
132	33	39	20	20	18	116	33	132	101
99	12	6	11	102	50	66	86	156	71
107	26	6	12	78	26	69	94	113	63
131	6	9	61	126	54	8	96	134	58
125	36	23	14	39	22	36	59	74	18
105	62	11	8	31	26	144	46	139	130
110	33	15	4	57	40	56	18	113	95
129	38	25	10	45	49	53	92	82	29
118	25	23	7	145	52	36	95	146	82
84	7	10	10	62	52	77	39	128	117
71	17	8	6	75	41	98	64	150	116
83	17	7	12	127	104	62	26	169	160
127	7	25	12	59	37	76	57	107	112
130	8	13	16	36	109	148	121	145	56
132	13	31	5	89	35	31	62	119	58
111	7	10	12	51	52	126	71	105	95
86	5	8	41	96	72	51	84	131	53
107	13	6	5	90	64	67	124	66	129

E_o	E_1	E_2	E_3	θ_1	θ_2	θ_3	θ_{12}	θ_{13}	θ_{23}	E_o	E_1	E_2	E_3	θ_1	θ_2	θ_3	θ_{12}	θ_{13}	θ_{23}
121	7	45	8	112	59	98	115	116	105	130	30	7	12	122	80	67	97	124	77
125	44	16	15	44	61	47	83	82	83	105	18	8	10	54	37	119	85	163	96
115	11	16	58	94	64	31	47	125	93	108	32	20	8	63	62	98	37	158	130
119	42	5	17	172	76	9	102	176	83	106	27	7	23	96	56	61	56	119	111
124	10	36	15	102	52	80	53	96	73	111	36	20	18	74	13	99	61	133	109
90	10	9	32	89	48	91	119	165	71	85	7	5	16	95	30	105	71	52	81
91	22	8	14	42	31	125	47	144	146	121	8	12	9	58	41	70	45	126	87
125	6	15	33	91	35	98	93	109	90	123	27	34	9	105	53	79	87	125	52
122	14	19	12	54	39	98	62	115	64	81	13	8	5	47	73	114	91	145	82
103	23	7	9	23	71	140	83	162	80	119	37	8	12	80	40	82	92	161	74
131	9	50	15	97	39	78	60	134	105	123	36	7	8	106	41	50	72	94	36
99	10	8	10	90	71	72	32	162	132	112	21	15	27	124	47	40	158	111	75
131	11	22	13	85	31	76	64	135	106	126	8	11	9	50	47	137	58	158	124
118	7	41	6	104	46	48	97	152	66	100	36	21	7	26	35	40	32	62	73
101	6	16	38	110	32	52	113	147	67	123	26	50	10	93	64	70	83	157	102
117	8	14	18	74	32	68	106	139	38	89	5	7	9	109	59	27	55	132	83
68	10	5	7	101	51	111	57	100	100	117	12	7	8	121	44	69	105	156	97
125	57	9	3	114	24	60	127	75	84	129	34	14	8	46	9	50	51	86	42
105	19	9	3	113	49	67	70	144	88	121	30	23	8	26	37	118	19	144	144
105	36	7	5	55	34	124	86	97	134	121	9	30	9	84	53	78	119	79	123
116	9	52	24	108	34	45	75	140	75	128	9	14	45	170	62	28	116	143	80
113	15	9	8	52	69	130	121	103	117	123	35	25	12	48	43	100	88	139	75
114	17	20	21	63	18	97	56	150	97	129	14	9	53	138	25	25	122	161	43
117	11	10	19	138	83	55	91	136	99	115	5	15	42	94	66	55	136	127	72
110	10	13	18	76	68	24	13	78	67	88	29	6	5	139	35	75	130	132	90
113	12	46	24	52	52	42	101	35	89	118	11	40	16	56	19	77	39	78	70
120	8	41	32	86	65	46	43	129	108	113	12	43	14	42	4	117	42	114	118
127	11	24	52	118	71	40	88	153	92	109	8	19	12	109	25	21	128	130	16
74	6	14	17	117	12	67	110	151	78	103	5	20	15	114	16	52	115	86	59
125	6	26	17	80	44	69	73	129	63	117	27	20	11	97	59	50	90	139	62
108	8	11	15	98	45	88	53	109	96	122	11	39	32	52	30	74	70	88	92
104	10	7	16	90	49	128	46	54	81	130	11	7	18	98	46	112	93	140	121
121	10	21	20	21	21	78	35	69	78	81	6	6	9	41	10	114	45	90	108
125	8	21	14	88	38	57	75	127	88	129	26	50	20	70	50	69	68	137	71
111	23	29	11	18	24	60	41	69	57	70	4	5	6	109	50	58	109	132	90
120	6	31	12	115	29	49	89	153	69	123	19	23	14	87	33	66	87	131	90
125	10	8	64	121	88	36	49	106	62	130	6	20	6	86	26	95	120	175	62
100	11	23	19	95	19	35	86	114	31	66	9	6	5	71	73	103	143	154	45
122	26	8	8	20	37	148	44	158	114	122	6	39	7	97	54	50	119	90	98
111	12	12	17	23	29	141	40	155	117	98	24	11	12	5	90	140	85	136	64
120	21	46	7	81	19	96	93	155	81	101	16	46	5	47	20	137	61	144	138
111	5	9	18	87	52	71	59	108	100	124	9	52	13	88	31	117	59	140	141
97	12	5	19	125	53	62	132	154	54	111	34	16	5	65	48	72	38	136	106
128	10	26	13	79	52	57	41	132	107	108	36	9	11	78	47	63	115	139	26
112	14	26	12	93	33	128	108	97	146	124	5	7	18	132	55	24	125	144	59
118	31	12	10	129	20	46	140	164	39	121	42	26	7	115	13	61	127	173	48
83	5	10	30	95	76	37	119	128	58	127	10	63	12	107	57	33	68	133	76
72	10	5	7	157	39	70	131	114	87	128	7	29	38	64	32	26	58	78	58
76	7	5	17	131	62	48	87	137	79	125	5	33	13	68	56	118	123	135	66
125	4	58	14	62	50	89	105	139	44	80	22	12	6	39	19	82	22	118	96
121	14	12	30	147	19	73	145	104	81	112	6	18	6	82	52	62	124	94	71
74	19	6	7	50	54	111	83	150	71	123	10	19	41	103	17	114	96	136	113
110	5	30	11	73	45	78	29	130	41	126	7	57	7	136	27	69	121	88	74
94	7	17	7	73	53	70	69	70	101	131	6	61	10	120	36	56	86	161	89
103	7	4	33	151	70	32	91	129	88	116	8	14	26	106	18	28	108	121	23
78	8	6	15	101	71	30	31	129	99	101	9	17	17	53	47	50	98	96	15
105	7	11	23	78	55	41	109	101	57	114	27	8	25	82	59	48	56	131	90
83	16	14	10	21	35	112	55	127	86	117	38	5	7	48	64	131	75	148	105
90	15	13	16	42	38	77	79	85	83	130	6	12	40	80	23	48	94	125	44

E_o	E_1	E_2	E_3	θ_1	θ_2	θ_3	θ_{12}	θ_{13}	θ_{23}
131	5	7	82	92	27	20	72	111	41
115	10	6	6	74	63	78	29	73	45
120	10	8	6	79	43	79	58	112	94
125	7	9	11	106	40	80	143	68	108
114	22	22	5	33	77	98	105	130	43
79	19	10	13	145	47	29	118	147	69
108	60	9	7	72	33	79	84	107	47
78	5	6	19	98	59	79	97	93	135
84	6	6	6	98	14	108	106	54	104
119	19	24	27	31	22	35	32	52	15
80	22	5	7	97	58	87	105	127	61
118	13	6	5	65	53	84	75	141	84
96	9	14	23	118	58	68	61	122	101
123	41	7	31	73	25	147	93	140	126
67	4	11	5	82	13	148	80	123	141
128	12	8	43	72	20	102	72	99	122
125	7	7	42	107	46	35	64	125	63
120	5	13	7	61	77	81	71	130	132
120	8	20	28	85	52	61	73	132	47
80	10	12	15	46	70	83	93	91	49
128	15	45	40	38	51	98	28	128	149
123	13	27	12	85	49	38	102	110	73
84	11	16	7	129	59	65	100	130	42
110	33	15	4	57	40	56	18	113	95
112	7	7	9	96	58	60	81	109	68
71	8	10	5	96	23	103	85	136	103
123	21	8	14	47	45	105	5	64	64
130	29	13	21	89	32	90	116	136	59
98	6	39	6	77	48	82	67	130	125
133	5	27	10	65	35	110	96	145	93
115	8	41	17	59	61	77	79	126	52
98	12	8	5	109	40	66	109	162	57
115	9	7	46	141	82	23	101	161	86
85	6	6	6	48	39	95	79	116	95
95	17	6	25	151	68	27	118	143	93
103	7	18	10	43	34	105	40	124	138
88	13	6	13	71	48	79	73	140	70
117	7	5	57	117	34	43	95	150	62
113	7	9	14	32	52	100	78	127	48
88	10	7	6	146	43	18	107	151	51
128	12	18	36	125	64	62	67	145	101
118	9	6	7	66	34	56	77	118	54
104	20	12	12	45	41	28	44	70	48
90	11	25	6	114	24	64	137	100	71
76	9	5	8	48	68	128	85	137	63
117	45	12	12	77	57	87	134	147	42
95	6	7	6	44	55	98	65	91	45
127	5	18	10	56	18	102	65	133	87
129	33	13	9	62	53	110	103	141	98
131	13	34	7	91	32	111	115	117	81
122	17	9	60	134	23	15	132	148	30
113	26	29	11	106	22	69	128	153	50
108	6	5	13	65	9	140	62	101	131
105	7	22	15	99	23	63	91	127	82
122	39	6	13	27	33	117	59	143	87
129	19	52	11	47	63	71	109	117	19
125	19	53	7	113	53	71	155	164	40
125	16	14	11	140	52	76	118	126	91
122	11	7	6	66	30	114	61	135	107

E_o	E_1	E_2	E_3	θ_1	θ_2	θ_3	θ_{12}	θ_{13}	θ_{23}
118	18	9	8	74	31	64	98	130	34
126	9	59	15	152	22	88	159	111	77
86	14	5	7	128	64	77	65	61	25
79	16	16	10	58	80	101	134	150	21
124	21	13	19	29	60	56	44	79	93
110	37	7	4	63	49	66	38	110	103
126	8	47	14	86	34	139	116	109	112
123	10	9	12	58	43	31	57	57	15
121	7	21	11	89	36	63	104	131	65
119	17	14	10	38	52	137	38	103	89
93	10	22	17	87	32	37	97	94	7
93	13	17	13	62	22	142	75	145	134
119	11	40	4	57	27	89	54	70	62
118	20	32	31	81	65	49	88	80	113
90	8	11	22	74	48	21	63	88	59
120	15	27	39	85	40	43	54	65	15
122	9	44	10	62	41	50	93	107	91
83	5	8	10	109	61	64	153	159	43
124	35	12	9	107	39	70	91	80	70
99	18	17	6	65	28	80	54	128	77
118	6	31	34	117	54	48	71	100	75
121	15	8	35	132	67	39	138	132	87
77	17	10	6	106	36	35	118	125	56
129	22	50	10	81	34	63	84	120	87
112	8	12	31	134	37	81	98	124	98
131	9	4	16	91	49	87	113	149	84
116	12	52	8	53	63	114	99	139	48
131	5	33	6	89	26	83	80	75	104
115	8	22	35	41	59	43	93	73	69
116	22	36	14	41	27	100	62	134	92
125	7	9	19	108	51	47	150	85	89
132	7	17	52	121	15	37	111	150	43
82	3	7	5	87	68	79	108	165	70
62	8	7	8	81	68	115	24	59	54
132	37	14	5	82	61	101	131	118	99
112	7	20	6	59	37	111	56	153	117
92	5	23	7	88	19	77	73	133	95
126	7	32	7	83	15	132	89	132	125
133	35	22	8	50	59	95	48	138	140
109	10	8	6	92	50	65	69	103	108
78	12	19	7	124	74	25	54	135	86
132	12	13	19	99	83	86	137	138	84
126	11	4	17	96	33	72	129	140	51
130	8	19	15	67	53	86	39	133	95
61	6	22	5	61	44	72	77	108	77
123	9	9	33	105	60	58	57	157	114
126	27	22	40	170	30	20	140	162	37
132	11	17	15	41	31	89	71	78	105
93	16	32	8	66	14	68	79	43	74
121	23	19	14	144	35	20	135	140	55
122	54	5	12	72	54	118	80	143	92
129	14	50	3	95	53	86	61	136	138
101	5	19	5	80	58	128	113	104	74
123	8	11	21	97	55	83	75	151	105
112	7	23	12	48	29	119	54	127	143
125	42	19	5	44	17	94	51	125	87
77	5	14	14	72	21	58	84	55	79
63	10	4	11	154	27	142	136	56	151
109	10	60	7	77	31	85	107	156	56

E_o	E_1	E_2	E_3	θ_1	θ_2	θ_3	θ_{12}	θ_{13}	θ_{23}	E_o	E_1	E_2	E_3	θ_1	θ_2	θ_3	θ_{12}	θ_{13}	θ_{23}
111	38	9	4	65	55	110	117	133	83	87	12	21	6	78	72	101	61	101	46
110	8	27	25	54	20	76	57	128	74	111	10	12	4	53	22	92	58	76	110
101	24	12	12	55	29	51	32	101	73	82	9	13	9	135	57	99	165	85	85
100	32	12	5	93	21	77	75	103	71	125	8	61	8	66	27	119	83	172	100
116	37	15	19	74	56	50	108	97	89	106	12	4	8	47	43	127	80	160	107
132	37	15	4	98	81	63	20	133	116	117	8	35	38	87	46	32	113	119	36
65	8	23	7	72	39	86	110	133	52	118	22	26	8	126	31	67	148	113	79
97	5	7	47	97	36	60	97	152	74	121	9	24	13	60	59	73	112	99	62
94	8	7	10	35	44	102	58	115	90	122	9	5	47	134	35	50	130	149	73
100	10	10	28	106	33	10	89	111	30	100	5	6	6	47	33	99	56	127	92
102	43	15	6	87	25	83	109	145	71	89	13	11	14	72	33	122	102	132	105
123	12	7	7	45	36	104	42	99	88	132	24	14	16	74	36	43	51	78	67
69	5	8	16	59	46	76	63	116	64	74	38	7	6	57	50	96	85	125	50
97	18	9	7	109	39	77	99	128	63	111	16	21	10	37	32	62	58	87	75
118	21	12	6	129	58	27	73	135	76	106	16	4	8	167	46	31	129	156	62
96	13	7	17	90	41	132	77	133	117	124	6	14	6	53	44	132	27	167	149
120	19	5	8	130	28	68	126	83	70	105	17	15	5	15	9	81	17	88	78
105	11	32	7	110	24	74	96	53	77	89	10	8	6	118	24	57	128	151	39
114	11	9	43	78	19	130	64	127	145	127	6	44	13	40	28	128	64	153	100
68	6	7	18	42	58	110	62	123	106	109	30	7	15	72	49	88	31	151	133
109	11	4	5	114	13	86	106	128	98	133	10	63	5	76	33	89	47	104	94
113	10	8	41	136	73	40	106	143	99	130	9	27	4	94	35	95	63	151	117
120	39	4	11	84	47	81	68	150	109	100	4	12	22	84	33	111	98	139	112
122	23	5	27	64	48	118	83	144	101	105	27	19	6	45	65	104	73	111	116
84	6	10	11	59	80	153	109	144	83	93	10	29	9	82	36	119	116	126	89
126	24	27	7	46	63	68	81	107	63	110	8	21	41	73	19	71	71	105	71
89	9	38	7	52	17	94	68	96	96	118	5	6	63	118	34	43	114	153	49
98	8	25	16	110	40	136	98	112	137	114	7	34	22	130	67	54	105	150	100
92	13	19	7	50	76	89	27	85	76	106	12	8	11	55	35	52	63	105	47
128	16	37	6	89	39	95	55	143	109	117	22	53	6	51	17	82	59	103	67
130	5	9	15	95	34	44	115	126	22	116	16	22	33	47	31	75	34	108	106
102	37	15	9	47	33	74	60	99	44	117	9	4	51	89	26	105	64	166	129
85	5	13	7	48	14	138	55	122	133	111	4	20	5	60	60	99	79	157	94
124	9	17	32	52	41	77	57	115	92	114	5	21	16	67	85	115	78	158	123
128	16	35	22	61	49	13	27	65	58	113	17	10	24	110	53	67	92	125	114
113	26	41	12	35	33	87	28	109	119	126	6	69	10	38	22	121	55	155	106
102	8	3	6	119	36	65	98	143	98	90	10	28	4	75	46	51	64	101	84
92	8	7	10	110	45	73	70	98	91	118	4	17	17	84	25	88	106	109	90
101	8	6	3	78	8	64	86	135	57	106	7	18	34	111	46	38	65	143	83
125	8	43	8	118	21	86	105	119	104	121	7	20	7	49	71	96	89	117	36
127	33	46	8	59	22	85	46	104	105	106	12	11	14	73	64	50	115	51	115
76	10	10	9	35	69	124	95	143	101	86	13	9	7	74	62	98	113	116	118
91	11	11	8	109	15	47	108	113	49	128	17	26	6	47	44	115	88	120	85
119	24	3	4	64	14	93	68	157	89	109	11	15	20	9	60	50	64	58	68
73	6	16	17	64	51	88	94	87	113	126	51	19	6	65	50	50	76	59	97
124	20	54	11	67	37	77	59	115	111	116	43	5	7	68	36	112	98	158	85
112	27	10	10	66	60	44	62	97	92	129	6	68	9	59	81	84	43	137	156
125	8	11	20	19	77	148	86	136	108	66	8	7	5	99	29	91	106	80	68
111	9	10	32	39	30	67	58	101	68	120	7	8	18	102	19	73	89	158	84
119	15	6	30	112	72	30	105	97	99	117	34	10	32	44	36	59	52	102	61
102	17	9	7	146	30	62	164	120	70	125	43	9	10	130	33	36	122	149	30
121	5	24	54	95	28	37	118	118	32	121	6	14	7	88	28	77	64	127	99
131	21	47	20	80	21	39	65	94	37	110	21	6	10	122	38	54	122	165	59
119	51	35	4	22	30	76	11	92	91	104	7	10	8	76	31	105	87	131	107
72	26	7	8	94	29	94	92	169	89	121	22	23	30	68	50	77	107	140	34
107	10	11	29	95	21	51	79	109	69	130	9	19	5	106	27	107	122	108	87
131	14	9	6	82	72	47	15	127	119	124	16	25	30	59	36	111	56	155	130
132	6	42	11	88	44	72	116	128	75	102	7	8	23	61	27	58	67	88	66
99	6	31	29	128	45	56	121	75	84	131	6	31	24	45	61	70	83	112	40

E_0	E_1	E_2	E_3	θ_1	θ_2	θ_3	θ_{12}	θ_{13}	θ_{23}
130	17	16	7	71	42	83	108	126	52
130	6	53	6	83	59	126	116	151	81
129	8	9	5	76	30	104	69	150	108
102	9	9	42	89	18	49	90	131	49
78	10	18	15	128	52	54	118	145	83
89	16	16	21	39	26	53	79	113	66
129	27	23	11	52	40	56	66	93	87
129	5	60	9	83	64	66	98	125	89
131	6	4	8	131	53	58	80	170	110
124	44	6	14	100	32	92	106	165	78
112	20	8	9	64	45	207	90	111	88
116	8	26	17	59	9	101	55	143	109
101	27	29	8	151	46	71	119	138	89
128	9	59	8	72	31	141	66	102	111
103	12	51	5	144	46	44	104	147	67
125	36	20	9	121	91	62	31	154	142
90	5	19	6	111	17	96	123	138	80
94	10	32	11	80	50	53	101	115	82
91	7	7	31	91	57	79	46	133	94
109	15	8	16	64	49	41	54	94	47
111	22	15	16	63	59	64	92	99	8
89	22	17	8	33	25	55	41	80	47
90	8	15	15	90	57	117	46	139	122
120	11	18	12	58	43	57	69	114	69
78	5	6	7	59	47	137	44	137	136
99	24	19	15	81	22	75	71	151	91
112	6	31	32	77	60	70	132	146	18
127	21	10	16	34	18	150	22	170	166
132	28	29	6	59	41	86	41	109	105
102	27	8	5	96	26	66	118	139	57
110	37	26	7	31	24	96	9	125	118
107	7	13	41	99	70	53	51	51	24
106	31	18	17	43	24	74	63	57	98
130	16	24	26	63	30	84	88	148	61
124	16	3	5	91	24	90	67	175	113
80	6	6	30	104	66	43	143	112	86
72	14	7	6	57	66	106	41	158	122
111	19	14	21	100	69	50	32	142	114
79	6	9	7	59	64	113	79	142	68
130	4	8	32	79	27	51	103	105	38
129	23	41	8	42	44	92	82	131	62
83	29	13	7	34	30	123	29	145	144
122	28	41	5	119	44	86	120	109	120
92	92	15	7	31	49	116	55	144	115
128	35	35	11	16	39	149	54	159	117
106	10	7	22	81	79	109	106	137	117
113	21	26	8	60	50	100	93	148	90
109	6	23	13	67	76	130	140	123	73
91	7	17	9	103	52	57	129	150	39
106	34	12	4	52	32	59	72	107	62
104	12	8	17	28	63	103	81	126	85
114	6	18	39	82	17	67	67	106	80
80	19	15	10	72	61	25	16	80	68
127	31	4	42	139	38	51	104	170	86
121	39	18	8	61	55	49	31	50	20
131	27	5	21	113	91	48	60	133	77
112	28	53	4	111	21	81	92	99	89
123	33	33	23	60	31	29	61	81	25
132	27	20	43	53	39	78	76	125	54

E_0	E_1	E_2	E_3	θ_1	θ_2	θ_3	θ_{12}	θ_{13}	θ_{23}
73	5	8	7	74	71	76	102	128	108
108	7	6	57	54	61	109	82	154	100
79	9	12	6	79	38	112	92	84	119
98	6	6	15	114	65	66	66	131	75
87	9	25	5	101	17	60	90	139	74
97	26	9	11	67	67	87	132	142	45
110	26	22	5	58	36	88	36	118	96
83	5	26	11	65	27	136	73	131	139
92	19	6	11	105	49	76	97	104	69
101	7	11	23	84	47	47	42	104	67
114	30	7	9	154	44	25	115	136	32
111	8	12	11	50	22	121	44	144	115
98	32	18	7	59	48	84	49	85	113
129	36	8	5	96	26	45	81	128	62
107	6	37	16	27	40	124	46	129	95
87	10	9	27	128	51	11	80	124	52
128	7	29	15	32	49	133	47	139	96
124	53	20	12	48	63	76	103	112	15
113	22	36	6	94	40	71	126	66	106
95	4	9	19	81	34	71	102	113	40
99	18	20	6	163	44	40	122	148	60
65	6	5	9	96	46	104	59	89	117
109	15	4	18	103	22	123	105	56	143
95	10	9	14	118	30	24	101	127	39
86	5	6	23	92	47	86	92	149	68
123	23	13	11	55	46	79	72	121	87
74	6	7	7	48	31	143	57	161	123
104	12	5	46	117	51	41	74	139	89
124	4	41	14	85	47	40	60	119	84
122	33	8	10	93	17	34	85	113	42
117	12	20	26	104	21	54	114	143	41
130	16	25	20	32	38	75	49	101	94
121	10	10	18	78	32	111	98	150	81
105	7	6	8	141	50	45	95	129	72
127	4	6	20	60	33	112	91	160	80
111	12	27	22	41	36	95	56	133	79
95	8	14	23	90	32	43	86	91	75
112	25	7	8	79	39	81	76	140	115
49	6	8	6	77	45	99	82	139	78
117	23	21	6	87	40	97	56	138	116
122	10	23	37	119	51	56	72	165	107
124	24	5	27	74	41	38	78	112	54
120	13	40	13	106	41	127	147	127	86
82	37	6	5	84	44	70	47	95	78
123	25	24	13	124	15	67	118	152	79
116	13	7	28	79	19	109	64	160	123
102	7	15	11	134	66	64	73	151	123
111	16	6	4	137	68	17	81	147	84
79	24	6	5	161	16	19	126	151	62
96	26	7	5	113	39	73	97	173	87
93	7	29	3	100	18	77	106	125	64
103	15	24	13	42	20	50	55	20	55
115	9	16	8	55	45	52	55	92	56
120	11	12	14	158	48	35	143	124	56
125	37	17	4	50	17	86	36	112	92
92	6	20	17	129	55	104	77	124	137
106	14	4	16	75	28	48	69	109	74
108	12	8	11	55	50	79	82	111	104
120	12	5	18	139	64	88	104	119	84

E_o	E_1	E_2	E_3	θ_1	θ_2	θ_3	θ_{12}	θ_{13}	θ_{23}
118	10	11	51	83	58	35	63	103	48
105	7	19	17	67	60	102	122	104	68
103	17	9	10	110	83	65	70	93	25
108	9	12	12	80	64	95	120	82	59
107	4	13	18	88	14	86	98	159	79
118	10	53	12	20	67	74	81	91	72
86	7	5	11	88	21	34	82	119	40
131	5	22	47	68	14	28	72	88	26
82	14	4	12	50	38	112	73	80	118
112	13	11	10	111	46	102	68	139	140
98	15	9	10	66	30	140	86	93	128
110	6	38	5	86	19	84	72	139	91
115	4	31	8	78	21	7	99	140	91
102	13	28	6	101	18	41	112	139	34
120	6	6	62	34	43	109	45	142	114
91	11	7	6	87	41	65	77	143	77
89	12	4	11	155	57	17	110	152	70
121	7	24	28	62	59	67	63	97	24

E_0	E_1	E_2	E_3	θ_1	θ_2	θ_3	θ_{12}	θ_{13}	θ_{23}
98	23	21	6	10	5	74	15	77	75
83	8	7	7	65	14	82	59	35	70
95	9	6	6	160	61	49	115	140	36
101	29	31	8	66	75	119	136	132	83
131	39	25	15	45	21	38	64	80	19
111	5	35	19	89	25	48	106	117	32
96	18	12	17	22	48	30	65	49	41
94	14	15	4	71	18	106	62	139	118
113	17	5	25	30	36	79	58	109	55
107	6	16	17	60	43	77	89	124	38
121	5	17	5	123	30	54	118	159	53
116	20	10	4	95	23	105	105	151	87
122	35	38	8	73	60	57	131	73	72
125	7	32	13	136	45	49	130	154	34
103	59	8	8	43	32	84	57	96	62
101	19	8	15	121	68	47	71	156	93
72	8	8	19	42	53	117	82	141	65

References

REFERENCES

Abate E., Bellini G., Fiorini E., Ratti S., (1961) Il Nuovo Cimento 22, 1206

Adams & Edmunds (1950) AERE - G/R - 568

Anderson D.W. (1960) Ph.D. thesis Cambridge

Austin S.M., Salmon G.L., Clegg A.B., Foley, K.J., & Newton D. (1962) Proc. Phys. Soc. 80, 383

Azhgirei L.S., Vzorov I.K., Zrelov V.P., Mescheryakov M.G., Neganov B.S., Pyndin R.B. & Shabudin A.F. (1959) N.P. 13, 258

Balashov V.V. & Boyarkina A.N. (1964) Bull. Acad. Sc. USSR. Phys. Ser. 28, 277

Baz A.I. (1956) J.E.T.P. 4 (31) 704

Bernardini G., Booth E.T., & Lindenbaum S.I. (1952) Phys. Rev. 85, 826

Bertini H.W. (1963) Phys. Rev. 131, 1801

Bertini H.W. (1964) Private communication

Blokhintsev D.I. (1958) J.E.T.P. 6 (33) 995

Böck B. (1960) CERN Report 60-7

Bohr N. (1937) Science 86, 161

Bowman M.R. (1964) D. Phil. thesis Oxford

Bradner H. (1960) An. Rev Nucl. Sc. 10, 109

Brueckner K.A. & Levinson C.A. (1955) Phys. Rev. 97, 1344

Brueckner K.A. (1955) Phys. Rev. 97, 1353

Brueckner K.A., Eden R.J. & Francis N.C. (1955) Phys. Rev. 97, 1366

" " " (1955) Phys Rev. 98, 1445

Bugg D.V. (1959) Prog. Nucl. Phys. 7, 2

Bunakov V.E. (1963) Phys. Lett. 7, 140

Chew G.F. & Wick G.C. (1952) Phys. Rev. 85, 636

Cladis J.B., Hess W.N. & Moyer B.J. (1952) Phys. Rev. 87, 425

Clegg A.B., Foley K.J., Salmon G.L. & Segal N.E. (1961) Proc. Phys. Soc. 78, 681

Clegg A.B. (1963) Proceedings of the International Conference on High Energy Physics and Nuclear Structure CERN 63-28

Combe J. (1955) J. de Phys. 16, 445

Combe J. (1956) Supp. Nu. Cim. 3, 182; Cüer P., Samman A. & Combe J. (1955) Compt. Rend. 240, 1527

Cook L.J., McMillan E.M., Peterson J.M. & Sewell D.C. (1949) Phys. Rev. 75, 7

Crandall E.W., Millburn G.P., Pyle R.V. & Birnbaum W. (1956) Phys. Rev. 101, 329

Crennell D.J. (1963) D. Phil. thesis Oxford

Cüer P. & Combe J. (1954) Compt. Rend. 239, 351

Cüer P., Combe J & Samman A (1955) Compt. Rend. 240, 75

Cüer P., Samman A. & Combe J (1955) Compt. Rend. 240 1527

Dickens J.K., Haner D.A. & Waddell C.N. (1963) Phys. Rev. 132, 2159

Dodd C. (1956) Prog. Nucl. Phys. 5, 142

Dostrovsky I., Rabinowitz P., Bivins R. (1958) Phys Rev. 111, 1659

Dowell J.D., Frisken W.R., Martelli G. & Musgrave B. (1960) Proc. Phys. Soc. 75, 24

Elton L.R.B. & Gomes L.C. (1957) Phys. Rev. 105, 1027

Elton L.R.B. (1961) "Nuclear Sizes" O.U.P. p. 65

Fretter W.B. (1953) Ann. Rev. Nucl.Sc. 5, 145

Friedman J. (1956) reported by Metropolis et al. p.189

Garron J.P., Jackmort J.C., Riou M., Ruhla G., Reillac J. & Strauch K. (1962) N.P. 37, 126

Glaser D.A. (1952) Phys. Rev. 87, 665

Goldberger M.L. (1948) Phys. Rev. 52, 295

Gooding T.J. & Pugh H.G. (1960) N.P. 18, 46

Goswami A. & Pal M.K. (1963) N.P. 44, 294

Gottfried K. (1963) Ann. of Phys. 21, 29

Gradstejn (1962) Private communication

Grover J.R. & Caretto A.A. (1964) Ann. Rev. Nucl. Sc 14, 51

Herman & Hofstadter (1960) "High Energy Electron Scattering Tables" Stanford U.P. 1960

Hartree D.R. (1928) Proc. Camb. Phil. Soc. 24, 89

Hess W.N. (1958) Rev. Mod. Phys. 30, 368

Hofstadter R. (1957) Ann. Rev. Nucl. Sc. 7, 231

Hopkins H.W.K. (1961) D. Phil. thesis Oxford

James A.N. & Pugh H.G. (1963) N.P. 42, 441

Johansson A. & Sakamoto Y. (1963) N.P. 42, 625

Lane A.M. & Wandel C.F. (1955) Phys. Rev. 98, 1524

Lane A.M. & Wilkinson D.H. (1955) Phys. Rev. 97, 1199

Livingstone M.S. & Bethe H.A. (1937) Rev. Mod. Phys. 9, 201

McKenzie J. (1960) Ph.D. thesis, Cambridge

McEwen J.G., Gibson W.M. & Duke P.J. (1957) Phil. Mag. 8th series 2, 231

Metropolis N., Bivins R., Storm M., Turkevich A., Miller J.M. & Friedlander G. (1958) Phys. Rev. 110, 185

Miller J.M. & Hudis J. (1959) Ann. Rev. Nucl. Sc. 9, 159

Morrison D.L. & Caretto A.A. (1962) Phys. Rev. 127, 1731

Ostroumov V.I. & Filov R.A. (1960) J.E.T.P. 10 (37) 459

Perfilov N.A. & Serebrennikov Yu.I. (1961) J.E.T.P. 13 (40) 274

Pickavance T.G. & Cassels J.M. (1952) Nature 169, 520

Radvanyi P. & Génin J. (1960) J. de Phys. 21, 322
Rich M. & Madey R. (1954) UCRL 2301 Rev. Tables
Riley K.F., Pugh H.G. & Gooding T.J. (1960) N.P. 18, 65

Samman A. (1956) Compt. Rend. 242, 2232

Samman A. (1956) Compt. Rend. 242, 3062

Samman A. & Cüer D. (1958) J. de Phys. 19, 1; see also under Cüer and under Combe

Serber R. (1947) Phys. Rev. 72, 1114

Sheline R.K. & Wildermuth K. (1960) N.P. 21, 196

Squires E.J. (1958) Proc. Phys. Soc. 72, 433

Sternheimer R.M. (1960) Phys. Rev. 117, 485

Tyrén H., Hillman P. & Maris T.A.J. (1959) N.P. 7, 1

Tyrén H., Kullander S., Sundberg O., Ramachandran R., Isacsson P. & Berggren T. USAF Grant No. AF-AFOSR18-64

Wattenberg A., Odian A.C., Stein P.C., Wilson H. & Weinstein R. (1956) Phys. Rev. 104, 1710

Weisskopf V. (1937) Phys. Rev. 52, 295

Yuasa T. & Poulet H. (1963) J. de Phys. 24, 1062 and private communications

Zhdanov A.P. & Fedotov P.I. (1960) J.E.T.P. 11 (37) 280
(1962) J.E.T.P. 14 (41) 1330
(1964) J.E.T.P. 18 (45) 513